Interface Engineering for Perovskite Solar Modules and Multi-Junction Photovoltaics

Zur Erlangung des akademischen Grades eines

DOKTORS DER INGENIEURWISSENSCHAFTEN (Dr.-Ing.)

von der KIT-Fakultät für Elektrotechnik und Informationstechnik des Karlsruher Instituts für Technologie (KIT)

angenommene

Dissertation

von

M.Eng. Hang Hu
geb. in Huibei, V.R. China

Tag der mündlichen Prüfung: 18.03.2024

Hauptreferent: **Prof. Dr. Ulrich W. Paetzold**
Karlsruher Institut für Technologie

Korreferenten: **Prof. Dr. Felix Deschler**
Universität Heidelberg

Kurzfassung

Solarenergie ist eine der nachhaltigsten Energiequellen um zukünftig den steigenden globalen Energiebedarf zu decken. Photovoltaik ist die Schlüsseltechnologie für die weltweiten Bemühungen um eine netto-kohlenstofffreie Energieerzeugung zu erreichen. In den letzten Jahren sind Perowskit-Solarzellen als äußerst vielversprechende Technologie der nächsten Generation von Photovoltaik aufgekommen. Sie versprechen hohe Wirkungsgrade in Kombination mit niedrigen Herstellungskosten. Die Technologie eröffnet zudem eine neue Ära ultrahocheffizienter Mehrfachsolarzellen auf Perowskit-Basis bei denen die obere Perowskit-Solarzelle mit breiter Bandlücke mit den darunterliegenden Solarzellen bestehend aus Perowskit, Kupfer-Indium-(Gallium)-Selenid oder Silizium kombiniert wird. Mehrfachsolarzellen bieten einen Weg das Shockley-Queisser-Limit von Einzelsolarzellen zu überschreiten. Allerdings müssen für die zukünftige Kommerzialisierung eine Reihe von Schlüsselherausforderungen angegangen werden. Erstens motiviert der große Verlust von Leerlaufspannung in Sn-Pb-basierten Perowskit-Solarzellen und Tandems (Doppelsolarzellen) die nicht-strahlende Rekombination zu minimieren und die Ladungsextraktion zu verbessern. Zweitens werden hohe Wirkungsgrade (> 24%) bisher nur bei Solarzellen auf kleinen Flächen (~1 cm^2) erreicht und es müssen neue Verfahren für die Hochskalierung (> 10 cm^2) der Technologie entwickelt werden. Drittens befindet sich die Forschung zu Perowskit-Mehrfachsolarzellen (z.B. Dreifachsolarzellen) noch in einem frühen Stadium, so dass man sich auf die Herausforderungen und die Komplexität der Fabrikation konzentrieren muss. Ziel dieser Arbeit ist es, die oben genannten Herausforderungen (einschließlich Effizienz, Stabilität und Skalierbarkeit) bei der Entwicklung effizienter Sn-Pb-basierter Perowskit-Solarzellen sowie Perowskit-Perowskit-Tandems, Solarmodule und Dreifachsolarzellen anzugehen.

Diese Arbeit trägt zur Entwicklung von schmalbandigen Sn-Pb-basierten Perowskit-Solarzellen bei, indem sie eine Zwischenschicht an der Grenzfläche von schmalbandigem Perowskit und Elektronentransportschicht einführt. Eine Vielzahl von Zwischenschichten aus Fullerenen wurde in Pb-basierten Perowskiten (Bandlücken > 1,5 eV) umfassend untersucht, jedoch nicht in schmalbandigen Perowskit-Solarzellen. In dieser Arbeit werden daher zwei neuartige lösungsprozessierte Fullerenderivate als Zwischenschicht an der Grenzfläche zwischen schmalbandigem Perowskit und Elektronentransportschicht entwickelt. Die Auswirkungen der Zwischenschicht auf die Effizienz sowie der zugrundeliegende nicht-strahlende Rekombinationsmechanismus werden systematisch untersucht. Diese entwickelte Strategie ermöglicht effiziente schmalbandige Perowskit-Solarzellen und Vier-Terminal-Perowskit-Perowskit-Tandemsolarzellen.

Des Weiteren bringt diese Arbeit die Entwicklung der Hochskalierung von Mittelbandlücken-Perowskit-Solarzellen basierend auf Formamidinium-Bleiiodid ($FAPbI_3$) in der p-i-n-Architektur voran. $FAPbI_3$-basierte Perowskit-Solarzellen zeigten hohe Wirkungsgrade in Solarzellen auf kleinen Flächen, aber die Skalierbarkeit ist nicht gegeben. Die Auswirkungen von Hohlraumbildungen an der eingebetteten Grenzfläche zwischen Perowskit und Lochtransportschichtauf auf die nicht-strahlende Rekombination und

Ladungsextraktion werden für kleinflächige Solarzellen (0,105 cm^2) systematisch untersucht. Eine neuartige Strategie mit kontrolliertem Stickstofffluss während des vakuumunterstützten Materialformierungsprozesses mit Methylammoniumchlorid als Zusatz im Perowskit-Präkursor wird entwickelt, um hochwertige, großflächige, rakelbeschichtete Perowskit-Dünnschichten ohne Hohlräume und Löcher zu fabrizieren. Ein hoher Wirkungsgrad von 18,3% für vollständig skalierbare $FAPbI_3$-Perowskit-Solarminimodule (Aperturfläche von 12,25 cm^2) wird mit vernachlässigbarem Skalierungsverlust erreicht. Damit zeigt diese Arbeit eine bemerkenswerte Verbesserung für die Weiterentwicklung von Perowskit-Solarmodulen.

Außerdem beschreibt diese Arbeit monolithische Dreifach-Perowskit–Perowskit–Silizium-Solarzellen. In den letzten Jahren haben zahlreiche Berichte die Entwicklung von hocheffizienten Perowskit-Tandem-Solarzellen behandelt. Angesichts des noch höheren Potenzials von Dreifachsolarzellen zeigt diese Arbeit optische Simulationen und entwickelt experimentelle Optimierungen von Dreifach-Perowskit–Perowskit–Silizium-Solarzellen. Mit optimiertem Lichtmanagement wird die Stromabweichung minimiert und die Stromerzeugung auf 11,6 mA cm^{-2} maximiert. Eine wichtige Absorberschicht wird unter Verwendung einer Mittelbandlücken-Perowskit-Dünnschicht entwickelt, d.h. eine stabile, reine α-Phasen-$FAPbI_3$-Dünnschicht ohne Falten, Risse und Löcher, was hohe Leerlaufspannungen in den Dreifachsolarzellen ermöglicht. Die optimierten Dreifachsolarzellen zeigen einen hohen Wirkungsgradvon 24,4% und ausgezeichnete thermische Stabilität. Damit zeigt diese Arbeit einen signifikanten Fortschritt der Fabrikation von Perowskit-basierten Mehrfachsolarzellen.

Abstract

Soar energy is one of the most sustainable energy resources to target the increasing global energy demand in the future. Photovoltaic (PV) technologies are the key to global endeavours in achieving net-zero-carbon power. In recent years, perovskite solar cells (PSCs) arose as a highly promising technology for next-generation PV, promising high power conversion efficiencies (PCEs) in combination with low manufacturing costs. The technology further start a new era of ultra-high-efficiency perovskite-based multi-junction PVs, where wide bandgap perovskite top solar cells are combined with narrow bandgap perovskite, copper indium (gallium) selenide, or silicon (Si) bottom solar cells. Multi-junction solar cells offer a route to surpass the detailed-balance limit of single-junction solar cells. However, a number of key challenges need to be addressed for future commercialization. First, a large open-circuit voltage (V_{OC}) loss in Sn-Pb based PSCs as well as tandems (double junction) motivates to minimize non-radiative recombination and enhance charge extraction. Second, to date high PCEs (> 24%) are achieved only on small area devices (~1 cm^2) and the upscaling (> 10 cm^2) technology need to be developed. Third, as the research on multi-junction (such as triple junctions) perovskite-based PVs is still at an early stage, the processing challenges and complexities are needed to be focused on. The aims of this thesis are targeting the above-mentioned challenges (including efficiency, stability, and scalability) in developing efficient Sn-Pb based PSCs as well as all-perovskite tandems, solar modules, and triple-junction solar cells.

First, this thesis contributes to the development of narrow-bandgap (NBG) Sn-Pb based PSCs by introducing an interlayer at the interface of NBG perovskite/electron transport layer (ETL). A variety of fullerene interlayers have been extensively studied in Pb-based perovskite (bandgaps > 1.5 eV) but not in NBG PSCs. Two novel solution-processed fullerene derivatives are developed in this thesis as an interlayer at the interface of NBG perovskite/ETL. The effect of the interlayer on PV performance and the non-radiative recombination mechanism behind are systemically studied. This strategy is able to achieve an efficient NBG PSCs and four-terminal all-perovskite tandem solar cells.

Second, this thesis advanced the development in upscaling of middle-bandgap (MBG) formamidinium lead iodide ($FAPbI_3$) PSCs in *p-i-n* architecture. $FAPbI_3$ based PSCs were demonstrated high PCEs in lab-scale devices, but the scalability lags behind. The effect of interfacial voids at the buried interface of perovskite/hole transport layer (HTL) on the non-radiative recombination and charge extraction are systemically investigated within small-area (0.105 cm^2) PSCs. A novel strategy of well-controlled nitrogen flow during vacuum-assisted growth process and methylammonium chloride as an additive in the perovskite precursor is developed to obtain high-quality large-area blade-coated perovskite thin films free of voids and pinholes. A high PCE of 18.3% for fully scalable $FAPbI_3$ perovskite solar mini-modules (aperture area of 12.25 cm^2) is achieved with negligible up-scaling loss. This thesis shows a remarkable improvement for advancing perovskite solar module PVs.

Third, this thesis reports on monolithic triple-junction perovskite–perovskite–Si solar cells.

In recent years, a large number of reports have addressed the development of high efficiency perovskite tandem PV. Considering the even high potential of triple junction PV, this thesis develops optical simulations and experimental optimizations for triple-junction perovskite–perovskite–Si solar cells. With optimized light management, the current mismatch is minimized and then the current generation is maximized to 11.6 mA cm^{-2}. A key junction is developed using MBG perovskite thin film, *i.e.*, a stable pure-α-phase $FAPbI_3$ free of wrinkles, cracks, and pinholes, enabling a high V_{OC} in the triple-junction solar cells. The optimized triple-junction solar cells benefits with high PCE of 24.4% and excellent thermal stability. This thesis demonstrates a significant advancement in perovskite-based multi-junction solar cells.

Table of contents

1. Introduction

The demand for sustainable and renewable energy resources is increasing rapidly, since the current energy consumption relies heavily on unsustainable and non-renewable fossil fuels, such as finite oil, coal, and natural gas.[1] Fossil fuels will not be able to address our energy need in the future due to the global increase in oil or natural gas prices[1] and the emission of carbon dioxide (CO_2),[2] making it urgent to find alternative energy sources that are not only sustainable but also cost-effective and readily available. These will include solar, wind, tides, geothermal, and other sustainable energy sources. A transition to these cleaner and more sustainable energy sources is essential for resolving both environmental and economic challenges associated with traditional fossil fuel consumption.

Solar energy is recognized as one of the cleanest forms of zero-carbon electricity generation.[1] Photovoltaics (PVs) involve the direct conversion of sunlight into electricity using solar cells, *i.e.*, it harvests the abundant and renewable energy from the sun to generate clean electricity. PVs will play a key role in decarbonizing and increasing the global power sector.[3] For instance, the global deployment of photovoltaic PV systems suggested a significant ambitious goal of achieving ~75 terawatts (TW) of installed capacity by the year 2050, from a baseline installed capacity of ~1 TW in 2022.[3,4] This is in agreement with the goal of limiting global warming with an average increasing temperature below 1.5 °C that was stated in the 2015 International Paris Agreement.[4] Such ambitious target reveals that PVs are projected to dominate the global power industry for achieving a net-zero-carbon power supply in the future.[5]

Over the past decade, the cost of the PV module manufacturing has diminished drastically in utility scale. However, the balance of systems (BOS) costs still account to the most.[1,6,7] In this context, improving the overall power output of the PV module per unit area, *i.e.*, power conversion efficiency (PCE), is pivotal to further decrease the overall levelized cost of electricity (LCOE).[6,7] In current PV market, silicon (Si)-based solar cells still dominate the global market share. However, the PCE of Si PV is approaching its theoretical limit.[8,9] Building a multi-junction solar cell is a promising approach to surpass this detailed-balance limit for single-junction devices.[10] Metal halide perovskite semiconductors are emerging as the prime candidate of material class for the next generation of ultra-high-efficiency multi-junction PVs, given their tunable bandgaps (1.2 to 3.1 eV) and excellent optoelectronic properties (more details can be found in chapter 2). Recent breakthroughs in PCEs have been

achieved in various architectures, such as monolithic double-junction solar cells using perovskite–Si (PCE > 33%),[11–14] perovskite–copper indium (gallium) selenide (CI(G)S) (PCE > 24%),[11,15] and all-perovskite absorbers (PCE > 28%).[11,16–18] These advancements mark the beginning of a new era in perovskite-based multi-junction PVs. They may even compete with the very high PCEs reported for double- (PCE > 32%), triple- (PCE > 39%), and six-junction (PCE > 39%) solar cells based on epitaxial grown III–V crystalline semiconductor thin films.[9,11] Unlike epitaxial grown III–V semiconductors, perovskite thin films can be manufactured using simple and cost-effective processes.[19,20]

Perovskite solar cells (PSCs) have been considered as a highly promising material class for solar energy conversion with a rapid enhancement in PCEs in recent years. These single-junction solar cells achieved certified PCEs exceeding 26% in lab-scale devices with an area less than 1 cm²,[9] since the first reported PCE was 3.8% in 2009.[21] For a larger device with active area ~1 cm^2, the certified PCE realized >25%.[11] However, the PV performance for the mini-module dimension (>10 cm^2) is still far less than the smaller devices, *e.g.*, the certified PCE is 18.6% for the module (809.9 cm^2 designated area).[11] Perovskite thin films are fabricated by using solution-based methods at low temperature. PSCs are employed in both *n*-*i*-*p* (normal) or *p*-*i*-*n* (inverted) architectures, depending on which transport layers (*n*-type layer: electron transport layer; intrinsic layer: perovskite layer; *p*-type layer: hole transport layer) are fabricated first on the substrates (more details will be presented in chapter 2). For four-terminal (4T) tandem (*i.e.*, double-junction) stacks, each sub-cell is electrically isolated and can be fabricated independently, allowing for a large degree of freedom of utilizing *n*-*i*-*p* or *p*-*i*-*n* architectures. To date, most of the high PCEs of the state-of-the-art tandems were achieved in monolithic two terminal (2T) architecture employing *p*-*i*-*n*-based PSC sub-cell.[9,11] As *p*-*i*-*n* architecture is more appealing nowadays with an excellent operational stability and low-temperature-processed transport layers,[17,22,23] more researchers are focusing on it in the multi-junction PVs.

Performance, stability, and scalability are key challenges in the development and commercialization of PSCs. Tremendous studies focus on improving the PV performance for *p*-*i*-*n*-based PSCs. Interface engineering is the one of the most important aspects. In the *p*-*i*-*n* architecture, the open-circuit voltage (V_{OC}) losses ($V_{OC,loss} = E_g/q - V_{OC}$)[24] originate from the non-radiative recombination occurring in the bulk of perovskite thin film and/or the interfaces, such as the top interface (*e.g.*, perovskite/electron transport layer (ETL)) or the buried interface (*e.g.*, perovskite/hole transport layer (HTL)). The trap states at the interfaces and energy-level alignment will affect the non-radiative recombination as well as charge extraction within the single- or multi-junction PV devices.[16,25–27] Thus, interfacial optimization in multi-layer stacks is a very pivotal strategy to boost the PV performance and device stability. Searching for a suitable and useful passivation layer or interlayer at the interface (**Challenge 1**) and meanwhile investigating their mechanism (*e.g.*, non-radiative recombination and charge extraction) behind (**Challenge 2**) are still challenging, since a specific perovskite composition has different crystallization process, surface trap states, energy level, *etc*. This thesis explores different interface engineering strategies and studies on different perovskite compositions, such as narrow-bandgap Sn/Pb based perovskite (E_g =

1.25 eV) and middle-bandgap perovskite (E_g = 1.52 eV) at top surface or buried surface within small-area (~0.1 cm^2) single-junction device, further on large-area (> 10 cm^2) modules, tandem and triple-junction PVs.

Next to enhancing the PV performance, the scalability (**Challenge 3**) and active area (**Challenge 4**) of PSCs still lag behand conventional Si PVs, as nowadays very high PCEs were achieved in small-area (< 1 cm^2) dimensions.[9] To date, the PCEs of large dimensional devices (> 10 cm^2) achieved by up-scaling techniques in *p-i-n* architecture are far less than that of small-area devices.[11] Solution-based scalable methods need to optimize the perovskite compositions and precursor solvents to control the nucleation and crystallization in large-area thin films.[22] Therefore, improving film morphology and quality are critical to achieve high performance in large-area devices. A fast solvent extraction, *i.e.*, a well-controlled drying dynamics is key for processing high-quality large-area perovskite thin films.[28] This thesis resolve these challenges based on the widely-used N,N-dimethylformamide (DMF) and dimethyl sulfoxide (DMSO) solvent system, realizing efficient large-area solar modules by utilizing scalable methods.

Perovskite-based multi-junction (three or more than three junctions) PV has a higher theoretical PCE than a tandem architecture.[29,30] Developing this multi-junction PV is much more challenging than a tandem device. Although the triple-junction solar cells lag far behand with their PCE with very few reported prototypes and experimental realizations up to date, they are still showing a great potential for further improving the PV performance in the future. There are various challenges in developing highly efficient multi-junction solar cells, such as sequential processing of complicated multi-layer designs (**Challenge 5**), light management (**Challenge 6**), current matching among each sub-cell (**Challenge 7**), and low-loss tunnel/recombination junctions (**Challenge 8**). The processing of perovskite sub-cells is crucial for achieving high PCE and stability. This thesis realizes efficient triple-junction solar cells by developing an efficient and stable middle-junction perovskite solar cell.

The scope of this thesis is outlined as follows:

Chapter 2 provides fundamental basics of metal halide perovskite semiconductors, such as their structural and optoelectronic properties. Next, working principles and photovoltaic characteristics of single-junction PSCs are described. The non-radiative recombination and V_{OC} losses are further discussed. Finally, scalable processing modules and multi-junction PVs are introduced briefly.

Chapter 3 presents the theoretical principles and experimental fundamentals of materials, fabrications, and characterizations implemented in this thesis.

Chapter 4 targets with **Challenges 1 and 2**. This chapter introduces novel solution-processed fullerene derivatives as an interlayer at the interface between Sn/Pb-based NBG and ETL. V_{OC} loss is minimized and J_{SC} is improved. The non-radiative recombination mechanism and charge extraction are studied. Finally, highly efficient 4T all-perovskite PVs are demonstrated.

Chapter 5 deals with **Challenges 1 to 4**. This chapter presents upscaling achievement from lab-scale (0.105 cm^2) to mini-module (12.25cm^2) dimension based on formamidinium lead iodide ($FAPbI_3$) perovskite in *p-i-n* architecture. First, a void-free buried interface is achieved within small-area PSCs in *p-i-n* architecture by optimization of vacuum-assisted growth (VAG) process. Next, the effects of interfacial voids on non-radiative recombination and charge extraction are systemically studied. Further, a novel strategy implementing well-controlled nitrogen (N_2) flow during VAG process and incorporating methylammonium chloride (MACl) as an additive eliminates the interfacial voids in large-area processing with scalable methods. Finally, high performance of blade-coated PSCs and scalable mini-modules are demonstrated.

Chapter 6 solves the **Challenges 1, 2, and 5 to 8**. This chapter presents a remarkable achievement of 2T triple-junction perovskite–perovskite–Si solar cell. The optimization of light management for the top and middle perovskite sub-cells minimizes current mismatch and maximizes current generation. A key junction of this successful development is middle perovskite sub-cell using a stable pure-α-phase $FAPbI_3$ perovskite thin film. This approach minimizes the V_{OC} losses in the triple-junction solar cells. The non-radiative recombination at the interface of middle perovskite and ETL is investigated. Finally, high-efficiency triple junction solar cells are demonstrated with superior thermal stability.

Chapter 7 summaries the key results presented in this thesis. An outlook for future work in perovskite PVs is finally provided.

2. Theoretical background and fundamentals

This chapter begins with the basic fundamentals and theoretical background for the metal halide perovskite semiconductors and perovskite solar cells (PSCs), including the structural and optoelectronic properties for perovskite materials, and working principle and photovoltaic (PV) characteristics for PSCs. Afterwards, the scalable methods for large-scale processing and basic interconnection for mini-modules are discussed. Finally, perovskite based multi-junction architectures are introduced to go beyond the theoretical efficiency limit of single-junction devices.

2.1. Metal halide perovskite semiconductors

Perovskite family has a general stoichiometry of ABX_3, named after the mineralogist Count Lev Aleksevich Perovski, where A is a large cation, B is a middle-size cation, and X is an anion. In this section, we provide an overview of the state-of-the-art metal halide perovskite semiconductors.

2.1.1. Structural properties

The crystal structure of ABX_3 perovskite is described as a cuboctahedra arrangement, where the A-site is located at the center of a cuboctahedron with surrounding by corner-sharing octahedral BX_6 (Figure 2.1a). In a cubic perovskite crystal, cation A is typically cesium (Cs^+), methylammonium (MA^+), formamidinium (FA^+), *etc.*, cation B is lead (Pb^{2+}) and tin (Sn^{2+}) *etc.*, and anion X is typically iodide (I^-), bromide (Br^-), and chloride (Cl^-). Their crystallographic stability can be evaluated by a tolerance factor (t) and an octahedral factor (μ). These factors are expressed as follows:[31,32]

$$t = \frac{r_A + r_B}{\sqrt{2}\,(r_B + r_X)} \tag{2.1}$$

$$\mu = \frac{r_B}{r_X} \tag{2.2}$$

Where r_A, r_B, and r_X are ionic radius of the corresponding atoms. For halide perovskite compositions, the values of t and μ are in the range of $0.81 < t < 1.11$ and $0.44 < \mu < 0.90$,[31] respectively. When $0.8 < t < 1$, a cubic three-dimensional (3D) perovskite forms like in

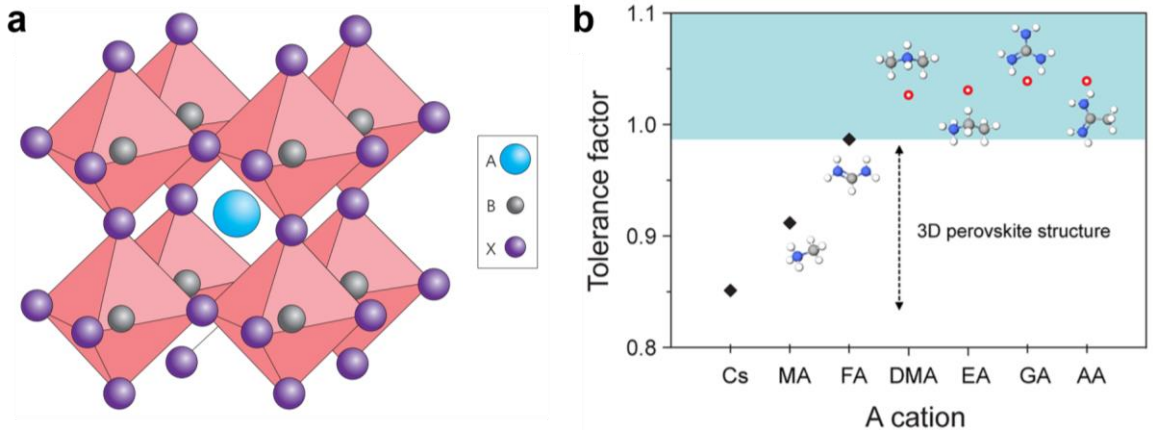

Figure 2.1. (a) Schematic illustration of cubic crystal structure of ABX_3 perovskite. Adapted from Ref.[31] with permission of Springer Nature Limited. (b) Goldschmidt tolerance factor of $APbI_3$ perovskites. Cs: cesium; MA: methylammonium; FA: formamidinium; DMA: dimethylammonium; EA: ethylammonium; GA: guanidinium; AA: acetamidinium. Adapted from Ref.[32] with permission of American Chemical Society.

Figure 2.1a. However, a larger (t > 1) or smaller (t < 0.8) *t* values lead to non-perovskite structures that have distinct forms of BX_6 octahedral connection.[32] A suitable cation, such as Cs^+, MA^+, or FA^+ fits into the stable 3D perovskite lattice,[32] as presented in Figure 2.1b.

2.1.2. Optoelectronic properties

Metal halide perovskite materials have a direct bandgap with a very high absorption coefficient ($\alpha > 10^4$ cm^{-1}),[33] *i.e.*, a thin-film (~350 nm) perovskite layer is efficient for light harvesting used in the high-performance PSCs. Their photo-generated excitons (*i.e.*, bound electron-hole pairs) have small binding energy (*e.g.*, 2 to 55 meV), which means spontaneous free charge-carrier generation created by a low energy (*i.e.*, occasion at room temperature) upon light absorption.[34] The free charge carriers were demonstrated a high mobility (~10 cm^2 V^{-1} s^{-1})[35] and a long diffusion length (up to micrometer range).[36]

Bandgap (E_g) tunability in a wide range (*e.g.*, 1.2 to 3.1 eV) is one of outstanding advantages that makes it possible for perovskite-based multi-junction solar cells. E_g can be tailored by

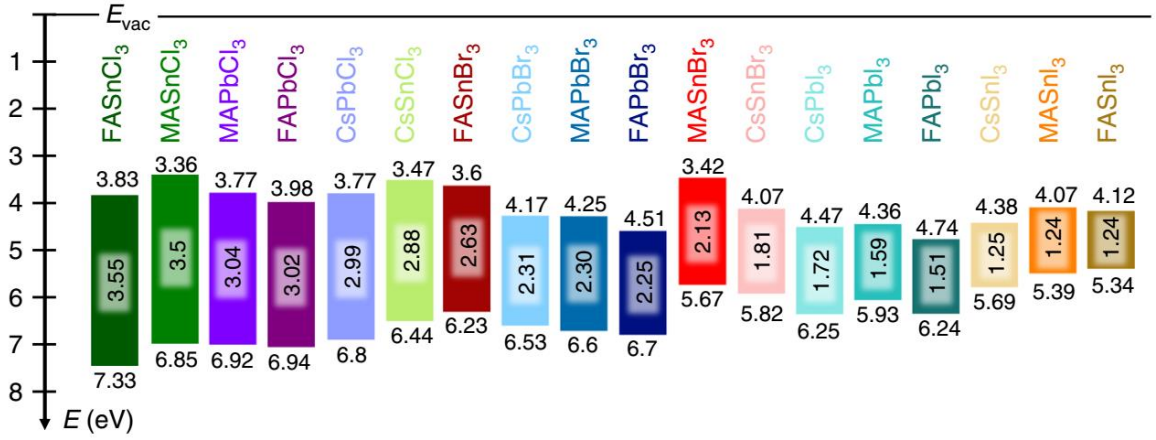

Figure 2.2. Schematic energy level diagram of diffident perovskite compositions. Adapted from Ref.[37] with permission of Springer Nature Limited.

simply varying cations or anions.[37] For instance, by partially replacing Pb^{2+} with Sn^{2+} we can obtain narrow-bandgap (NBG) perovskite (*e.g.*, E_g down to 1.2 eV, Figure 2.2), which is interesting in all-perovskite tandem architectures. By partially replacing I^- with Br^- and tuning the cation ratio of Cs/FA, the wide-bandgap (WBG) (*e.g.*, E_g > 1.6 eV) perovskites can be reached and these PSCs are widely used as sub-cells in tandem solar cells with combinations of Silicon (Si), copper indium (gallium) selenide (CI(G)S), and NBG perovskite.

2.1.3. Processing of perovskite thin films

The basic fabrication methods for high-quality perovskite thin films involves solution processing or thermal evaporation. Solution-based methods include so-called 'one-step' and 'two-step sequential' approaches. In 'one-step' method, the perovskite precursor (*i.e.*, a liquid solution of desired perovskite dissolved in combined solvents (*e.g.*, DMF/DMSO), and/or together with additives) is deposited on the substrates by spin-coating. During spin-coating process, an anti-solvent treatment, vacuum-quenching, or gas-blowing is applied. Post-annealing at a moderate temperature (*e.g.*, 100–150 °C) is needed to obtain crystalized perovskite thin films. In this theses, we develop vacuum-assisted growth for processing of high-quality Sn-Pb based[16] and $FAPbI_3$ perovskite thin films[27] for single-junction and multi-junction PVs.

The 'two-step sequential' approach needs to deposit PbX_2 (X = I^- or Br^-) layer first by spin-coating or thermal evaporation. The sequential deposition can be implemented by spin-coating or thermal evaporation of AX (A=Cs^+, FA^+, MA^+) layer. Thermal evaporation approach employs single-, dule-, or multi-source deposition without using any solvents, which is beneficial for better control film morphology and composition of large-scale substrates.[5] More upscaling methods will be discussed in section 2.3.2.

2.2. Perovskites solar cells

In this section, we discuss the operational principles of PSCs, corresponding PV characteristics, and recombination mechanism within PSCs.

2.2.1. Working principles

Power generation in a PSC includes several key steps (Figure 2.3a): (1) incident absorption of photons by perovskite thin film, (2) the generation of excitons (*i.e.*, bound electron-hole pairs), (3) separation of photo-generated excitons into charge carriers (*i.e.*, electrons and holes), (4) charge extraction by the selective contacts (*i.e.*, hole transport layer (HTL) and electron transport layer (ETL)), and (5) charge collection by the electrodes.

In a *p*-*i*-*n* or *n*-*i*-*p* architecture of PSCs (more details of the architectures will be discussed in section 3.2), an intrinsic (*i*) perovskite semiconductor is sandwiched between *p*-type (*i.e.*, HTL) and *n*-type (*i.e.*, ETL) contacts. Figure 2.3b and 2.3c show the band diagram of representative *p*-*i*-*n* PSC. In the dark condition without bias applied, the Fermi level (E_F)

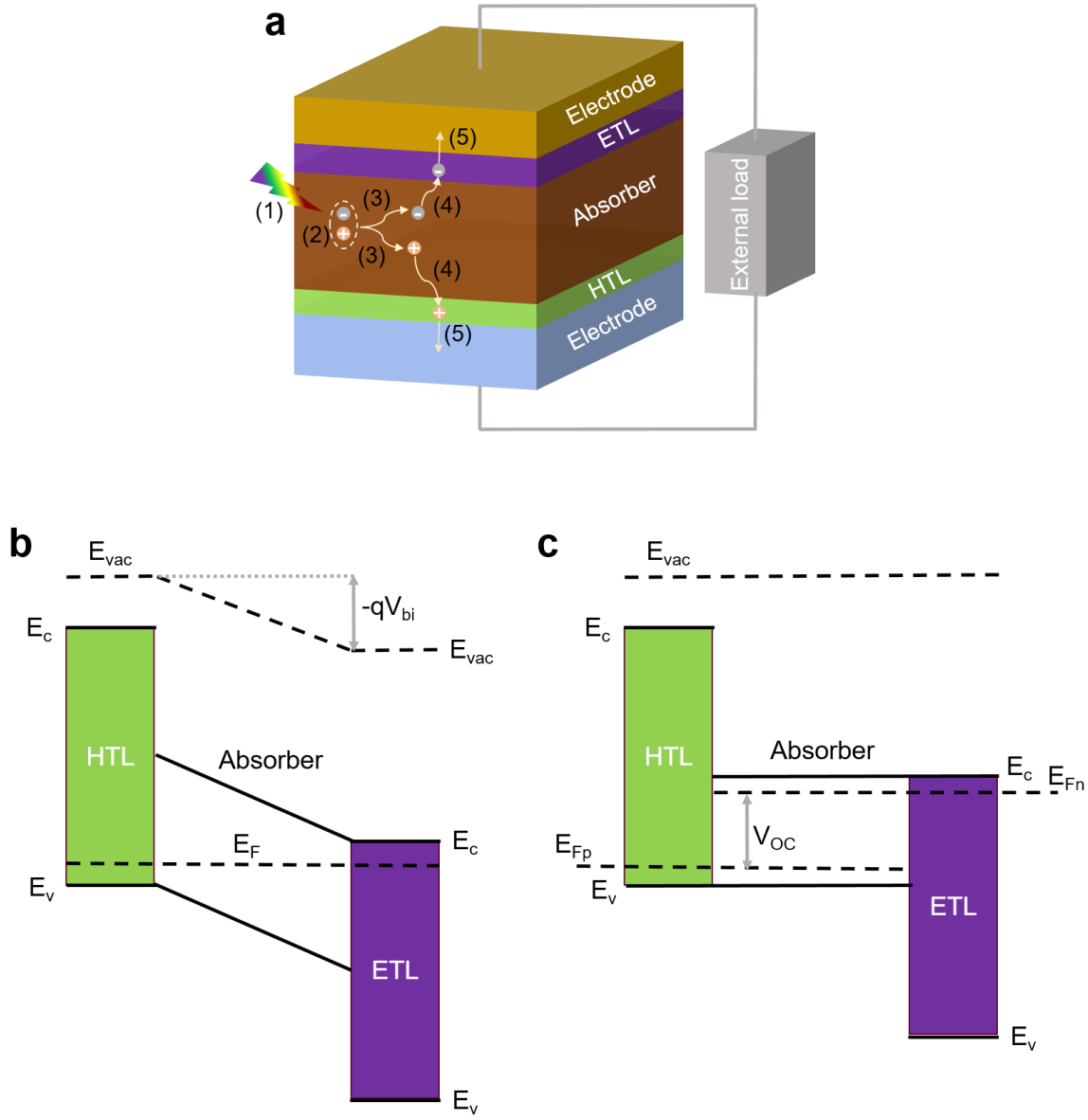

Figure 2.3. (a) Schematic illustration of power generation in a *p-i-n*-based PSC. Energy level diagrams at open circuit conditions in a *p-i-n*-based PSC under (b) the dark and (c) the illumination. E_{vac}: the vacuum level; E_c: the conduction band; E_v: the valence band; E_F: the Fermi level, E_{Fn}: the quasi Fermi level for electrons; E_{Fh}: the quasi Fermi level for holes; q: the electron charge; V_{bi}: the built-in potential.

equilibrates over the full device (Figure 2.3b). The equilibration generates a built-in potential (V_{bi}) as it presents a large difference in work functions between HTL and ETL. The band levels of perovskite layer are inclined over its complete thickness along with an electrical field in the intrinsic region.[38] In consequence, the electrical field realizes selectivity for the HTL or ETL and the V_{bi} acts as a driving force for charge separation and collection.

Upon illumination, electrons in the perovskite semiconductor are excited from the valence band to conduction band, resulting in splitting of E_F into quasi Fermi levels for electrons and holes (Figure 2.3b), *i.e.*, E_{Fn} and E_{Fp}, respectively. A photovoltage is generated that is equal to the difference between E_{Fn} and E_{Fp}. Under an open-circuit condition, this photovoltage is defined as a maximum voltage, *i.e.*, the open-circuit voltage (V_{OC}). In this case, the quasi-

Fermi level splitting produces flat bands in the semiconductor and the V_{OC} is limited by the work functions of HTL and ETL.[38] Under operation conditions (*i.e.*, continuous illumination and an applied bias), the PSC produces both photocurrent and photovoltage, as a result of generation of output power.

2.2.2. Photovoltaic characteristics

A solar cell can be considered as a single diode with a photocurrent source, a series resistance (R_s), and a shunt resistance (R_{sh}) in an electrically equivalent circuit,[39] as shown in Figure 2.4. R_s and R_{sh} represent electrical resistance and leakage current due to defects or impurity, respectively. The output current (I) is determined as follows:

$$I = I_{ph} - I_d - I_{sh} \tag{2.3}$$

where I_{ph}, I_d, and I_{sh} represent photo-generated current, dark current, and shut current, respectively. The current density (J (V)) can be expressed as follows:

$$J(V) = J_{ph} - J_0 \left(\exp \frac{q\,(V + J(V)\,A\,R_s)}{n_{id}\,k_B\,T} - 1 \right) - \frac{V + J(V)\,A\,R_s}{R_{sh}} \tag{2.4}$$

where J_0 is the dark saturation current density, q is the elementary charge, V is the voltage, A is the active area of solar cell, n_{id} is the ideality factor, k_B is the Boltzmann constant, and T is temperature. In the current density-voltage (J-V) characteristics, an ideal solar cell is considered with neglecting the parasitic resistances, *i.e.*, R_s = 0 and R_{sh} = ∞. Thus, the equation (2.4) can be simplified as follows:

$$J(V) \approx J_{ph} - J_0 \left(\exp \frac{q\,V}{n_{id}\,k_B\,T} - 1 \right) \tag{2.5}$$

When the applied voltage is zero, *i.e.*, V = 0, $J(0) \approx J_{ph}$, this case is so-called short-circuit condition. The corresponding current density is called short-circuit current (J_{SC}), *i.e.*, $J_{SC} = J(0) \approx J_{ph}$ (see Figure 2.5a).

At an open-circuit condition, *i.e.*, $J(0)$ = 0. The corresponding applied voltage is called open-

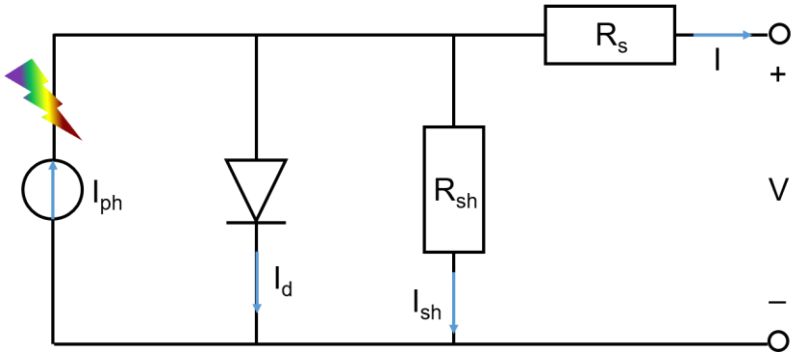

Figure 2.4. An equivalent circuit of a solar cell considering a single-diode model. I_{ph}: photo-generated current; I_d: dark current; I_{sh}: shut current; R_s: series resistance; R_{sh}: shunt resistance.

circuit voltage (V_{OC}) and therefore:

$$J(V_{OC}) \approx J_{ph} - J_0 \left(\exp \frac{q\, V_{OC}}{n_{id}\, k_B\, T} - 1 \right) = 0 \tag{2.6}$$

V_{OC} can be expressed as follows:

$$V_{OC} \approx \frac{n_{id}\, k_B\, T}{q} \ln \left(\frac{J_{ph}}{J_0} + 1 \right) \tag{2.7}$$

In a typical *J*-*V* characteristic as shown in Figure 2.5a, the maximum power output density (P_{MPP}) is obtained when the solar cell operates at the maximum power point (MPP):

$$P_{MPP} = J_{MPP}\, V_{MPP} \tag{2.8}$$

Fill factor (FF) is described as follows:

$$FF = \frac{J_{MPP}\, V_{MPP}}{J_{SC}\, V_{OC}} \tag{2.9}$$

The power conversion efficiency (PCE) is defined as a fraction of P_{MPP} and the power density of incident light ($P_{incident}$):

$$PCE = \frac{P_{MPP}}{P_{incident}} = \frac{FF\, J_{SC}\, V_{OC}}{100\ \text{mW cm}^{-2}} \tag{2.10}$$

where $P_{incident}$ is considered testing under a standard AM1.5G illumination (100 mW cm^{-2}).

The external quantum efficiency (EQE) is a basic and important characterization to verify the J_{SC} of a solar cell. EQE is defined as the ratio of the number of photo-generated electrons to the number of incident photons. The integration of EQE at the wavelength range of λ_1 to λ_2 is used to evaluate the maximum current density generated in a solar cell, *i.e.*, J_{SC}, and therefore:

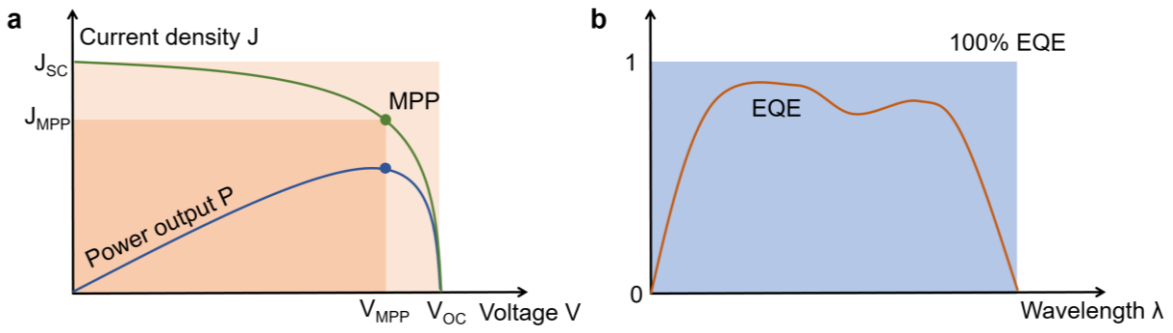

Figure 2.5. (a) Current density-voltage (*J*-*V*) and corresponding power output characteristics, and (b) external quantum efficiency (EQE) spectrum of a solar cell. J_{SC}: short-circuit current density; V_{OC}: open-circuit voltage; When the power output achieves the maximum, $V = V_{MPP}$ and $J = J_{MPP}$.

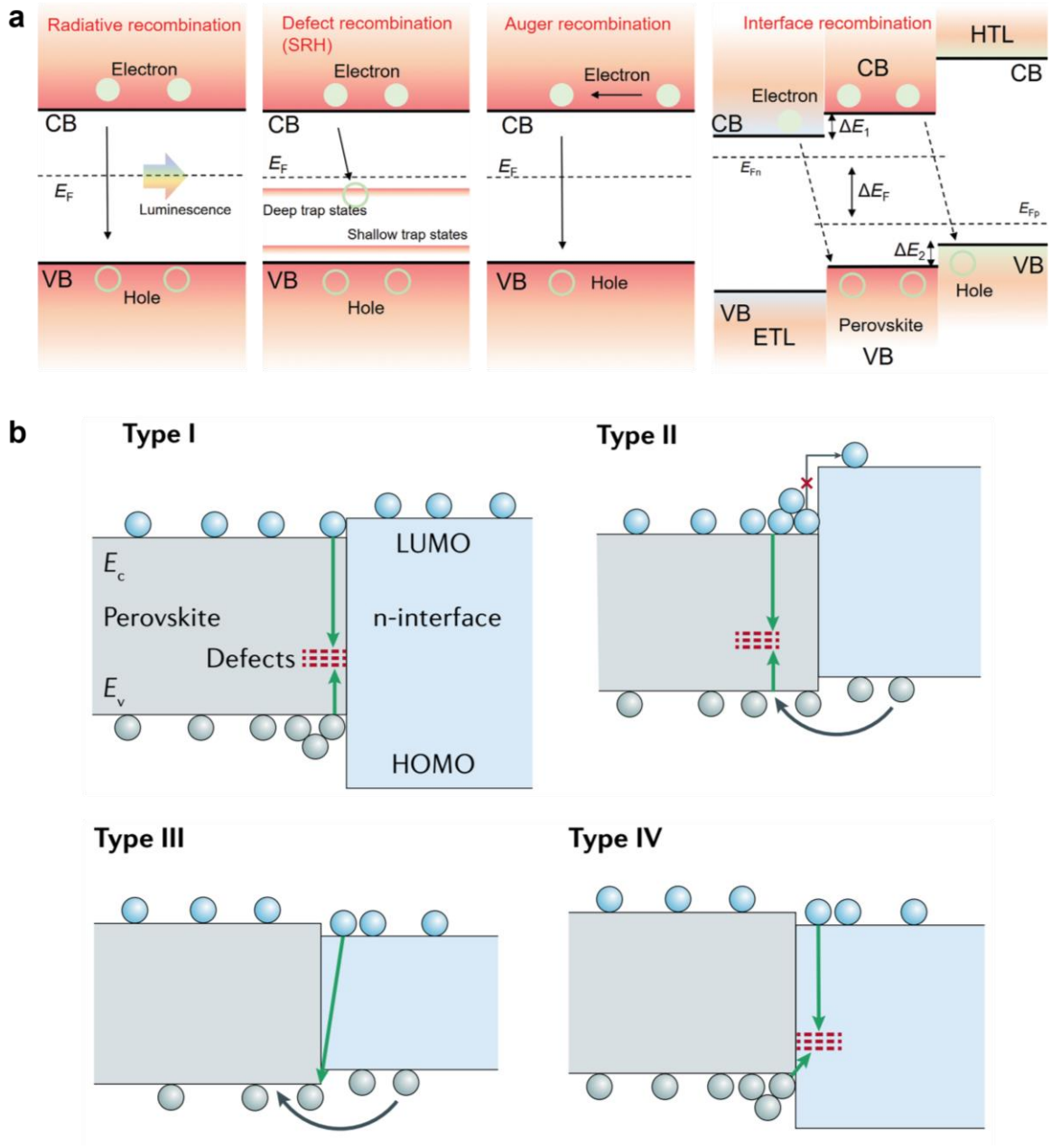

Figure 2.6. (a) Schematic illustration of various recombination processes within solar cells. E_f: the Femi level; E_{Fn}: the quasi Fermi level for electrons; E_{Fh}: the quasi Fermi level for holes; CB: conduction band minimum; VB: valence band maximum; HOMO: highest occupied molecular orbital; LUMO: lowest unoccupied molecular orbital; ΔE_1: band offset between perovskite and electron transport layer (ETL); ΔE_2: band offset between perovskite and hole transport layer (HTL); SRH: Shockley-Read-Hall recombination. Adapted from Ref.[40] with permission of Wiley. (b) Schematic diagrams of interface-induced recombination losses at perovskite/ETL interface: type I is deep-level defects within perovskite thin film, type II is defects within the perovskite and unfavorable energy-level alignment at the interface, type III is back-transfer-induced recombination, and type IV is defect-assisted recombination in the ETL. Adapted from Ref.[25] with permission of Springer Nature Limited.

$$J_{SC} = q \int_{\lambda_2}^{\lambda_1} \mathrm{EQE}(\lambda)\ \Phi_{\mathrm{AM1.5G}}(\lambda)\, d\lambda \tag{2.11}$$

where $\Phi_{AM1.5G}(\lambda)$ is the photo flux incident to a solar cell per unit area at a wavelength of λ, and q is the elementary charge. Figure 2.5b shows a typical EQE spectrum of a solar cell, which provides the information of optical (*e.g.*, reflection, parasitic absorption) and electrical (*e.g.*, recombination) losses.

2.2.3. Recombination mechanism

Charge-carrier recombination includes radiative and non-radiative recombination within solar cells. The radiative recombination origins from the electron-hole recombination from the conduction band (CB) and valance band (VB) without electron relaxation process,[40] as shown in Figure 2.6a. Defect-assisted (or so-called Shockley-Read-Hall (SRH)) recombination, Auger recombination, and interface-induced recombination contribute to non-radiative recombination, as shown in Figure 2.6a. Auger recombination occurs in the case of high charge carrier density ($>10^{17}$ cm^{-3}),[25] which is secondary or negligible within PSCs as the reported charge carrier density is in the range of 10^{13} to 10^{17} cm^{-3}.[25,40,41] Therefore, SRH and interface recombination dominate the non-radiative recombination within PSCs. SRH recombination primarily stems from the un-coordinated ionic defects (*i.e.*, deep-level defects), which can trap the free charge carriers at the gap states.[40] However, the shallow trap states (near to the VB and CB) are considered negligible impact on the non-radiative recombination as the excited charge carriers are easily de-trapped in case of enhanced thermal energy and reduced non-radiative recombination.[25,40]

The interface-induced recombination is normally caused by the surface defects, energy-level alignment, and charge-carrier back transfer.[25] Figure 2.6b shows different types of interfacial recombination at the typical perovskite/ETL interface. The defects located within perovskite thin film or ETL will induce defect-assisted recombination like type I and IV. Unfavorable energy-level alignment at the interface will result in back-transfer-induced recombination like type II and III. A perfect interface has a superior energy levels and minimal defects on both layers of perovskite and ETL. Proper energy-level alignment and low defect density between perovskite and ETL or HTL are the key for efficient charge extraction. Interface engineering is an important strategy to reduce the non-radiative recombination and improve charge extraction. In this thesis, we applied different strategies to reduce non-radiative recombination within PSCs, modules, and multi-junction solar cells at the buried interface (*e.g.*, HTL/perovskite, see chapter 5) or top interface (*e.g.*, perovskite/ETL, see chapter 4 and 6).

2.3. Scalable processes and solar modules

Upscaling lab-scale devices into module dimensions is one of the challenges within perovskite PV field. To date, the record efficiencies are realized in typical small-area (< 1 cm^2) devices, whereas the large-area perovskite PV devices (> 10 cm^2) are still far less efficient. From the lab-scale solar cells to the modules, Martin A. Green classified the sizes into four categories since 1993 (reported in the Solar Cell Efficiency Tables (54 versions)): lab cells (< 10 cm^2), mini-module (10–200 cm^2), sub-module (200–800 cm^2), and module

(>800 cm^2).[42] In this section, we introduce perovskite thin film mini-modules and scalable methods.

2.3.1. Interconnection of perovskite thin film solar modules

A typical perovskite thin film solar module consists of sub-cells that are electrically interconnected in series, as shown in Figure 2.7. A module has two areas: active area can absorb light and energy conversion occurs, whereas dead area does not generate electricity. Three laser-scribed steps (P1, P2, P3) are usually used for interconnection. The transparent conductive oxidize (TCO) front electrode is patterned (P1) by laser scribing. Next, the bottom transport layer, perovskite layer, and top transport layer are deposited on the laser-scribed substrates. These layers then are laser-scribed (P2) to create isolated and opened channels between each sub-cell. Finally, a metal contact is deposited as the top contact that is also connected to the bottom TCO. The following laser scribing (P3) isolates each sub-cell and completes the module architecture. The active region and dead region are produced by confining between P1 and P3. The geometric fill factor (GFF) is defined by the ratio of active area to the designed area (more calculation details can be found in section 3.2).

The V_{OC} of a module is the sum of V_{OC} from all sub-cells. In an ideal condition, each sub-cell has the same V_{OC}. However, in the practice, the main total V_{OC} loss stems from the large-area film quality of perovskite layer, *e.g.*, thickness uniformity, grain size and film morphology.[43] If the R_s is considered very small , the J_{SC} of a module is determined by the smallest J_{SC} of a sub-cell. In the industry, the PCE loss from cell to module mainly attributed two factors: (1) J_{SC} loss through R_s due to the lateral resistivity of large-scale TCO, and (2) no power output from dead area and edge region.[43]

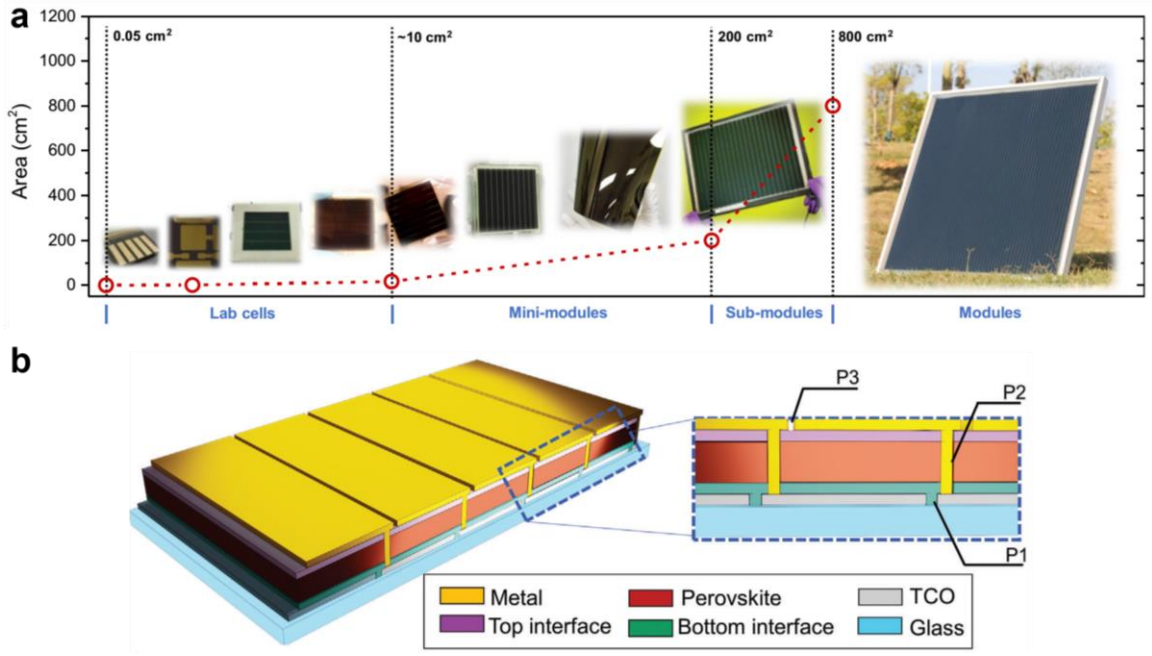

Figure 2.7. (a) PV modules designated with corresponding sizes. Reproduced from Ref.[42] with permission of Elsevier. (b) Schematic illustration of a typical perovskite mini-module. Adapted from Ref.[43] with permission of Wiley.

2.3.2. Scalable processing of perovskite solar modules

Spin-coating is a conventional method used for fabrication of lab-scale perovskite thin films. However, it is not suitable for large-area module manufacturing due to its poor uniformity and coverage. It also not a cost-effective fabrication as a significant amount of perovskite precursors (~95%) is wasted after processing.[43] Therefore, various scalable techniques have been applied to the large-area deposition of perovskite layer, such as blade (doctor) coating, slot-die coating, spray coating, inkjet printing, thermal evaporation, *etc*.[44] Slot-die coating and blade coating enable large-area deposition with minimal solution waste, which can be integrated into upscaling processes, *e.g.*, roll-to-roll and sheet-to-sheet deposition systems.[43] Inkjet printing is a material-efficient technology and offers freedom for the fabrication of arbitrary shape and area.[45] Spray coating is high-throughput processing technology that can be used for a wide range of coating of large-area perovskite thin films, organic HTLs, metal-oxide materials, and transparent conductive thin films.[46] Compared with other processes, thermal evaporation is beneficial for the fabrication of tandem architecture, which is a

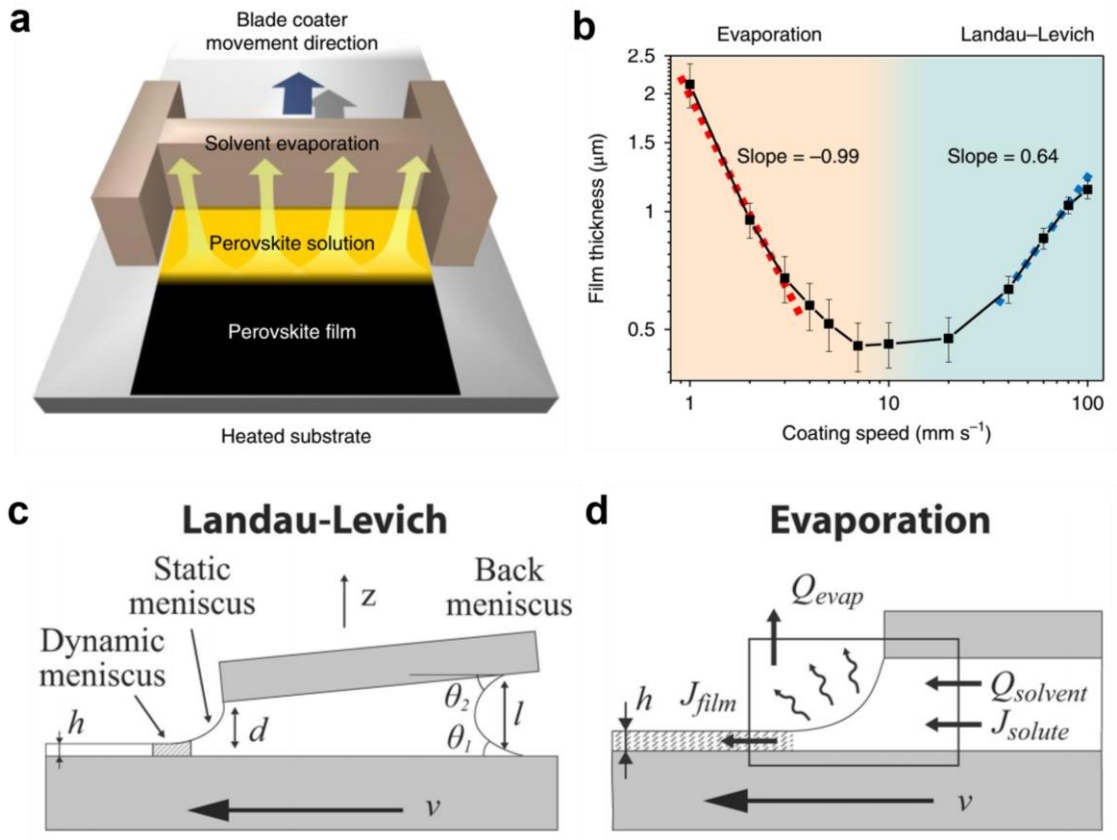

Figure 2.8. (a) Schematic illustration of the blade-coating process in the Landau-Levich mode. (b) $MAPbI_3$ thickness variation as a function of blade-coating speed on a pre-heated (at 145 °C) substrate. Adapted from Ref.[22] with permission of Springer Nature Limited. Schematic illustration of (c) evaporation and (d) Landau-Levich regimes. h: film thickness; v: the speed of the blade or substrate; Q_{evap}: the flow rate of solvent leaving the box by evaporation; $Q_{solvent}$: the flow rate of solvent entering the box; J_{film}: the outward mass flux in the film; J_{solute}: the inward mass flux in solution; d: the meniscus height; z: the vertical direction; θ_1, θ_2, and l are geometric parameters for the dynamic meniscus. Adapted from Ref.[47] with permission of American Chemical Society.

solvent-free process to avoid solvent damage to the underlying layers.[44]

Blade coating is an established and effective strategy for fabrication of large-area perovskite thin films. First, the liquid precursor is loaded onto the substrate. Then, the knife-type coater is used to spread the precursor (Figure 2.8a). The formation of perovskite thin film consists of several basic stages:[48,49] (i) formation of wet thin film (deposition of perovskite precursor on the substrates), (ii) drying process (solvent extraction out of the wet thin film and increase in precursor concentration), (iii) start of nucleation (growth of nuclei through supersaturation and initiation of crystallites), (iv) crystallization (growth of crystalline and formation of crystalline grains). The ink engineering (*e.g.*, precursor composition, additive incorporation, solvent selection, *etc*.) and fluid dynamics (*e.g.*, deposition speed, drying condition, *etc*.) are critical to scaling-up the perovskite thin film. For example, in the blade-coating process for $MAPbI_3$ perovskite, the thickness of perovskite wet film increases at a high blade-coating speed in the Landau-Levich regime (Figure 2.8b), as the wet film is dragged out (by viscous forces) and then dried out (Figure 2.8c). In contrast, the thickness decreases when using a higher coating speed in the evaporation regime due to mass-transport effects (Figure 2.8b and 2.8d).[22,47] Therefore, the interaction between perovskite liquid and substrate needs to be considered to better understanding the film formation.

Understanding the ink chemistry is important for large-scale fabrication. The perovskite precursor ink normally contains polar aprotic solvents, such as high boiling-point N,N-dimethylformamide (DMF) and dimethyl sulfoxide (DMSO). These solvents can be easily removed by centrifugal force during the high-speed rotation in the spin-coating process. However, for large-scale processing, drying process has an intrinsic longer time that is key for nucleation and crystallization of the perovskite thin films. Fast removal of solvents is pivotal to produce high-quality large-area perovskite thin films. For blade-coating process, rapid solvent evaporation is required to produce homogenous and pinhole-free perovskite thin films. For instance, some strategies were used for rapid evaporation of solvents or to improve the crystallization, such as new volatile solvents (like a low boiling point), surfactants, additives, and alternative quenching methods.[44]

2.4. Perovskite based multi-junction solar cells

2.4.1. Theoretical efficiency limits for single-junction solar cells

A real solar cell cannot achieve 100% PCE in converting sunlight into electrical energy. Many factors affect the maximum (theoretical) PCE, such as absorption limitations, energy losses, mismatch with solar spectrum, *etc*. Under a standard solar radiation condition (AM 1.5G, *i.e.*, 100 mW cm^{-2}), this theoretical limit (*i.e.*, known as the detailed-balance limit[50]) is roughly 33.7% for a single-junction solar cell with a bandgap of 1.34 eV,[8] as shown in Figure 2.9. In principle, when incident photons reach the absorber layer, only those with energy precisely matching the bandgap ($h\nu = E_g$, where ν is the frequency of the photon) can be absorbed, actively contributing to the generation of photocurrent. Photons with lower energy ($h\nu < E_g$), however, pass through the absorber layer, resulting in transmission losses (see in Figure 2.9). Photons with energy exceeding the bandgap ($h\nu > E_g$) are absorbed,

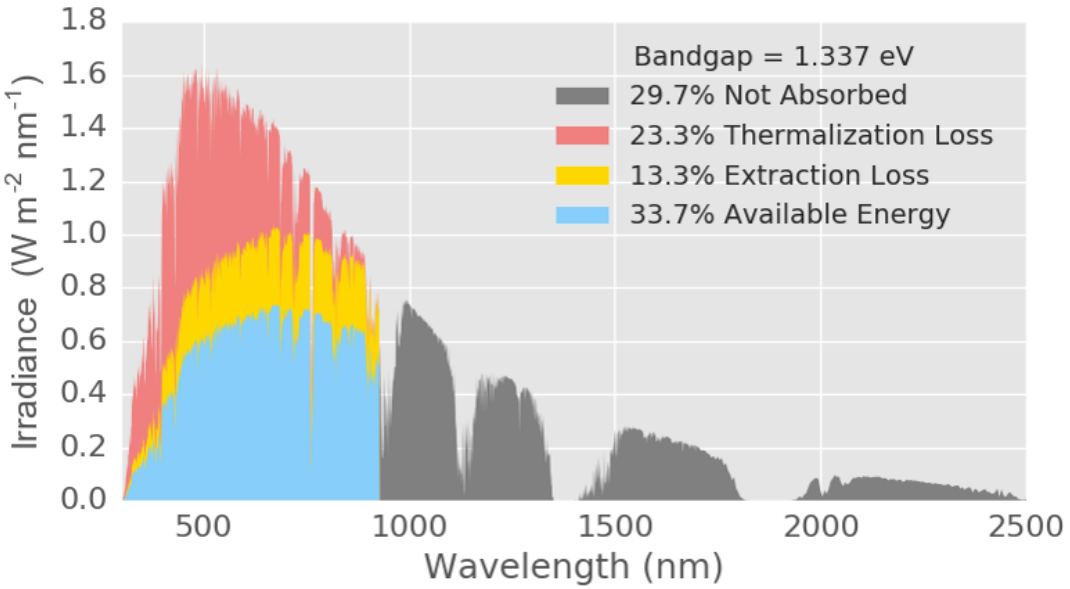

Figure 2.9. A standard spectrum of AM 1.5G irradiance and corresponding non-absorbed, thermalization, and extraction losses for a solar cell based on 1.337 eV bandgap (calculated from detailed-balance limit). Adapted with permission from Ref.[8]

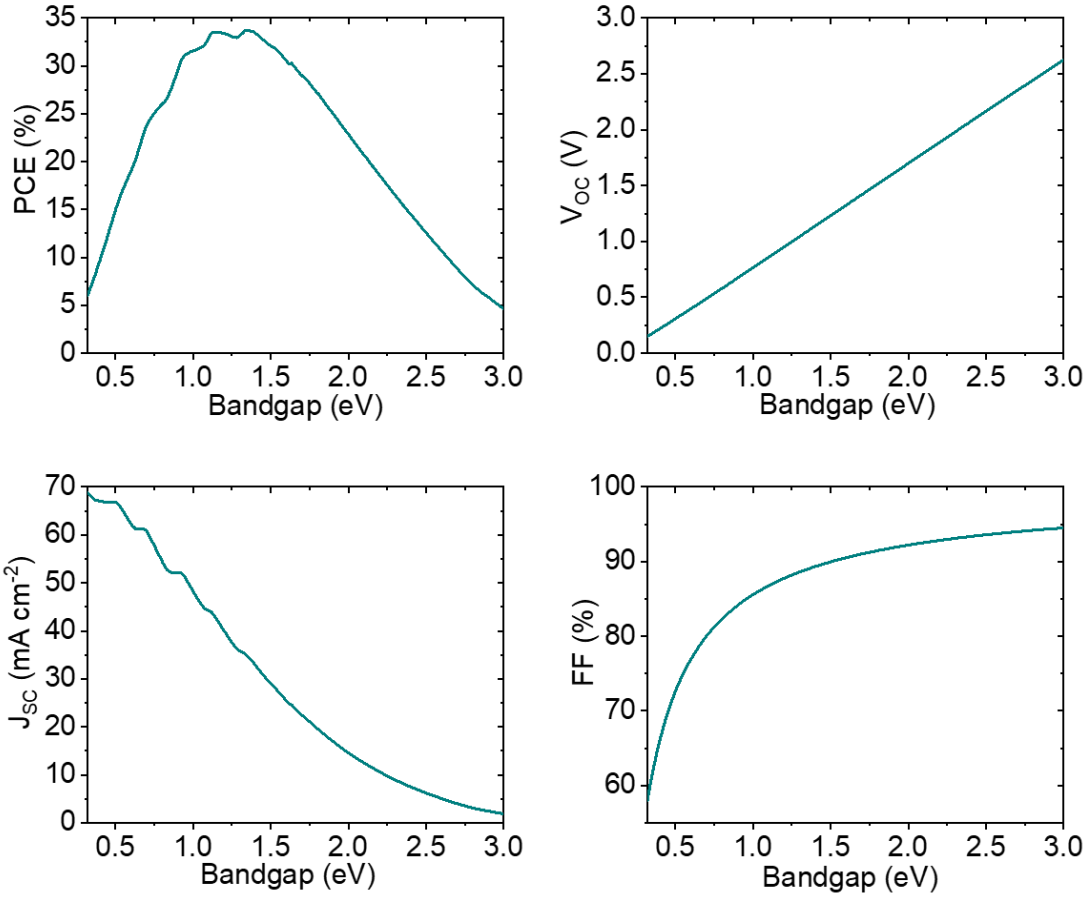

Figure 2.10. Theoretical limits of power conversion efficiency (PCE), open-circuit voltage (V_{OC}), fill factor (FF), and short circuit current (J_{SC}) as a function the bandgap of the absorber (calculated according by detailed-balance limit). Adapted with permission from Ref.[8]

initiating the generation of electron-hole pairs. Nevertheless, the surplus energy of the excited electron or generated hole is transferred to thermal equilibrium (lattice vibrations, *i.e.*, phonons),[51] making it inaccessible for extraction as electrical energy (thermalization loss, see in Figure 2.9). However, in a real solar cell, not all charge carriers generated by photons with energy $h\nu = E_g$ can be effectively collected and extracted from the absorber layer to the electrodes, resulting in extraction losses (see in Figure 2.9). Therefore, according to the detailed-balance limit, the theoretical efficiency limits for single-junction solar cells as a function of the absorber bandgap are assumed as follows:

(1) 100% absorption for all photons with $h\nu > E_g$,
(2) 100% generation of electron-hole pairs upon absorption,
(3) 100% collection of photo-generated electrons and holes,
(4) 0% absorption for all photons with $h\nu < E_g$,
(5) Only occasion of radiative recombination.

Figure 2.10 shows the theoretical limits of the PV parameters (PCE, V_{OC}, J_{SC}, and FF) using different absorber bandgap according to the calculation from detailed-balance limit.[8] The theoretical PCE of Si (E_g = 1.12 eV) solar cells is ~33.4% based on standard AM 1.5G irradiation.

2.4.2. Perovskite based multi-junction solar cells

According the detailed-balance model, thermalization and transmission losses are the main limitations of the theoretical PCE of a single-junction solar cell, as discussed in Figure 2.9. For an absorber with increasing E_g (*e.g.*, WBG), the transmission loss dominates, and a with decreasing E_g (*e.g.*, NBG) will increase the thermalization loss. A multi-junction architecture stacking several absorbers with different E_g have provided a promising route to decrease

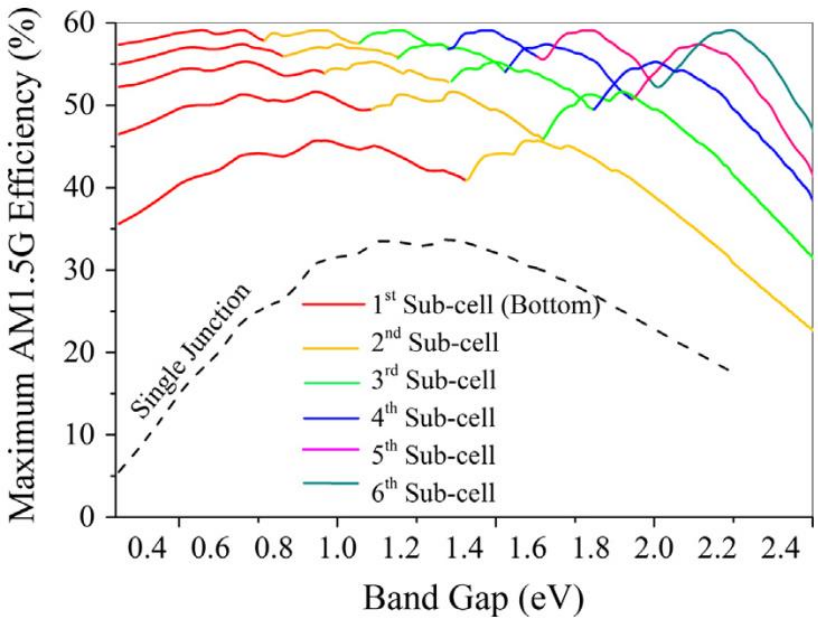

Figure 2.11. Maximum efficiencies for multi-junction stacks up to six absorber bandgaps. Adapted from Ref.[10] with permission of Elsevier.

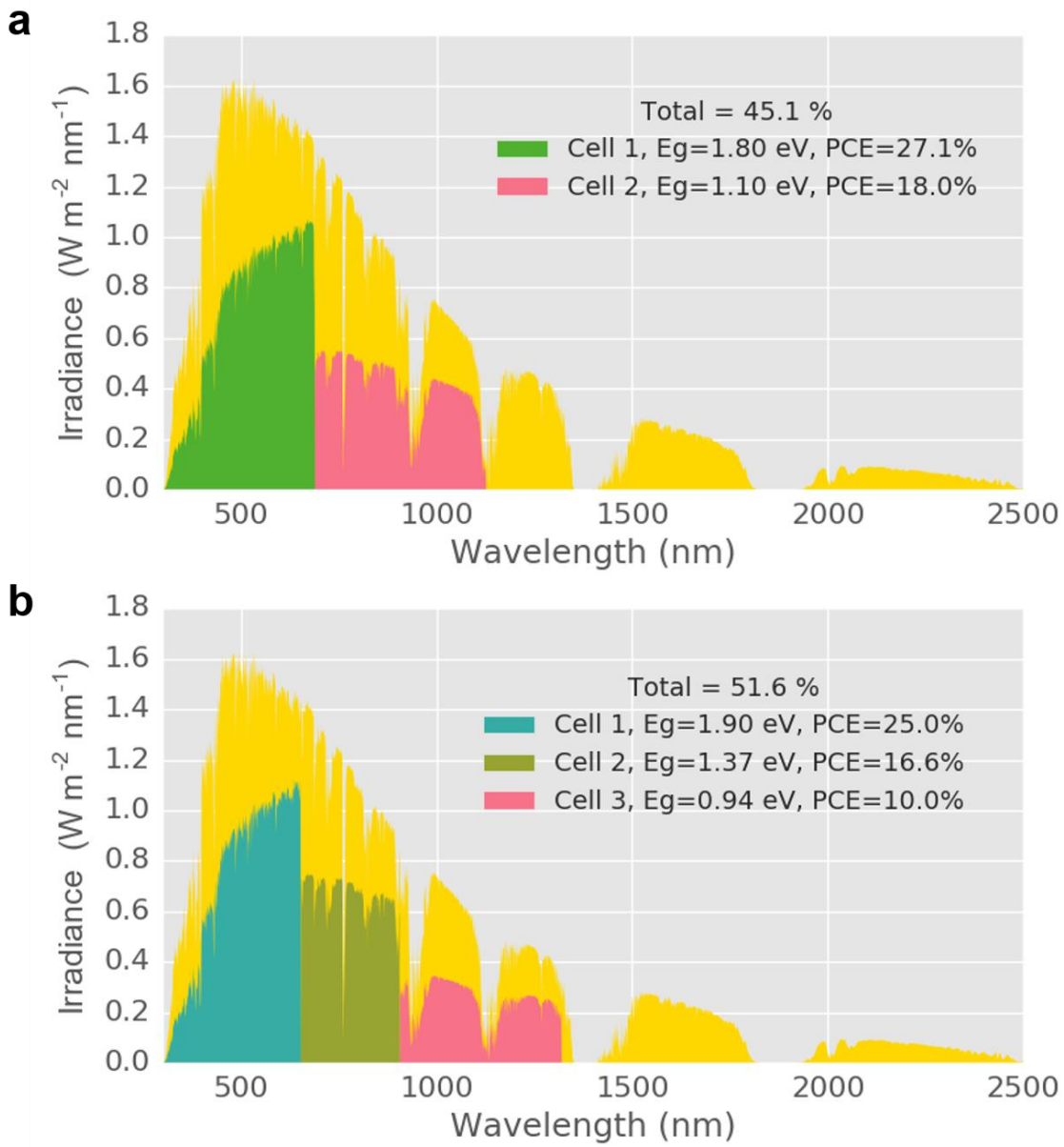

Figure 2.12. A standard spectrum of AM 1.5G irradiance and corresponding theoretical absorption fraction from each sub-cell for (a) tandem (double-junction) and (b) triple-junction solar cells (calculated from detailed-balance limit). Adapted with permission from Ref.[8]

these losses and thereby surpass this detailed-balance limit of a sing-junction solar cell. Figure 2.11 shows the maximum theoretical PCEs that can be realized by utilizing serval absorbers. The maximum PCE of the multi-junction solar cell enhances with increasing the number of sub-cells, which rely less on the sub-cells with narrow E_g.[10] As shown in Figure 2.12, the triple-junction architecture is calculated to be a higher theoretical PCE of 51.6% than a tandem (double-junction) architecture (45.1%).[8,29,30]

For a tandem architecture (Figure 2.13a and 2.13b), the top WBG absorber harvests high-energy photons ($h\nu > E_g$) but transmit low-energy photons ($h\nu < E_g$), while the bottom NBG absorber harvests low-energy photons ($h\nu < E_g$). Therefore, the NBG absorber reduces the transmission loss and WBG absorber minimizes the thermalization loss, *i.e.*, improving the

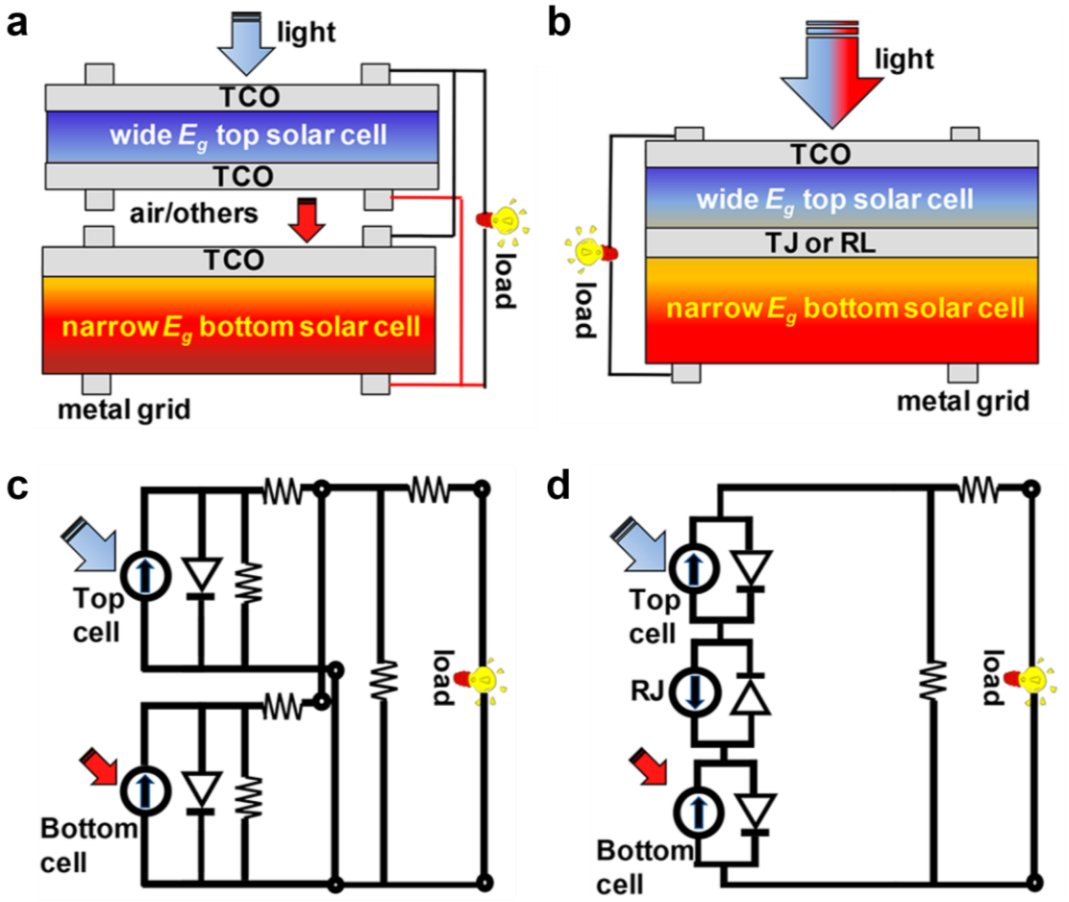

Figure 2.13. Schematic diagrams of (a) four-terminal (4T) and (b) two-terminal (2T) tandem solar cells. Equivalent circuits of 4T (c) and (d) 2T tandem solar cells. TCO: transparent conductive oxide; TJ: tunnel junction; RL: recombination layer. Adapted from Ref.[6] with permission of American Chemical Society.

utilization of the entire solar spectrum (Figure 2.13a). For a triple-junction architecture, these losses can be further minimized by using a narrower E_g in the bottom sub-cell and a wider E_g in the top sun-cell (Figure 2.13b).

Monolithically integrated two-terminal (2T) and mechanically integrated four-terminal (4T) multi-junction solar cells are the most common architectures that have their own advantages and disadvantages.[6] Each sub-cell in 4T architecture is independently fabricated in optical coupling connection, which has less constraints according the fabrication methods from other sub-cells (Figure 2.13a). The total PCE of 4T is a sum of independent PCEs from each sub-cell (Figure 2.13c). However, the optical losses are high owing to the parasitic absorption and reflection losses from TCO, other layers, and the interfaces. In addition, the fabrication process and assembly are more complex and costly. In contrast, each sub-cell in 2T architecture are connected in series with optical and electrical coupling (Figure 2.13b). 2T solar cells are more attractive in the future PV market with potentially lower cost and lighter weight.[6] However, the fabrication remains many challenges, such as current matching (Figure 2.13d), lattice matching, light management, processing compatibility, and low-loss of recombination layers and tunneling junctions.[6]

The PCE of the 2T multi-junction is limited by the smaller current generation in one of the sub-cells. Therefore, current mismatch will result in reduced PV performance of 2T multi-junction solar cell. Current matching is pivotal and can be achieved through balanced light distribution, *i.e.*, the thickness and bandgap optimization of each sub-cell. The combination in bandgap range can be calculated through optical simulations as reported in our previous work.[52–55] In order to maximize the current generation in multi-junction architecture, light management is needed to minimize the optical losses (*e.g.*, reduce parasitic absorption and anti-reflection in different function layers). For a perovskite-based tandem architecture, minimizing the optical losses is mainly realized by optimizing the interconnection layers and top electrode.[56]

High transparency to the entire solar spectrum is indispensable for the top electrode in both 2T and 4T cells. In particular, in 4T tandem architecture, an excellent transmittance to infrared light region is necessary for the back electrode of the top cell and the front electrode of the bottom cell.[56,57] TCO is the most common transparent electrodes, including indium tin oxide (ITO), fluorine-doped tin oxide (FTO), indium zinc oxide (IZO), and hydrogen-doped indium oxide (IOH). ITO is the most widely used as it has high transmittance in the entire visible light and near-infrared range and low resistivity.[58] In our previous work, IOH is often employed in all-perovskite[16,17,57] and perovskite-CIS[15] tandems to further reduce parasitic absorption of TCO. Furthermore, a buffer layer beneath TCO is required to serve as protection layer since TCO layer is deposited by magnetron sputtering. Atomic-layer deposited tin oxide (SnO_x) with low parasitic absorption is frequently utilized to fabricate robust perovskite-based multi-junction solar cells.[13,15,17,20] TCO thin films have also been used as recombination layers in the interconnection structure of multi-junction solar cells, *e.g.*, SnO_x/TCO/HTL stack reduces the parasitic absorption compared with SnO_x/Au/HTL stack in all-perovskite tandems.[17] In addition to TCO layers, self-assembled monolayers with low parasitic absorption and good charge extraction were recently developed to replace the conventional HTLs.[13,15,17] Antireflection coatings (*e.g.*, MgF_2, LiF) and light trapping structures (*e.g.*, textured Si cells) can further reduce optical losses within perovskite-based multi-junction solar cells.[6,56] In recent years, monolithic three-terminal (3T) solar cells combining with the advantages (very low parasitic absorption) from 4T and 2T architectures have been reported, which exhibit a great potential for achieving higher energy yield.[59–62]

3. Materials, fabrications, and characterizations

In this chapter, we present experimental fabrication and characterization techniques in sections 3.1 and 3.2. The fabrication processes include spin-coating (for perovskite layers, electron transport layers (ETLs), hole transport layers (HTLs), and fullerene derivative interlayers), thermal evaporation (for ETL, barrier layers, anti-reflective layers, and metal contacts), sputtering (for HTLs, and transparent conductive oxide (TCO) front electrode), atomic layer deposition (ALD) for SnO_x, laser scribing for interconnection, and blade-coating for modules (*i.e.*, HTLs and $FAPbI_3$ perovskite thin film). The characterization techniques include material and photo-physical characterizations on thin films and devices (in section 3.3). The last section of 3.4 describes the simulation for triple-junction solar cells.

3.1. Materials and solution preparation

This section describes the materials and preparation of perovskite precursors. Four different perovskite precursors were developed in this thesis, including a ~1.26 eV narrow bandgap (NBG) perovskite $Cs_{0.025}(FA_{0.83}MA_{0.17})_{0.975}Sn_{0.5}Pb_{0.5}I_3$, a ~1.63 eV wide bandgap (WBG) perovskite $Cs_{0.1}(FA_{0.83}MA_{0.17})_{0.9}Pb(I_{0.83}Br_{0.17})_3$, a ~1.52 eV middle bandgap (MBG) $FAPbI_3$, and a ~1.84 eV WBG perovskite $FA_{0.8}Cs_{0.2}Pb(I_{0.5}Br_{0.5})_3$.

3.1.1. Materials

Materials for perovskite precursors

Lead iodide (PbI_2, TCI), lead bromide ($PbBr_2$, TCI), tin iodide (SnI_2, Alfa Aesar), cesium iodide (CsI, Alfa Aesar), cesium bromide (CsBr, Alfa Aesar), formamidinium iodide (FAI, GreatCell Solar), formamidinium bromide (FABr, GreatCell Solar), methylammonium iodide (MAI, Alfa Aesar), methylammonium chloride (MACl, Dyenamo), lead thiocyanate ($Pb(SCN)_2$, Sigma Aldrich), and tin fluoride (SnF_2, Sigma Aldrich).

Materials for electron transport layers (ETLs) and hole transport layers (HTLs)

Tin (IV) oxide nanoparticles (SnO_2 colloid precursor, Alfa Aesar), fullerene (C_{60}, Sigma Aldrich), phenyl-C61-butyric acid methyl ester (PCBM, Sigma Aldrich), indene-C60-propionic acid butyl ester (IPB, Solenne BV.), and indene-C60-propionic acid hexyl ester (IPH, Solenne BV.), poly[bis(4-phenyl)(2,4,6-trimethylphenyl)amine] (PTAA, M_w=17,800

g/mol, EM INDEX), Poly(3-hexylthiophene-2,5-diyl) (P3HT, 1-Material), [2-(9H-carbazol-9-yl)ethyl] phosphonic acid (2PACz, TCI), 2,2',7,7'-tetrakis[N,N-di(4-methoxyphenyl)amino]-9,9'-spirobifluorene (spiro-MeOTAD, Luminescence Technology), lithium bis(trifluoromethanesulfonyl) imide, and 4-tetra-butylpyridine.

Materials for other layers

2,9-dimethyl-4,7-diphenyl-1,10-phenanthroline (BCP, Lumescence Technology), lithium fluoride (LiF, Luminescence Technology), magnesium fluoride (MgF_2, Sigma Aldrich), molybdenum oxide (MoO_x, Luminescence Technology), tetrakis(dimethylamino)tin(IV) (TDMASn, Strem Chemicals). Conductive oxide front electrode (TCO) targets: indium tin oxide (ITO), indium zinc oxide (IZO), hydrogen-doped indium oxide (IOH) (InO/ZnO target, Kurt J. Lesker Company), and nickel oxide (NiO_x) (NiO_x target, Kurt J. Lesker Company).

Solvents

Dimethylformamide (DMF, Sigma Aldrich), dimethyl sulfoxide (DMSO, Sigma Aldrich), ethyl ethanoate (EA, Sigma Aldrich), chlorobenzene (CB, Sigma Aldrich), anhydrous ethanol (VWR Chemicals), toluene (Sigma Aldrich), 1,2-dichlorobenzene (Sigma Aldrich), and acetonitrile (ACN, Sigma Aldrich).

3.1.2. Solution preparation

Preparation of $Cs_{0.025}(FA_{0.83}MA_{0.17})_{0.975}Sn_{0.5}Pb_{0.5}I_3$ perovskite (~1.26 eV) precursor

The NBG perovskite has a composition of $Cs_{0.025}(FA_{0.83}MA_{0.17})_{0.975}Sn_{0.5}Pb_{0.5}I_3$. A 1.7 M NBG perovskite precursor was prepared by dissolving 0.85 M SnI_2, 0.85 M PbI_2, 1.36 M FAI, 0.34 M MAI, 0.01 M $Pb(SCN)_2$, and 0.057 M SnF_2 in a mixture solvent of DMF/DMSO with a volume ratio of 9:1. A 21.8 μL CsI stock solution (1.5 M in DMSO) was then added in the main perovskite solution. The perovskite was prepared in a N_2-filled glovebox, which was controlled with O_2 < 0.2 ppm and H_2O < 0.4 ppm.

Preparation of $FAPbI_3$ perovskite (~1.52 eV) precursor

The 1.3 M MBG $FAPbI_3$ perovskite was prepared by dissolving 1.43 M PbI_2 and 1.3 M FAI in a mixture solvent of DMF/DMSO with a volume ratio of 4:1. 30 mol% MACl was applied in the precursor for processing modules (see in chapter 5) and triple-junction architecture (see in chapter 6). The perovskite was prepared in a N_2-filled glovebox, which was controlled with O_2 < 0.5 ppm and H_2O < 0.4 ppm.

Preparation of $Cs_{0.1}(FA_{0.83}MA_{0.17})_{0.9}Pb(I_{0.83}Br_{0.17})_3$ perovskite (~1.63 eV) precursor

The 1.3 M WBG $Cs_{0.1}(FA_{0.83}MA_{0.17})_{0.9}Pb(I_{0.83}Br_{0.17})_3$ perovskite was prepared by dissolving 1.1 M PbI_2, 0.2 M $PbBr_2$, 1.0 M FAI, and 0. 2 M FAI in a mixture solvent of DMF/DMSO with a volume ratio of 4:1. A 88.9 μL CsI stock solution (1.5 M in DMSO) was then added in the main perovskite solution.

Preparation of $FA_{0.8}Cs_{0.2}Pb(I_{0.5}Br_{0.5})_3$ perovskite (~1.84 eV) precursor

The 0.8 M WBG $FA_{0.8}Cs_{0.2}Pb(I_{0.5}Br_{0.5})_3$ perovskite was prepared by dissolving 0.4 M PbI_2, 0.4 M $PbBr_2$, 0.32 M FAI, 0.32 M FAI, 0.08 M CsI, and 0.08 M CsBr in a mixture solvent of DMF/DMSO with a volume ratio of 4:1.

3.2. Thin film depositions and device fabrications

In this thesis, NBG (~1.26 eV) PSCs in *p-i-n* architecture were fabricated and employed in two-terminal (2T) devices combined with semitransparent WBG (~1.63 eV) PSCs, which will be presented in chapter 4. MBG $FAPbI_3$ PSCs were developed in *p-i-n* architecture, and scaled-up to module dimension using scalable methods. The results will be discussed in chapter 5. We designed 2T perovskite–perovskite–Si triple-junction solar cells from simulations to experimental optimizations. The corresponding results will be presented in chapter 6.

3.2.1. Thin film depositions

NBG perovskite (~1.26 eV) thin film deposition

$Cs_{0.025}(FA_{0.83}MA_{0.17})_{0.975}Sn_{0.5}Pb_{0.5}I_3$ NBG perovskite thin films were deposited by vacuum-assisted growth (VAG) method.[16] The perovskite precursor was spin-coated on PTAA-based substrates at 5000 rpm for 10 s, and then the wet thin film was transferred promptly into a home-made vacuum chamber for an optimized vacuum time of ~10 s. The dried thin film was finally annealed at 100 °C for 7 min.

MBG perovskite (~1.52 eV) thin film deposition

$FAPbI_3$ MBG perovskite thin films were deposited by vacuum-assisted growth (VAG) and anti-solvent (AS) quenching methods.[27] For VAG process, the perovskite precursor was spin-coated on 2PACz-based substrates at 5000 rpm for 30 s then the wet thin film was transferred promptly into a home-made vacuum chamber for an optimized vacuum time of 30 s. For AS process, the perovskite precursor was spin-coated on 2PACz-based substrates at 1000 rpm for 10 s and 5000 rpm for 40 s. 150 µL of EA was dropped at 30 s during the second step of spin coating. The wet thin film without MACl additive was annealed at 150 °C for 30 min. The wet thin film with MACl additive was annealed at 120 °C for 20 min.

WBG perovskite (~1.63 eV) thin film deposition

$Cs_{0.1}(FA_{0.83}MA_{0.17})_{0.9}Pb(I_{0.83}Br_{0.17})_3$ WBG perovskite thin films were deposited by the AS method. The perovskite precursor was spin-coated on SnO_x-based substrates at 1000 rpm for 10 s and 6000 rpm for 20 s. 100 µL of CB was dropped at 10 s during the second step of spin coating. The wet thin film was annealed at 100 °C for 1 h.

WBG perovskite (~1.84 eV) thin film deposition

$FA_{0.8}Cs_{0.2}Pb(I_{0.5}Br_{0.5})_3$ WBG perovskite thin films were deposited by the AS method. The

perovskite precursor was spin-coated at 1000 rpm for 10 s and 5000 rpm for 30 s. 150 µL of EA was dropped at 11 s during the second step of spin coating. The wet thin film was annealed at 150 °C for 20 min.

Atomic layer deposition of SnO_x thin film

We fabricated a 35 nm SnO_x thin film (measured on a silicon wafer) by atomic layer deposition (ALD) with a target of 300 cycles using a Picosun ALD system (R200 Advanced) at 90 °C. TDMASn (pulse time 1.6 s, purge time 12 s) and water (pulse time 0.1 s, purge time 16 s) was used as the precursors, and high-purity argon (Ar, 99.999%) was employed as carrier gas and purge gas.[17] Line flows of 120 and 150 standard cubic centimeters per minute (sccm) were set for TDMASn and water, respectively. To ensure thermal equilibrium before starting the deposition, TDMASn source was preheated for 1 h at 70 °C.

3.2.2. Device fabrications

Fabrication of opaque NBG (~1.26 eV) PSCs

NBG PSCs were fabricated in a *p-i-n*-based architecture with the layer stack of ITO/PTAA/$Cs_{0.1}(FA_{0.83}MA_{0.17})_{0.9}Pb(I_{0.83}Br_{0.17})_3$/interlayer/$C_{60}$/BCP/Ag, as shown in Figure 3.1. Different fullerene derivatives, *i.e.*, PCBM, IPB, IPH, were employed as an interlayer, see in chapter 4. ITO substrates (sheet resistance of 15 Ω sq^{-1}, thickness of ~120 nm, Luminescence Technology) were first cleaned in ultrasonic bath for 15 min using deionized water, acetone, and isopropanol, respectively. ITO substrates were then treated with an oxygen plasma for 3 min. For the PTAA HTL, 1.5 mg mL^{-1} solution was prepared by dissolving PTAA material in toluene. PTAA solution was spin-coated on an ITO substrate at 4000 rpm for 30 s, then the wet thin film was annealed at 100 ℃ for 10 min. Before processing perovskite thin films, 70 µL of DMF was spin-coated on PTAA layer and the substrate was annealed at 100 ℃ for 2 min to improve wettability for the perovskite precursor.[63–65] The NBG thin film was deposited on top of the PTAA layer as described above. Afterwards, 5 mg mL^{-1} (dissolving in 1,2-dichlorobenzene) fullerene derivatives (*i.e.*, PCBM, IPB, IPH) solution was spin-coated at 2000 rpm for 60 s onto perovskite thin film as an interlayer. Finally, the layer sequential of ~25 nm C_{60}, ~3 nm BCP, and ~100 nm Ag were thermally evaporated. A 125 nm MgF_2 layer was thermally evaporated as an antireflection coating on the glass side of champion PSCs.

Fabrication of semi-transparent WBG (~1.63 eV) PSCs

Semi-transparent WBG PSCs were fabricated in a *n-i-p* architecture (see Figure 3.2), *i.e.*, IOH/SnO_2 nanoparticles/$Cs_{0.1}(FA_{0.83}MA_{0.17})_{0.9}Pb(I_{0.83}Br_{0.17})_3$/Spiro-MeOTAD/$MoO_x$/IZO/$MgF_2$. This device was used in 4T architecture in chapter 4. For the ETL, the solution of SnO_2 nanoparticles was diluted to 2% volume ratio with deionized water. Then, it was spin-coated on top of cleaned IOH substrate at 4000 rpm for 30 s and the substrate was annealed at 200 °C for 30 min in air. The WBG perovskite thin film was fabricated as described above. For preparing the HTL precursor, 80 mg of Spiro-MeOTAD was dissolved in 1 mL

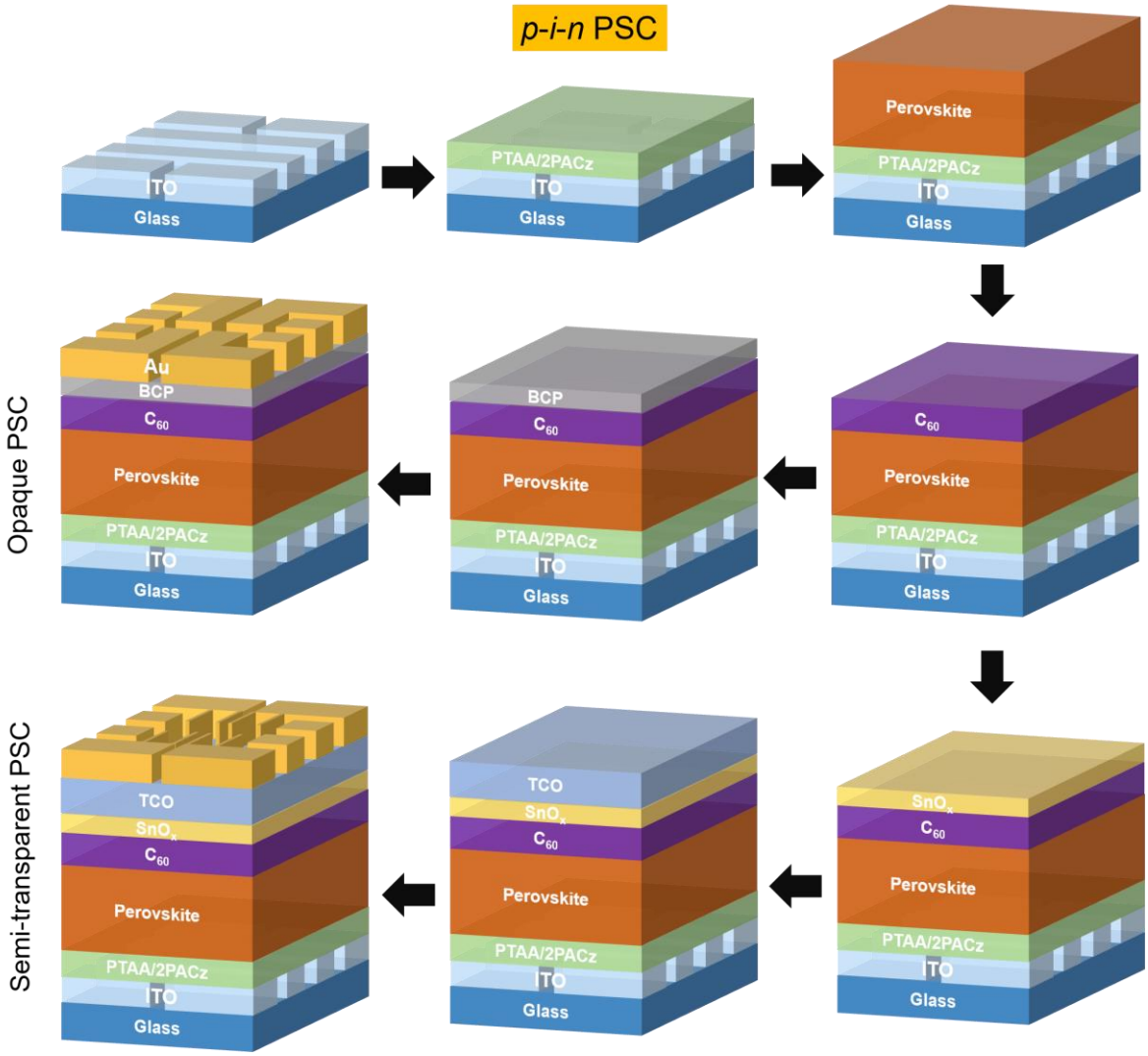

Figure 3.1. Schematic illustration of fabrication process for opaque and semi-transparent PSCs based on *p-i-n* architecture.

CB with adding 17.5 µL of lithium bis(trifluoromethanesulfonyl) imide solution (520 mg mL^{-1} in ACN) and 28.5 µL of 4-tetra-butylpyridine. The HTL solution was spin-coated at 4000 rpm for 30 s and was kept for overnight in a dry box. Finally, ~10 nm MoO_x was thermally evaporated, ~165 nm IZO was sputtered, and ~165 nm MgF_2 was thermally evaporated to complete the semi-transparent device.

Fabrication of opaque MBG (~1.52 eV) and WBG (~1.84 eV) PSCs

Opaque MBG (~1.52 eV) and WBG (~1.84 eV) PSCs were fabricated in a *p-i-n* architecture (see Figure 3.1) with the layer stack of ITO/2PACz/perovskite/(LiF)/C_{60}/BCP/Au. For 2PACz solution, a ~0.475 mg mL^{-1} solution was prepared in anhydrous ethanol. Then, it was spin-coated on the cleaned ITO substrate at 3000 rpm for 30 s and annealed at 100 °C for 10 min. $FAPbI_3$ thin films were fabricated by using VAG and AS methods. $FA_{0.8}Cs_{0.2}Pb(I_{0.5}Br_{0.5})_3$ thin film was fabricated by using AS method and a 1 nm LiF thin film then was thermally evaporated on top. Finally, the sequential layers of ~30 nm C_{60}, ~5

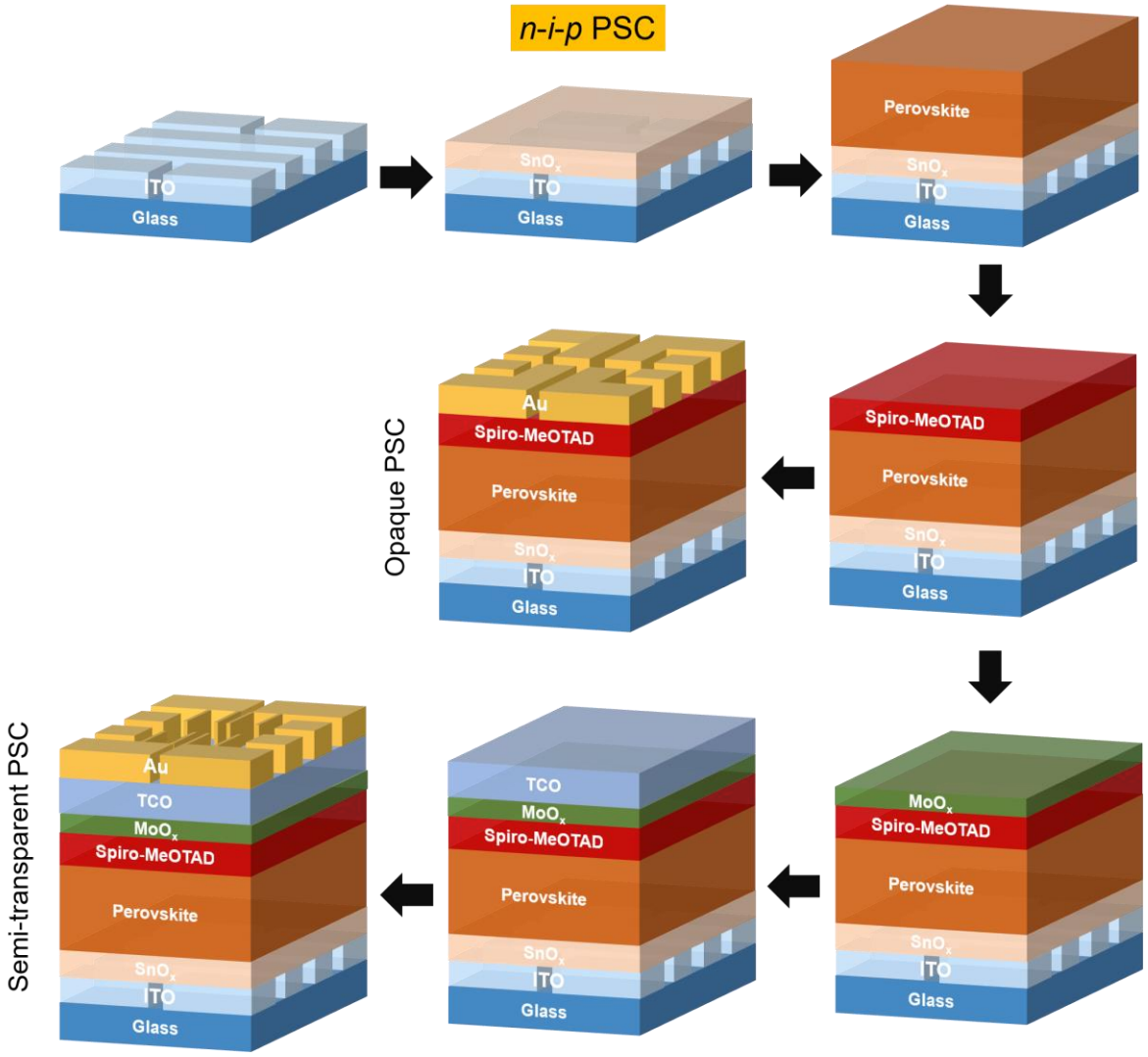

Figure 3.2. Schematic illustration of fabrication process for opaque and semi-transparent PSCs based on *n-i-p* architecture.

nm BCP, and ~75 nm Au were thermally evaporated. A 125 nm MgF_2 was thermally evaporated as an antireflection coating on the glass side of champion PSCs.

Fabrication of semi-transparent MBG (~1.52 eV) and WBG (~1.84 eV) PSCs

Semi-transparent MBG (~1.52 eV) PSCs were fabricated in a *p-i-n* architecture (see Figure 3.1) with the layer stack of ITO/2PACz/perovskite/(LiF)/SnO_x/C_{60}/TCO/Au. The MBG and WBG semitransparent devices were used for middle and top sub-cells in triple-junction architecture, see chapter 6. 2PACz and perovskite layers were fabricated in the same manner as opaque devices. A thinner layer of ~15 nm C_{60} was thermally evaporated. Then a ~35 nm thick of SnO_x layer was fabricated by the described ALD process and a top TCO was sputtered. Three different recipes were optimized, see chapter 6 in Figure 6.7b.

- Recipe 1: ~90 nm IZO fabricated by using a low deposition pressure of 0.8 mTorr and a high power supply of 200 W.

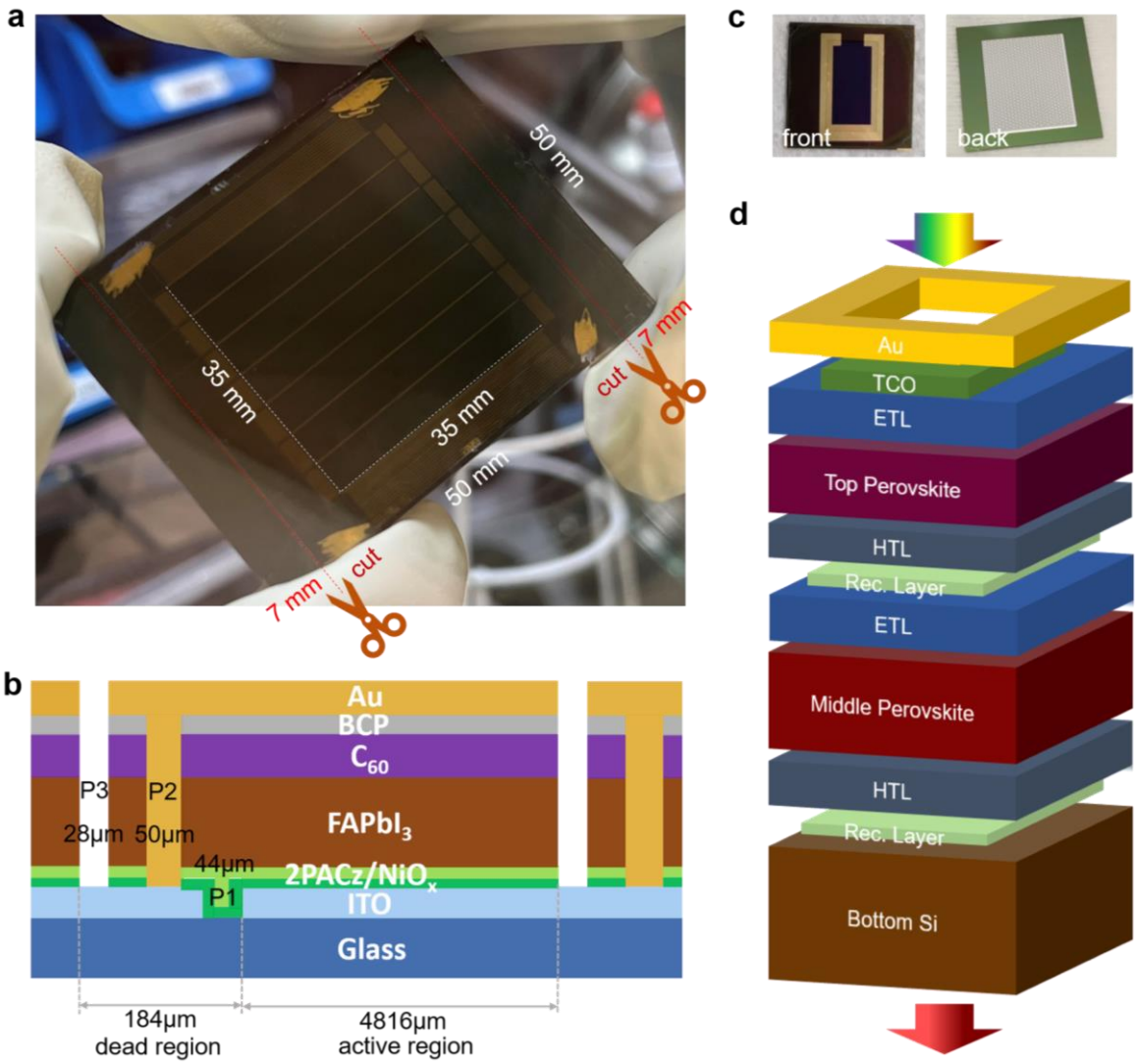

Figure 3.3. (a) Photograph and (b) schematic illustration of *p-i-n*-based $FAPbI_3$ perovskite solar module. The 6.4 × 5.0 cm^2 substrate was cut into 5.0 × 5.0 cm^2 module dimension with 3.5 × 3.5 cm^2 = 12.25 cm^2 aperture area design. The widths of P1, P2, and P3 scribing lines are 44, 50, and 28 μm, respectively. The dead and active regions are calculated to 184 and 4816 28 μm, respectively. (c) Photograph and (d) schematic illustration of perovskite–perovskite–Si triple-junction solar cell. The bottom Si cell was provided by Solar Energy Research Hamelin (ISFH).

- Recipe 2: ~165 nm IZO fabricated by using a high deposition pressure of 1.5 mTorr and a low power supply of 100 W;
- ~120 nm IOH

Finally, a 75 nm grid Au (fingers in the edges of top TCO area) and a ~125 nm MgF_2 was thermally evaporated to complete the semi-transparent device.

Laser scribing lines for modules

Substrate dimensions (see chapter 5 in Figure 5.23):

- Initial dimensions: 6.4 × 5 cm^2.

- Twice of 0.7 cm width in each edge of substrate length were cut away (see Figure 3.3a).
- Final module dimension: 5 × 5 cm² (see Figure 3.3a).

Scribing lines (see Figure 3.3b and 5.24 in chapter 5 for layout details):

- Three scribing lines, labeled as P1, P2, and P3, were employed in the modules.[17,66]
- A layout of 3.5 × 3.5 cm^2 with an aperture area of 12.25 cm² was used for scribing.
- P1 was used to ablate the ITO layer.
- P2 was used to ablate multilayers consisting of NiO_x/2PACz/$FAPbI_3$/C_{60}/BCP.
- P3 was used to ablate multilayers consisting of NiO_x/2PACz/$FAPbI_3$/C_{60}/BCP/Au.

Scribing line widths and geometric fill factor (GFF) (see Figure 3.3b, 5.23, and 5.24 in chapter 5):[27]

- The width of P1: 44 μm.
- The width of P2: 50 μm.
- The width of P3: 28 μm.
- The width of dead region: 184 μm.
- GFF: 96.3%.

Upscaling $FAPbI_3$ solar cells and modules

For scalable PSCs, the large substrate was precut and divided into 32 individual pieces, each with dimensions of 1.6 × 1.6 cm². A 5 nm NiO_x layer was sputtered on 6.4 × 5 cm² substrate dimensions and a diluted 2PACz solution (~0.158 mg mL^{-1}) was blade-coated on top. In the blade-coating process for $FAPbI_3$ thin films, the following parameters were optimized:

- N_2 gas flow: ~180 cm^3 min^{-1}.
- Vacuum time: ~30 s.
- Concentration of diluted perovskite precursor: 0.65 M.
- Blade gap: 100 μm.
- Blade rate: 15 mm s^{-1}.

Finally, the layer sequential of ~30 nm C_{60}, ~5 nm BCP, and ~100 nm Au were thermally evaporated. A 125 nm MgF_2 was thermally evaporated as an antireflection coating on the glass side of champion PSCs and modules.

Fabrication of silicon solar cells

Si solar cells were provided by Institute for Solar Energy Research Hamelin (ISFH, see Figure 3.3c). The fabrication details as follows:[55]

- Wafer selection: Chosen wafers were polished *n*-type Float Zone (FZ) wafers with an approximately 2 Ω cm resistivity and a thickness of roughly 200 μm. The wafer was etched with potassium hydroxide (KOH) before the fabrication.
- Silicon dioxide (SiO_x) growth: A thick SiO_x was grown to insulate the rear minority carrier hole contact from potential defects at the cleaved edges. Selectively ablating the SiO_x on the rear side defines the active area. KOH was used for etching to remove

any laser-induced damage. On the front side, the SiO_x layer was eliminated using a single-side treatment with hydrofluoric (HF) acid.

- Depositing and doping amorphous silicon (a-Si) layer: An a-Si layer was deposited over the SiO_x layer. Doping was introduced by implanting pH to the front side and Boron to the rear side.
- Creating passivating contacts: Passivating contacts were produced using electron- and hole-selective polysilicon-on-passivating-oxide (*n*-POLO and *p*-POLO) contacts through furnace annealing and oxidation.
- Patterning rear side SiO_x: After KOH etching and texturizing, laser ablation was used to selectively pattern the SiO_x layer on the rear side, leaving only *p*-POLO contact islands.
- Front side modifications: The front side underwent a treatment involving the removal of SiO_x protection on the front *n*-POLO contact by single-side HF. Additionally, the Poly-Si layer on the front contact was thinned to around 50 nm.
- Layering for passivation: The rear side was passivated with a layer stack consisting of aluminum oxide (Al_2O_3), silicon nitride (SiN_y), and SiO_x. On the front side, an Al_2O_3 layer was added to facilitate hydrogenation of the *n*-POLO front contact.
- Preparing electrical contacts: Local ablation of the dielectric layer stack on the rear side was performed to enable electrical contact with the metal.
- Creating front contact: HF was used to remove Al_2O_3 hydrogenation source. On the front *n*-POLO contact, an ITO layer with a thickness of 20 nm was sputtered.
- Creating back contact: A rear-side aluminum (Al) was evaporated as back contact.
- Cleaving wafer: 16 × 16 mm² dimensions containing 1 cm² cells were cleaved from the wafer.

Fabrication of monolithic perovskite–perovskite–Si triple-junction solar cells

We use Si (~1.1 eV) as bottom cell, MBG $FAPbI_3$ (~1.52 eV) as middle cell, and WBG (~1.84 eV) as top cell in triple-junction architecture (see Figure 3.3d). The architecture is Si cell/ITO/NiO_x/2PACz/$FAPbI_3$/C_{60}/SnO_x/ITO/NiO_x/2PACz/$Cs_{0.2}FA_{0.8}Pb(I_{0.5}Br_{0.5})_3$/LiF/$C_{60}$/$SnO_x$/IZO/Au/$MgF_2$. The fabrication procedure for other layers is the same as with the semi-transparent devices. The recombination layer used ITO with a thickness of 15−20 nm. A ~300 nm c-shape Au was thermally evaporated with a defined active area of 52.25 mm^2. We performed optical simulations and experimental optimizations in chapter 6.

3.3. Characterization techniques

In this section, we describe different material and photo-physical characterizations employed on thin films and devices. The corresponding results and discussion will be presented in chapter 4–6.

3.3.1. Thin film characterizations

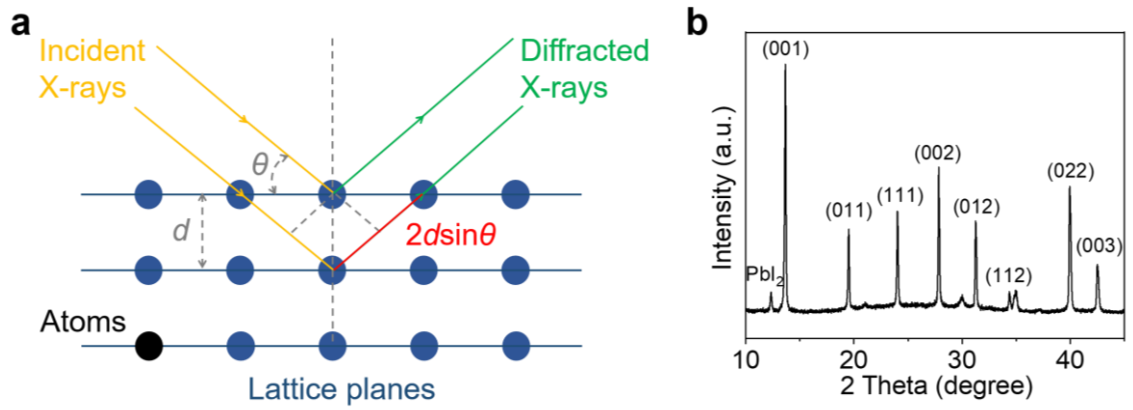

Figure 3.4. (a) Schematic illustration of X-Ray diffraction (XRD) principle and (b) a XRD pattern of $FAPbI_3$ thin film based on ITO/2PACz substrates used in chapter 6.

X-ray diffraction (XRD)

X-Ray diffraction (XRD) analysis is widely used technique that provides detailed information about the crystal structure of a specific crystalline material. It relies on the principle of X-ray interference and diffraction with periodic array of material atoms (see Figure 3.4a). High-energy electromagnetic waves are generated by emission of an X-ray source. Then, X-rays interact with the crystal lattice and scattered by electrons surrounding atoms. This scattering follows specific patterns due to the ordered arrangement of atoms in the crystal lattice. X-rays are diffracted at specific angles related to the distance between the crystal planes and the wavelength of the X-rays. This relationship is expressed by Bragg's law as follows:

$$n\,\lambda = 2\,d\,\sin(\theta) \tag{3.1}$$

where n is an integer, λ is the X-ray wavelength, d is the spacing between diffracting planes of the crystal, and θ is the incident angle of the X-ray. As the scattered X-rays create a diffraction pattern, this pattern consists of peaks of X-ray intensity at various angles. These angles are indicative and can be mathematically analyzed to determine the crystal lattice parameters.

This technique is used to determine the crystal structure of perovskite materials in chapter 5 and 6. In this thesis, XRD measurements were conducted on the layer stack of ITO/2PACz/$FAPbI_3$ (see Figure 3.4b) based on Bruker D2Phaser system using Cu-Kα radiation (λ = 1.5405 Å) in Bragg–Brentano configuration and a LynxEye detector.

X-ray photoelectron spectroscopy (XPS)

X-ray Photoelectron Spectroscopy (XPS) is a surface-sensitive analytical technique used to determine the chemical composition of materials, especially the surficial atomic layers. It works on the principle of photoelectric effect and provides information about elemental and chemical state composition. XPS typically employs aluminum (Al Kα) or magnesium (Mg Kα) X-rays generated from a monochromatic X-ray source. The X-ray beam is focused onto

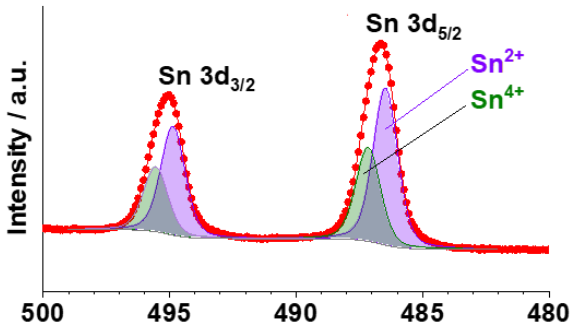

Figure 3.5. XPS spectra of Sn-Pb based NBG perovskite used in chapter 4.

the surface of the sample, and high-energy X-ray photons interact with the atoms in the sample. The energy can be transferred to a core electron, causing the core electron to be ejected from its shell and overcoming the binding energy (E_b). The ejected electron is referred to as a photoelectron. The photoelectron is emitted with kinetic energy (E_k), which depends on the energy of the incident X-ray photon ($h\nu$) and the binding energy of the core electron. The E_b can be calculated as follows:

$$E_b = h\nu - (E_k + \varphi) \tag{3.2}$$

$$\varphi = E_{vac} - E_f \tag{3.3}$$

Where φ is the work function, *i.e.*, energy difference between Femi level (E_f) and vacuum level (E_{vac}). By analyzing the E_b and E_k of, the elements and chemical states of the sample can be identified. The peak positions and shapes provide information about the valence states, oxidation states, and chemical environments of the elements.

In this thesis, we utilized XPS measurements to investigate the Sn state of Sn-Pb based NBG perovskite (see Figure 3.5). A Kα instrument (Thermo Fisher Scientific) was utilized with a monochromatic Al Kα X-ray source (an energy of 1486.6 eV). The X-ray beam had a spot size of 400 μm. In these measurements, charge neutralization was not applied because the samples were conducting electricity effectively. Data acquisition and processing were used by Thermo Avantage software. The binding energies in the XPS spectra were referenced to the C 1s peak of hydrocarbons, which is typically found at 285.0 eV. To analyze the XPS spectra, one or more Voigt profiles were used. Voigt profiles are mathematical functions that describe the shapes of spectral lines. For accurate quantification, various parameters were considered, including the analyzer transmission function, Scofield sensitivity factors, and effective attenuation lengths (EALs) for photoelectrons.[67] EALs were determined using the standard TPP-2M formalism.[68]

Ultraviolet photoelectron spectroscopy (UPS)

Ultraviolet Photoelectron Spectroscopy (UPS) is a surface-sensitive analytical technique used to study the electronic structure of materials, especially the energy distribution of electrons near the sample surface. The UPS principle is based on the photoelectric effect, first described by Albert Einstein. Electrons within a material have discrete energy levels.

High-energy photons (in the ultraviolet range) strike the sample surface and excite electrons from that material from one of these energy levels (usually the highest occupied molecular orbital (HOMO) or valence band (VB)) to a higher energy level (*i.e.*, lowest unoccupied molecular orbital (LUMO) or conduction band (CB)) or even eject it from the material entirely. The energy of the incident photon must be higher than the work function (φ) of the material (the minimum energy needed to remove an electron from the surface). The kinetic energy can be measured for these ejected electrons, which is directly related to the energy levels of the electrons within the material. The resulting UPS spectrum shows the number of electrons at each kinetic energy level. The HOMO (or VB) and φ of the material can be determined.

In chapter 4, we performed UPS measurements on the Sn-Pb NBG perovskite thin films with and without fullerene derivatives. A Thermo Scientific Escalab 250Xi was used with He I (21.2 eV) source. For most of the samples, a bias of -3 V was used, while the perovskite sample had a bias of -2 V. The energy resolution of the measurements was ~150 meV. The pass energy of the electron analyzer was set at 4 eV. The base pressure in the analysis chamber before conducting the UPS measurements was less than 10^{-10} mbar. Fermi levels of NBG perovskite and fullerene derivatives are calculated as follows (see Figure 3.6):[69,70]

$$\varphi = E_{\mathrm{vac}} - E_{\mathrm{f}} \tag{3.4}$$

$$\varphi = h\nu - \left(E_{\mathrm{cut-off}} - E_{\mathrm{f-spectrometer}}\right) \tag{3.5}$$

$$\mathrm{HOMO\ (or\ VB)} = E_{\mathrm{f}} - E_{\mathrm{onset}} \tag{3.6}$$

$$\mathrm{LUMO\ (or\ CB)} = \mathrm{HOMO\ (or\ VB)} + E_{\mathrm{g}} \tag{3.7}$$

where E_{f} is the Fermi level, $E_{\mathrm{cut\text{-}off}}$ is the cut-off binding energy at the secondary electron

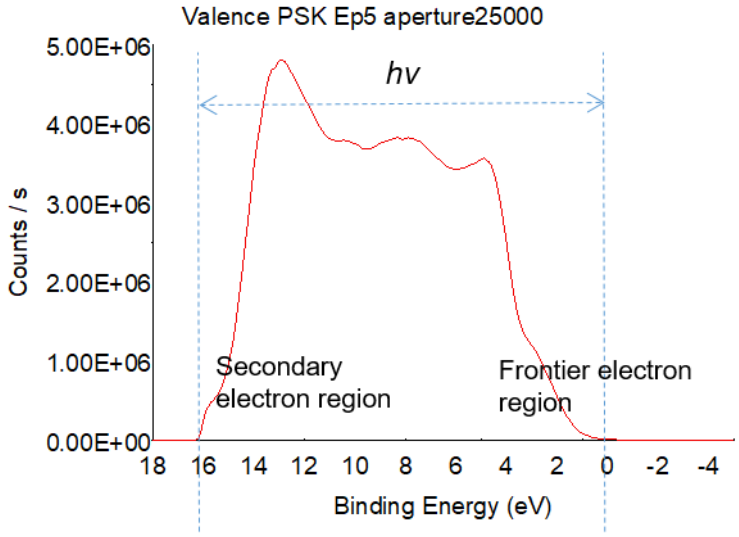

Figure 3.6. UPS spectrum of the secondary electron cutoff (left) and the frontier electron region (right) for Sn-Pb based NBG perovskite used in chapter 4.

region, E_{vac} is the vacuum energy level, hv is the emission energy of the He I (21.2 eV) source, and E_{onset} is the binding energy at the frontier electronic structure region. A sputter-cleaned silver sample was used to determine the position of $E_{f\text{-}spectrometer}$. The $E_{cut\text{-}off}$ of NBG, C_{60}, PCBM, IPB, and IPH are 16.3, 16.5, 16.6, 16.7, and 16.7 eV, respectively (Figure 4.4a and 4.5a in chapter 4). The corresponding φ were thus calculated to be -4.9, -4.7, -4.6, -4.5, and -4.5 eV, respectively (Figure 4.4b in chapter 4). The E_{onset} of NBG, C_{60}, PCBM, IPB, and IPH are 0.4, 1.6, 1.4, 1.4, and 1.4 eV, respectively (Figure 4.4a and 4.5a in chapter 4). Therefore, the HOMO or VB were calculated to be -5.3, -6.3, -6.0, -5.9, and -5.9 eV, respectively (Figure 4.4b in chapter 4). The band gaps (E_g) for NBG, C_{60}, PCBM, IPB and are 1.26, 1.90, 2.03, 2.07, and 2.07, respectively (Figure 4.3e, and 4.5e–4.5f in chapter 4). The corresponding LUMO or CB can be calculated to be -4.0, -4.4, -4.0, -3.8, and -3.8, respectively (Figure 4.4b in chapter 4).

Ultraviolet-visible (UV-Vis) spectroscopy

The interaction of a material with electromagnetic radiation in the UV and visible wavelength of the spectrum is the primary focus of UV-Vis spectroscopy. This interaction causes electrons to be excited from their ground state to higher energy levels (usually the first singlet excited state), and absorbance spectra can disclose important information about the electronic structure and characteristics of the chemical. A typical setup for thin-film measurement has a double beam instrument using a single source and a monochromator. A splitter and a series of mirrors are also used to make the beam reachable to a reference sample and an analysed sample. The in formation of transmittance (T) and reflectance (R) of thin films can be determined. The absorptance (A) can be calculated as follows:

$$A = 1 - T - R \tag{3.8}$$

This measurement can also evaluate the optical bandgap (E_g) for the thin films as follows:[71]

$$\alpha\, h\, \nu^{1/\gamma} = \mathrm{B}\left(h\,\nu - E_g\right) \tag{3.9}$$

where α is absorption coefficient of thin film, hv is the energy of the photons, B is a constant, and γ is a factor of the nature of the electron transition that is equal to 2 or 1/2 for the indirect and direct transition bandgaps of semiconductors, respectively.[71] Tauc plot (*i.e.*, $(\alpha hv)^2$ *vs.* hv) can be evaluated the bandgap of semiconductor.

In this thesis, a PerkinElmer Lambda 1050 spectrophotometer was used as an integrating sphere to measure T and R for perovskite (chapter 4 and 5) and fullerene derivative (chapter 4) thin films.

Scanning electron microscopy (SEM)

Scanning electron microscopy (SEM) is an imaging technique that uses a focussed beam of high-energy electrons (typically 0.2 to 40 keV) to see the surface morphology and composition of a sample. SEM is based on a range of signals generated by interactions between the high-energy electron beam and atoms in the sample.

- Secondary electrons (SE): SE are ejected from the sample surface with low energy (a few KeV). SE signals provide detailed information of surface morphology of the sample, *e.g.*, topography and texture. SE detectors are standard equipment in all SEMs showing surface details.
- Back-scattered electrons (BSE): In an electron beam, BSE are primary electrons interacting with sample atoms and then scattering backward. BSE signals are associated with the density of sample elements in the sample, providing information about the composition and distribution of the sample elements.
- Characteristic X-rays: Characteristic X-rays are generated when inner shell electrons in the sample atoms were replaced by high-energy electrons. Each element has a unique emission of X-rays. Energy dispersive X-ray spectroscopy (EDS) detectors are widely utilized in SEM for elemental analysis in the sample.
- Cathodoluminescence (CL): CL is light (photons) emission when the material is exposed to the electron beam, providing optical and electronic information of materials, *e.g.*, defects, impurities, as well as the distribution of elements in the sample.

These various signal types provide different features about surface and composition in the sample.

In this thesis, a Zeiss LEO1530 VP SEM with an in-lens detector was used to capture cross-sectional and top-view SEM pictures of the perovskite thin films (chapter 5 and 6) and the layer stack of $FAPbI_3/C_{60}/SnO_x$ thin films (chapter 6). SEM images were taken with a 5-kV acceleration voltage and a 20 µm aperture size.

Atomic force microscopy (AFM)

Atomic Force Microscopy (AFM) is a high-resolution surficial imaging technique used to study the surface properties of nanomaterials. It working principle is based on measuring forces between a sharp probe tip and the surficial atoms of a sample. Various interactions (*e.g.*, electrostatic forces, Van der Waals forces, capillary forces) between surface atoms and the probe tip occurs when the probe tip hovers over the sample surface. The cantilever is force sensitive, which bends or deflects as the forces vary. The probe is raster-scanned across the surface of the sample. The height of the cantilever is modified at each location to maintain a consistent contact force, and this modification is recorded. The accumulation of these height changes over a large region results in a picture known as a topographic map. The data may be utilized to create a two- or three-dimensional pictures of the sample surface. Various information, *e.g.*, height, roughness, adhesion, electrical properties, and *etc*., may be retrieved by examining the forces and deflections.

In chapter 5 to 6, the surface topography, profile, and roughness of perovskite thin films and $FAPbI_3/C_{60}/SnO_x$ layer stack were collected by Nanowizard AFM (JK instrument).

Optical microscopy

Optical microscopy, often known as light microscopy, is a technique for observing and studying microscopic level. It needs visualizing and magnifying samples using visible light and a combination of lenses. In chapter 5, a ZEISS Axioplan 2 microscope was used to collect optical microscopy images of perovskite thin films.

Surface profile and thickness

A profilometer is used to determine the surface profile, roughness, and thickness of a material, especially thin films. It works by physically probing the surface with a stylus while recording the changes in the vertical position of the stylus. In chapter 4 and 5, Bruker Dektakt XT profilometer was used to measure the thickness of perovskite thin films.

Contact angle

The measuring of contact angles is a technique used to assess the wetting qualities of a liquid on a solid surface. It reveals the insights of a liquid distribution on a certain solid material surface. A hydrophobic surface (typically $\theta > 90$ degrees) has a high contact angle, indicating that the liquid does not effectively wet the surface. In contrast, a hydrophilic surface (typically $\theta < 90$ degrees) a low contact angle that indicates the liquid wetting or spreading out on the surface. In chapter 4 and 6, OCA 100 (Data Physics Instruments GmbH) was used to measure contact angle in the ambient air at the room temperature. 1 µl drop of water or DMF was employed on the measurements.

Steady-state and time-resolved photoluminescence spectroscopy (PL and TRPL)

Photoluminescence (PL) is a widely used technique for characterizing optoelectronic semiconductors. When a thin film is exposed to incident light with a higher energy (*i.e.*, an energy greater than the bandgap), the photons are absorbed by the thin-film material and the electrons are excited from the valence to the conductance band. After thermally relaxation, the photo-excited carriers spontaneously recombine with the holes in conduction band. Excess energy is released as light (spontaneous emission) in the case of direct semiconductors. A spectrometer is used to collect the emitted PL. The intensity and wavelength of the emitted light reveal important information about the electrical structure, bandgap energy, and the existence of defects or impurities of the examined thin film. In chapter 4, the FLSP920 Fluorescence Spectrometers (Edinburgh Instruments Ltd.) fitted with a Hamamatsu R2658P photomultiplier were used for steady-state PL measurements on perovskite and perovskite/interlayer thin films. The excitation light was supplied by a 635nm LED (PDL-800D, PicoQuant).

Time-Resolved TRPL spectroscopy is based on the dynamics of PL emissions from materials over extremely small time periods, generally ranging from picoseconds (10^{-12} s) to nanoseconds (10^{-9} s). This gives useful information on the recombination and relaxation processes of excited electrons and holes in a thin-film material. In chapter 4–6, TRPL was performed using the TCSPC acquisition technique on a FLSP920 Fluorescence Spectrometer (Edinburgh Instruments Ltd.). As the excitation light, a picosecond pulsed laser diode (PicoQuant, 635 nm) was externally activated by a delay generator (repetition rate: 500 kHz).

A photomultiplier tube (Hamamatsu R928P) was used to capture the emission. The measurements were taken in the ambient air.

Photoluminescence quantum yield (PLQY)

Photoluminescence Quantum Yield (PLQY) is used to quantify efficiency in converting absorbed photons into emitted photons, *i.e.*, the ratio of the number of emitted photons (PL) to the number of absorbed photons.

in emitting photons as a result of PL of a thin-film material, which is light emission observed when a material absorbs photons and re-emits them at longer wavelengths (lower energy).

In chapter 5 and 6, we performed PLQY measurements on $FAPbI_3$ thin films and $FAPbI_3/C_{60}/SnO_x$ stacks in ambient air inside an integrating sphere (LabSphere, 15 cm diameter). Through a tiny entrance port, a green laser (Coherent or LD-515-10MG from Roithner Lasertechnik) was directed into the sphere. The radiation from the sphere's exit port was collected and guided by an optical fiber to the spectrometers (QE65 Pro from Ocean Optics and AvaSpec-ULS2048x64TEC from Avantes). A calibration lamp (HL-3plus-INT-Cal from Ocean Optics) was used to calibrate the spectral response. The integration time was used to reconstruct raw observed spectra into power spectra. To prevent specular reflection toward the entrance port, the samples were arranged at a 15° angle to the laser beam. The 'implied V_{OC}' ($V_{OC\text{-}imp}$) can be calculated as follows:[72–74]

$$V_{\mathrm{OC-imp}} = \frac{\Delta E_{\mathrm{F}}}{q} = V_{\mathrm{OC-rad}} + \ln(\mathrm{PLQY})\, k_{\mathrm{B}}\, \frac{T}{q} \tag{3.10}$$

where k_B is the Boltzmann constant, T is the temperature (300 K), q is the elementary charge.

3.3.2. Device characterizations

Current-density-voltage (*J-V*)

The performance of the devices was characterized using a class AAA 21-channel LED solar simulator (Wavelabs Solar Metrology Systems Sinus-70) along with a source meter (Keithley 2400). This setup provided an air-mass AM 1.5G spectrum, which simulates standard sunlight with an intensity of 100 mW cm^{-2}. The scan rate during measurements was maintained at 0.6 V s^{-1}. To ensure accuracy, a certified silicon reference solar cell (KG0, Newport) was employed to calibrate the illumination intensity of the solar simulator.

Maximum power point (MPP) tracking

The stabilized power conversion efficiency (SPCE) was determined through maximum power point (MPP) tracking, which was conducted under continuous AM 1.5G illumination. It's important to note that the temperature of the devices was not controlled or regulated during *J-V* measurements.

Thermal stability

To evaluate the thermal stability, the devices were subjected on a hotplate at a temperature of 85 °C while being kept in the dark. This thermal stability test assists to assess how the devices perform under elevated temperatures, which is important for understanding their reliability and durability under real-world operating conditions.

External quantum efficiency (EQE)

The external quantum efficiency (EQE) spectra for the single-junction, tandem, and triple-junction solar cells were measured using a Bentham PVE300 system equipped with modulated monochromatic light. In these measurements, a chopping frequency was set at ~580 Hz with an integration time of 500 ms.

To ensure the accuracy and reliability of the EQE measurements for triple-junction architecture, the EQE response was calibrated using certified reference cells of Si and germanium (Ge). Si reference cells were used for the wavelength region from 300 to 1100 nm, while Ge reference cells were used for the region from 1000 to 1300 nm. Each sub-cell was characterized for its EQE separately, and this was achieved by utilizing a combination of different filters and bias light sources to saturate the other two sub-cells.

- For the top cell, light-emitting diodes (LED) with wavelengths of 780 nm and 940 nm were used in combination with a long-pass filter (FGL850M), which allows light with a wavelength longer than 850 nm to pass through.
- For the middle cell, LEDs emitting at 465 nm and 940 nm were used along with the same long-pass filter (FGL850M).
- For the bottom cell, LEDs with wavelengths of 465 nm and 780 nm were employed, along with a bandpass filter (FGB37M) that allows light in the range of 335 to 610 nm to pass through.

This approach ensured that each sub-cell was selectively illuminated and evaluated for its EQE without interference from the others.

Electroluminescence (EL) and photoluminescence (PL) imaging

Electroluminescence (EL) and photoluminescence (PL) images were captured using a high-resolution 2.1-megapixel scientific complementary metal-oxide-semiconductor (sCMOS) camera, specifically the Quantalux sCMOS camera, provided by Thorlabs. To obtain high-quality images, optical filters were used in the imaging setup. A 775 nm shortpass filter from Edmund Optics was placed on top of a 665 nm longpass filter supplied by Thorlabs. This combination of filters was used to eliminate the excitation light during PL imaging, ensuring that only the emitted light was detected.

For excitation during PL imaging, two blue LED bars manufactured by CCS Inc. were employed as the light source. These LED bars emitted light in the blue part of the spectrum, which is suitable for exciting PL in the perovskite thin films or solar cells.

To observe EL and PL, the perovskite thin films or solar cells (chapter 6) were subjected to an electrical bias. This bias was applied using a Keithley 2450 SourceMeter Unit (SMU),[17]

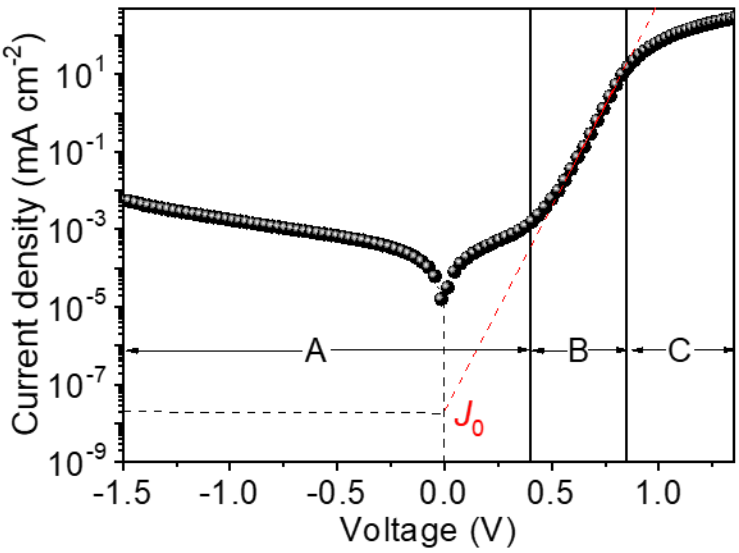

Figure 3.7. Dark current-density-voltage (*J-V*) characteristic of the NBG PSC employed in chapter 4. The reverse saturation current density (J_0) can be obtained by fitting the dark *J-V* curve in region B.

a versatile instrument often used in electrical characterization. This setup allowed for the controlled application of electrical bias to the samples. All of these measurements were carried out in ambient air.

Dark current-density-voltage (dark *J-V*)

Dark current-density-voltage (*J-V*) measurements were conducted using a PAIOS (Fluxim AG) system with a white LED (Cree XP-G). V_{OC} can be estimated by the following equation:[16,75]

$$V_{OC} = \frac{k_B T}{q} \ln\left(\frac{J_t}{J_0} + 1\right) \tag{3.11}$$

where k_B is the Boltzmann constant, q is the elementary charge, T is the absolute temperature, J_t is the theory of current density, and J_0 is the reverse saturation current density. We obtained J_0 by fitting the dark *J-V* curve in region B (see Figure 3.7). It is obvious that a lower J_0 result in a higher V_{OC} within devices.

Ideality factor

In solar cells, the ideality factor (n_{id}) is an important parameter that offers information on the dominant recombination process that occurs within the solar cell. It is commonly employed

in diode-based solar cell models, such as the Shockley-Read-Hall (SRH) recombination model, which explains the recombination of charge carriers (electrons and holes) within the solar cell. One strategy to study the n_{id} is to measure the V_{OC} of the device at various light intensities (I) and analyze its changes. This can be determined by the slope of logarithm of V_{OC} *vs.* the light intensity. In the context of description, logarithmic V_{OC} can be linear fitted by the following equation:[16,76]

$$\frac{\partial V_{OC}}{\partial(\ln I)} = \frac{n_{id}\, k_B\, T}{q} \tag{3.12}$$

where k_B is the Boltzmann constant, T is the absolute temperature, and q is the elementary charge. The n_{id} value can provide information about these mechanisms:[77]

- In case of n_{id} = 1: This is ideal diode behavior, indicating that the dominant recombination mechanism is band-to-band radiative recombination.
- When n_{id} is approaching 2: This indicates the presence of additional recombination mechanisms, such as SRH or so-called trap-assisted non-radiative recombination.

In chapter 4–6, the light-intensity-dependent V_{OC} was performed by PAIOS system with a white LED (Cree XP-G).

Space-charge-limited current (SCLC)

Space-charge-limited current (SCLC) measurements are commonly used to evaluate trap density and charge carrier mobility. SCLC were performed by PAIOS system in the dark at 0–2 V with a settling time of 40 ms. In chapter 4, electron-only devices (ITO/NBG/interlayer/C_{60}/BCP/Ag) were fabricated to estimate the electron trap density ($n_{t(e)}$). In chapter 5, electron- (ITO/SnO_2/$FAPbI_3$/C_{60}/BCP/Au) and hole-only devices(ITO/2PACz/$FAPbI_3$/P3HT/Au) were fabricated to evaluate $n_{t(e)}$ and hole trap density ($n_{t(h)}$). In chapter 6, electron-only semitransparent devices (ITO/SnO_2/$FAPbI_3$/C_{60}/SnO_x/IZO/Au) were fabricated to evaluate $n_{t(e)}$. The dark *J-V* curve is generally classified into three regions (see Figure 3.8): liner Ohmic at low bias, trap-filled limited (TFL) at intermediate bias, and nonlinear SCLC at high bias. The trap-filling limit voltage (V_{TFL}) is defined as a kink point (see Figure 3.8) between the Ohmic and TFL areas,

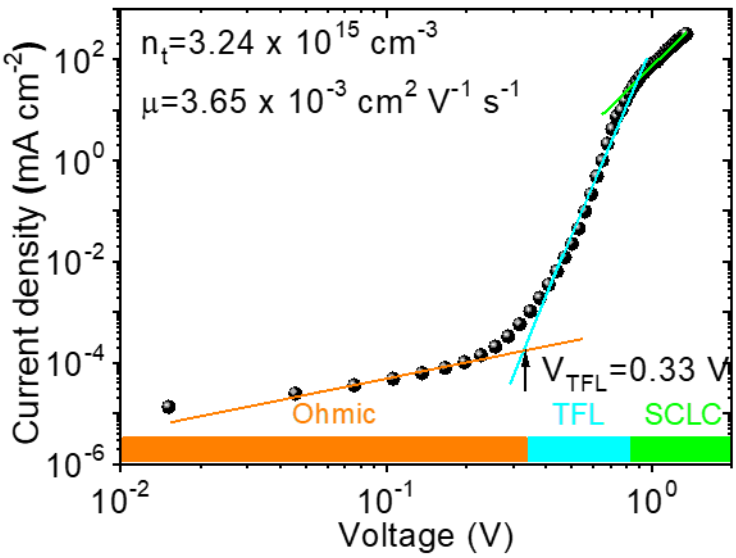

Figure 3.8. Dark *J-V* characteristic of the electron-only device based on ITO/NBG/interlayer/C60/BCP/Ag architecture employed in chapter 4. Three regions of Ohmic, TFL, and SCLC are classified. The trap density (n_t) and charge carrier mobility (μ) were calculated by SCLC methods.

and hence the n_t may be represented using the following equation:[16,78–82]

$$n_t = \frac{2\,V_{TFL}\,\varepsilon\,\varepsilon_0}{q\,L^2} \tag{3.13}$$

where V_{TFL} is the trap-filling limit voltage, ε is the relative dielectric constant of perovskite, ε_0 is the vacuum permittivity, L is the thickness of the perovskite thin film, and q is the elementary charge.

In SCLC region (see Figure 3.8), the charge carrier mobility (μ) can be obtained by fitting with Mott-Gurney law:[79,83–87]

$$\mu = \frac{8\,L^3}{9\,\varepsilon\,\varepsilon_0}\,\frac{J}{V^2} \tag{3.14}$$

where J is the dark current and V is the applied bias.

Mott–Schottky (MS)

Mott-Schottky (MS) is an electrochemical technique for determining the flat band potential (V_{fb}) and charge carrier density (N_A) in semiconductors or solar cells. The PAIOS system was used with a constant frequency of 10 kHz and an amplitude of 70 mV to execute the MS technique on the devices in the dark. MS model is based on capacitance-voltage (C^{-2}-V) characteristics using the following equation:[85,88]

$$C^{-2} = \frac{2\,(V_{fb} - V)}{A^2\,q\,\varepsilon\,\varepsilon_0\,N_A} \tag{3.15}$$

where C is the capacitance, V_{fb} is the flat band potential, V is the applied bias, A is the active area, q is the elementary charge, ε is the relative dielectric constant of perovskite, and ε_0 is the vacuum permittivity. Since the MS behavior is not clearly evident in *p-i-n* based PSCs, the application of this approach remains a challenge.[89,90] In chapter 4, V_{fb} and N_A are relative numbers used for comparison, and the obtained N_A values were denoted as apparent charge carrier density N.

Photocurrent density

The charge extraction efficiency can be obtained by the relationship between the photocurrent density (J_{ph}) and the effective voltage (V_{eff}).[91] J_{ph} is defined as the difference between the current densities under illumination (J_L) and in the dark (J_D), expressed as follows:[91–93]

$$J_{ph} = J_L - J_D \tag{3.16}$$

$$V_{eff} = V_0 - V \tag{3.17}$$

where V represents applied voltage and V_0 is the voltage when J_{ph} = 0. V_0 is regarded to close the built-in potential (V_{bi}).[93,94] The charge extraction probability can be evaluated by

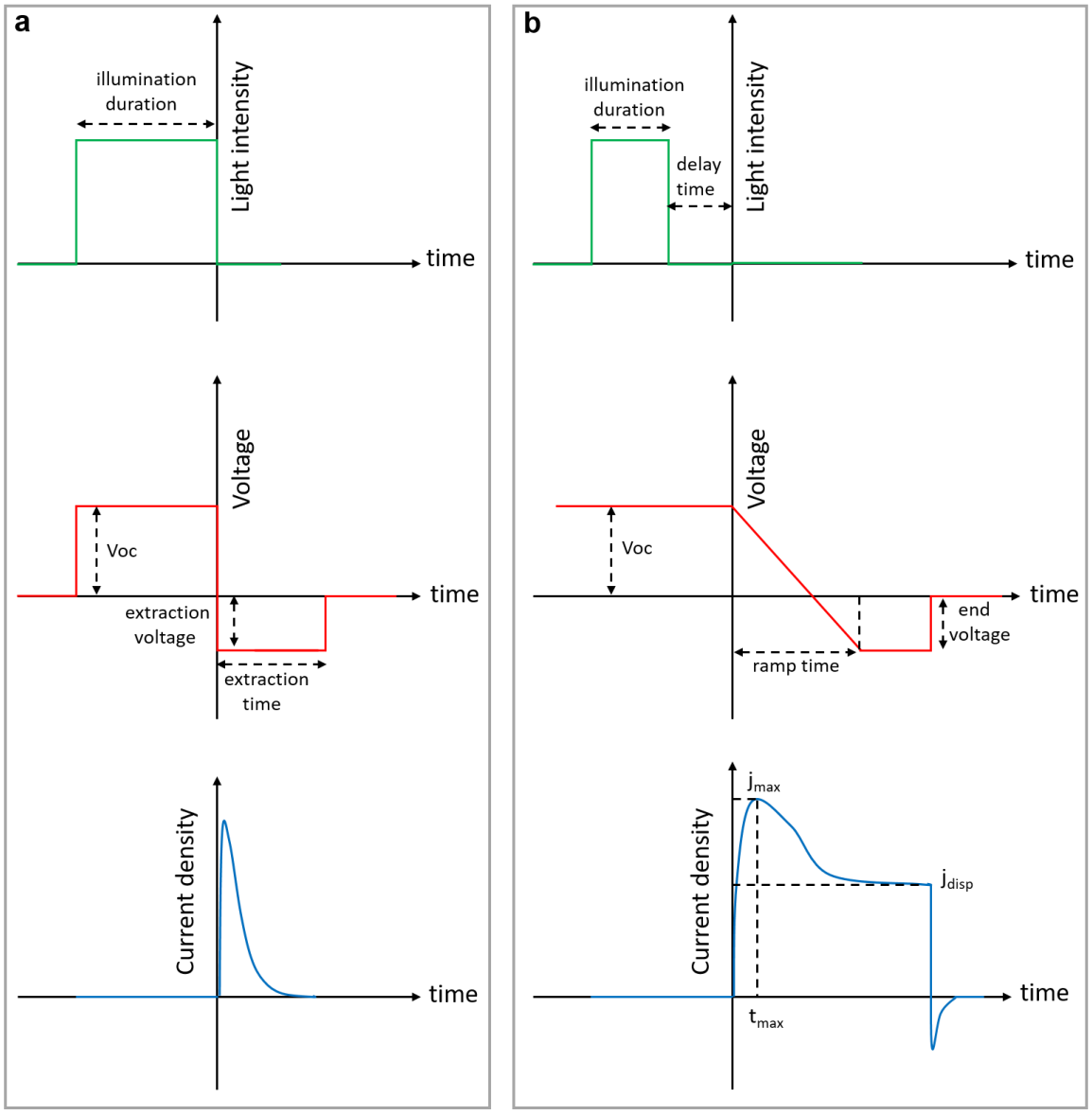

Figure 3.9. Schematic illustration of (a) CE and (b) Delay-time-CELIV measurements. Adapted from supplemental information of Ref.[27] with permission of Elsevier.

normalizing J_{ph} to saturated value (J_{sat}), *i.e.*, J_{ph}/J_{sat}, where J_{sat} is only associated with the quantity of incoming photons absorbed.[95,96] We characterized the charge extraction ability for the NBG PSCs based on an interlayer in chapter 4.

Charge extraction (CE)

Charge extraction (CE) is used to measure the charge-carrier density (n_{CE}) in a photovoltaic device. The device is initially kept at open-circuit and illuminating conditions to keep the current at zero (see Figure 3.9a). Then the light source is turned off and meanwhile zero or a negative extraction voltage is applied. The charge carriers are extracted and the current is integrated over time to quantify the n_{CE} by the following equation:[97–99]

$$n_{CE} = \frac{1}{L\,q}\left(\int_0^{t_e} j(t)\,d(t) - (V_a - V_e)\,C_{geom}\right) \tag{3.18}$$

where L is the thickness of perovskite thin film, q is the elementary charge, t_e is the extraction time, $j(t)$ is the transient current density, C_{geom} is the geometric capacitance, V_a is the voltage applied prior extraction (in this case it is V_{OC}), and V_e is the extraction voltage.

In chapter 5, CE was performed on $FAPbI_3$ based PSCs using PAIOS system under a varied illumination intensity (1−100 mW cm^{-2}). The illumination duration was set to 100 us.

Delay-time charge extraction by linearly increasing voltage (Delay-time-CELIV)

Delay-time charge extraction by linearly increasing voltage (Delay-time-CELIV) is also used to measure the charge-carrier density (n_{CELIV}) in a photovoltaic device. In Delay-time-CELIV, the device was initially kept at the open-circuit and illuminating (100 mW cm^{-2}) conditions to ensure the current flow at zero (see Figure 3.9b). The light source was then switched off and a delay time applied. During the delay time, the device was still kept at open-circuit condition during. After delay time, a linearly negative ramp voltage (V) was applied and a constant displacement current density (j_{disp}) was induced and can be calculated as follows:[100–105]

$$j_{disp} = \frac{1}{S}\frac{dV}{dt}\,C_{geom} = \frac{1}{S}\frac{dV}{dt}\,(A\,t)\,\frac{S\,\varepsilon\,\varepsilon_0}{L} = \frac{A\,\varepsilon\,\varepsilon_0}{L} \tag{3.19}$$

$$V = A\,t \tag{3.20}$$

where S is the active area of the device, C_{geom} is the geometric capacitance, A is the ramp

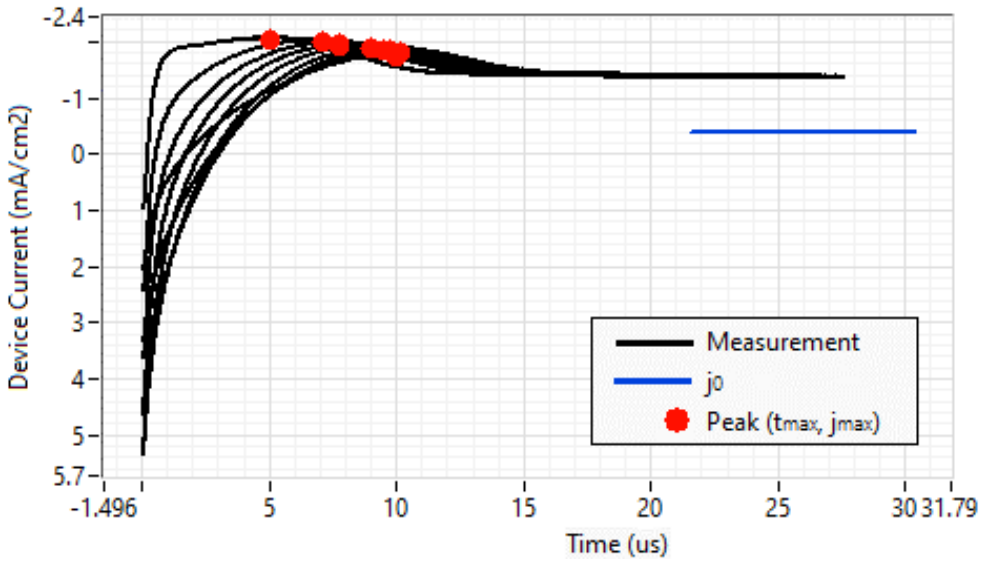

Figure 3.10. Device current density *vs.* time curves of Delay-time-CELIV measurements for $FAPbI_3$ based PSCs employed in chapter 5. The maximum value of transient current density (j_{max}) links to the time (t_{max}). Adapted from supplemental information of Ref.[27] with permission of Elsevier.

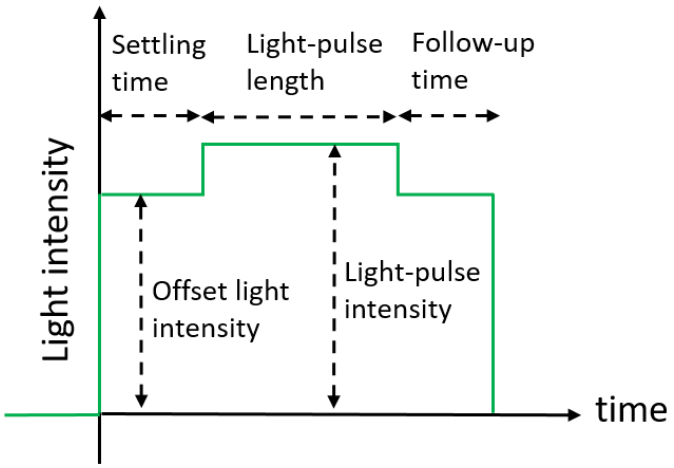

Figure 3.11. Schematic illustration of scheme for transient photo-voltage (TPV) measurement.

rate, ε_0 is the vacuum permittivity, ε is the relative dielectric permittivity, and L is the thickness of perovskite thin film. The charge carriers were extracted and an overshoot of transient current density ($\Delta j = j - j_{disp}$) was induced on top of the j_{disp} (see Figure 3.10). Integrating Δj yields the extracted charge-carrier density n_{CELIV}.

In chapter 5, Delay-time-CELIV was performed on $FAPbI_3$ based PSCs using PAIOS system under an illumination intensity of 100 mW cm^{-2}. The light-pulse length was set to 100 us. The ramp rate was fixed at 40 V ms^{-1}.

Transient photo-voltage (TPV)

Transient photo-voltage (TPV) is based on recording the response to a light-pulse. The device is kept in open-circuit condition during the entire measurement to keep the current at zero (see Figure 3.11). A small light pulse is normally introduced to a constant offset light intensity, and the voltage decay and the voltage decay is examined after the light is turned off. The decay is normally fitted with a mono-exponential curve to obtain the corresponding lifetime.

In chapter 6, a PAIOS system was used in TPV measurements on semi-transparent $FAPbI_3$ PSCs with employing a high resistor (1 MΩ). A small perturbation light pulse (*i.e.*, ~5 mW cm^{-2}) to the background illumination is applied to a constant offset light intensity.

Electrical impedance spectroscopy (EIS)

Electrochemical impedance spectroscopy (EIS) is commonly used for characterizing charge-carrier dynamics in photovoltaic devices. EIS involves applying a small alternating current (AC) signal companied with DC offset voltage to an electrochemical system, and the current response is measured. If the amplitude is small enough, the device will behave linearly at the designated working point, *i.e.*, the current response has the same frequency as the applied AC voltage sinus. EIS provides impedance (Z) at a large range of frequencies, *e.g.*, from mHz to MHz. Z can be expressed as follows:

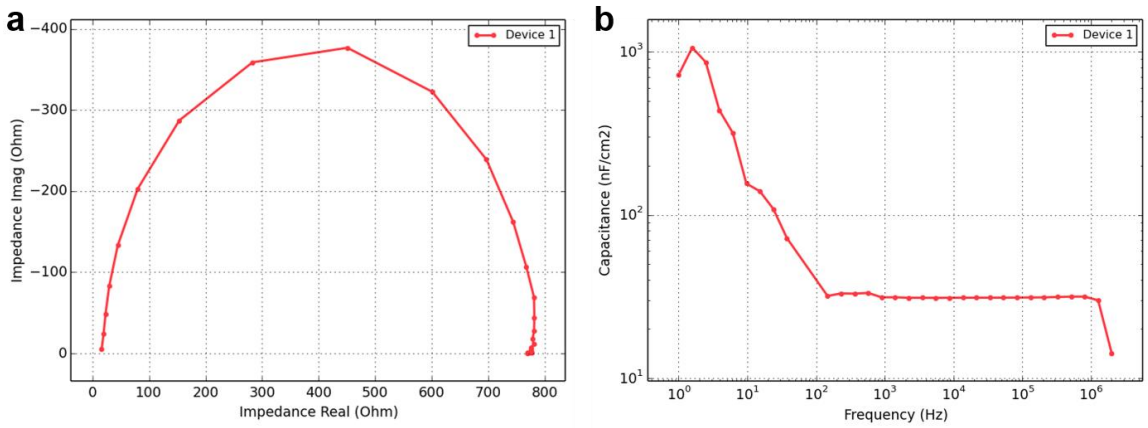

Figure 3.12. Representative (a) Nyquist and capacitance-frequency (*C-f*) plots obtained from EIS measurements.

$$Z = \frac{V_0 \ \sin \omega t}{I_0 \ \sin(\omega t - \theta)} = Z_0 \ \frac{\sin \omega t}{\sin(\omega t - \theta)} \tag{3.21}$$

$$\omega \ = \ 2 \, \pi \, f \tag{3.22}$$

when t = 0, V_0, I_0, and Z_0 are the amplitudes (or modulus) of the voltage, current, and impedance respectively. ω is the angular frequency, f is the frequency, and θ is the phase shift.

The impedance $Z(\omega)$ can also be expressed by Euler's low:

$$Z(\omega) = Z_0 \ (\cos \theta + j \ \sin \theta) \tag{3.23}$$

where j is the current response.

Thus, the real ($Re(Z)$) and imaginary ($Im(Z)$) parts of impedance represent as follows (see Figure 3.12a):

$$Re(Z) = Z' = Z_0 \ \cos \theta \tag{3.24}$$

$$Im(Z) = Z'' = Z_0 \ \sin \theta \tag{3.25}$$

An amplitude of 30 mV were applied in EIS. Different bias was employed in characterizing different perovskite based PSCs.

Electron capture radius

The critical radius (R_c) is defined as the distance at which charges may escape the electrostatic field using thermal energy ($k_B T$), and it can be represented as follows:[69,106,107]

$$R_c = \frac{q^2}{4 \, \pi \, k_B \, T \, \varepsilon_r \, \varepsilon_0} \tag{3.26}$$

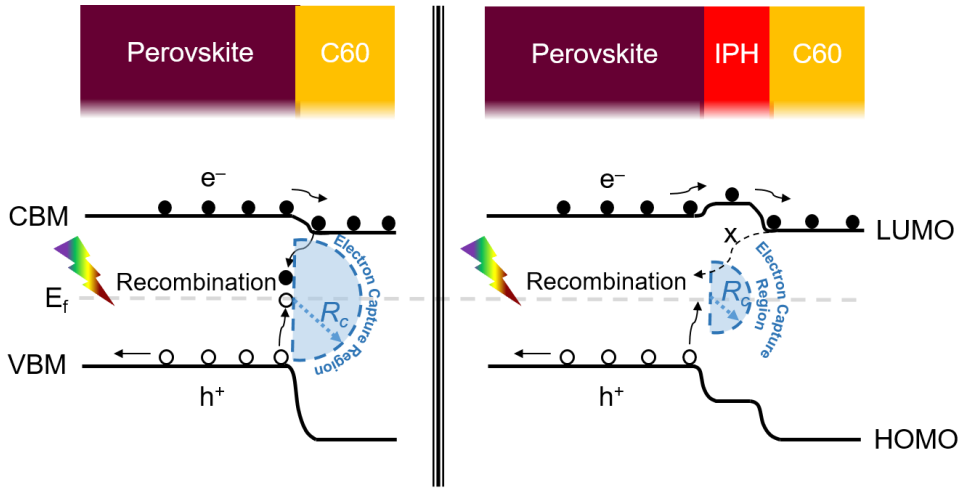

Figure 3.13. Schematic comparison of electron capture radius at the interfaces of perovskite/C_{60} or perovskite/IPH/C_{60}, where the perovskite and IPH interlayer were employed in chapter 4.

where q is electron elementary charge, k_B is the Boltzmann constant, T is the temperature, ε_0 is the vacuum permittivity, and ε_r is the relative dielectric constant of the thin film.

ε_r can be estimated by creating an parallel plate capacitor as follows:[69,108]

$$\varepsilon_r = \frac{C\,d}{A\,\varepsilon_0} \tag{3.27}$$

where C is the capacitance, A is the active area of the parallel plate capacitor, and d is the thickness of the parallel plate capacitor.

In chapter 4, ε_r was evaluated by characterizing parallel plate capacitors, *i.e.*, C_{60} or C_{60}/interlayer thin films. A larger ε_r can reduce R_c, which can effectively screen the electrostatic force and thus reducing the recombination at the interface (see Figure 3.13).[107] This ε_r could be related to the alkyl chain effect ε_r.[107–109]

3.4. Simulations for triple-junction architecture

In this section, we present the simulations for multi-junction architecture, *i.e.*, perovskite–perovskite–Si monolithic triple-junction solar cells (MTJSCs). The experimental optimization will be discussed in chapter 6. An open-source modelling platform EYcalc was used for simulations.[53] This modelling platform has been employed for 2T perovskite–CIS and all-perovskite tandems.[15,52,54] The optical simulations involve using advanced optical data and electrical parameters that were obtained through extensive optical and electrical characterization of single-junction devices, as described in the previous publication.[54] A 1.84 eV top perovskite with a thickness of 200 nm and a 1.52 eV middle perovskite with a thickness of 1000 nm were used to create the champion perovskite–perovskite–Si MTJSCs. The simulation details of architecture and thickness for the champion device are shown in Table 3.1. The best simulated PCE for this architecture is 24.8% with a V_{OC} of 2.95 V and a FF of 0.717. The current generation from each junction is 12.0, 11.7, and 15.4 mA cm^{-2} for

Table 3.1. Simulated architecture and thickness of champion perovskite–perovskite–Si MTJSC with employing 1.84 eV perovskite top cell and 1.52 eV perovskite middle cell.

Material	Thickness (nm)
MgF_2	125
IZO	90
SnO_x	20
C_{60}	15
Perovskite (1.84 eV)	200
NiO_x/2PACz	5
ITO	15
SnO_x	20
C_{60}	15
Perovskite (1.52 eV)	1000
NiO_x/2PACz	15
ITO	5
a-Si(n)	40
a-Si(i)	10
c-Si	250000
a-Si(i)	10
a-Si(p)	10
ITO	80
Ag	250

the top, middle, and bottom cells, respectively. More details will be discussed in section 6.2.

4. Fullerene-derivative interlayers for Sn-Pb based perovskite in tandem photovoltaics

Interface engineering is considered as a facile and effective approach to achieve highly efficient perovskite solar cells (PSCs). While a variety of fullerene interlayers have been extensively studied for Pb-based perovskite (bandgaps >1.5 eV), there has been limited exploration of fullerene interlayers in narrow-bandgap (NBG) PSCs containing a mixture of Sn and Pb counterparts. In this chapter, we investigate two newly developed solution-processed fullerene derivatives, specifically indene-C60-propionic acid butyl ester (IPB) and indene-C60-propionic acid hexyl ester (IPH), as potential interlayers in NBG PSCs. Our investigations reveal that devices incorporating the IPH interlayer exhibit the highest performance metrics, featuring an impressive short-circuit current density (J_{SC}) of 30.7 mA cm^{-2} and a notably reduced loss in open-circuit voltage (V_{OC}) of 0.43 V. We attribute this reduction in V_{OC} deficit to the reduced losses in non-radiative recombination, *i.e.*, decreased charge-carrier-back-transfer recombination owing to the formation of a higher conduction band offset ~0.2 eV (> 0 eV), and a minimized trap-assisted recombination due to decreased trap density at the NBG/interlayer/C_{60} interfaces. The significant improvement in J_{SC} is attributed to the enhanced charge extraction within PSCs. By employing a NBG PSC featuring the IPH interlayer, we were able to achieve a respectable power conversion efficiency (PCE) of 24.8% in a four-terminal all-perovskite tandem solar cell. We highlight the promising potential of these fullerene interlayers in advancing the performance of NBG PSCs and tandems.

This chapter is based on our publication in *Advanced Functional Materials* by Hang Hu *et al.* with the title of "Sn-Pb mixed perovskites with fullerene-derivative interlayers for efficient four-terminal all-perovskite tandem solar cells".[16] Most of the graphs in this chapter are adapted or reproduced with permission of Wiley.

Acknowledgments and contributions

Hang Hu, Prof. Dr. Ulrich W. Paetzold, and Dr. Bahram Abdollahi Nejand conceived the idea. Hang Hu developed research plans and designed the experiments. Hang Hu fabricated PSCs. Dr. Somayeh Moghadamzadeh optimized NBG recipe. Dr. Raheleh Azmi performed

UPS and XPS measurements. Dr. Yang Li performed steady-state PL. Dr. Milian Kaiser and Jan C. Fischer conducted TRPL. Qihao Jin conducted AFM and contact angle measurements. Dr. Julia Maibach assisted to analyse UPS data. Dr. Ihteaz M. Hossain provided WBG semi-transparent filters. Hang Hu did the rest of the characterizations and data analysis. Moritz Schultes (KIT) and Erik Ahlswede (KIT) provided the IOH substrates. Karlsruhe Nano Micro Facility (KNMF) and Helmholtz Research Infrastructure at KIT are acknowledged for supporting UPS and XPS characterization. Prof. Dr. Ulrich W. Paetzold and Dr. Bahram Abdollahi Nejand supervised the project.

4.1. Introduction

All-perovskite tandem solar cells represent a promising approach to surpass the power conversion efficiency (PCE) limits (*i.e.*, according to the detailed-balance limit) of single-junction devices. These tandem cells involve the combination of wide-bandgap (WBG) PSCs, typically with a bandgap of 1.7–1.8 eV, and NBG PSCs with a bandgap ranging from 1.2–1.3 eV.[78,110,111] One of the key advantages of this technology is its potential to achieve high PCEs while benefiting from solution processing and low-temperature fabrication methods.[78,112] Despite some remarkable achievements in all-perovskite tandem solar cells, such as PCEs >28% for four-terminal (4T)[113] and two-terminal (2T) architectures,[112,114,115] there remains major obstacles in realizing the full potential of this all-thin-film tandem technology,[110,112] specifically, the limited performance and stability of NBG perovskite sub-cells that currently reach PCEs of approximately 23.8%.[115,116]

One of the major challenges in achieving highly efficient Sn-Pb mixed NBG PSCs involves the critical issue, *i.e.*, the inherent unstable Sn-based materials.[112,117] The instability of Sn-based perovskites is primarily attributed to the rapid oxidation of Sn^{2+} to Sn^{4+}, even under conditions of very low oxygen content.[118] This oxidation process leads to the formation of Sn vacancies, resulting in non-radiative recombination losses, both within the bulk and at the interfaces of the PSCs. Numerous strategies have been reported in the literature to mitigate Sn oxidation and enhance the stability of Sn-based perovskites. These approaches include the incorporation of various antioxidant additives, such as SnF_2,[119,120] $SnCl_2$,[121] guanidinium thiocyanate,[112] methylammonium thiocyanate,[122] ascorbic acid,[123] hydroxybenzene sulfonic acid,[124] metallic Sn powder,[78,125,126], alkylammonium pseudo-halogen,[116] *etc*. These additives were designed to counteract the oxidative processes that contribute to the instability of Sn-based perovskite materials and devices.

Indeed, achieving high-quality thin films with uniform and pinhole-free morphologies for Sn-based perovskites is a challenging target. One of the key difficulties arises from the rapid crystallization and film formation that occurs during the solution processing.[127] This fast crystallization process can readily induce interfacial defects at the surface and/or grain boundary of the resulting Sn-based perovskite thin films, thereby leading to significant non-radiative recombination losses.[127] To address these challenges and enhance the film morphology of NBG perovskite thin films, several strategies have been introduced. These approaches include the incorporation of halides into the perovskite structure,[128,129] the

utilization of a two-step deposition method,[63,114] the application of hot-casting techniques,[130] the implementation of gas-quenching process,[65] and the adoption of vacuum-assisted growth control (VAG) methods.[131] Each of these strategies aimed to improve the quality and uniformity of the NBG perovskite thin films, ultimately reducing non-radiative recombination losses and enhancing device performance.[131]

In PSCs, non-radiative recombination losses at the interfaces (*e.g.*, perovskite/electron transport layer (ETL) or perovskite/hole transport layer (HTL)) are associated to trap-assisted recombination and charge-carrier-back-transfer recombination. The former is dominated by the trap density at the interfaces, and the latter is influenced by energy-level alignment and back transfer of charge carriers.[25,26] Ideally, a perfect interface would exhibit minimal interfacial defects and perfect energy-level alignment.[25] To minimize interfacial non-radiative recombination in perovskite photovoltaics, various interface-engineering strategies were employed to reduce trap density at the interfaces of perovskite/ETL or perovskite/HTL.[132–134] Surface trap states usually arise from facilely produced defects at the perovskite surface.[135,136] In Sn-based perovskites, the trap sates have been identified as Sn cation or iodide vacancies that is a critical factor to deteriorate operational efficiency and stability.[137–141] For instance, previous reports have demonstrated that passivation techniques applied at the interface of Sn-based perovskites/HTL can effectively reduce trap-assisted non-radiative recombination.[92,142] In addition, the incorporation of pure Pb-based 2D or 3D perovskite, *i.e.*, forming an 2D/3D or 3D/3D heterojunction at the interface of NBG perovskites/ETL, led to improved device efficiency and stability.[115,143–145] However, unlike their pure Pb-based counterparts, implementing effective passivation strategies in Sn-based perovskites remains a challenge, such as 2D/3D or 3D/3D heterojunction, graded interfaces, or doping. This is due to potential issues such as the incorporation of excessive bulky organic cations,[143] energetic surface mismatches, and the presence of multiple defects within these materials, making tailored passivation more complex.[26]

The utilization of fullerene derivatives, such as the standard phenyl-C61-butyric acid methyl ester (PCBM), as an interlayer between the perovskite layer and the ETL in Pb-based PSCs has been a well-established technique. The goal of this method is to minimize the energy barrier and interfacial traps at this key interface contact. Furthermore, because of their favorable electron mobility and low resistance at the perovskite surface, fullerene derivatives like PCBM serve as effective ETL materials for Pb-based PSCs. Some fullerene derivatives have also been used effectively to improve the performance of NBG PSCs. For example, using PCBM as an interlayer between NBG perovskite and C_{60} has been demonstrated to significantly increase the V_{OC} in PSCs by reducing interfacial traps and thereby leading to reduced non-radiative recombination. In recent work by A. Rajagopal *et al.*, a fullerene derivative known as graded fluoroalkyl-substituted fullerene (DF-C_{60}) was found to be suitable as an interlayer in NBG PSCs with a composition of $MAPb_{0.5}Sn_{0.5}I_3$. Their study demonstrated that the presence of DF-C_{60} reduced trap states on the surface of the perovskite thin film, resulting in improved device performance, notably achieving a high V_{OC} of 0.89 V. These successful studies (as summarized in Table 4.1) motivate future research into

Table 4.1. Summary of different interlayers at the interface of NBG perovskite and transport layer. Adapted from Ref.[16] with permission of Wiley.

Perovskite	Interlayer	E_g (eV)	V_{OC} (V)	J_{SC} (mA cm^{-2})	FF	PCE (%)	V_{OC} loss (V)	Ref.
$FA_{0.6}MA_{0.4}Sn_{0.6}Pb_{0.4}I_3$	PFI	1.22	0.78	27.22	0.74	15.85	0.44	[146]
$FASn_{0.5}Pb_{0.5}I_3$	PCP-Na	-	0.78	28.51	0.73	16.27	-	[142]
$(FASnI_3)_{0.6}(MAPbI_3)_{0.4}$	PBDB-T: ITIC	1.25	0.86	27.92	0.75	18.03	0.39	[92]
$Cs_{0.025}FA_{0.475}MA_{0.5}Sn_{0.5}Pb_{0.5}I_{3-x}Br_x$	EDA	1.25	0.86	31.86	0.80	21.74	0.39	[147]
$MAPb_{0.5}Sn_{0.5}I_3$	DF-C_{60}	1.2	0.87	26.1	0.69	15.61	0.33	[148]
$FA_{0.5}MA_{0.5}Sn_{0.5}Pb_{0.5}I_3$	PCBM	1.25	0.75	30.56	0.76	17.59	0.50	[149]
$Cs_{0.025}(FA_{0.83}MA_{0.17})_{0.975}Sn_{0.5}Pb_{0.5}I_3$	IPH	1.26	0.83	30.7	0.73	18.6	0.43	This work

Non-fullerene interlayer

PFI: perfluorinated ionomer; PCP-Na: a pH neutral anionic conjugated polymer with alkylsulfonate side group; PBDB-T: poly[(2,6-(4,8-bis(5-(2-ethylhexyl)thiophen-2-yl)-benzo[1,2-b:4,5-b0]dithiophene))-alt-(5,5-(10,30-di-2-thienyl-50,70-bis(2-ethylhexyl)benzo[10,20-c:40,50-c0]dithiophene-4,8-dione))]; ITIC: 3,9-bis(2-methylene-(3-(1,1-dicyanomethylene)-indanone))-5,5,11,11-tetrakis(4-hexylphenyl)-dithieno[2,3-d:20,30-d0]-s-indaceno[1,2-b:5,6-b0]-dithiophene; EDA: ethylenediamine.

Fullerene interlayer

DF-C_{60}: hybrid fluoroalkyl-substituted fullerene; PCBM: phenyl-C61-butyric acid methyl ester; IPH: indene-C60-propionic acid hexyl ester.

fullerene-derivative interlayers, as well as a better understanding of their effect on device performance and stability of NBG PSCs.

To explore unknown fullerene derivatives, in this chapter, we study novel interlayers in NBG PSCs and evaluate their influence on device performance and non-radiative recombination losses. At the interface between NBG perovskite thin film and the ETL in *p-i-n* architecture, we introduced three fullerene-derivative interlayers, *i.e.*, IPB, IPH, and PCBM. Through our comprehensive analysis, IPH is demonstrated as the most effective interlayer for enhancing the performance of NBG PSCs, *i.e.*, improved V_{OC} and J_{SC}. On the one hand, IPH exhibits a higher conduction band offset (CBO), effectively suppressing charge-carrier-back-transfer recombination. On the other hand, devices with IPH interlayers display reduced trap-assisted recombination, resulting from a decrease in trap density at the perovskite/ETL interface. These combined effects reduce non-radiative recombination within PSCs with IPH interlayers, thus leading to decrement in V_{OC} loss. Furthermore, the use of IPH interlayers at the interface of perovskite/ETL improves charge extraction, resulting in a considerable increase in J_{SC}. As a consequence, devices with IPH interlayers achieve a great PCE of 18.6%, along with an enhanced V_{OC} of 0.83 V and a J_{SC} of 30.7 mA cm^{-2}. This performance surpasses those of devices with PCBM interlayers or without any interlayer. Afterwards, we demonstrate efficient all-perovskite tandem solar cells in 4T architecture that combined a semi-transparent WBG PSC (bandgap of 1.63 eV) and a NBG PSC (bandgap of 1.26 eV)

with an IPH interlayer. These tandem solar cells achieve a promising PCE of 24.8% and a stabilized PCE of 23.7% for 5 minutes under AM 1.5G.

4.2. Sn-Pb based narrow-bandgap perovskite solar cells

As discussed in section 4.1, the Sn-Pb mixed NBG perovskite has a rapid crystallization during the solution processing,[127] which makes it challenge to form uniform perovskite thin film free of pinholes. In this regard, we adopted the vacuum-assisted growth control (VAG) method, as described in previous publications,[131,150] to produce high-quality NBG perovskite thin films. The perovskite composition is triple-cation NBG with a bandgap of 1.26 eV, *i.e.*, $Cs_{0.025}(FA_{0.8}MA_{0.2})_{0.975}Sn_{0.5}Pb_{0.5}I_3$, abbreviated as CsFAMAPbSnI. The Cs content was optimized to 2.5% in our previous research to enhance the operational photo-stability of PSCs.[150] We fabricated NBG PSCs in *p-i-n* planar with the following layer stacks: glass/indium tin oxide (ITO)/poly[bis(4-phenyl)(2,4,6-trimethylphenyl)amine] (PTAA)/ CsFAMAPbSnI/interlayer/C_{60}/2,9-dimethyl-4,7-diphenyl-1,10-phenanthroline (BCP)/silver (Ag), as shown in Figure 4.1a. The interlayers used in this study include PCBM, IPB, and IPH (see Figure 4.1b). We determined the thickness of perovskite and interlayer with ~600 nm and ~8 nm (see Figure 4.1c and 4.1d), respectively. All fullerene-derivative interlayer deposited on top of NBG had a similar thickness by controlling the solution in the same standard concentration of 5 mg mL^{-1}.

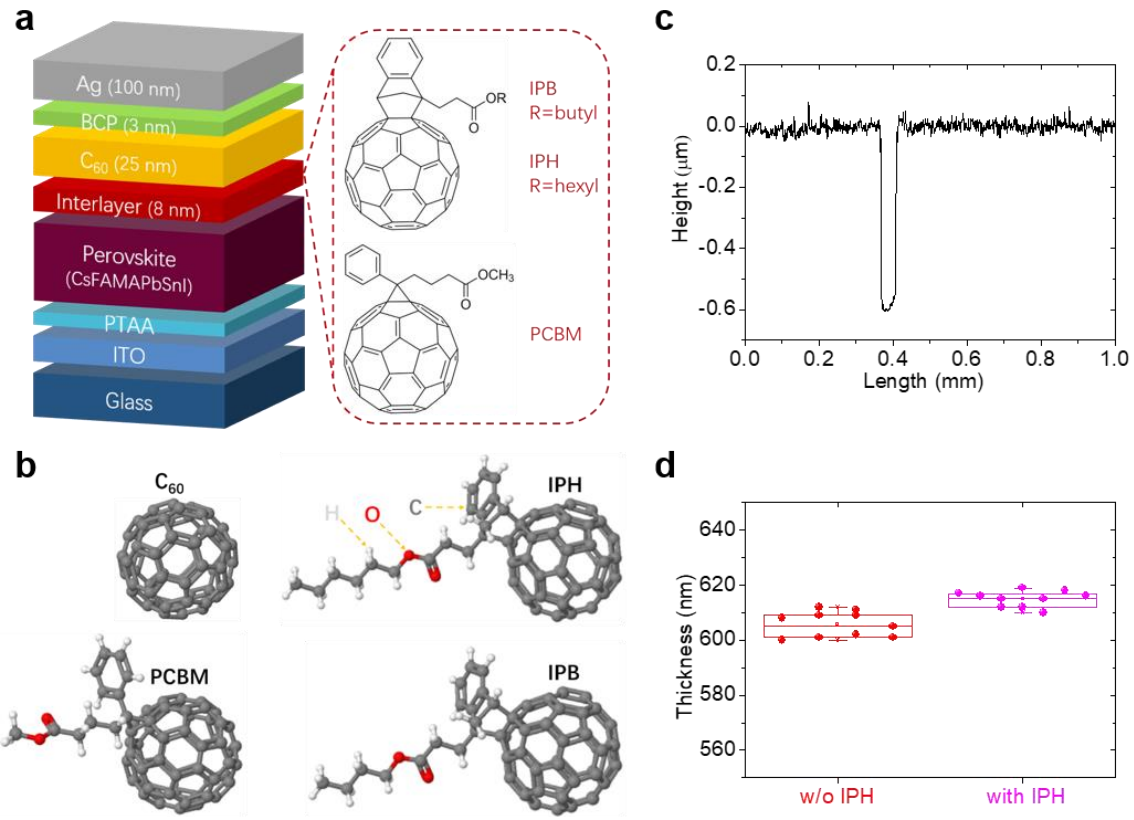

Figure 4.1. (a) Schematic of NBG PSCs in *p-i-n* architecture using different fullerene-derivative interlayers (PCBM, IPB, IPH) and (b) their chemical structures. (c) The profile and (d) measured thickness of NBG perovskite thin films with and without IPH interlayer. Reproduced from Ref.[16] with permission of Wiley.

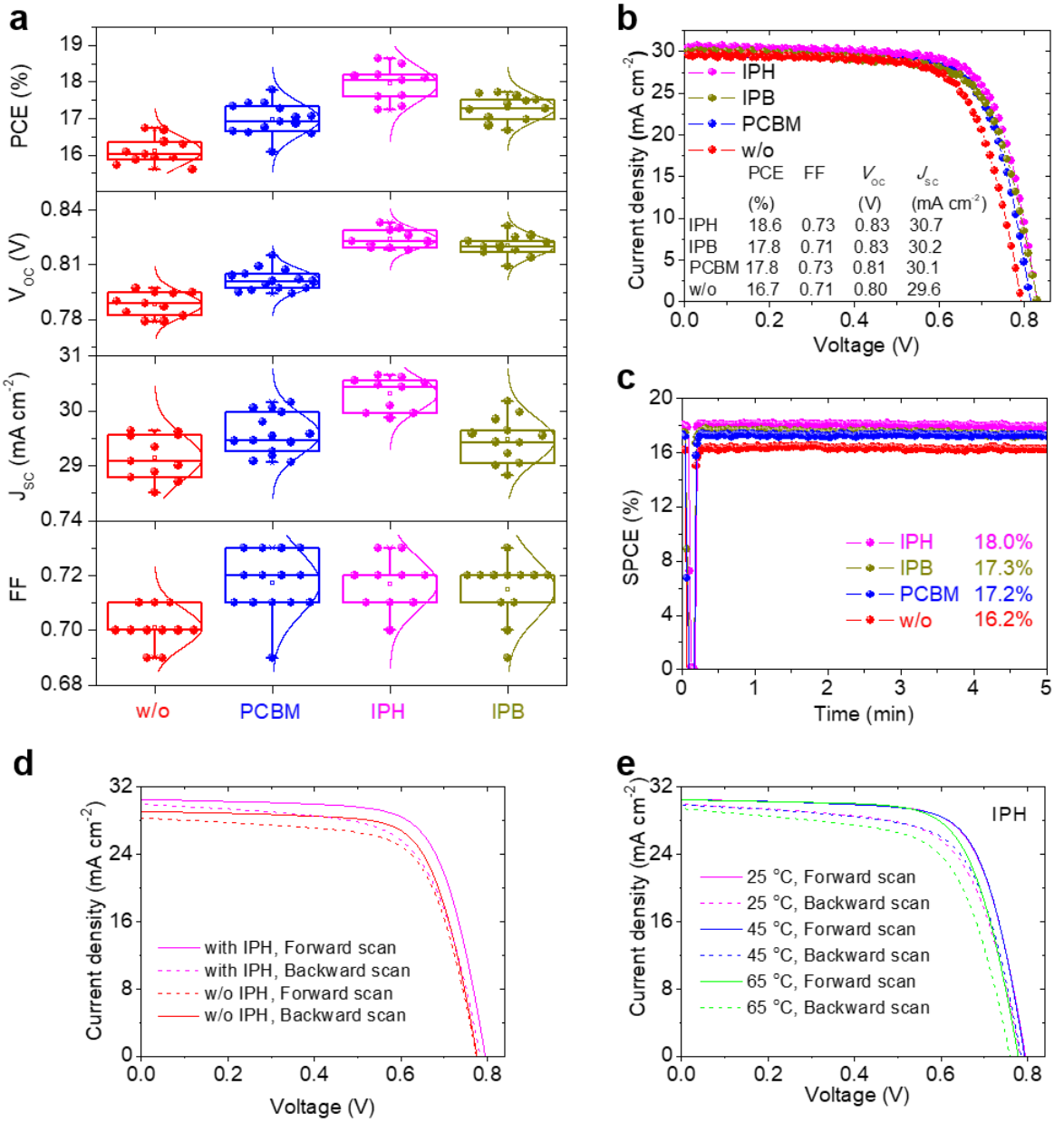

Figure 4.2. (a) Statistics of photovoltaic parameters for NBG PSCs based on different interlayers. (b) *J-V* characteristics of the champion PSCs obtained from backward scan. (c) Stabilized power conversion efficiency (SPCE) under continuous AM 1.5G illumination of the champion PSCs. *J-V* characteristics of PSCs (c) with and without IPH interlayer in comparison with forward and backward scans and (d) with IPH interlayer in comparison with different temperature measurement. Reproduced from Ref.[16] with permission of Wiley.

We evaluate the photovoltaic performance of the PSCs with different interlayers. As illustrated in Figure 4.2a, the average values of PCE improve from 16.1% (for control PSCs without interlayer) to 17.0%, 17.3% and 17.9% for PSCs with PCBM, IPB, and IPH interlayers, respectively. It is apparent that V_{OC}, FF, and J_{SC} experience similar improvement trend. Figure 4.2b shows backward *J-V* curves of the best PSCs with different interlayers. The control PSC exhibits a best PCE of 16.7%, FF of 0.71, V_{OC} of 0.80 V and J_{SC} of 29.6 mA cm^{-2}. For PCBM interlayer, the best PCE of 17.8% mainly benefits from the enhanced J_{SC} of 30.1 mA cm^{-2} with a slightly increased FF of 0.73, whereas IPB based devices

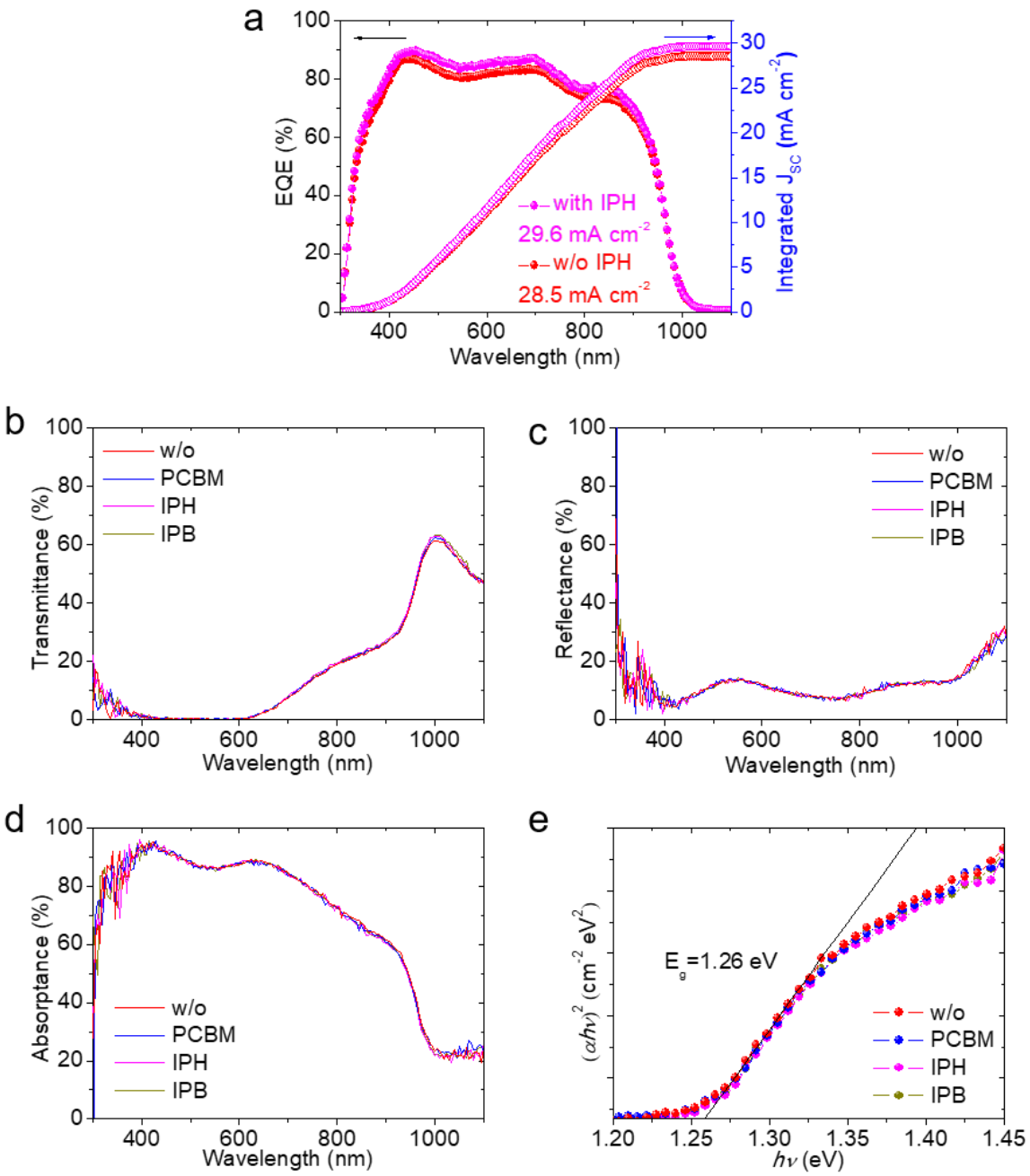

Figure 4.3. (a) External quantum efficiency (EQE) spectra of the champion PSCs with and without IPH interlayer. (b) Transmittance, (c) reflectance, (d) absorptance spectra, and (e) Tauc-plots of ITO/PTAA/NBG/interlayer/C_{60} layer stack. Reproduced from Ref.[16] with permission of Wiley.

achieve a best PCE of 17.8% owing to the improved V_{OC} of 0.83 V and J_{SC} of 30.1 mA cm^{-2} (Figure 4.2b). In striking comparison, the champion device from IPH interlayer delivers the best PCE of 18.6%, mainly attributing to the enhanced V_{OC} of 0.83 V, J_{SC} of 30.7 mA cm^{-2} and FF of 0.73 (see Figure 4.2b and A1a). The champion PSC with IPH interlayer yields a stabilized power conversion efficiency (SPCE) of 18% that was tracking at the maximum power point (MPP) under AM 1.5G (100 mW cm^{-2}) irradiation, which is much higher than 16.2% for control PSC without interlayer (see Figure 4.2c and A1b). We highlight that the

champion PSC with IPH interlayer has a V_{OC} loss of just 0.43 V, *i.e.*, $V_{OC,loss} = E_g/q - V_{OC}$ = 0.43 V, which is one of the lowest values for reported NBG PSCs (see Table 4.1).

However, we find IPH interlayer does not reduce the hysteresis, as shown in Figure 4.2d and 4.2e. Given that the improved J_{SC} from 28.5 to 29.6 mA cm^{-2} for PSCs with IPH interlayer reflects a broadband improvement in external quantum efficiency (EQE, as shown in Figure 4.3a), we determined the optical characteristics of NBG perovskite thin films. The optical spectra and bandgaps do not change much after deposition of various interlayers, as

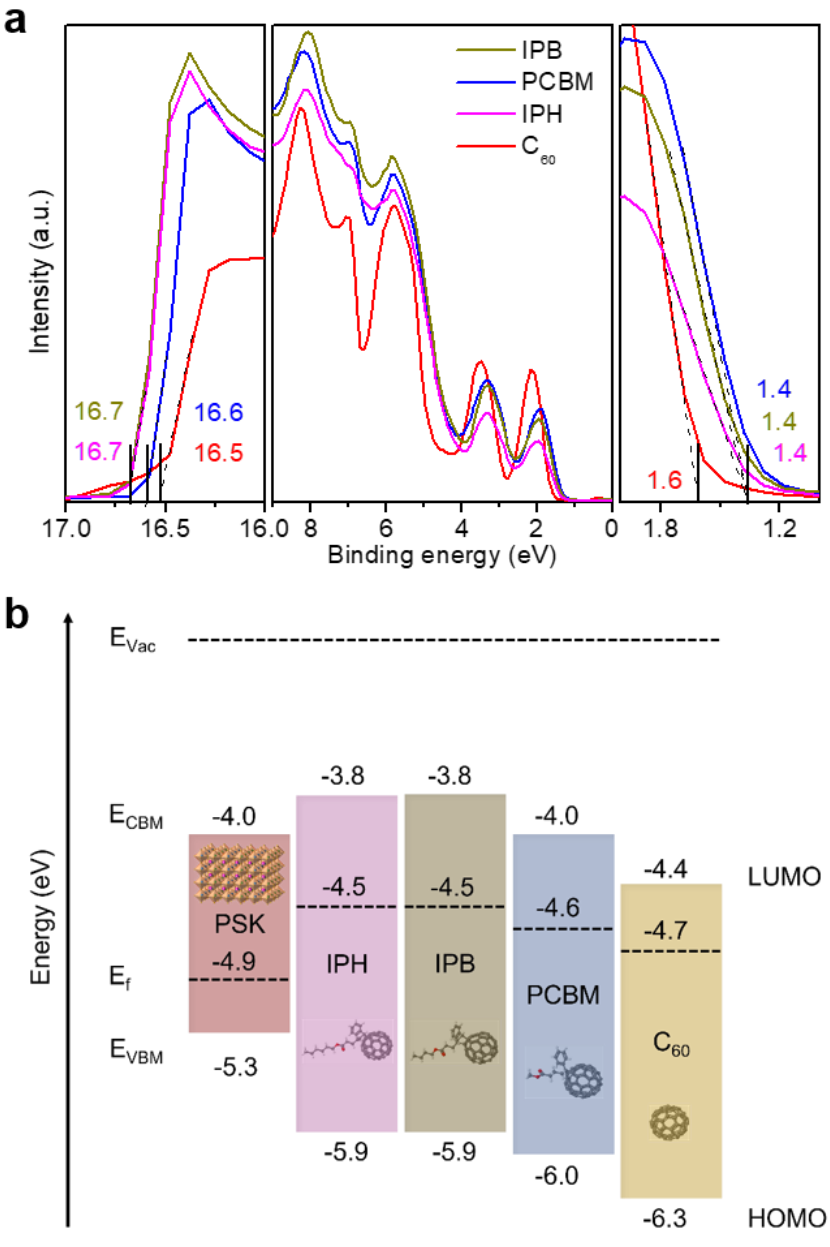

Figure 4.4. (a) Ultra-violet photoelectron spectroscopy (UPS) spectra of the secondary electron cutoff (left panel), the valence region (middle panel), and the HOMO onset position (right panel) for various fullerene derivatives. (b) Energy-level diagram for NBG perovskite and fullerene derivatives. E_{vac}: vacuum level; E_f: Fermi level; CBM: conduction band minimum; VBM: valence band maximum; HOMO: highest occupied molecular orbital; LUMO: lowest unoccupied molecular orbital. Adapted from Ref.[16] with permission of Wiley.

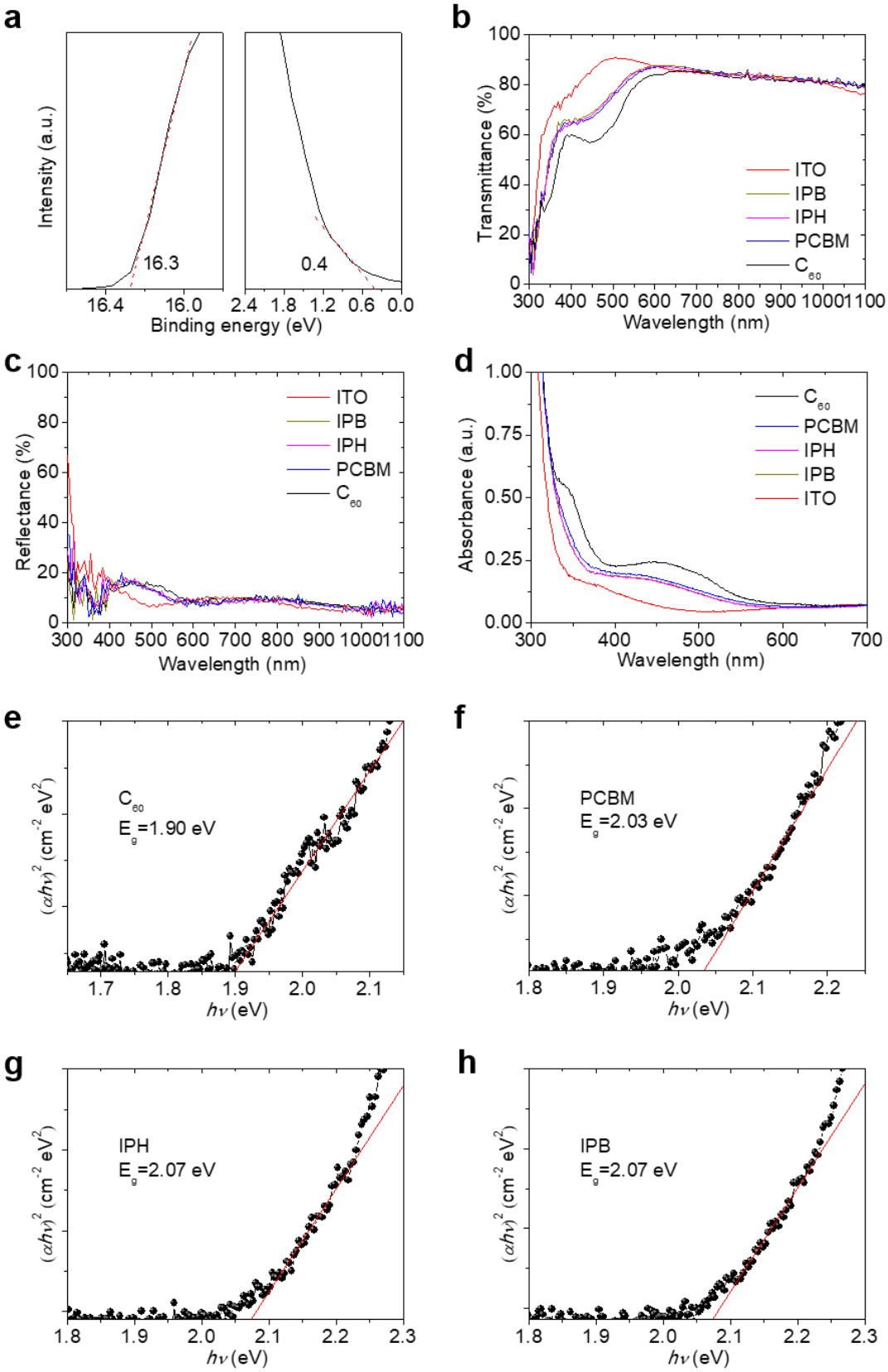

Figure 4.5. (a) UPS spectra of the secondary electron region (left panel) and the valence band maximum region (right panel) for NBG perovskite. (b) Transmittance, (c) reflectance, (d) absorbance spectra, and (e)–(h) Tauc-plots of the various fullerenes. All fullerenes were deposited on glass/ITO substrates. Adapted from Supporting Information of Ref.[16] with permission of Wiley.

illustrated in Figure 4.3b−4.3e. It is reasonable to conclude that fullerene-derivative interlayers promote charge extraction rather than light harvesting,[149,151] as we will examine further in section 4.5.

4.3. Energy-level alignment

In this section, we investigate energy levels for the stack of perovskite/interlayer/ETL. A proper energy-level alignment is favorable to an efficient charge extraction within PSCs. Ultraviolet photoelectron spectroscopy (UPS) was used to explore the energy levels for NBG perovskite, C_{60}, and different derivatives (see Figure 4.4). The work function is derived from the secondary electron cutoff (Figure 4.4a and 4.5a; left panel), while the highest occupied molecular orbital (HOMO) is estimated from the HOMO onset position (Figure 4.4a and 4.5a; right panel). Tauc plots are used to determine the band gaps of C_{60} and fullerene derivatives, as shown in Figure 4.55b−4.55h. The hole quasi-Fermi level ($E_{f,h}$) is consistent for all devices as it is defined by the energy alignment at the PTAA/perovskite interface. It is apparent that PCBM, IPB, and IPH have higher values of lowest unoccupied molecular orbitals (LUMO) than C_{60} (see Figure 4.4b). During illumination, a higher LUMO of IPB or IPH allows for a higher electron quasi-Fermi level ($E_{f,e}$) at the perovskite/interlayer interface. As a result, incorporation of IPB and IPH interlayers promotes higher V_{OC} within PSCs due to the formation of larger quasi-Fermi level splitting between $E_{f,h}$ and $E_{f,e}$.[151,152] It should be noted that IPB and IPH have higher electron affinity than NBG perovskite (see Figure 4.6), *i.e.*, higher LUMO levels than LUMO of C_{60} and conduction band minimum (CBM) of NBG perovskite (see Figure 4.4b and 4.6), which indicates a spike-like energy structure at the perovskite/interlayer interface, *i.e.*, $CBO_{NBG/C60} = E_{LUMO(IPH)} - E_{CBM(NBG)} > 0$ eV. This contrasts with the cliff-like CBO observed at the perovskite/C_{60} interface, *i.e.*,

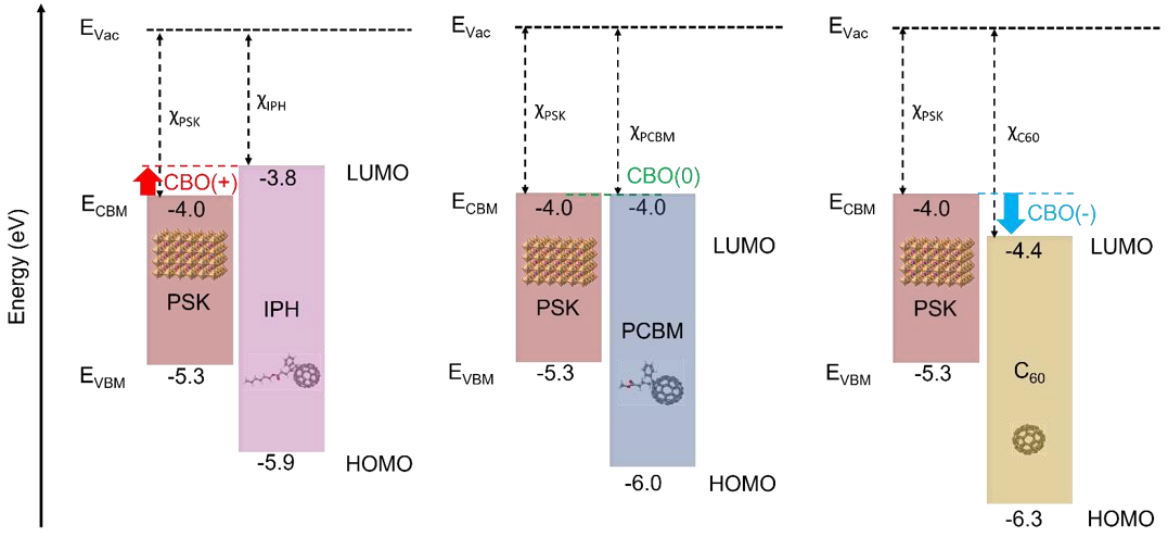

Figure 4.6. Energy-level alignment diagram for perovskite/interlayer or perovskite/C_{60} interface. (+), (0), and (-) indicate positive, zero, and negative conduction band offset (CBO), respectively. CBM: conduction band minimum; VBM: valence band maximum; HOMO: highest occupied molecular orbital; LUMO: lowest unoccupied molecular orbital; χ: the electron affinity. CBO (+): $\chi_{PSK} > \chi_{IPH}$; CBO (0): $\chi_{PSK} = \chi_{PCBM}$; CBO (-): $\chi_{PSK} < \chi_{C60}$. Adapted from Supporting Information of Ref.[16] with permission of Wiley.

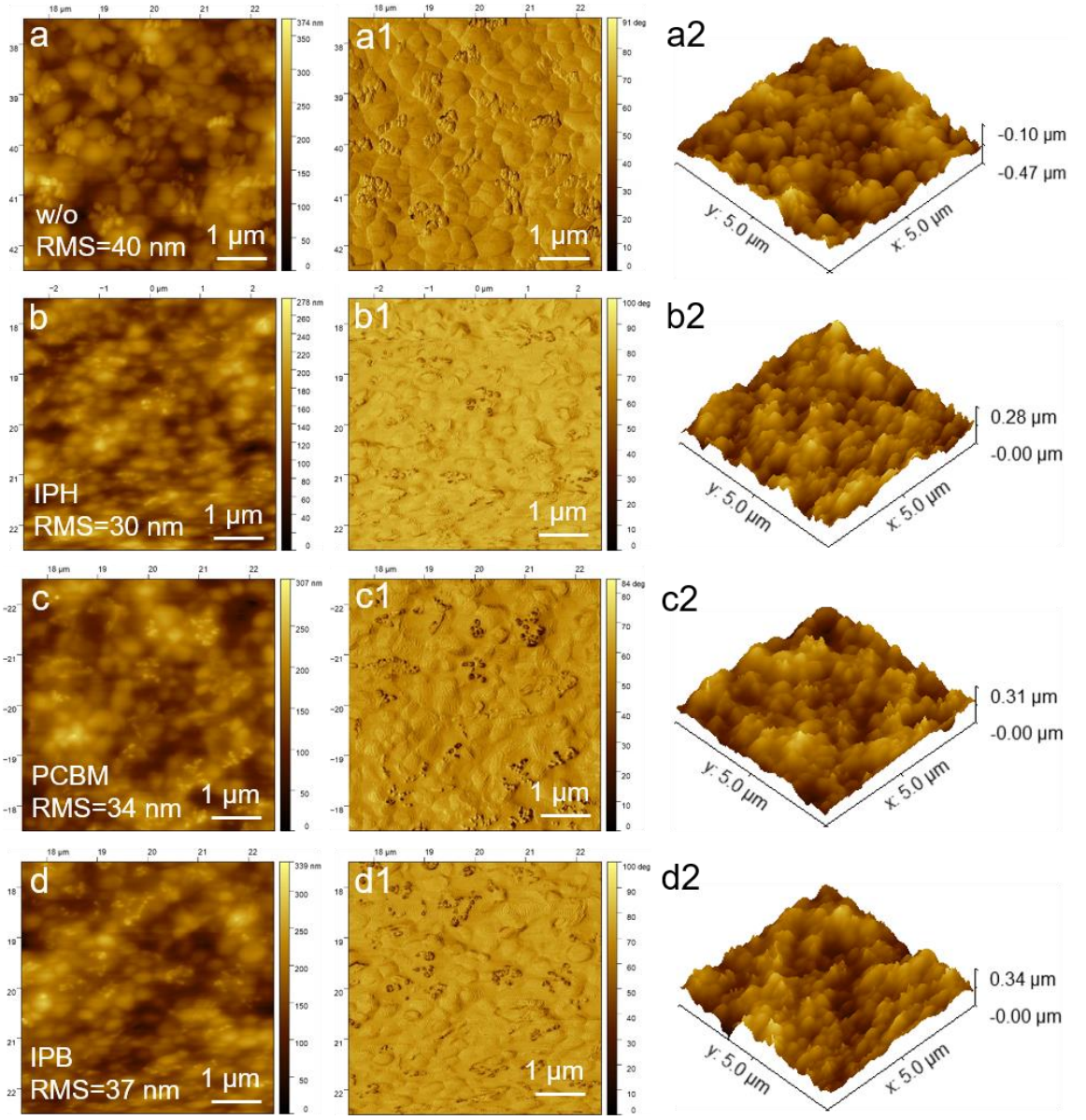

Figure 4.7. Atomic force microscopy (AFM) of (a)−(d) 2D topography, (a1)−(d1) phase, (a2)−(d2) 3D images for NBG perovskite thin film with and without interlayers. (a)w/o, (b) IPH, (c) PCBM, (d) IPB. Adapted from Supporting Information of Ref.[16] with permission of Wiley.

$CBO_{NBG/C60} = E_{LUMO(C60)} - E_{CBM(NBG)} < 0$ eV (see Figure 4.4b and 4.6). In accordance with the literature,[149,153–156] it is expected that a negative CBO (< 0 eV) facilitates the backward flow of photo-generated electrons from C_{60} to NBG perovskite, inducing an undesired recombination of photo-generated charge carriers at this interface and resulting in V_{OC} loss. In contrast, a spike-like CBO (> 0 eV) serves as a barrier, inhibiting undesirable recombination at this interface and reducing V_{OC} loss. Moreover, the activation energy (E_a) for charge carrier recombination is closely related to the absolute value of CBO, *i.e.*, $E_a = E_g - |CBO|$). The E_a decreases when the |CBO| increases, leading to an enhanced recombination at the perovskite/ETL interface.[154,155] We highlight that selecting an appropriate CBO for an interlayer is critical for optimizing the interface contact of perovskite/ETL. Later, we will discuss the possible recombination mechanism in section 4.6.

4.4. Characteristics of non-radiative recombination

After demonstrating that the IPH interlayer improves the photovoltaic performance within NBG PSCs, *i.e.*, V_{OC} and J_{SC}, in this section, we use various photo-physical and material characterizations to investigate the impact of these interlayers on non-radiative recombination. Typically, as non-radiative recombination centers tend to originate from surface or grain boundaries,[127] our initial investigation focuses on the surface properties and the state of Sn within the perovskite thin films. All perovskite thin films demonstrate identical bandgap (E_g = 1.26 eV, see Figure 4.3e) and morphology (see Figure 4.7) and with and without fullerene-derivative interlayers. However, as the NBG perovskite surface are filled with fullerene derivatives, we detect decreased roughness (Figure 4.7) and increased contact angles (Figure 4.8) for the perovskite thin films with interlayers. Since previous research has identified Sn cation vacancies as non-radiative recombination centers,[137–141] we conducted X-ray photoelectron spectroscopy (XPS) to study the Sn states for perovskite thin

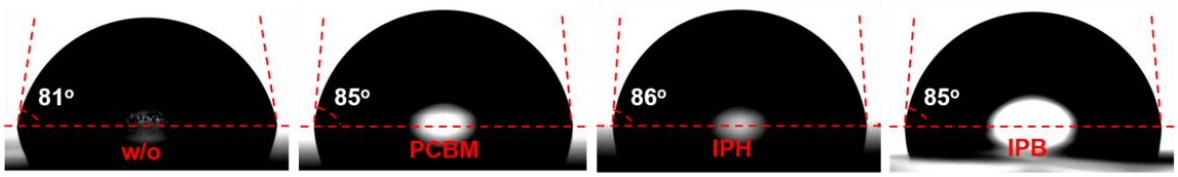

Figure 4.8. Contact angle measurement for NBG perovskite thin films with and without interlayers. Adapted from Supporting Information of Ref.[16] with permission of Wiley.

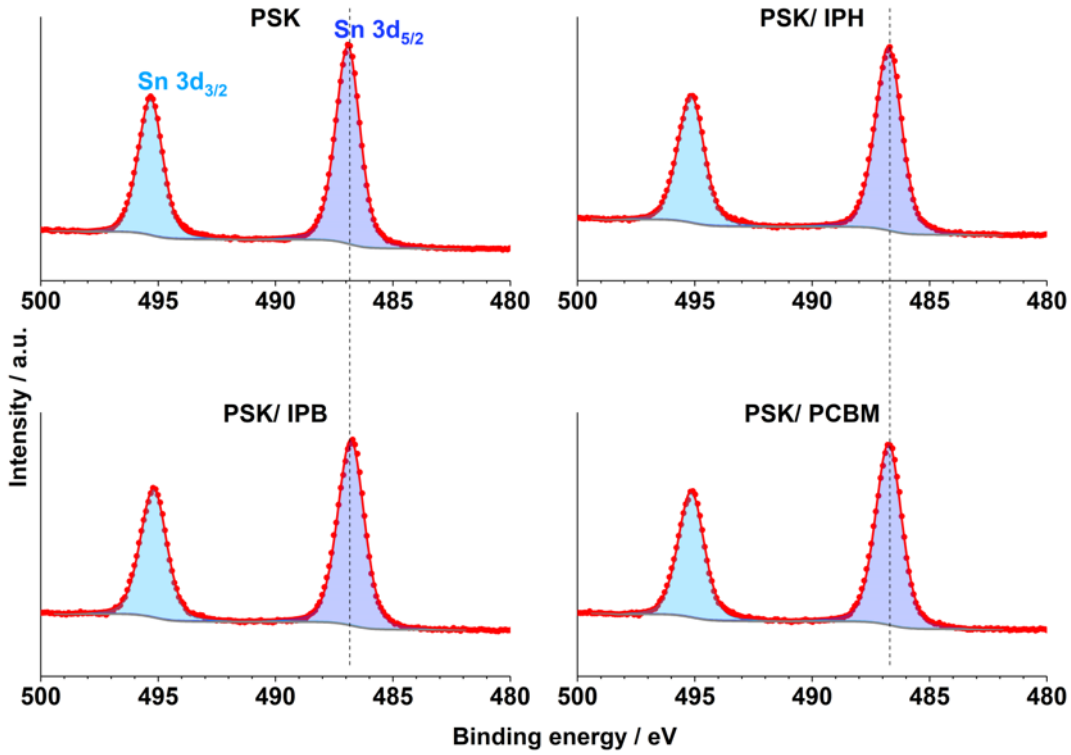

Figure 4.9. XPS spectra of Sn 3d for NBG perovskite with and without interlayers. Adapted from Supporting Information of Ref.[16] with permission of Wiley.

films with and without interlayers. However, we do not detect any significant shifts in the Sn 3d peaks (see Figure 4.9). This implies that the fullerene-derivative interlayer deposited on the surface of NBG perovskite does not serve as an oxidation barrier for Sn. We conclude that the addition of fullerene-derivative interlayers does not lead to significant variations in optical, morphological, and Sn-state characteristics (see Figure 4.3, 4.7−4.9).

We performed steady-state photoluminescence (PL) and time-resolved photoluminescence (TRPL) to extract direct observation of charge carrier dynamics between perovskite thin film and interlayer. As depicted in Figure 4.10a and A2a, C_{60} ETL as well as fullerene derivative interlayer effectively quench PL due to a significant reduction in PL intensity compared with that of pristine perovskite thin film (no C_{60} and no interlayer). We attribute these decrease to the electron transfer (*i.e.*, from the perovskite to C_{60}) and trap-assisted non-radiative recombination at the interface.[92,142] Interestingly, the perovskite/IPH/C_{60} stack displays higher PL intensity than the perovskite/C_{60} stack (see Figure 4.10a and A2a), demonstrating improved band-to-band radiative recombination of free charge carriers as the trap-assisted recombination is minimized by incorporation of IPH interlayer. To collect more in-depth information, the lifetime of perovskite thin films with and without interlayer are evaluated by the TRPL. As shown in Figure 4.10b, the TRPL curves were fitted by

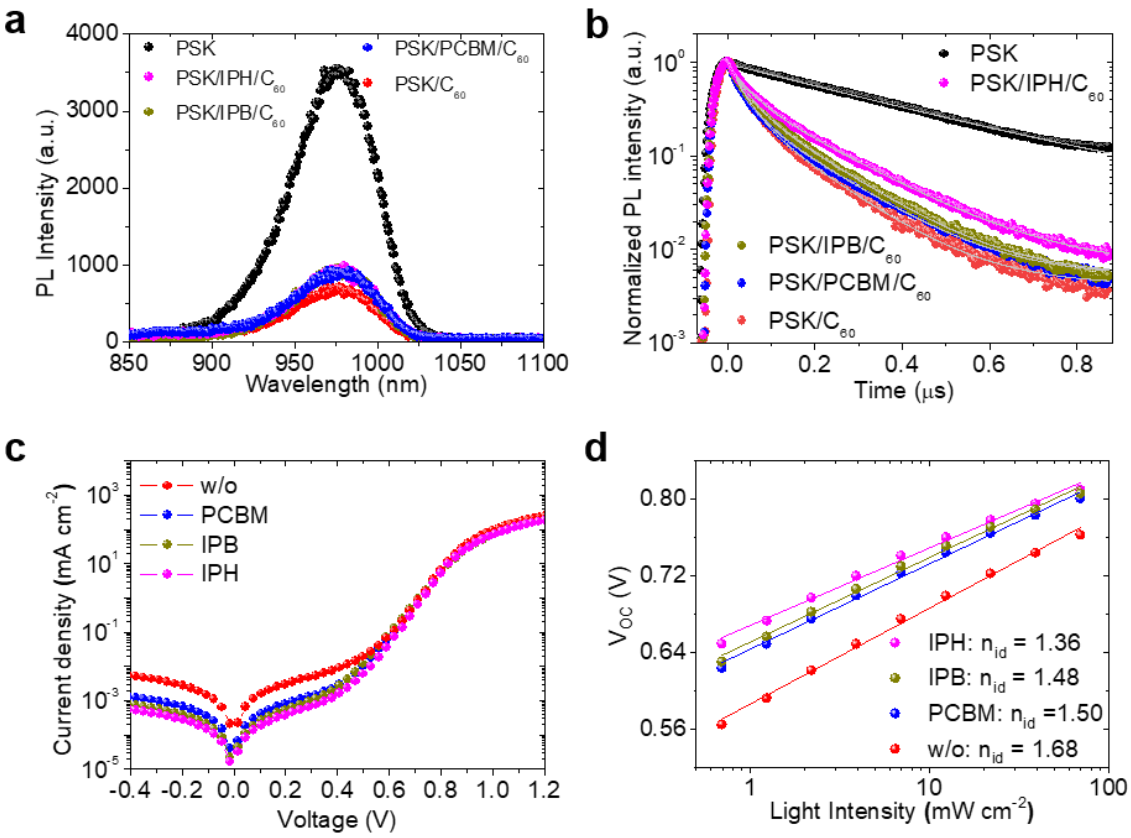

Figure 4.10. (a) Steady-state photoluminescence (PL) and (b) time-resolved photoluminescence (TRPL) of NBG perovskite thin film and perovskite/C_{60} stack with and without fullerene derivatives. All samples were fabricated on glass/AlO_x (deposited via atomic layer deposition) substrates. (c) Dark current-density-voltage (*J-V*) characteristics and (d) light intensity dependent V_{OC} for the champion PSCs. Reproduced from Ref.[16] with permission of Wiley.

Table 4.2. Summary of TRPL measurements for NBG thin films with and without interlayers. Adapted from Supporting Information of Ref.[16] with permission of Wiley.

Samples	τ_1 (ns)	Fraction 1	τ_2 (ns)	Fraction 2
NBG	355	-	-	-
NBG/C_{60}	34	0.681	131	0.319
NBG/PCBM/C_{60}	33	0.649	143	0.351
NBG/IPB/C_{60}	36	0.578	142	0.422
NBG/IPH/C_{60}	42	0.503	170	0.497

The data were fitted with a mono-exponential equation: $Y = A \exp(-t/\tau)$, and bi-exponential equation: $Y = A_1 \exp(-t/\tau_1) + A_2 \exp(-t/\tau_2)$. τ_1 and τ_2 reveal a fast lifetime and a slow lifetime, respectively.

mono- (for pristine perovskite thin film) or bi-exponential decay (for perovskite/ETL stack) model. The fast lifetime (τ_1) is described as fast electron transfer from perovskite to C_{60}, and slow lifetime (τ_2) can be attributed to non-radiative recombination at the perovskite bulk and/or interfaces.[151,157–160] Perovskite/IPH/C_{60} layer stack delivers the highest τ_2 of 170 ns, which is much higher than IPB (142 ns), PCBM (143 ns), and without interlayer (131 ns), as presented in Figure 4.10b and Table 4.2. This further demonstrate minimized trap-assisted non-radiative recombination within PSCs using IPH interlayer.[92,142,161]

We further conducted the dark *J-V* and light intensity dependent V_{OC} measurements for the best PSCs. The comparison analysis of dark saturation current density (J_0) (Figure 4.10c and A2b) and ideality factor (n_{id}) (Figure 4.10d) supports the enhancement in V_{OC} due to reduced non-radiative recombination. Compared to PSCs without interlayer, J_0 and n_{id} values are lower in all PSCs with interlayers, suggesting reduced non-radiative recombination. In particular, the lowest J_0 of 0.28×10^{-7} mA cm^{-2} and n_{id} of 1.36 are observed in the PSC with IPH interlayer, whereas the reference PSC without interlayer has higher J_0 of 10^{-7} mA cm^{-2} and n_{id} of 1.68 (see Figure 4.10c, A2b, and 4.10d). These data align with our earlier findings, demonstrating that IPH is the most efficient interlayer for minimizing non-radiative recombination loss.[75,76,95,96,129]

To further validate the reduced non-radiative recombination, we employed electrical impedance spectroscopy (EIS) to analyze the charge-carrier dynamics within the PSCs. The Nyquist plots obtained at short-circuit conditions are depicted in Figure 4.11a, featuring distinct semicircles primarily in the low-frequency region. A smaller semicircle in the high-frequency region, as shown in Figure 4.11b, is negligible and hence excluded. These semicircles predominantly denote the charge recombination resistance (R_{rec}) at the interface between the perovskite and ETL.[149,161,162] We note that R_{rec} substantially exceeds the charge transfer resistance (R_{ct}), leading us to simplify the equivalent circuit to encompass solely the series resistance (R_s) and the parallel resistance R_{rec}, coupled with recombination capacitance (C_{rec}) (see Figure 4.11c). The larger semicircles (Figure 4.11a) signify significantly higher R_{rec} (see Table 4.3) for all PSCs featuring fullerene-derivative interlayers compared to the PSC lacking an interlayer. This observation strongly suggests the presence of a formidable recombination barrier within PSCs incorporating fullerene-derivative interlayers. Specifically, the PSC integrated with the IPH interlayer displays the highest R_{rec} of 28.2

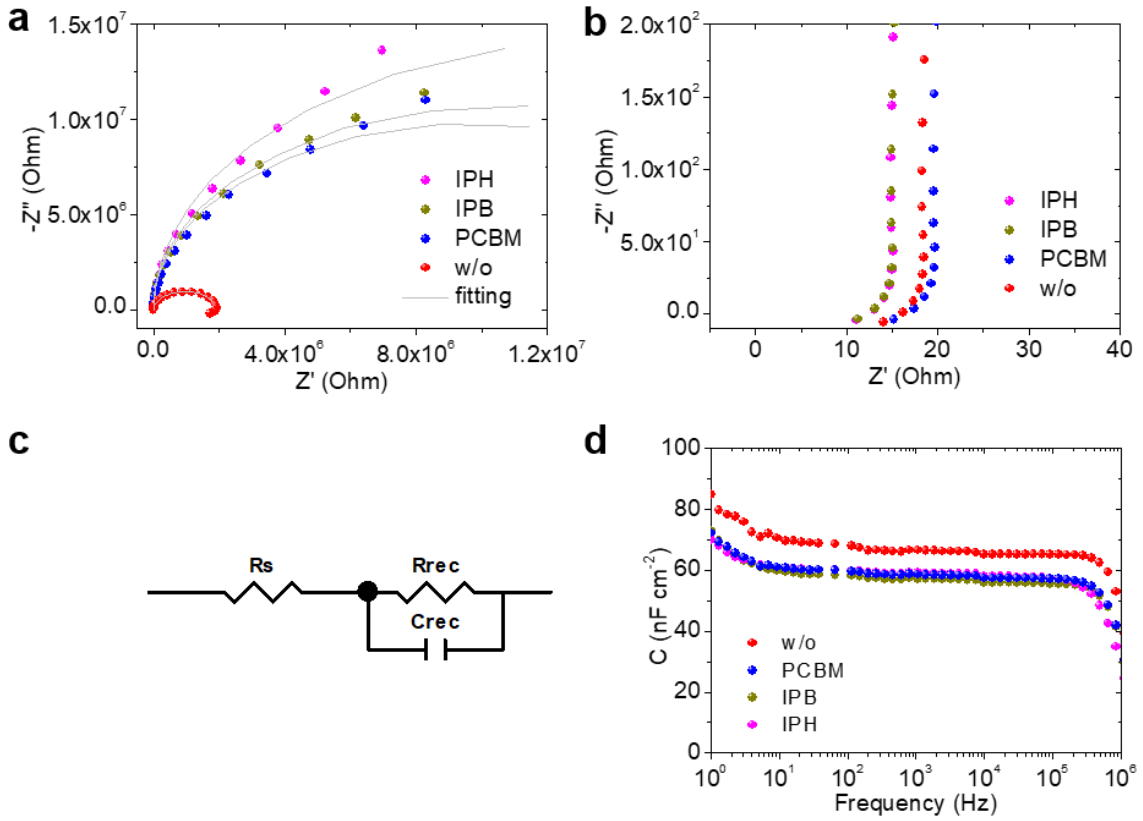

Figure 4.11. (a) Nyquist plots (symbols) and (b) zoomed-in region in high frequency for the best PSCs. The solid lines are fitting curves. (c) the equivalent circuit diagram obtained from Z-View. R_s: the series resistance; R_{rec}: the charge recombination resistance; C_{rec}: charge recombination capacitance. (c) Corresponding capacitance-frequency plots. Reproduced from Supporting Information of Ref.[16] with permission of Wiley.

MΩ, whereas the PSC without an interlayer exhibits the lowest R_{rec} of 1.9 MΩ. Moreover, compared to the interlayer-free PSC, lower C_{rec} values are observed in the low-frequency region of the capacitance-frequency (*C-f*) characteristics (see Figure 4.11d). This implies a reduced ionic accumulation at the interface of perovskite/IPH/C_{60}. Such ionic accumulation is associated with trap-assisted non-radiative recombination.[149] Consequently, the charge carrier lifetime ($\tau_{eis} = R_{rec}C_{rec}$) for the PSC with IPH interlayer is calculated to be 203 ms. for PSC with the IPH interlayer. This value stands in stark contrast to the τ_{eis} of 14 ms for interlayer-free PSC. The substantially prolonged τ_{eis} for PSCs with IPH interlayer implies that photo-generated charge carriers have more time for efficient charge transfer from the

Table 4.3. Summary of electrical impedance spectroscopy (EIS) for NBG PSCs. Adapted from Supporting Information of Ref.[16] with permission of Wiley.

Devices	R_s (Ω)	R_{rec} (MΩ)	C_{rec} (nF)	τ_{eis} (*ms*)
IPH	16.0	28.2	7.2	203
IPB	15.8	21.4	7.0	150
PCBM	20.4	19.6	6.8	133
w/o	19.6	1.9	7.6	14

R_s: the series resistance; R_{rec}: the charge recombination resistance; C_{rec}: charge recombination capacitance; τ_{eis}: charge carrier lifetime; $\tau_{eis} = R_{rec}C_{rec}$. All data were fitted by Z-View.

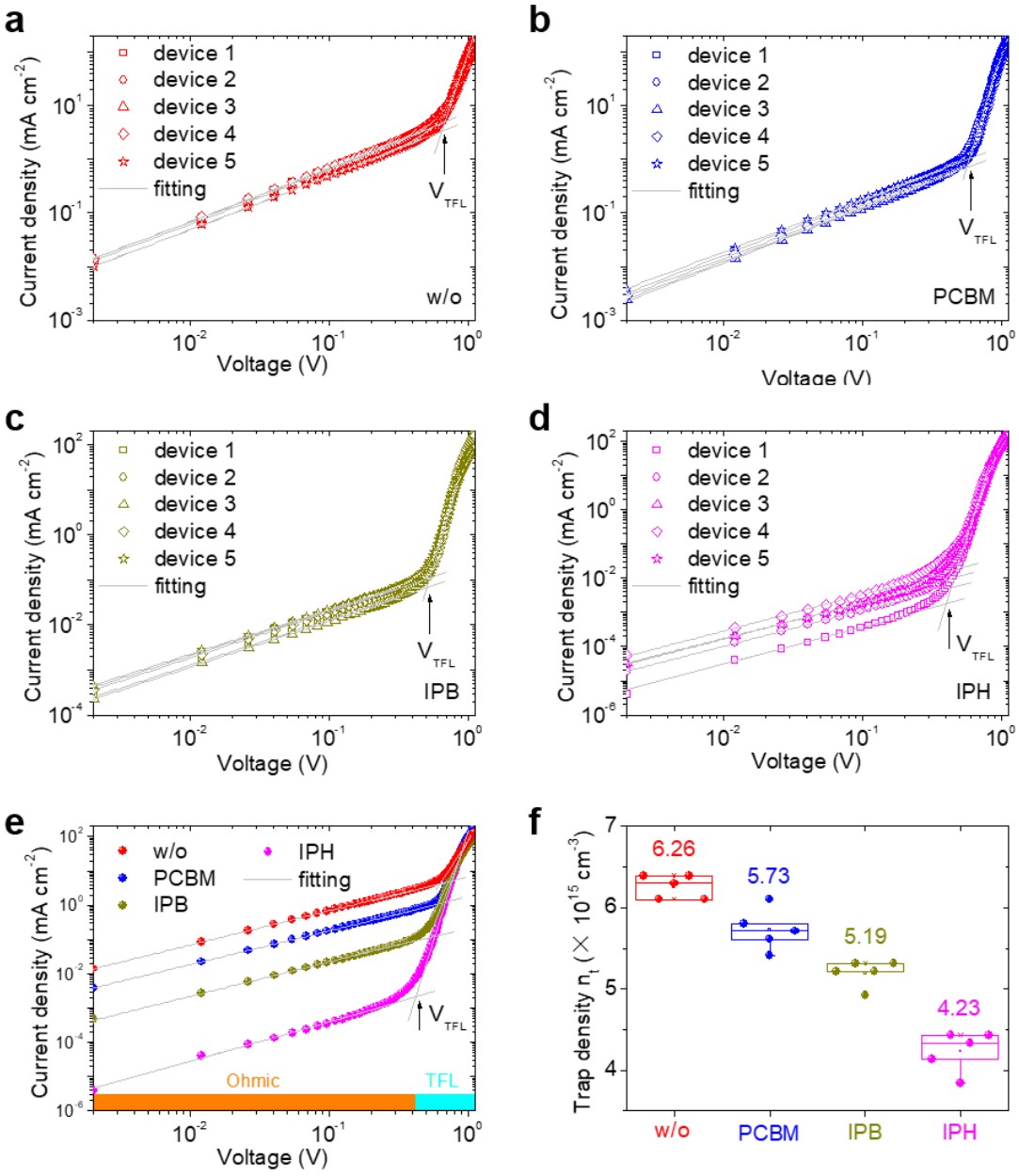

Figure 4.12. (a)−(e) Dark *J-V* characteristics of electron-only devices. V_{TFL} is kink point. (f) Statistics of the trap density (n_t) obtained by space-charge-limited current (SCLC) method. Reproduced from Ref.[16] with permission of Wiley.

perovskite layer to the ETL before encountering any potential recombination. Although τ_{eis} values may exhibit variation under different measurement conditions, such as variations in light intensity or bias, our analysis considers τ_{eis} as a relative value suitable for rigorous quantitative evaluations.[149,161] The enhancement in τ_{eis} for PSC with IPH interlayer consistently supports the conclusion of reduced non-radiative recombination, aligning well with our observations from TRPL (see Figure 4.10b).

In the literature, it has been demonstrated that interfacial trap states play a pivotal role in trap-assisted non-radiative recombination.[25,26] To delve deeper into this aspect, we employed the space-charge-limited-current (SCLC) technique for assessing trap density (n_t).

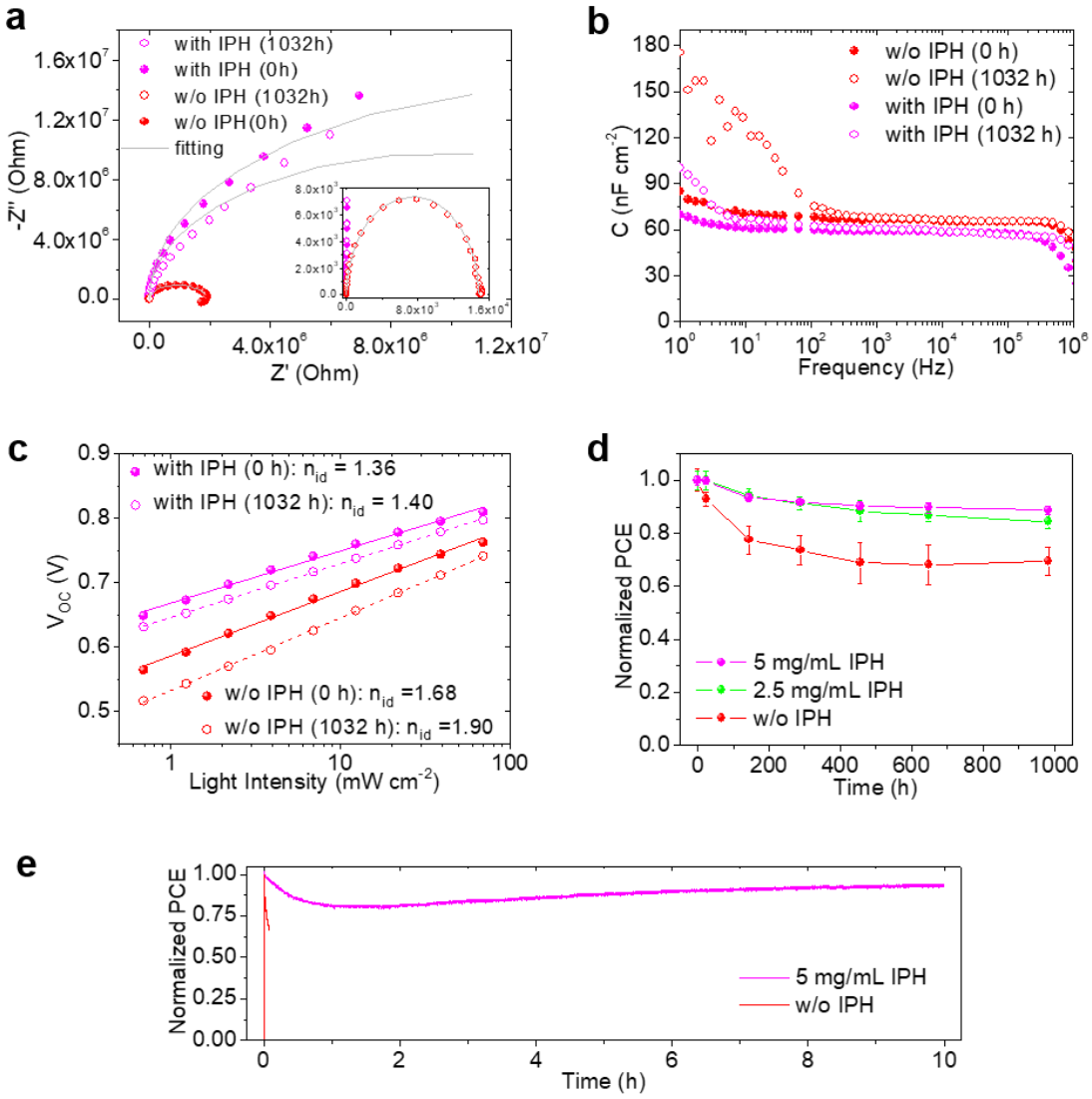

Figure 4.13. (a) Nyquist (inset shows zoomed-in region), (b) capacitance-frequency, and (c) light intensity dependent V_{OC} for fresh and aged PSCs. (d) PCE evolution and for champion PSCs with (5 and 2.5 mg mL^{-1}) and without IPH interlayer. (e) Stabilized power conversion efficiency (SPCE) under continuous illumination of aged PSCs (storage in nitrogen-filled glove box at 25 ºC for 1032 h). All measurements were performed in nitrogen-filled glove box at 25 ºC. Adapted from Supporting Information of Ref.[16] with permission of Wiley.

Specifically, electron-only devices with the architecture of ITO/IPH (with or without)/NBG/C_{60}/BCP/Ag were fabricated for subsequent SCLC analyses. Figure 14.12a−14.12e show the dark current-density-voltage (*J*-*V*) characteristics of these devices, both with and without interlayer. We performed calculations to determine n_t, averaging the values obtained from the devices within the same batch (see Figure 4.12f). The device incorporating IPH interlayer exhibits a significantly lower n_t of 4.23×10^{15} cm^{-3}, compared to the device without an interlayer that has n_t of 6.26×10^{15} cm^{-3}. We attribute this reduction in n_t to the suppressed interfacial trap states by IPH interlayer,[135,139,148,151] ultimately leading to the inhibition of trap-assisted non-radiative recombination within the PSCs. These diminished traps states may stem from the reduced defects present in the surface of the perovskite thin films.[135,136,160]

We further evaluate non-radiative recombination for aged PSCs that were stored in a nitrogen-filled glove box for over 1000 hours. As shown in Figure 4.13a–4.13c, the aged PSCs with IPH interlayer experienced a lower degree of non-radiative recombination when compared to the aged PSC without interlayer. Consequently, the PSCs incorporating IPH interlayers (fabricated with concentrations of 2.5 and 5 mg mL^{-1}) retain approximately 90% of their initial PCE, while the PSCs without interlayer experience a significant performance decline and finally maintain roughly 70% of their initial PCE, as depicted in Figure 4.13d. Furthermore, the aged PSC with IPH interlayer (for 5 mg mL^{-1}) exhibits superior operational stability (see Figure 4.13d). These results prove the mitigated non-radiative recombination by using IPH interlayer within NBG PSCs in the storage of an inert environment.

4.5. Characteristics of charge extraction

In this section, we delve into understanding how charge extraction contributes to the increased J_{SC} observed in PSCs with IPH interlayer. We will assess the charge extraction

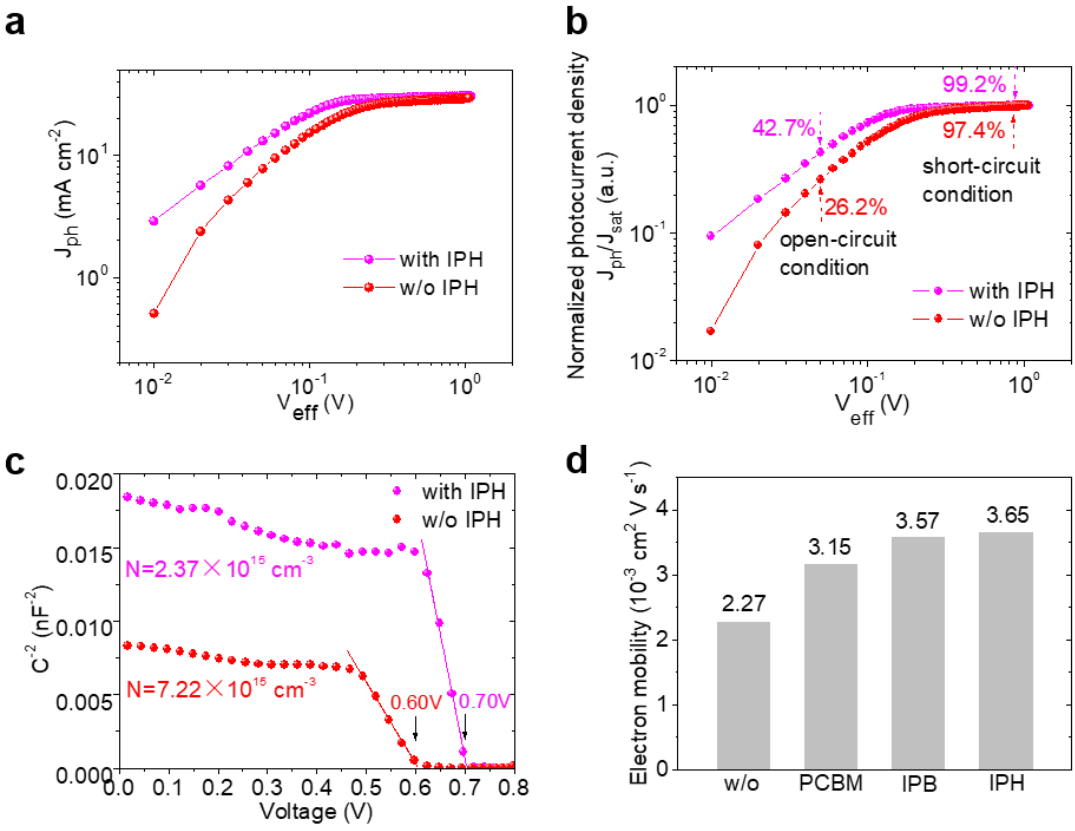

Figure 4.14. (a) Relationship between photocurrent density (J_{ph}) and effective voltage (V_{eff}), (b) normalized photocurrent density (J_{ph}) with the respect of saturated value (J_{sat}) as a function of V_{eff}. The PSCs with and without IPH interlayer were determined at AM 1.5G (100 mW cm^{-2}) irradiation. The values of J_{ph}/J_{sat} represents charge extraction probability: 42.7% (at open-circuit, V_{eff} = 0.05 V) and 99.2% (at short-circuit, V_{eff} = 0.88 V) for PSC with IPH interlayer; 26.2% (at open-circuit, V_{eff} = 0.05 V) and 97.4% (at short-circuit, V_{eff} = 0.85 V) for PSC without. (c) Mott–Schottky plots for PSCs. The apparent charge carrier density (N) was calculated by Mott-Schottky method. (d) Comparison of electron mobility μ for electron-only devices determined by using space-charge-limited-current (SCLC) method. Reproduced from Ref.[16] with permission of Wiley.

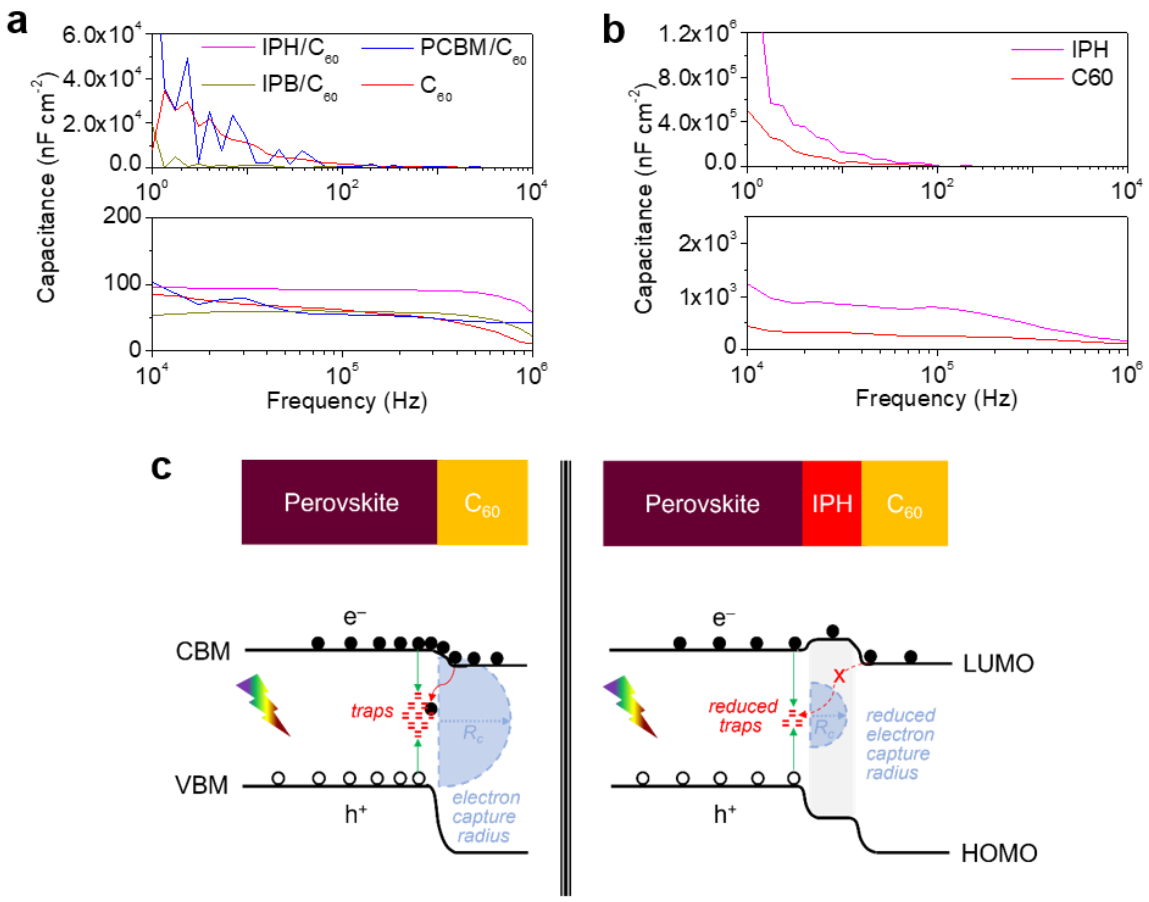

Figure 4.15. (a) Capacitance-frequency (*C-f*) plots of the devices based on the architectures of (a) ITO/interlayer/C_{60}/BCP/Ag or ITO/C_{60}/BCP/Ag, and (b) ITO/IPH/Ag or ITO/C_{60}/Ag. (c) Schematic comparison of electron capture radius at the interfaces of perovskite/C_{60} or perovskite/IPH/C_{60}. Adapted from Supporting Information of Ref.[16] with permission of Wiley.

efficiency by examining the relationship between photocurrent density (J_{ph}) and effective voltage (V_{eff}).[91] This analysis is commonly employed to charge carrier collection efficiency in organic solar cells.[93,94] In the context of Sn-based PSCs, it provides insights into charge transport and collection properties at the perovskite/HTL interface.[92] The relationship between J_{ph} and V_{eff} follows a linear increase in J_{ph} for low V_{eff} values (<0.1 V) but eventually reaches a saturated value (J_{sat}) at sufficiently high V_{eff} (>0.7 V) (see Figure 4.14a). Importantly, J_{sat} values, which are mainly limited by the quantity of absorbed photons,[95,96] are quite comparable for both PSCs, whether or not the IPH interlayer is incorporated. This suggests that the IPH interlayer does not directly impact the external quantum efficiency (EQE), consistent with the absorption data in Figure 4.3. Consequently, the higher J_{ph} can be attributed to a greater probability of successful charge extraction.[91–93] To quantify this charge extraction probability (J_{ph}/J_{sat}), we normalize J_{ph} to J_{sat} (see Figure 4.14b). Interestingly, the PSC featuring the IPH interlayer consistently exhibits a higher charge extraction probability across the entire range from open-circuit to short-circuit conditions. Specifically, at open-circuit (V_{eff} = 0.05 V), the values of J_{ph}/J_{sat} for PSCs with and without IPH interlayer are 42.7% and 26.2%, respectively. At short-circuit (V_{eff} = 0.88 V for IPH interlayer and V_{eff} = 0.85 V for without interlayer), the values are 99.2% and 97.4%,

respectively. This J_{ph}/J_{sat} improvement of ~2% at short-circuit condition closely aligns with contribution to J_{SC} enhancement of ~1 mA cm^{-2}, revealing enhanced charge extraction at the perovskite/IPH/C_{60} interface.

In addition, we further provide Mott-Schottky analysis. A relative reduction in charge carrier density observed in Figure 4.14c indicates reduced charge accumulation at the perovskite/IPH/C_{60} interface,[78,87,161,163] thus improving J_{SC} within PSC.[91–93,164] This enhanced charge extraction likely results from improved electron mobility[92,151] (see Figure 4.14d) and a smaller electron capture radius[69,106,107] (see Figure 4.15 and calculation details in section 3.3.2) within PSC with IPH interlayer.

4.6. Charge recombination mechanisms

In section 4.5, we investigated charge-carrier dynamics in depth and will address potential paths for non-radiative recombination in this section. Two main mechanisms are considered to contribute to interfacial non-radiative recombination losses in PSCs: trap-assisted recombination (*i.e.*, path 1) and charge-carrier-back-transfer recombination (*i.e.*, path 2).[25] In the interlayer-free PSC (see Figure 4.16a), trap states capture photo-generated charge carriers via path1, and cliff-like CBO ($CBO_{NBG/C60}$ = -0.4 eV, see Figure 4.6) results in backward flow of injected electrons (from C_{60} to the perovskite) via path 2.[149,153–156] In contrast to the PSC with IPH interlayer (see Figure 4.16b), photo-generated charge carriers escape from the trap states due to the reduced n_t (see Figure 4.12), and a spike-like CBO ($CBO_{NBG/IPH}$ = 0.2 eV, see Figure 4.6) acts as a barrier to prevent the backward flow of injected electrons. In summary, based on our comprehensive characterizations, the IPH interlayer emerges as the most effective interlayer for achieving high device performance with reduced non-radiative recombination, *i.e.*, minimized trap-assisted recombination due to reduced n_t and reduced charge-carrier-back-transfer recombination due to the presence of a higher CBO (> 0 eV).

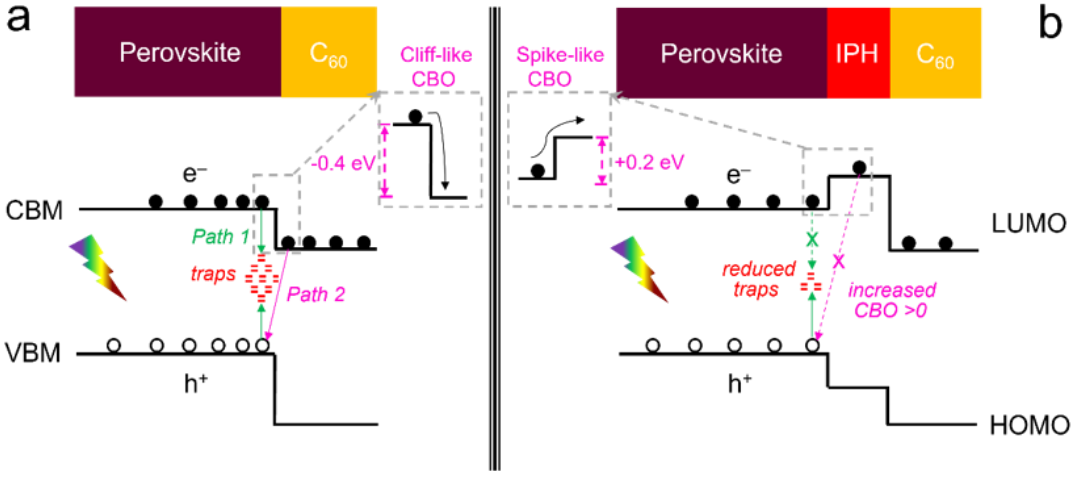

Figure 4.16. Schematic illustration of the non-radiative recombination process at (a) a cliff-like and (b) a spike-like interface of perovskite/ETL. CBO: conduction band offset. CBM: conduction band minimum; VBM: valence band maximum; HOMO: highest occupied molecular orbital; LUMO: lowest unoccupied molecular orbital; CBO: conduction band offset. Adapted from Ref.[16] with permission of Wiley.

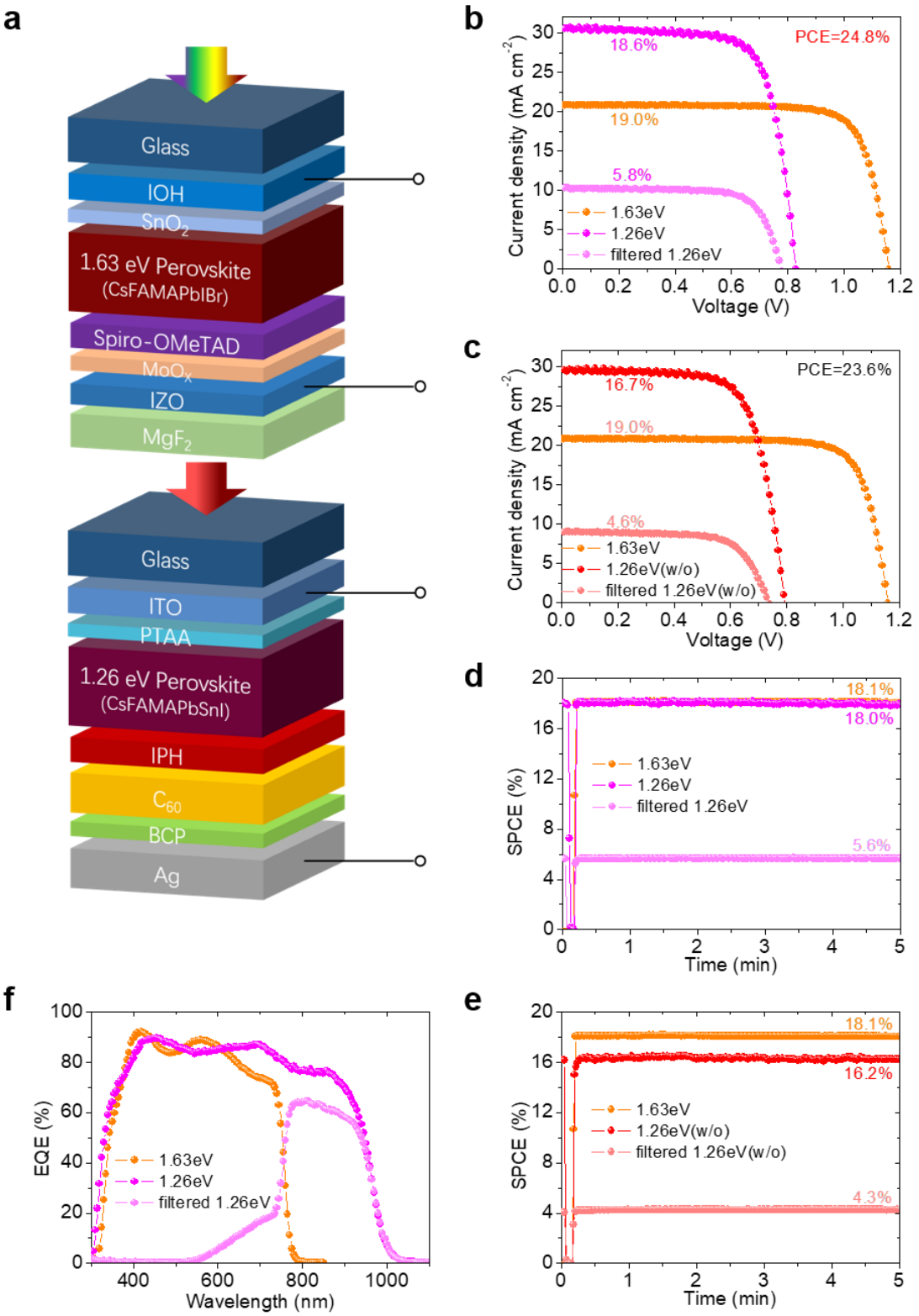

Figure 4.17. (a) Schematic illustration of 4T all-perovskite tandem architecture. (b), (c) *J-V* characteristics and (d), (e) stabilized power conversion efficiency (SPCE) under continuous AM 1.5G illumination of the best WBG top cell (E_g = 1.63 eV), NBG bottom cell (E_g = 1.26 eV), and filtered bottom cell. NBG bottom cells were based on IPH interlayer ((b), (d)) and without interlayer ((c), (e)). (f) EQE spectra of the champion WBG top cell, NBG bottom cell with IPH interlayer, and filtered NBG bottom cell with IPH interlayer. Reproduced from Ref.[16] with permission of Wiley.

Table 4.4. Summary of photovoltaic performance for single-junction and 4T tandem solar cells. Adapted from Ref.[16] with permission of Wiley.

Solar cells	J_{SC} (mA cm^{-2})	V_{OC} (V)	FF	PCE (%)	SPCE (%)
Top solar cell, 1.63 eV	20.8	1.16	0.79	19.0	18.1
Bottom solar cell, 1.26 eV (with IPH)	30.7	0.83	0.73	18.6	18.0
Bottom solar cell, 1.26 eV (with IPH, filtered)	10.1	0.78	0.74	5.8	5.6
4T tandem solar cell (with IPH)	-	-	-	24.8	23.7
Bottom solar cell, 1.26 eV (without IPH)	29.6	0.80	0.71	16.7	16.2
Bottom solar cell, 1.26 eV (without IPH, filtered)	9.0	0.74	0.69	4.6	4.3
4T tandem solar cell (without IPH)	-	-	-	23.6	22.4

J_{SC}: short-circuit current density; V_{OC}: open-circuit voltage; FF: fill factor; PCE: power conversion efficiency; SPCE: stabilized power conversion efficiency.

4.7. All-perovskite four-terminal tandem solar cells

In this section, we demonstrate highly efficient 4T tandem solar cells with mechanical integration of NBG (E_g = 1.26 eV) bottom solar cell and semitransparent WBG (E_g = 1.63 eV) top solar cell. We fabricated semitransparent WBG top cell in the same architecture that has been published in previous work,[150,165] *i.e.*, glass/hydrogen-doped indium oxide In_2O_3:H (IOH)/SnO_2 nanoparticles/$Cs_{0.1}(FA_{0.83}MA_{0.17})_{0.9}Pb(I_{0.83}Br_{0.17})_3$/2,2',7,7'-tetrakis[N,N-di(4-methox-yphenyl)amino]-9,9'-spirobifluorene (spiro-MeOTAD)/molybdenum oxide (MoO_x)/indium zinc oxide (IZO)/magnesium fluoride (MgF_2), as shown in Figure 4.17a. This architecture includes a sputtered IZO thin film with 165 nm thickness as the rear electrode. A 10-nm MoO_x thin film was deposited on top of spiro-MeOTAD thin film that serves as a HTL and prevents damaging from IZO sputtering process.[131,150,165,166] A 165-nm MgF_2 antireflection coating was used to reduce reflection loss, especially for NBG PSCs.[131,150,165,166] The semitransparent filter was fabricated under the same condition with WBG semitransparent PSCs.

We evaluate the photovoltaic performance in tandem architecture. With a WBG filter, NBG bottom cell with IPH interlayer realizes the best PCE of 5.8% and SPCE of 5.6% (see Figure 4.17b, 4.17d, and Table 4.4), which are higher than PCE of 4.6% and SPCE of 4.3% for the device without interlayer (see Figure 4.17c, 4.17e, and Table 4.4). Considering the PCE of 19.0% and SPCE of 18.1% for the champion WBG top cell, we achieve a champion PCE of 24.8% (*i.e.*, 5.8% + 19.0% = 24.8%) and SPCE of 23.7% (*i.e.*, 5.6% + 18.1% = 23.7%) for

our 4T all-perovskite tandem solar cell. These values are higher than the tandem device without interlayer (PCE = 23.6%, SPCE = 22.4%). We attribute the enhancement of PCE in tandem devices with an IPH interlayer to the increased J_{SC} and V_{OC} compared to devices without interlayer (see Table 4.4). In addition, we obtain integrated J_{SC} of 19.8 and 9.1 mA cm^{-2} from EQE spectra (see Figure 4.17f) for the top WBG and bottom filtered NBG cells, respectively, which agrees well with *J-V* data (Table 4.4). We conclude that IPH interlayer provides an effective strategy for further improving the performance of all-perovskite tandem photovoltaics.

4.8. Summary

In this chapter, we incorporate two innovative fullerene derivative interlayers in NBG PSCs and investigate their effect on device performance and non-radiative recombination. The PSCs with IPH interlayer achieve an impressive champion PCE of 18.6% and SPCE of 18.0%, which are much higher than the devices with PCBM (PCE = 17.8%, SPCE = 17.2%), IPB (PCE = 17.8%, SPCE = 17.3%), and without (PCE = 16.7%, SPCE = 16.2%) interlayer. This significant enhancement in PCE is primarily attributed to the improved V_{OC} (*i.e.*, by 20 mV) and J_{SC} (*i.e.*, by 1.1 mA cm^{-2}) facilitated by the IPH interlayer. The V_{OC} loss of only 0.43 V is among the lowest values compared to the published work of NBG PSCs.

The optical properties, perovskite morphologies, and Sn state of perovskite do not change much with incorporation of fullerene derivative interlayer, which are confirmed from, UV-Vis, AFM, contact angle, and XPS, respective. Various characterizations including PL, TRPL, EIS, SCLC, and UPS, reveal that the boosted V_{OC} when using an IPH interlayer is ascribed to the reduction in non-radiative recombination at the perovskite/ETL interface. We attribute this reduced non-radiative recombination to two factors: deduced n_t leads to reduced trip-assisted recombination, a higher positive CBO = 0.2 eV (>0 eV) suppresses charge-carrier-transfer-back recombination. The photocurrent density and Mott-Schottky analyses reveal the enhancement in charge extraction within PSCs, which explains the improvement of J_{SC}.

Last, we demonstrate efficient 4T all-perovskite tandem solar cells using NBG (E_g = 1.26 eV) bottom solar cell and semitransparent WBG (E_g = 1.63 eV) top solar cell. We achieve a champion PCE of 24.8% and SPCE of 23.7% in 4T architecture with IPH interlayer, which are higher that of without interlayer (PCE = 23.6%, SPCE = 22.4%). The performance improvement is attributed to the increased V_{OC} and J_{SC}. We highlight that utilization of IPH interlayer provides a promising approach to boost the photovoltaic performance for NBG PSCs as well as all-perovskite tandem solar cells.

5. Buried interface engineering for scalable processing of *p-i-n*-based $FAPbI_3$ perovskite solar modules

Formamidinium lead iodide ($FAPbI_3$) is regarded as a promising semiconductor within the realm of perovskite solar cells (PSCs), mainly attributed to its impressive power conversion efficiency (PCE) and robust operational stability. However, regarding scalable techniques and fabrication protocols for processing of $FAPbI_3$ perovskite solar modules, there still remain challenges that have not been addressed so far. In this chapter, a novel and advanced development is presented: the realization of a void-free buried interface within PSCs with a *p-i-n* architecture. This achievement enables upscaling of lab-scale PSCs, typically confined to dimensions below 1 cm^2, to the dimension of mini-modules exceeding 10 cm^2. Through the systematic implementation and modulation of nitrogen (N_2) flow during the vacuum-assisted growth (VAG) of perovskite thin films, in combination with the incorporation of methylammonium chloride (MACl) as an additive, the interfacial voids within blade-coated, large-scaled $FAPbI_3$ layers are effectively eliminated. We demonstrate impressive PCEs of 20.0% for blade-coated PSCs with an active area of 0.105 cm^2, and 18.3% for fully scalable modules with an aperture area of 12.25 cm^2 and a geometric fill factor (GFF) of 96.3%.

This chapter is based on our publication in *Joule* by Hang Hu *et al.* with the title of "Void-free buried interface for scalable processing of *p-i-n*-based $FAPbI_3$ perovskite solar modules".[27] Most of the graphs in this chapter are adapted or reproduced with permission of Elsevier.

Acknowledgments and contributions

Hang Hu, Prof. Dr. Ulrich W. Paetzold, and Dr. Bahram Abdollahi Nejand conceived the idea. Hang Hu developed research plans and designed the experiments. Hang Hu fabricated PSCs and modules. David B. Ritzer performed the laser scribing for modules. Alexander Diercks conducted SEM. Dr. Yang Li performed TRPL. Roja Singh carried out XRD and stability testing. Dr. Paul Fassl conducted PLQY and data analysis. Qihao Jin conducted AFM and contact angle measurements. Dr. Fabian Schackmar and Dr. Bahram Abdollahi Nejand constructed the vacuum-quenching system. Hang Hu did the rest of the

characterizations and data analysis. Prof. Dr. Ulrich W. Paetzold and Dr. Bahram Abdollahi Nejand supervised the project.

5.1. Introduction

$FAPbI_3$ has gained attention due to its (1) good thermal stability for black cubic phase (α-$FAPbI_3$),[167–169] and (2) efficient light absorption with relatively low band gap of around 1.48 eV. This band gap aligns well with the optimal range for solar absorption according to the detailed-balance theory (1.1–1.4 eV).[167]

Two basic architectures are utilized for PSCs: *n-i-p* and *p-i-n* configurations. The *n-i-p* architecture has shown higher reported PCEs (>23%) for $FAPbI_3$ PSCs.[80,170–175] The *p-i-n* architecture, although particularly interesting for tandem solar cells due to the advantages of good operational stability and low-temperature processing,[22,23] has lower reported maximum PCEs (~22.13%) so far.[74,176] In comparison with the *n-i-p* architecture, $FAPbI_3$-based PSCs with *p-i-n* architecture still face challenges related to PCE, phase stability, and scalability.

Addressing the key challenge of processing pure $FAPbI_3$ thin films needs to mitigate the instability issue of the photoactive α-$FAPbI_3$ phase. Notably, this phase exhibits a trend to undergo a transition into the photo-inactive yellow orthorhombic phase (δ-$FAPbI_3$) at room temperature, particularly when subjected to conditions of elevated moisture or the presence of polar solvents.[177–179] To stabilize α-$FAPbI_3$, tremendous progress has been made to improve perovskite crystallization/morphology, including additive engineering,[180] compositional engineering,[174,181] and interfacial engineering.[181,182] These strategies have been widely used in *n-i-p*-based PSCs, but very few were reported for the *p-i-n* architecture. One of the most promising strategies involves optimizing interfaces and crystallization through the introduction of MACl. This approach was proven successful in *p-i-n*-based $FAPbI_3$ PSCs for improving the morphology of perovskite thin films, using as a post-treatment for the surface and as a precursor additive.[74,183] Zhang *et al.* highlighted that [2-(3,6-Dimethoxy-9H-carbazol-9-yl)ethyl] phosphonic acid (MeO-2PACz) as a hole transport layer (HTL) stabilizes α-$FAPbI_3$ by reducing defects at grain boundaries,[74] thereby minimizing losses in open-circuit voltage (V_{OC}).[17] It should be noted that the buried interface within *p-i-n*-based $FAPbI_3$ PSCs remains an area that has been relatively unexplored in literatures.[184–186] This interface plays a pivotal role in device stability and performance.[187–189] Previous literatures indicated that this interface might contain interfacial voids or uncoordinated Pb^{2+} defects, resulting in inefficient charge carrier extraction and severe non-radiative recombination. This leads to significant reductions in both short-circuit current density (J_{SC}) and V_{OC}.[185,189] In contrast, numerous investigations of $FAPbI_3$ PSCs have focused on enhancing the electron transport layer (ETL)/perovskite interface in the *n-i-p* architecture. For example, utilizing mesoporous TiO_2 has been demonstrated to improve PV performance due to effective charge extraction, as well as reducing degradation when exposed to ambient air.[168,190] This efficient charge carrier extraction mechanism explains the notable improved J_{SC} in many *n-i-p*-based PSCs. Therefore, key improvements of the buried

interface are needed for highly efficient *p-i-n*-based $FAPbI_3$ PSCs for improving α-phase stability, minimizing non-radiative recombination, and enhancing charge extraction.

Next to enhancing the device stability and performance, implementing scalable methods for processing of large-area *p-i-n*-based $FAPbI_3$ PSCs poses a significant challenge. There are very few reported scalable fabrication techniques of high-purity $FAPbI_3$-based in the *p-i-n* architecture. Only a couple of studies focus on blade-coated PSCs (18.41% PCE with 0.09 cm^2 active area)[191] and solar mini-modules (12.52% PCE for 25 cm^2 aperture area with a GFF of 73.3% based on calculations).[192] Solution-based scalable processes necessitate optimized compositional and solvent engineering to improve crystallization of large-area perovskite thin films.[22] The nucleation and crystallization are critical determinants for controlling the film morphology and quality, particularly related to pinholes and voids, which are linked with solvent evaporation kinetics. A fast extraction rate of solvents from the wet perovskite thin film is key for generating homogenous and pinhole-free large-area perovskite thin film.[28] Therefore, well-controlled drying dynamics as well as solvent compositions emerge as an indispensable approach for improving morphology and uniformity of large-area perovskite thin films.[193] A noteworthy approach of co-solvent systems showed that introducing a mixed ink of ethyl alcohol, 2-methoxyethanol, or acetonitrile, together with established common solvents such as N,N-dimethylformamide (DMF) and dimethyl sulfoxide (DMSO), improves the film quality and optimizes buried interface.[28,194] A recent study reported that perovskite intermediary phase could be regulated by the substitution of DMSO with hydriodic acid and N-methyl-2-pyrrolidone during the fabrication of blade-coated $FAPbI_3$ thin films for mini-modules.[192] In addition, the deployment of an N_2-assisted drying during the blade-coating procedure demonstrates a promising route for control crystallization kinetics.[17,189,194,195] So far, morphology formation and buried interface engineering for blade-coated large-area $FAPbI_3$ thin films (derived from the conventional solvent systems using DMF/DMSO) has not been investigated in detail.

This chapter presents a void-free buried interface for the fabrication of high-quality α-$FAPbI_3$ PSCs (0.105 cm^2) in a *p-i-n* architecture that enables upscaling to mini-module devices (12.25 cm^2). It is demonstrated that the buried HTL/$FAPbI_3$ interface is free of interfacial voids when utilizing the vacuum-assisted growth (VAG) method developed during the PhD thesis. PSCs employing this VAG approach achieve a remarkable champion PCE of 22.3% (backward scan). In contrast, the reference process employing the conventional anti-solvent (AS) quenching step is shown to result in voids at the buried HTL/$FAPbI_3$ interface. The findings reveal that the presence of voids significantly contributes to high V_{OC} loss due to non-radiative recombination loss and reduced J_{SC} ascribed to poor charge extraction. Using the developed VAG approach together with a controlled N_2 flow allows fabrication of uniform void-free large-area blade-coated α-$FAPbI_3$ thin films via introduction of MACl additive in the perovskite precursor. Consequently, this achievement enables the development of blade-coated PSCs (active area of 0.105 cm^2) as well as solar mini-modules (aperture area of 12.25 cm^2, geometric fill factor of 96.3%). Impressively, these devices yield PCEs of 20.0% and 18.3% (backward scan), respectively.

5.2. Spin-coated *p-i-n*-based $FAPbI_3$ perovskite solar cells

The VAG strategy exhibits advantages in processing of high-quality perovskite thin films with wide range bandgaps, *i.e.*, wide- (*e.g.*, 1.78 eV) and narrow bandgap (*e.g.*, 1.25 eV) perovskite PSCs, and larger device dimension for application in solar modules or two-terminal (2T) all-perovskite tandem arthitectures.[16,17,131] We first focus on the investigation of spin-coated small-area PSCs, and then extend to blade-coated PSCs and solar min-

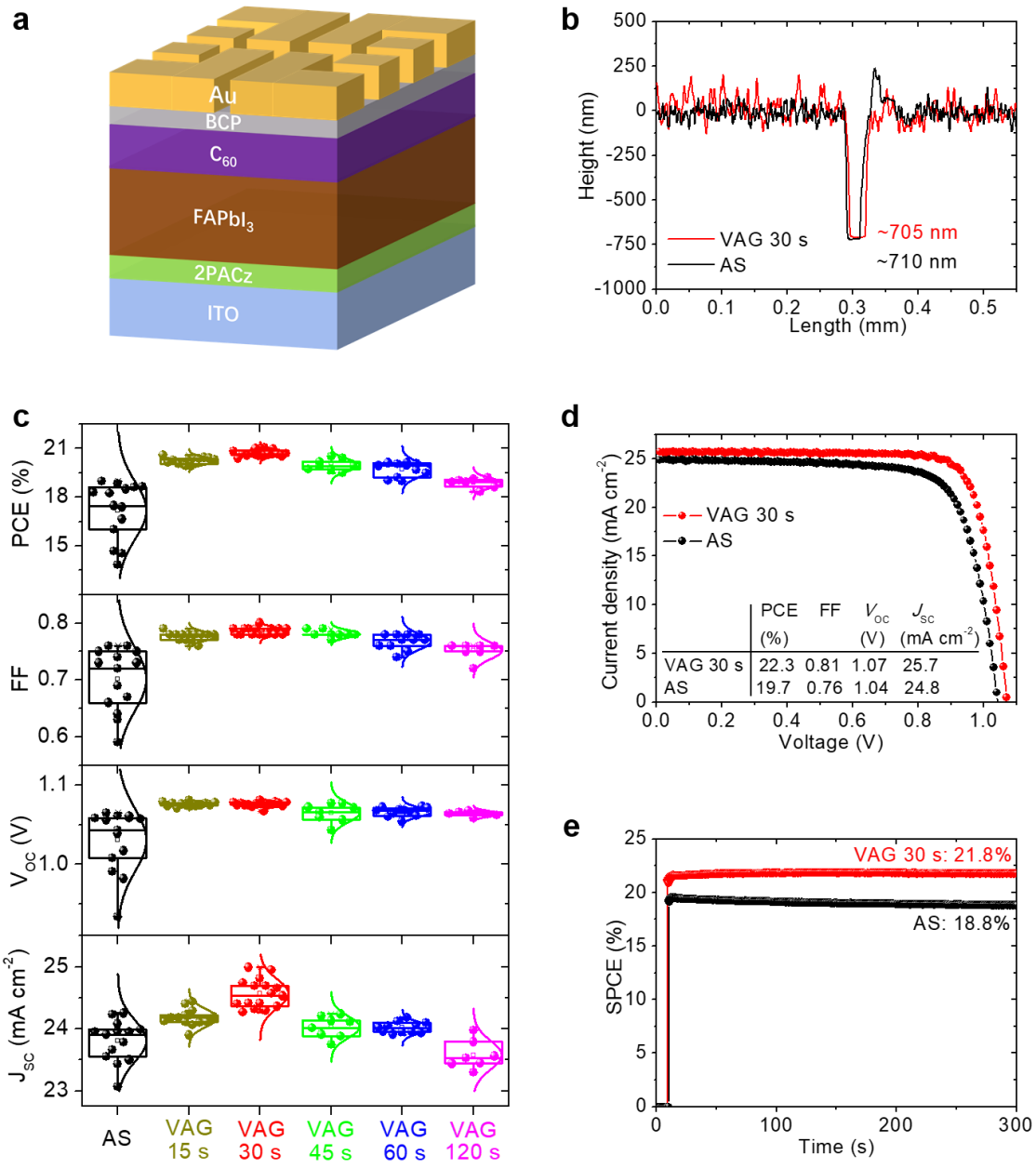

Figure 5.1. (a) Schematic of $FAPbI_3$ PSCs based on *p-i-n* architecture. (b) Thickness of $FAPbI_3$ thin films. (c) Statistics of photovoltaic performance for the PSCs (without MgF_2 antireflection coating). The vacuum time of vacuum-assisted growth (VAG) process is varied from 15 to 120 s. (d) Current-density-voltage (*J-V*) characteristics and (e) stabilized power conversion efficiency (SPCE) of champion PSCs fabricated with VAG and anti-solvent (AS) quenching (with MgF_2 antireflection coating). Reproduced from Ref.[27] with permission of Elsevier.

modules.

The lab-scale devices have an active area of 0.105 cm^2. The employed *p-i-n* architecture is based on the stack of glass/indium tin oxide (ITO)/[2-(9H-carbazol-9-yl)ethyl] phosphonic acid (2PACz)/$FAPbI_3$/Fullerene (C_{60})/2,9-dimethyl-4,7-diphenyl-1,10-phenanthroline (BCP)/Au (see Figure 5.1a). First, conventional AS quenching and the VAG methods were compared to investigate the PV performance of the PSCs. The vacuum time during the VAG process was varied with 15, 30, 45, 60, and 120 s. All perovskite thin films have a similar thickness of ~700 nm (see Figure 5.1b). The PSCs fabricated with VAG (denoted as VAG-PSCs) demonstrate higher yield and reproducibility compared to the PSCs fabricated by AS

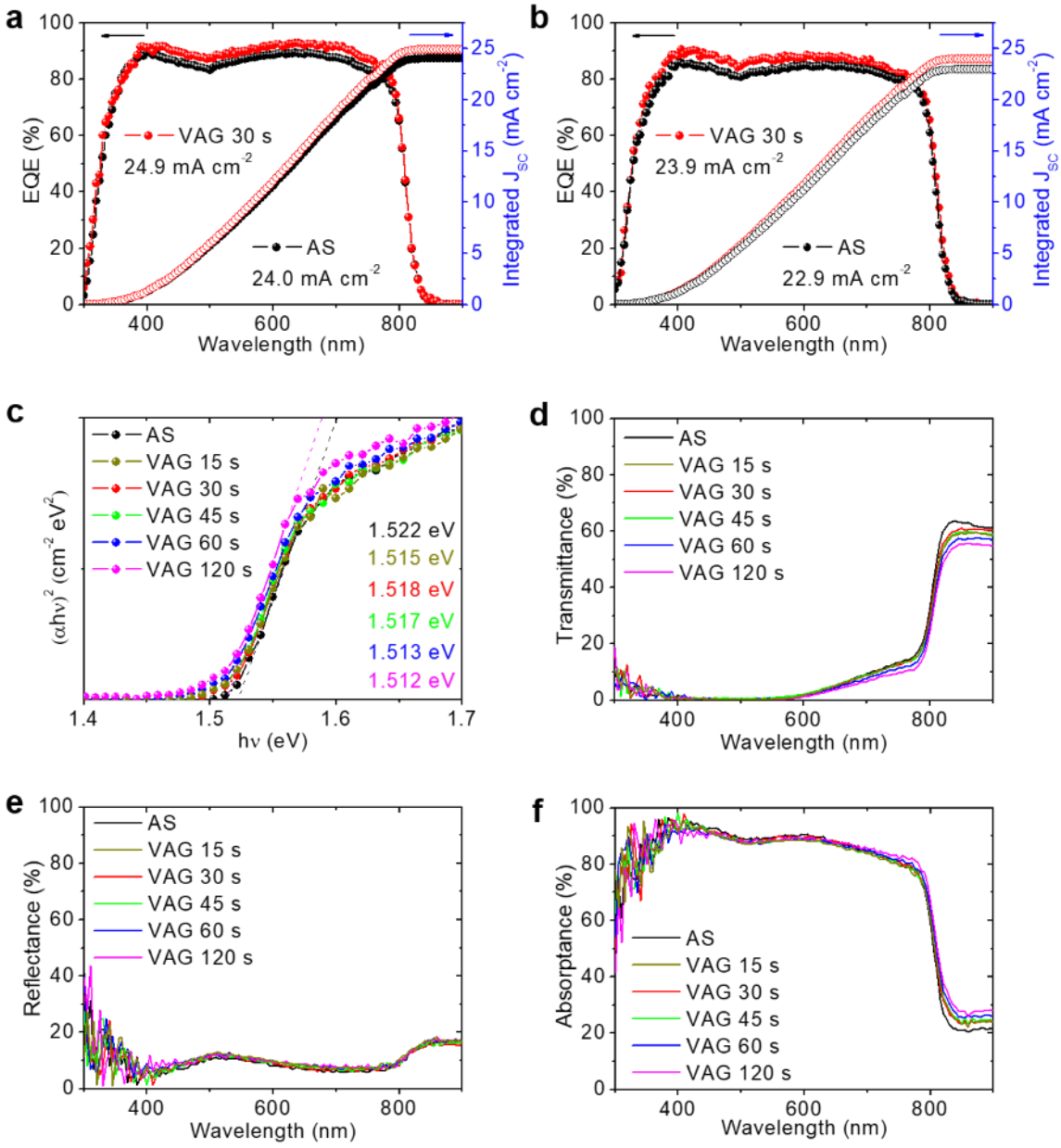

Figure 5.2. External quantum efficiency (EQE) spectra for the champion PSCs (a) with and (b) without MgF_2 antireflection coating. (c) Tauc-plots, (d)Transmittance, (e) reflectance, and (f) absorptance spectra. Reproduced from Supplemental information of Ref.[27] with permission of Elsevier.

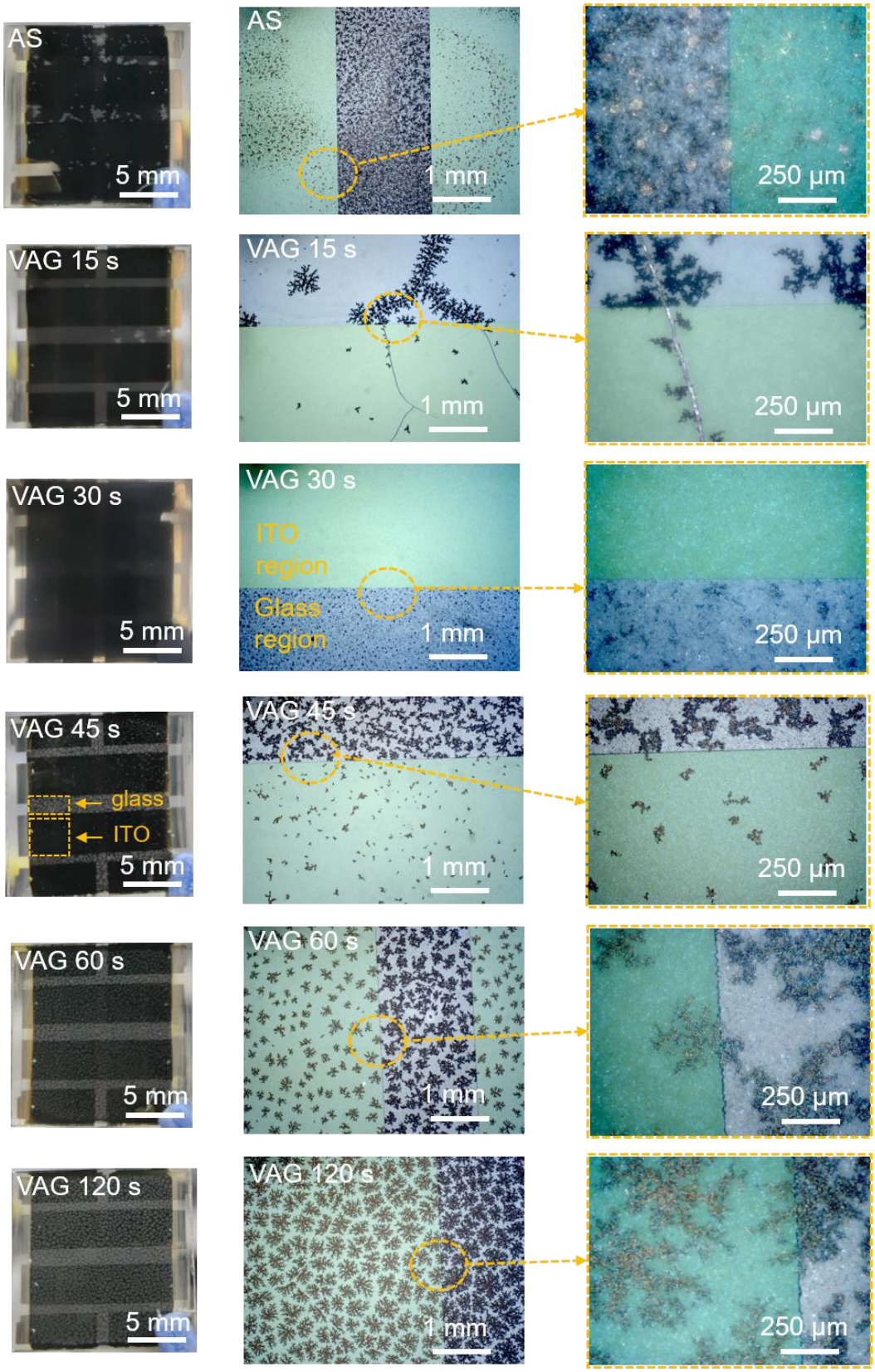

Figure 5.3. Photographs and corresponding optical microscopic images of $FAPbI_3$ PSCs based on *p-i-n* architecture (visualized from glass side, substrate dimension: 1.6 × 1.6 cm^2). The devices were fabricated via AS and VAG method (vacuum time varies from 15 to 120 s). The white spots in photographs and dark region in optical microscopic images indicate interfacial voids. Reproduced from Ref.[27] with permission of Elsevier.

(denoted as AS-PSCs), as illustrated in Figure 5.1c. The AS-PSCs exhibit an average PCE of 17.2% in the backward scan direction, while the average PCE of VAG-PSCs improves to 20.2% (VAG 15 s) and further to a maximum of 20.7% (VAG 30 s). Further increasing the vacuum time results in a decline of average PCE with 20.0% for VAG 45 s, 19.7% for VAG 60 s and 18.9% for VAG 120 s. Fill factor (FF), V_{OC}, and J_{SC} exhibit similar trends. To further improve the device performance, MgF_2 antireflection layer was deposited on the best PSCs. VAG 30 s yields the champion PSC delivering a remarkable PCE of 22.3% with a high FF of 0.81, V_{OC} of 1.07 V, and J_{SC} of 25.7 mA cm^{-2} (see Figure 5.1d). It is worth noting that, to our best knowledge, this is the highest reported PCE for $FAPbI_3$-based PSCs based on the *p-i-n* architecture. In contrast, the best AS-PSC exhibit a PCE of 19.7%, with a FF of 0.76, a V_{OC} of 1.04 V, and a J_{SC} of 24.8 mA cm^{-2}. Furthermore, the champion VAG 30 s PSC also delivers a stabilized power conversion efficiency (SPCE) of up to 21.8% under continuous AM 1.5 G (100 mW cm^{-2}) irradiation during 5-min maximum power point (MPP) tracking (see Figure 5.1e). We find a broadband enhancement in the external quantum efficiency (EQE) of VAG 30 s PSC compared to AS-PSC (Figure 5.2a and 5.2b), where the increase in integrated J_{SC} is consistent with the values of the *J-V* characteristics in Figure 5.1d. We consider the enhancement of J_{SC} is not attributed to the minor changes in absorption and corresponding optical spectra (Figure 5.2c–5.2f), but predominately stem from improved charge carrier extraction governed by the buried interfaces of $2PACz/FAPbI_3$,[189] as will be elaborated on in the analysis in section 5.5. We note that the V_{OC} enhancement is not related to a change in the perovskite bandgap (~1.52 eV, as illustrated in Tauc plots in Figure 5.2c), but dominated by reduced non-radiative recombination, as will be investigated in section 5.4.

5.3. Spin-coated perovskite thin films and buried interface

In general, the buried interface of $2PACz/FAPbI_3$ is as important as the top interface of $FAPbI_3/C_{60}$. As presented in Figure 5.3, we observe a large number of "white" spots visualized from the glass side of the actual photographs of AS-PSCs. Interestingly, the white spots reduce significantly in case of VAG 15 s. We find the perovskite layers get rid of the spots when the vacuum time is increased further to 30 s. However, with further increasing the vacuum time, the spots become more concentrated and larger. To reveal the nature of

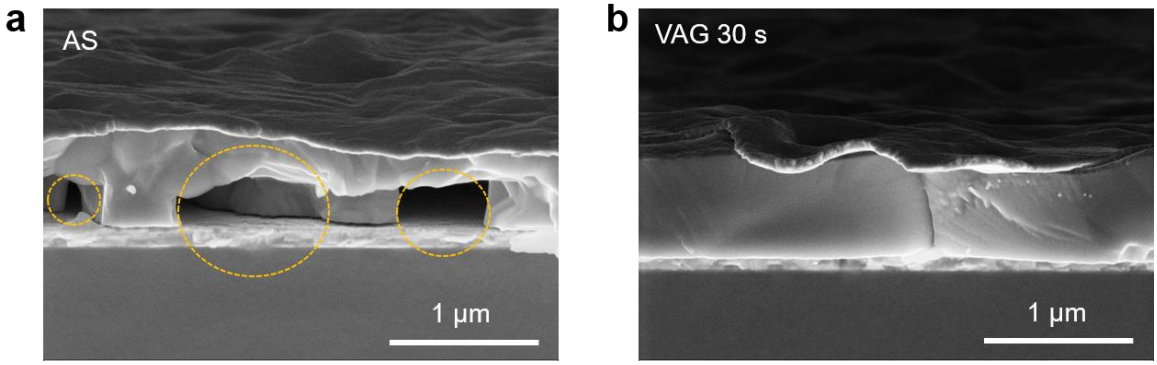

Figure 5.4. Cross-section scanning electron microscopy (SEM) images for (a) AS and (b) VAG-30-s PSCs. Reproduced from Ref.[27] with permission of Elsevier.

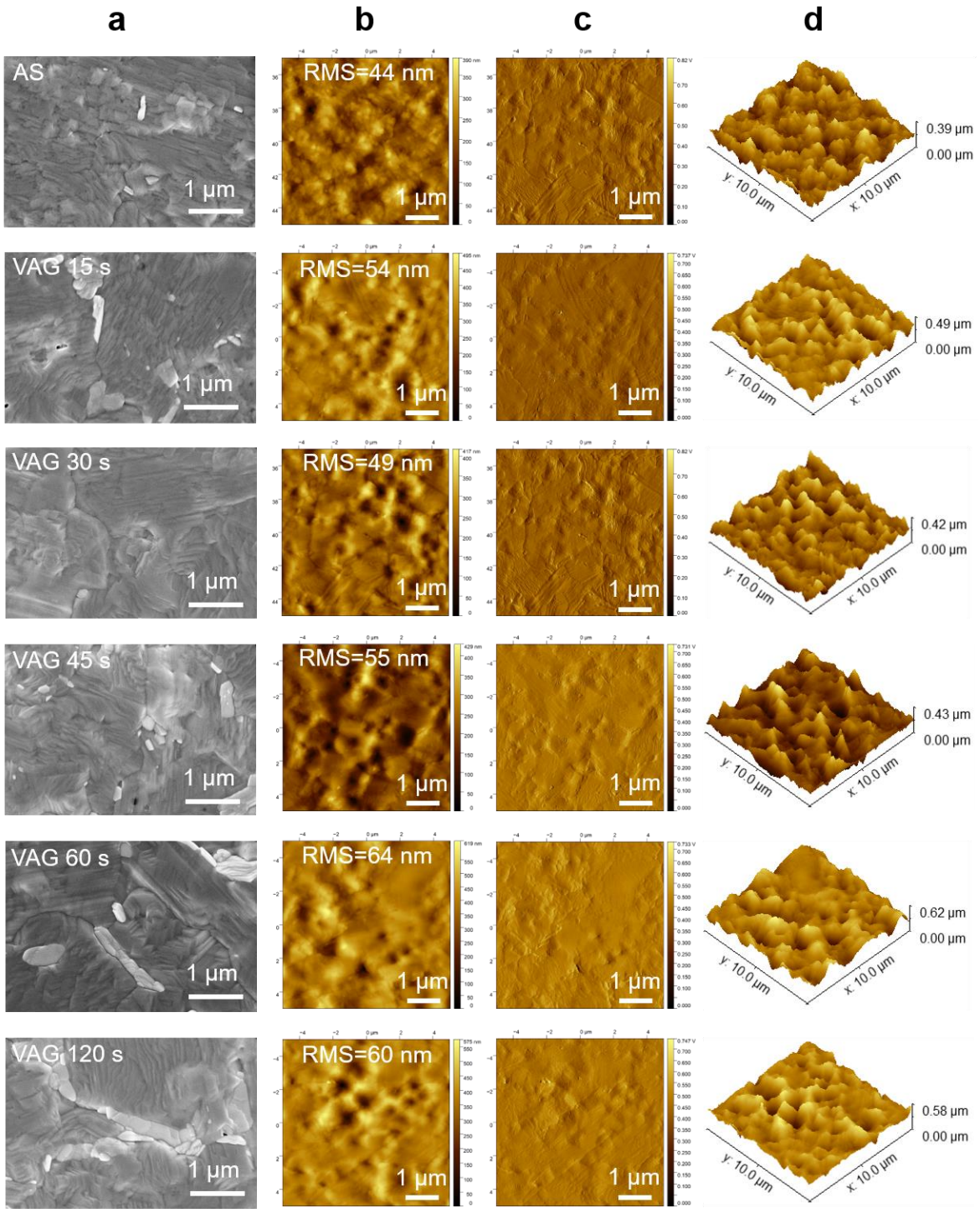

Figure 5.5. (a) Top-view scanning electron microscopy (SEM), (b) atomic force microscopy (AFM), corresponding (c) 2D topography phase and (d) 3D view images for AS and VAG PSCs. Adapted from Supplemental information of Ref.[27] with permission of Elsevier.

the spots, we collected optical microscopes images from the glass side. In Figure 5.3, we observe a high density of the spots in AS-PSCs. For a short vacuum time of 15 s, some cracks and spots appear. In contrast, the optimal vacuum time of 30 s exhibits no such spots. For a longer vacuum time ≥ 45 s, the spots reappear, expand and concentrate throughout the perovskite thin films, even distributing over the glass region (*i.e.*, ITO-etched area, as shown

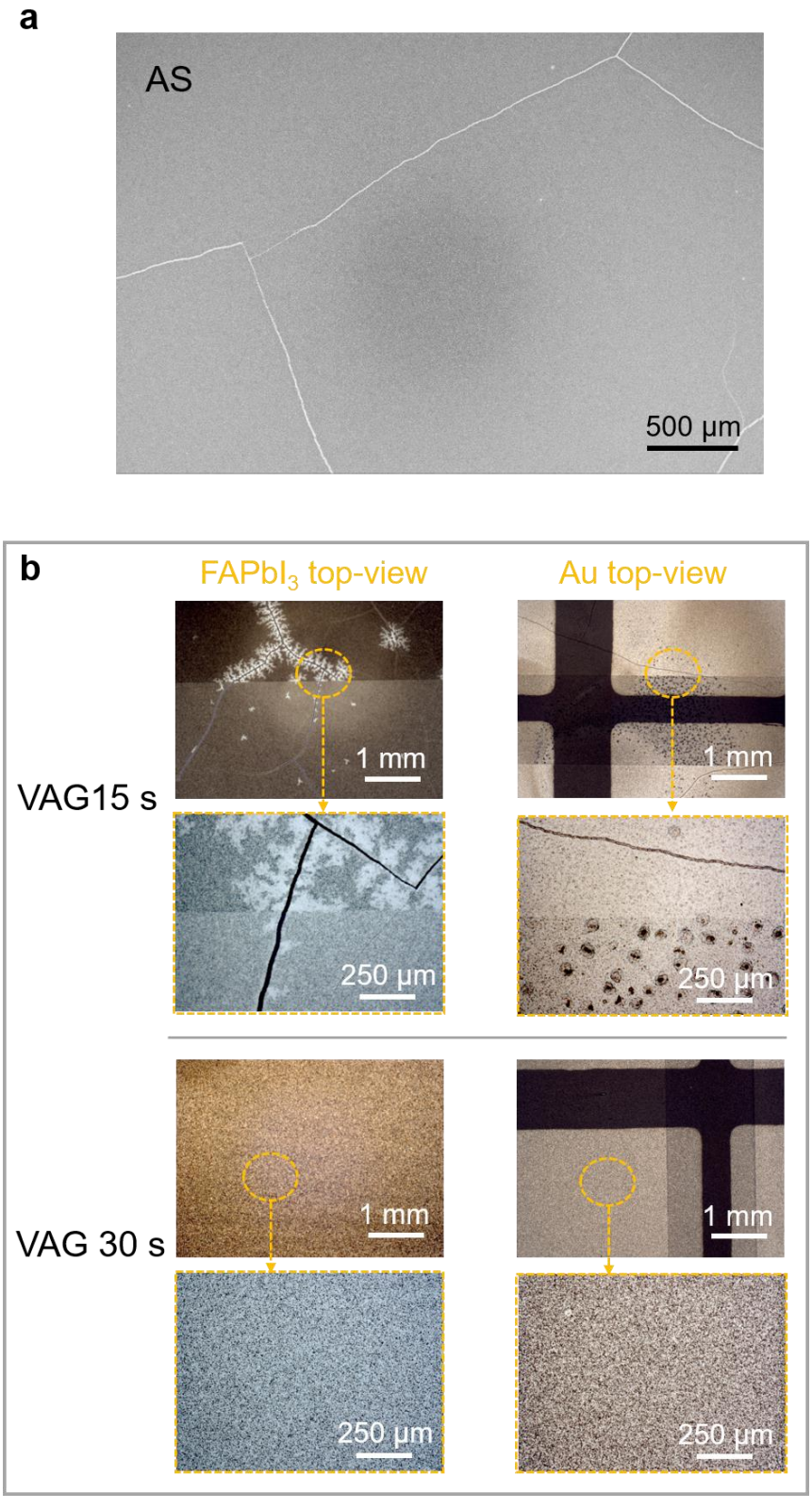

Figure 5.6. (a) Top-view scanning electron microscopy (SEM) images for AS-$FAPbI_3$ thin films. (b) Optical microscopic images for AS and VAG 30 s $FAPbI_3$ thin films and corresponding Au surfaces of the full devices. Adapted from Supplemental information of Ref.[27] with permission of Elsevier.

in Figure 5.3). The produced spots size is up to several hundreds of micrometers for the longest vacuum times ≥ 60 s. We further confirm these spots are indeed voids within the

interfaces between the HTL and perovskite layer (Figure 5.3) *via* cross-sectional scanning electron microscopy (SEM) images in Figure 5.4. These voids are a general phenomenon also observed in other mixed-cation perovskites containing DMSO solvent even for PSCs with a high photovoltaic performance,[80,171,189,196] and are more evident in large-area and thick perovskite films.[189] J. Huang and coworkers discovered that the voids near the substrates/perovskite interface stem from volume collapse at sites where trapped high–boiling-point DMSO would eventually escape from the film, especially during and after annealing.[189] The crystallization of perovskite films starts from the top surface as the solvents evaporates faster than at the inner interface and thus form a solid film to restrict the rest of DMSO inside the film. During the VAG process, for a short vacuum time < 30 s the wet perovskite films are not dried enough and would trigger some cracks and corresponding voids. For a too long vacuum time > 30 s, the solid film formed at the perovskite surface and restricts more DMSO solvent at the interfaces of 2PACz/$FAPbI_3$. Thus, a longer vacuum time induces an even higher concentration of voids with larger dimensions. For an optimal vacuum time of 30 s, the extraction of the high boiling solvents (such DMSO) and the solidification of the perovskite thin film are in balance. As a result, a homogenous and void-free perovskite thin film with relatively big grains is formed, as is further demonstrated in a thorough investigation of the thin film morphology in Figure 5.5 using SEM and atomic

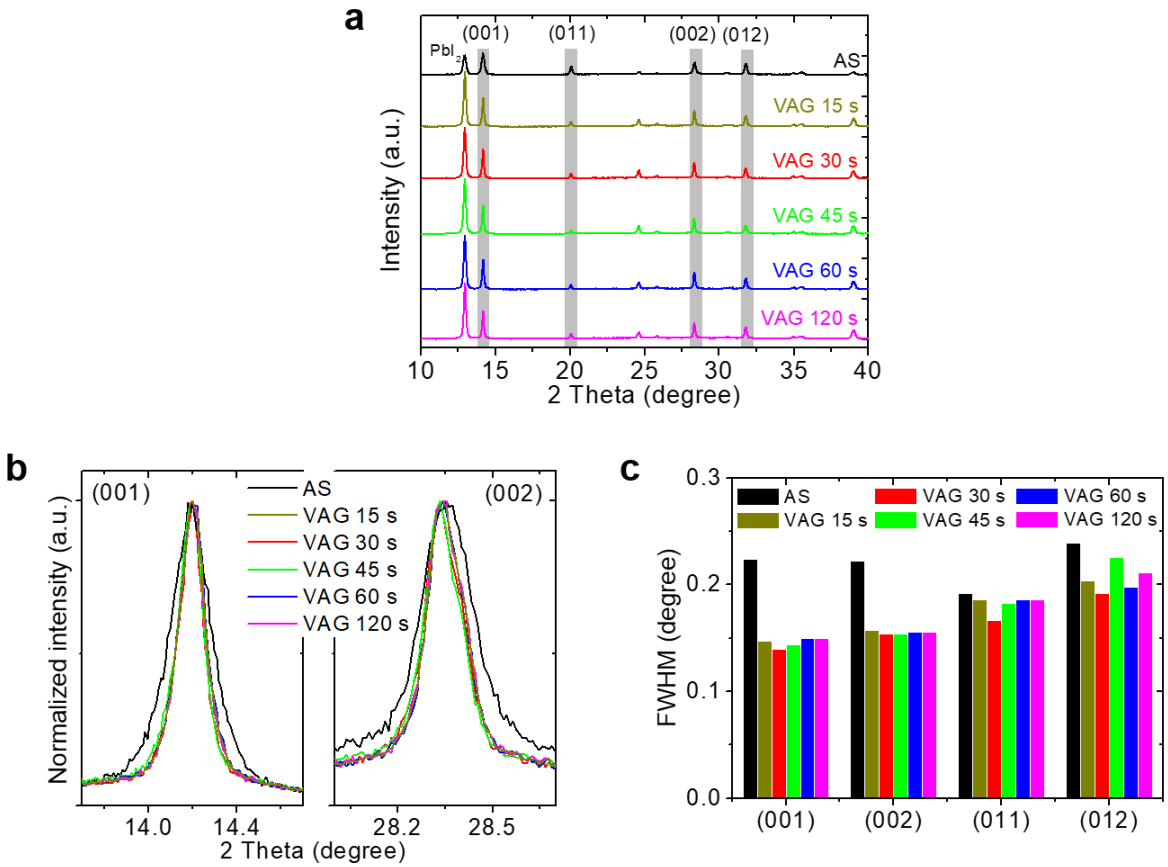

Figure 5.7. (a) X-ray diffraction patterns (XRD), (b) zoom-in peaks of (001) and (001) planes, and corresponding full width at half maximum (FWHM) for $FAPbI_3$ perovskite thin films. Reproduced from Ref.[27] with permission of Elsevier.

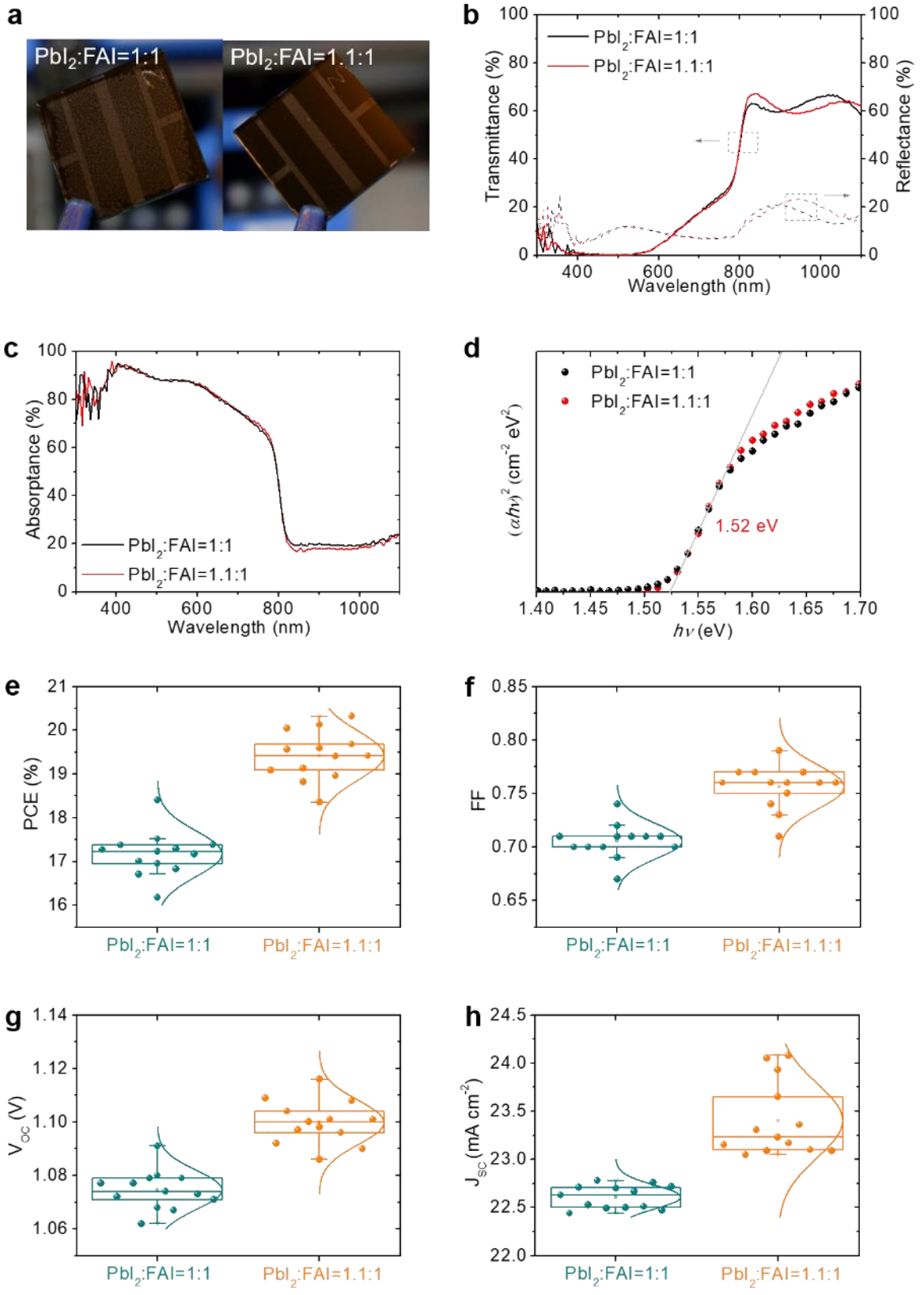

Figure 5.8. (a) Photographs (substrate dimension: 1.6 × 1.6 cm^2), (b) transmittance & reflectance, (c) absorptance spectra, and (d) Tauc-plots of $FAPbI_3$ thin films. Statistical distribution of PV performance: (e) PCE, (f) FF, (g) V_{OC}, and (h) J_{SC}. The devices were fabricated with VAG process with PbI_2/FAI ratio of 1 M : 1 M and 1.1 M : 1 M. Reproduced from Supplemental information of Ref.[27] with permission of Elsevier.

force microscopy (AFM). We highlight that these cracks in the perovskite thin films in case of AS and VAG 15 s (see in Figure 5.6) are a result of an insufficient solvent extraction, which also causes associated voids during the annealing stage.

X-ray diffraction (XRD) was performed to analyze the crystal structures of the fabricated perovskite films. The α-phase was produced during annealing the $FAPbI_3$ thin films, according to the expected diffraction peaks of (001), (011), (002), and (012) in the XRD patterns (see Figure 5.7a).[170,176] The reduction of the full width at half maximum (FWHM) for the diffraction peaks in case of VAG thin films reflects the improved crystal sizes compared to AS thin films (Figure 5.7b and 5.7c). In particular, VAG 30 s thin films exhibit the narrowest diffraction peaks in (001) and (002) planes (VAG 30 s: $FWHM_{(001)} = 0.140°$, $FWHM_{(002)} = 0.154°$; AS: $FWHM_{(001)} = 0.224°$, $FWHM_{(002)} = 0.222°$) indicating larger crystallites (Figure 5.7b).

An evident PbI_2 peak is found in the obtained XRD results (see Figure 5.7a). This arises from the incorporation of 10 mol% excess PbI_2 as an integral component of the standard recipe employed for the preparation of the perovskite precursor. Notably, the excess PbI_2 has been used as a means to reduce trap states within the *p-i-n*-based FAPbI3 PSCs.[74] It should be highlighted that the strategic introduction of excess PbI_2 serves as the pivotal

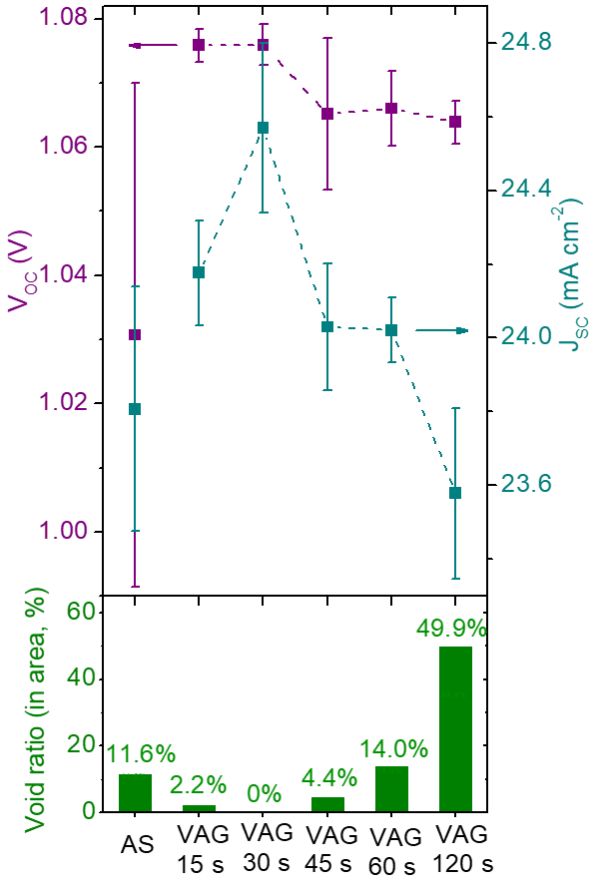

Figure 5.9. The impact of void ratio (in area) on V_{OC}, and J_{SC} of PSCs. Reproduced from Ref.[27] with permission of Elsevier.

purpose of achieving void-free $FAPbI_3$ thin films (Figure 5.8.a). In this regard, it is imperative to emphasize that the introduction of excess PbI_2 does not change the light-harvesting characteristics or the inherent bandgap of the perovskite thin films (Figure 5.8b−5.8d). Rather, its impact manifests through the substantial enhancement in device performance parameters, *i.e.*, FF, V_{OC}, and J_{SC} (see Figure 5.8e−5.8h).

The buried voids are considered to act as insulating barriers between HTL and perovskite thin film, demonstrating a direct influence on device performance as already discussed above (Figure 5.1c). This is because voids impede efficient extraction, leading to a noticeable reduction in current generation from the device. Furthermore, these voids contribute to a decrease in voltage, primarily attributed to non-radiative recombination losses resulting from trap states accumulating at the surfaces of these voids. Thus, we caculate the void ratio of AS- and VAG-$FAPbI_3$ thin films and further link it to V_{OC} and J_{SC} of PSCs in the following (Figure 5.9). For VAG times $\leqslant$ 45 s, a void ratio of < 5% is observed for VAG-$FAPbI_3$ thin films (in area, see Figure B1), as compared to 11.6% for AS-$FAPbI_3$ thin film. The lower void ratio can be correlated to a higher corresponding V_{OC} and J_{SC} in PSCs, especially in case of void-free PSCs for the optimum vacuum time of 30 s. With further increasing vacuum time up to 120 s, the void ratio increases to 49.9% due to apparently expanded size and increased number of voids as discussed before (Figure 5.9 and B1). The high void ratio is supposed to reduce the bottom contact area between HTL and $FAPbI_3$ active layer at the buried interface which can induce non-radiative recombination loss and poor charge extraction, as will be discussed in section 5.5.

5.4. Characteristics of non-radiative recombination

The above results demonstrate that VAG is an efficient route to fabricate high-efficiency *p-i-n*-based $FAPbI_3$ PSCs with improved buried interfaces and film quality, which has a direct influence on the photovoltaic performance, *i.e.*, V_{OC} (associated with non-radiative recombination) and J_{SC} (related to charge extraction). To investigate the influence of the interfaces and perovskite quality on V_{OC} in more detail, we conducted a series of material and photo-physical characterizations. We first applied time-resolved photoluminescence (TRPL) to understand the charge-carrier dynamics for a half-layer stack of PSC. $FAPbI_3$ thin films were fabricated on ITO/AlO_x (AlO_x was fabricated by atomic layer deposition (ALD) as an insulating layer) and ITO/2PACz (as an HTL) substrates. Ethylene-vinyl-acetate copolymer was used for encapsulation against moisture ingress on top of $FAPbI_3$ thin films. As shown in Figure 5.10a, the AlO_x/$FAPbI_3$ layer stack exhibits a mono-exponential decay and the fitted value of charge-carrier lifetime τ is dominated by non-radiative recombination at the bulk and grain boundaries of $FAPbI_3$ thin films.[16,80,131] Compared to AS thin films, we observe a slight increase in τ from 425 ns to 465 ns for VAG 30 s thin films. This suggests a reduction of trap-assisted non-radiative recombination in the perovskite films. This variation in τ could be related to the larger grain size with fewer grain boundaries of perovskite thin film.[131] With an addition of the HTL as a potential quencher, the 2PACz/$FAPbI_3$ layer sequence exhibits a bi-exponential decay and the corresponding charge-carrier lifetimes τ_1 and τ_2 denote the fast and slow lifetime constants, respectively

(Figure 5.10b). Here, τ_1 can be associated with either trap-filling processes and/or charge transfer from perovskite to 2PACz, while the non-radiative recombination at grain boundaries and the bulk and/or 2PACz/$FAPbI_3$ buried interface is related to τ_2.[16,151,157,197] It is a remarkable highlight that τ_2 of 730 ns for VAG 30 s thin films is significantly higher than 266 ns for AS thin films (see Table 5.1). The significantly increased lifetime is mostly ascribed to the decreased non-radiative recombination at the interface of 2PACz/$FAPbI_3$ due to the decreased interfacial defects from voids, according to the comparison in Figure 5.10a.[73]

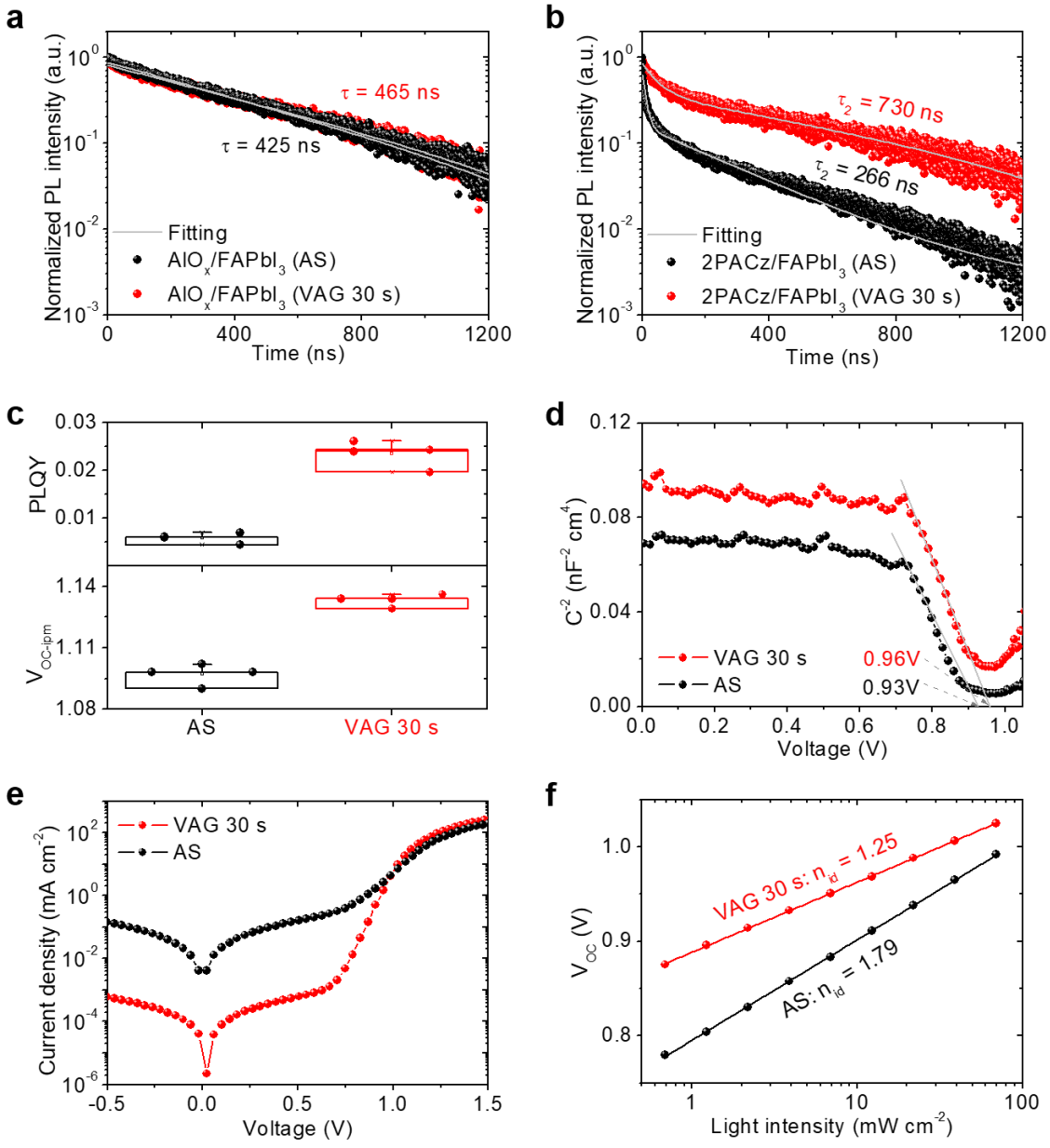

Figure 5.10. Time-resolved photoluminescence (TRPL) for $FAPbI_3$ thin films based on (a) ITO/AlO_x (AlO_x fabricated with ALD) and (b) ITO/2PACz glass substrates. (c) Photoluminescence quantum yield (PLQY) and the corresponding implied V_{OC} ($V_{OC\text{-}imp}$) of ITO/2PACz/$FAPbI_3$ stacks. (d) Mott–Schottky plots, (e) dark current-density–voltage (J–V) characteristics, and (f) light intensity dependence of the V_{OC} of PSCs. Reproduced from Ref.[27] with permission of Elsevier.

Table 5.1. Summary of time-resolved photoluminescence (TRPL) measurements. Adapted from Supplemental information of Ref.[27] with permission of Elsevier.

Samples	τ_1 (ns)	Fraction 1	τ_2 (ns)	Fraction 2	τ_{avg} (ns)
$AlO_x/FAPbI_3$ (AS)	-	-	-	-	425
$AlO_x/FAPbI_3$ (VAG 30 s)	-	-	-	-	465
$2PACz/FAPbI_3$ (AS)	11	0.759	266	0.241	72
$2PACz/FAPbI_3$ (VAG 30 s)	49	0.533	730	0.467	390

The data were fitted with a mono-exponential equation: $Y = A \exp(-t/\tau)$, and bi-exponential equation: $Y = A_1 \exp(-t/\tau_1) + A_2 \exp(-t/\tau_2)$. τ_1 and τ_2 reveal a fast lifetime and a slow lifetime, respectively.

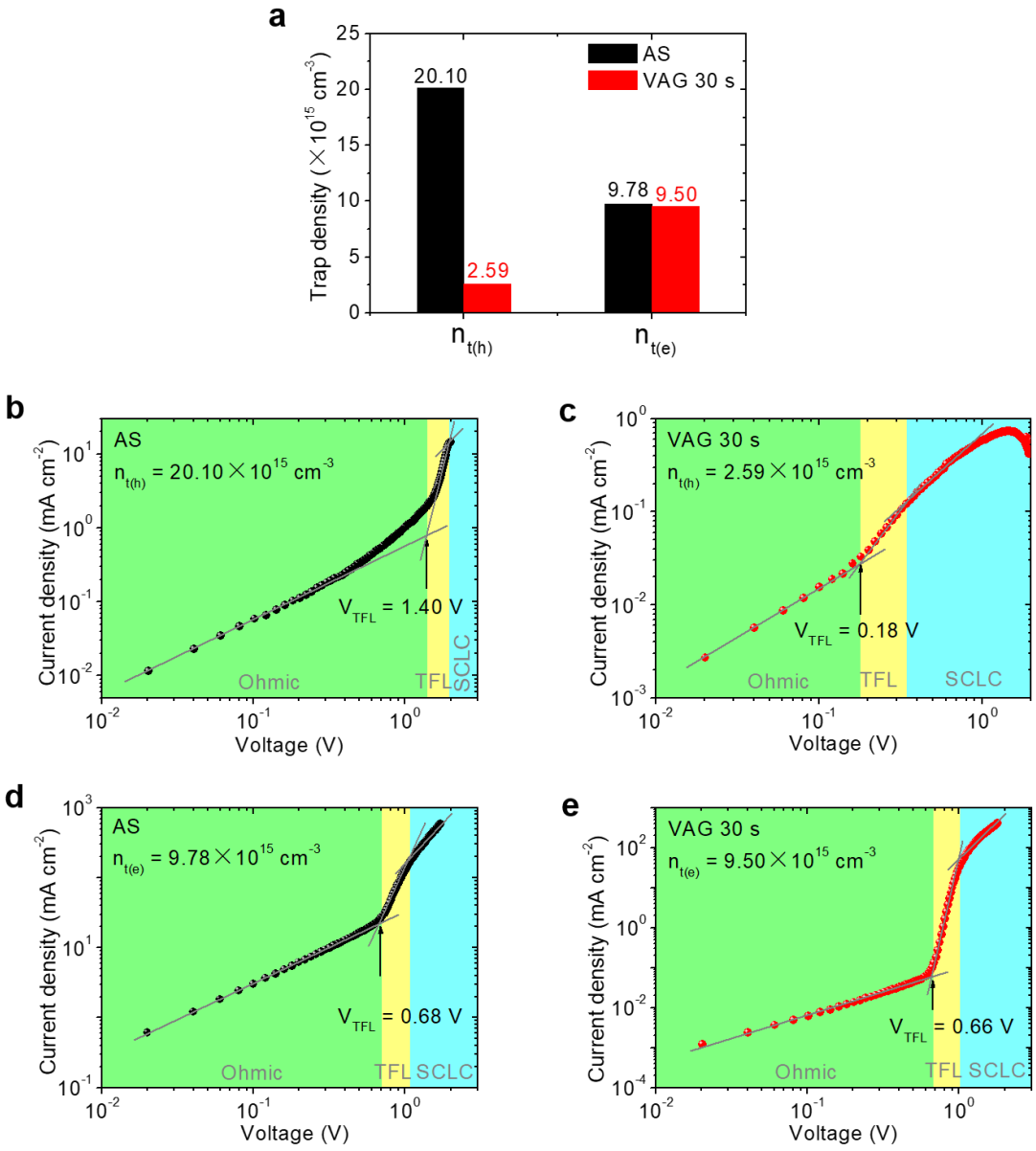

Figure 5.11. (a) Hole ($n_{t(h)}$) and electron trap density ($n_{t(e)}$) evaluated from space-charge-limited current (SCLC) method. Dark *J-V* characteristics of (b), (c) hole- and (d), (e) electron-only devices. V_{TFL} is a kink point. Reproduced from Ref.[27] with permission of Elsevier.

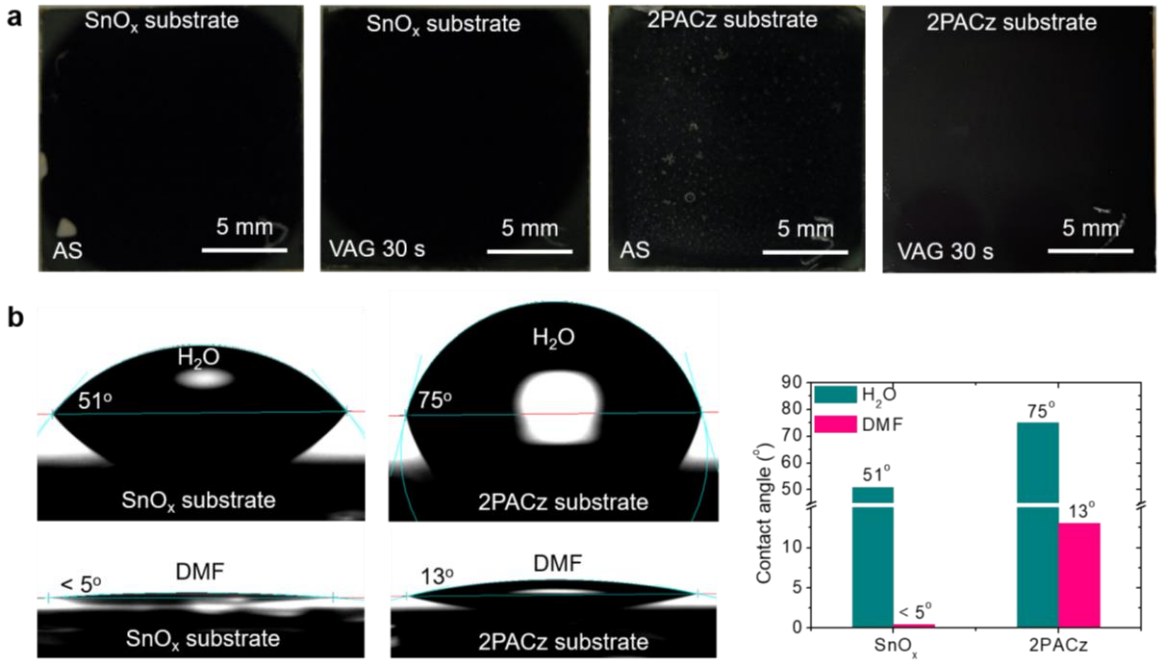

Figure 5.12. (a) Photographs (glass side, substrate dimension: 1.6 × 1.6 cm^2) and (b) contact angles of spin-coated $FAPbI_3$ thin films fabricated on ITO/SnO_x and ITO/2PACz substrates. Adapted from Supplemental information of Ref.[27] with permission of Elsevier.

To further quantify the reduction in non-radiative recombination within the half-layer stack consisting of ITO/2PACz/$FAPbI_3$, we conducted photoluminescence quantum yield (PLQY) measurements and determined the corresponding implied open-circuit voltage ($V_{OC\text{-}imp}$) as described in literature.[72,73] As illustrated in Figure 5.10c, the VAG 30 s sample has a PLQY increase of one order of magnitude to around 2.3×10^{-2} compared to the AS sample with an average PLQY of 5.8×10^{-3}. The notable rise in average $V_{OC\text{-}imp}$ from 1.097 V to 1.133 implies a reduction in non-radiative recombination for the VAG 30 s sample. It is noteworthy that this absolute enhancement aligns closely with the observed average increase in V_{OC} within the PSCs (Figure 5.1c). This further suggests that the enhancement of V_{OC} is indeed a consequence of the reduced non-radiative recombination at the buried interface of 2PACz/$FAPbI_3$.

Next, for a more comprehensive investigation of non-radiative recombination, complete PSCs are investigated in more detail. Mott–Schottky plots (Figure 5.10d) directly demonstrate a higher flat-band potential of VAG 30 s PSCs (0.96 V) compared with the AS PSC (0.93 V), which implies an increased driving force for photo-generated charge carrier separation that is able to attain a higher V_{OC}.[198,199] The dark current-density-voltage (*J-V*) (Figure 5.10e) and light-intensity dependent V_{OC} measurements (Figure 5.10f) also support this hypothesis. It is evident that the VAG 30 s PSC exhibits significantly lower values for both the dark saturation current density ($J_0 = 4.07 \times 10^{-12}$ mA cm^{-2}) and the ideality factor (n_{id} = 1.25) as compared to the AS PSC ($J_0 = 2.45 \times 10^{-5}$ mA cm^{-2}, n_{id} = 1.79), indicating less trap-assisted non-radiative recombination which is mainly attributed to the discussed improvements at the 2PACz/$FAPbI_3$ interface.[16,161]

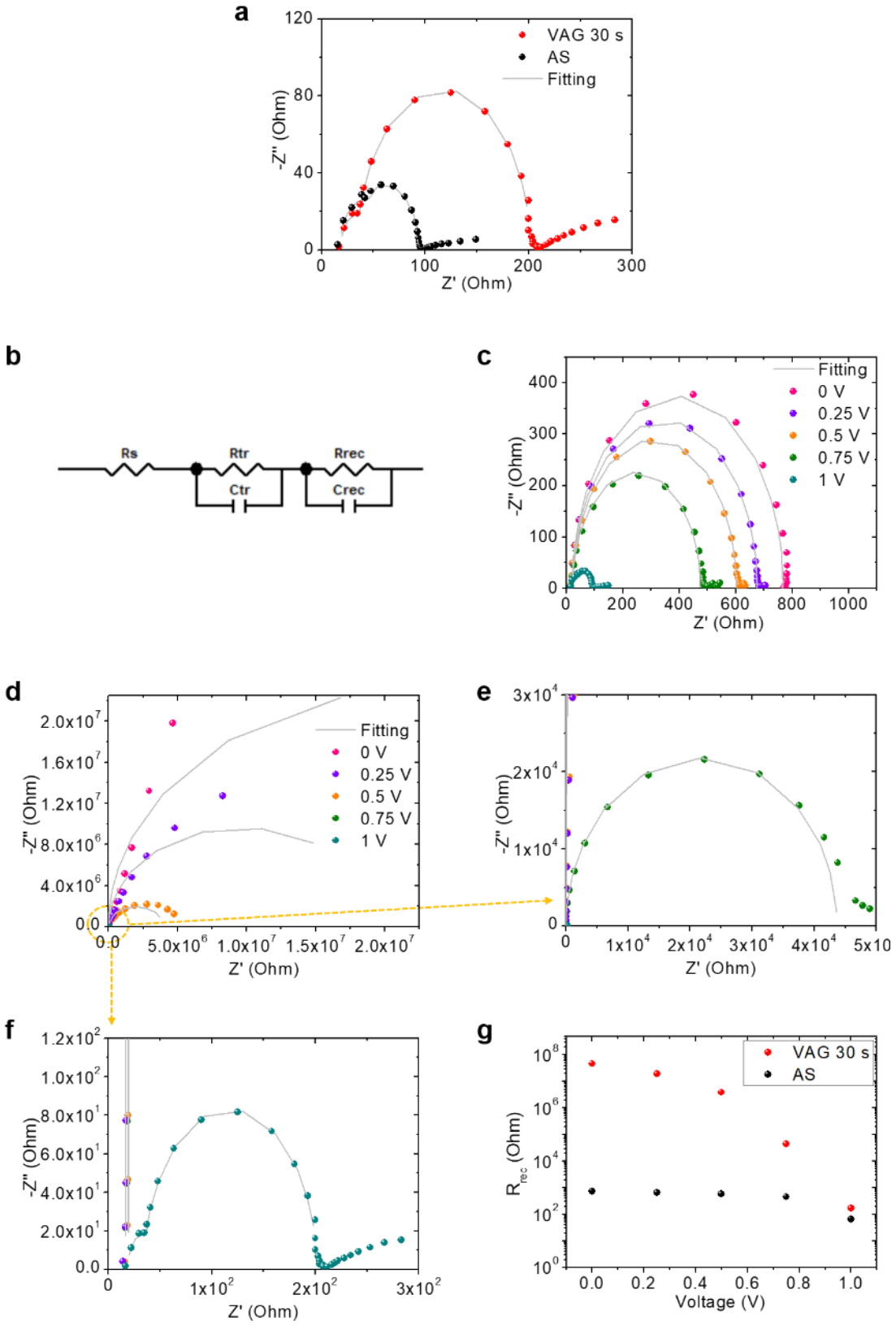

Figure 5.13. (a) Nyquist plots of PSCs measured in the dark with an applied bias of 1 V. (b) The equivalent circuit of the fitting. Nyquist plots measured in the dark with an applied bias varying from 1 to 0 V for PSCs fabricated via (c) AS and (d) VAG methods. (e) and (f) are zoom-in Nyquist plots of (d). (g) Relationship of calculated recombination resistance (R_{rec}) with applied bias. Reproduced from Supplemental information of Ref.[27] with permission of Elsevier.

Table 5.2. Summary of electrical impedance spectroscopy (EIS) measurements. Adapted from Supplemental information of Ref.[27] with permission of Elsevier.

Devices	Applied Voltage (V)	R_s (Ω)	R_{tr} (Ω)	C_{tr} (nF)	R_{rec} (Ω)	C_{tr} (nF)
AS	1	17.3	53.9	8.6	66.7	0.2
	0.75	22.2	-	-	452.8	4.4
	0.5	21.2	-	-	580.4	3.8
	0.25	21.2	-	-	654.4	3.8
	0	20.7	-	-	747.0	3.9
VAG 30 s	1	18.3	38.4	0.1	166.5	0.2
	0.75	19.1	-	-	4.4×10^4	4.1
	0.5	19.8	-	-	3.9×10^6	4.2
	0.25	16.9	-	-	1.9×10^7	4.5
	0	16.8	-	-	4.6×10^7	4.6

R_s: series resistance; R_{tr}: charge transport resistance; C_{tr}: charge transport capacitance R_{rec}: charge recombination resistance; C_{rec}: charge recombination capacitance. All data were fitted by Z-View.

In order to elucidate the underlying mechanisms responsible for the reduction in non-radiative recombination, we further employed space-charge-limited current (SCLC) measurements to assess the trap density (n_t).[16,78–82] As previously discussed, the trap-assisted non-radiative recombination is predominantly influenced by interfacial trap states, which have a more pronounced effect compared to those within the bulk of the perovskite layer (Figure 5.10a–5.10c). These interfacial trap states may originate from defects located at the interfaces of 2PACz/$FAPbI_3$ and/or $FAPbI_3$/C_{60}, which may capture free charge carriers.[80] We specifically fabricated electron- (ITO/2PACz/$FAPbI_3$/C_{60}/BCP/Au) and hole-only (ITO/$FAPbI_3$/Poly(3-hexylthiophen-2,5-diyl) (P3HT)/Au) devices for SCLC studies. Impressively, the hole trap density ($n_{t(h)}$) for the VAG 30 s sample is determined to be 2.59×10^{15} cm^3 (Figure 5.11a), which is an order of magnitude lower compared to AS sample (20.10×10^{15} cm^3). We attribute the high $n_{t(h)}$ in case of AS to a larger number of interfacial voids at the buried interface of 2PACz/$FAPbI_3$, whereas the $n_{t(h)}$ significantly decreases in case of VAG 30 s due to the void-free interface (see Figure 5.3 and 5.4). The buried interface was demonstrated to have a considerable number of defects, related to uncoordinated FA^+ or Pb^{2+} vacancies close to the voids, thus resulting in increased non-radiative recombination losses.[80,185,189] Furthermore, we demonstrate that the electron trap density ($n_{t(e)}$) within the VAG 30 s sample is only marginally lower in comparison to the AS sample. This is linked to the absence of voids at the SnO_x/$FAPbI_3$ interface, a feature common to both AS and VAG methods, coupled with the improved morphology evident in electron-only devices (Figure 5.12a). SnO_x is known to establish a more favorable interfacial contact with perovskite, hence diminishing the occurrence of void-based buried interfaces within the *n-i-p* configuration. Notably, SnO_x exhibits significantly greater hydrophilicity than 2PCAz monolayers (Figure 5.12b). Consequently, the interaction between organic HTLs (*e.g.*, 2PACz) and perovskite during the VAG procedure diverges from the situation when SnO_x are utilized underneath. This interaction can exert an additional influence on perovskite

nucleation and crystallization.[185] Given the consistent surface morphology observed in the $FAPbI_3$ thin films fabricated through the VAG and AS methods, *i.e.*, notably the absence of any changes in formation of the $FAPbI_3/C_{60}$ interface (see Figure 5.5), we deduce that the increased non-radiative recombination losses witnessed in AS PSCs predominantly origins from trap states localized at the 2PACz/$FAPbI_3$ buried interface (see Figure 5.10).

Next, we conducted electrochemical impedance spectroscopy (EIS) in the dark with varied applied bias of 1–0 V (roughly corresponding to conditions ranging from open-circuit to short-circuit) to better understand the transport and recombination of charge carriers within the PSCs.[16,161,162] We first obtained Nyquist plots with an applied bias of 1 V (close to V_{OC}), as shown in Figure 5.13a, which shows two semicircles at low- and high- frequency ranges. We did not take into account in fitting for the transmission line that looks like a straight line at the end of the low-frequency region as the charge-carrier diffusion is neglected in our PSCs. In general, the low-frequency semicircle is attributed to the charge recombination resistance (R_{rec}) at the perovskite bulk or at the interface, and the high-frequency semicircle is associated to charge transport resistance (R_{tr}). The fitted R_{rec} and R_{tr} in an equivalent circuit are shown in Figure 5.13b. It is apparent that the VAG 30 s PSCs exhibit a larger semicircle in the low-frequency range and a smaller semicircle in the high-frequency range. This implies a higher R_{rec} (166.5 Ω) and a lower R_{tr} (38.4 Ω) for the VAG 30 s PSCs in comparison to the AS PSCs (R_{rec} = 66.7 Ω, R_{tr} = 53.9 Ω) (see Figure 5.13a). These results conclusively signify a reduction in recombination and improved charge transport within the VAG 30 s PSCs. Further evidence for reduced recombination is discernible under different applied biases ranging from 1 to 0 V, as illustrated in Figure 5.13c−5.13f). The VAG 30 s PSCs exhibit remarkable higher R_{rec} (4.4×10^4–4.6×10^7 Ω) compared to the AS PSCs (452.8−747.0 Ω), as shown in Figure 5.13g and Table 5.2.

All the data derived from EIS align with the aforementioned results of TRPL, PLQY, Mott–Schottky, dark *J-V* characteristics, light-intensity dependent V_{OC} measurements, and SCLC analyses. In short summery, these findings highlight the optimized VAG process in enhancing the buried interfaces through the elimination of interfacial voids, thereby facilitating efficient charge transport and minimizing non-radiative recombination losses.

5.5. Characteristics of charge extraction

After demonstrating the correlation between the V_{OC} and non-radiative recombination, we investigate the impact of interfacial voids on charge extraction that is associated to the J_{SC}. We start with charge extraction (CE) measurements at varied illumination intensity (1−100 mW cm^{-2}) to evaluate the extracted charge-carrier density (n_{CE}). The initial process involves illuminating the device under open-circuit conditions, where no current is generated within the device. Subsequently, the illumination is switched off at t = 0 s, and meanwhile, a negative extraction voltage is applied. This procedure allows for the extraction of nearly all the excited charge carriers, thereby inducing a transient current. The determination of n_{CE} entailed the integration of the entire extracted current.[97–99] In comparison to the AS PSCs, our observations reveal a greater current extraction efficiency for the VAG 30 s PSCs,

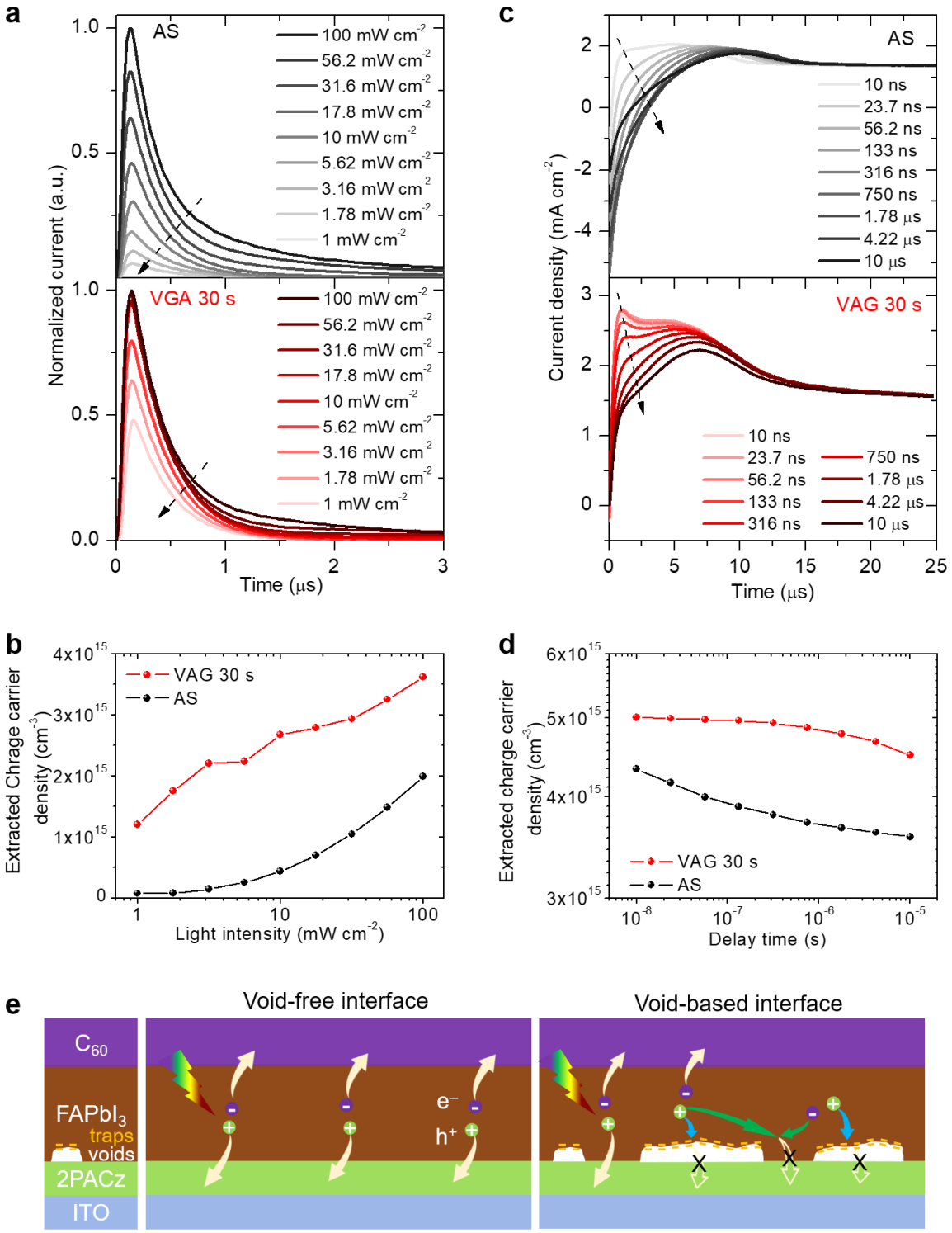

Figure 5.14. Charge extraction (CE) measurement at varied illumination intensities (1–100 mW cm^{-2}): (a) transient current *vs.* time profile and (b) extracted charge-carrier density. Delay-time-CELIV characterization with different delay time at a constant illumination intensity of 100 mW cm^{-2}: (c) Transient current density *vs.* time profile and (d) extracted charge-carrier density. (e) Schematic illustration of the charge extraction within PSCs based on void-free and void-based interfaces. Adapted from Ref.[27] with permission of Elsevier.

particularly under conditions of low light intensity (< 10 mW cm^{-2}) (Figure 5.14a and 5.14b). Additionally, it is observed that the transient current rapidly achieved its maximum value

when the light intensity exceeded 10 mW cm^{-2}. In summary, the calculated n_{CE} for the VAG 30 s PSCs consistently surpasses that of the AS PSCs across a range of illumination intensities (Figure 5.14b), thus demonstrating an enhancement in charge-carrier extraction.

Delay-time charge extraction by linearly increasing voltage (Delay-time-CELIV) was performed to further validate the enhancement of charge-carrier extraction in the VAG 30 s PSCs. This method provides insights into the dynamic processes of charge-carrier extraction and recombination, and it has been previously applied to both organic solar cells[100–102] and PSCs.[103–105] The initial step involves illuminating the device with a fixed light intensity of 100 mW cm^{-2} under open-circuit conditions to prevent any net current flow. Subsequently, the illumination is switched off, and the device remains at open-circuit conditions during a designated delay time. After this delay period, a linearly negative ramp voltage is applied at t = 0 s. The calculation details of charge-carrier density (n_{CELIV}) are described in section 3.3.2. AS PSCs show a single peak in a broader range observed at lower delay-time scales (< 50 ns). The extraction of photo-generated charge carriers reaches its maximum rate within 5–11 µs (Figure 5.14c). For VAG 30 s PSC, (1) two peaks are observed under lower delay-time scales (< 300 ns) where the first one reaches the maximum charge extraction rate at t < 2 µs and (2) only peak reaching the maximum charge extraction rate within 5–7 µs is observed under longer delay-time scales (300 ns–10 µs) (Figure 5.14c). It is hypothesized that longer delay times correspond to a severe charge-carrier recombination, thus resulting in a lower n_{CELIV} (see Figure 5.14d). We highlight that the n_{CELIV} for VAG 30 s PSC is always higher than that of AS PSC (Figure 5.14d) under different delay-time scales, aligning with the trend observed in the CE data (Figure 5.14b). In short summary, the data presented above demonstrate improved charge extraction within the devices processed *via* the developed VAG method.

Finally, we propose and discuss a possible pathway of charge extraction process in the PSCs (Figure 5.14e). In case of a void-free interface (*e.g.*, VAG 30 s PSCs), photo-generated charge carriers (electrons or holes) could be extracted efficiently by the ETL or HTL (Figure 5.14a). This perfect bottom contact (especially for the HTL/perovskite buried interface) results in a higher charge extraction ability which is reflecting in higher values of n_{CE} and n_{CELIV} for VAG 30 s PSCs as compared to AS PSCs (Figure 5.14b and 5.14d). In case of a void-based interface (*e.g.*, AS, VAG-60-s, and VAG-120-s PSCs, see Figure 5.3, 5.9, and B1), the hole extraction paths are somehow blocked by voids or generated holes need to travel a significantly longer path to reach the HTL, resulting in a lower n_{CE} and n_{CELIV} (Figure 5.14b and 5.14d). In addition, the large microstructure of voids in the buried interface easily accumulates numerous trap states.[74,185] The charge carriers, especially the holes, could be captured by the high density of traps around the voids (Figure 5.11), and/or recombine with free electrons in the diffusion paths (Figure 5.14e). We conclude that a higher void ratio results in an enhanced non-radiative recombination and poor charge extraction, thus leading to a lower V_{OC} and J_{SC} in PSCs (Figure 5.9 and B1).

5.6. Blade-coated perovskite thin films and scalable solar cells

In this section, we present PSCs fabricated on larger-area substrates (6.4 × 3.2 cm^2) utilizing fully scalable deposition processes (blade coating for both 2PACz and $FAPbI_3$ layers, vacuum deposition for C_{60}/Au/MgF_2 layer stack). The main challenge in blade coating based on large substrates is obtaining continuous and uniform perovskite thin films without voids

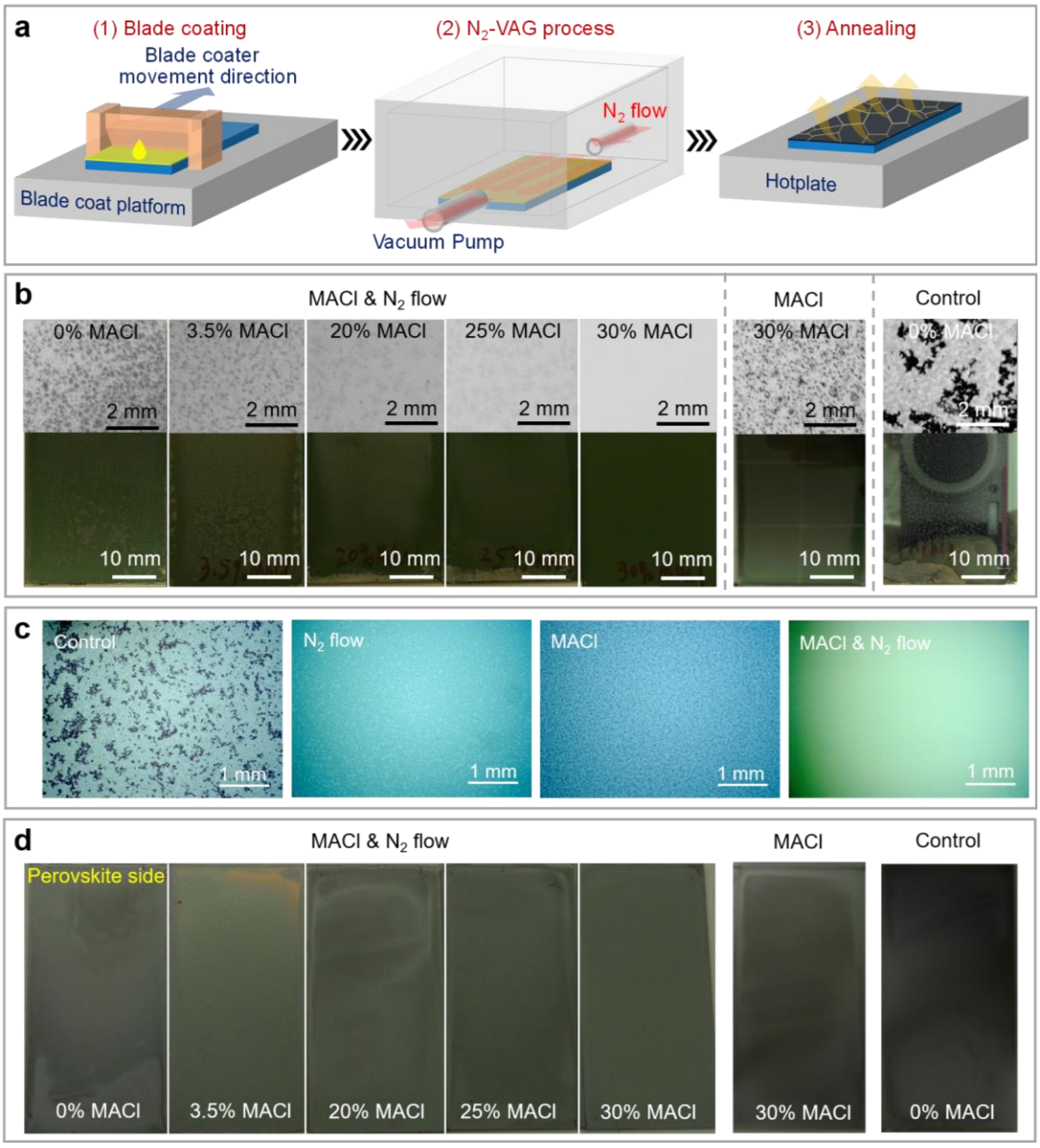

Figure 5.15. (a) Schematic illustration of perovskite fabrication process: blade coating, nitrogen-flow-combined vacuum-assisted growth (N_2-VAG), and post annealing. (b) Photographs and zoom-in optical microscopic images of glass side for bade-coated $FAPbI_3$ thin films (6.4 × 3.2 cm^2). (c) A low resolution of optical microscopic images. (d) Photographs of perovskite surface. The white area in photographs and dark area in microscopic images indicate voids at the buried interface. Reproduced from Ref.[27] with permission of Elsevier.

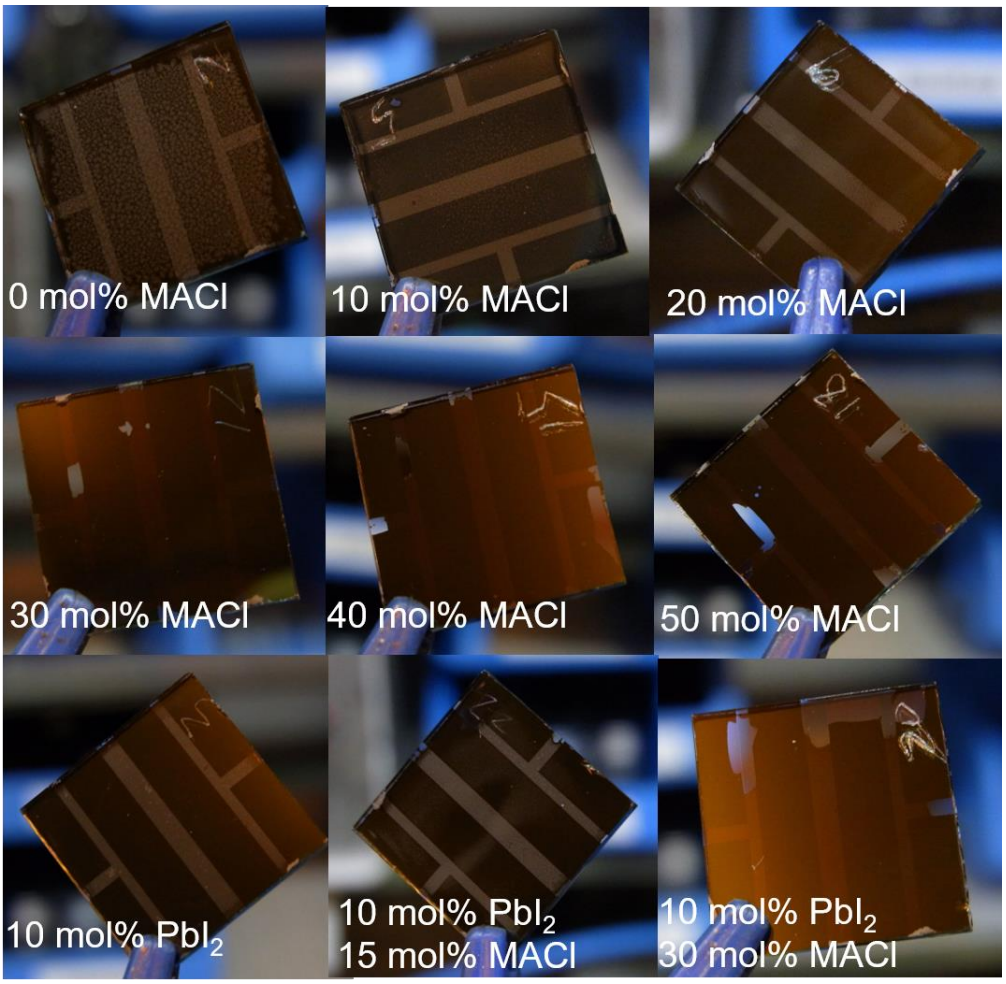

Figure 5.16. Photographs of spin-coated $FAPbI_3$ PSCs based on small substrate dimension of 1.6 × 1.6 cm^2. The PSCs were processed with different excess MACl or PbI_2 using VAG for 30 s vacuum time. Adapted from Supplemental information of Ref.[27] with permission of Elsevier.

at the buried interface. In the case of spin-coated small-area PSCs, the spinning rotation during the spin-coating process already aided in removing a majority of the precursor solution, effectively evaporating a significant portion of the solvents prior to the VAG step. However, when dealing with blade-coated large-area wet perovskite films, it needs several tens of minutes to achieve a fully dried film during the VAG step. As discussed in section 5.3, an extended vacuum time results in the formation of a greater quantity of interfacial voids. Thus, it is inevitable to utilize extra treatments to dry out the blade-coated perovskite ink. We developed a new strategy, namely nitrogen-flow-combined vacuum-assisted growth (N_2-VAG), to speed up the solvent extraction process. This N_2-assisted drying process has been used in our previous work.[17] The fabrication process of $FAPbI_3$ thin films based on large substrate (6.4 × 3.2 cm^2) is shown in Figure 5.15a. As visualized from the glass side in Figure 5.15b and 5.15c, we find a large number of spots (white ones in photographs and black ones in optical microscopic images) in the control films (no N_2 flow and no additives) with millimeter sizes that are considered as voids at the buried interface of HTL/$FAPbI_3$. These interfacial voids are significantly larger than that of spin-coating procedure since blade-coating processing has a low intrinsic rate of extraction of solvents in the absence of

any treatments. This further verifies how easily these voids can be generated in the blade-coating process on large-area substrates.

When N_2 flow (without any additives) was provided, the dimension of the voids decreases but does not eliminate (Figure 5.15b). This demonstrates that the N_2-VAG route is insufficient for producing high-quality, void-free $FAPbI_3$ thin films. To address this issue, we introduced an optimal amount of 30 mol% MACl additive in the perovskite precursor and used N_2 flow (denoted as MACl & N_2 flow), resulting in significant improvement in film quality of $FAPbI_3$ thin film free of voids (Figure 5.15b–5.15d). It has been proved that the containing MACl in precursor compositions induces an intermediate phase during the early drying and nucleation stages and further improve secondary crystallization during the

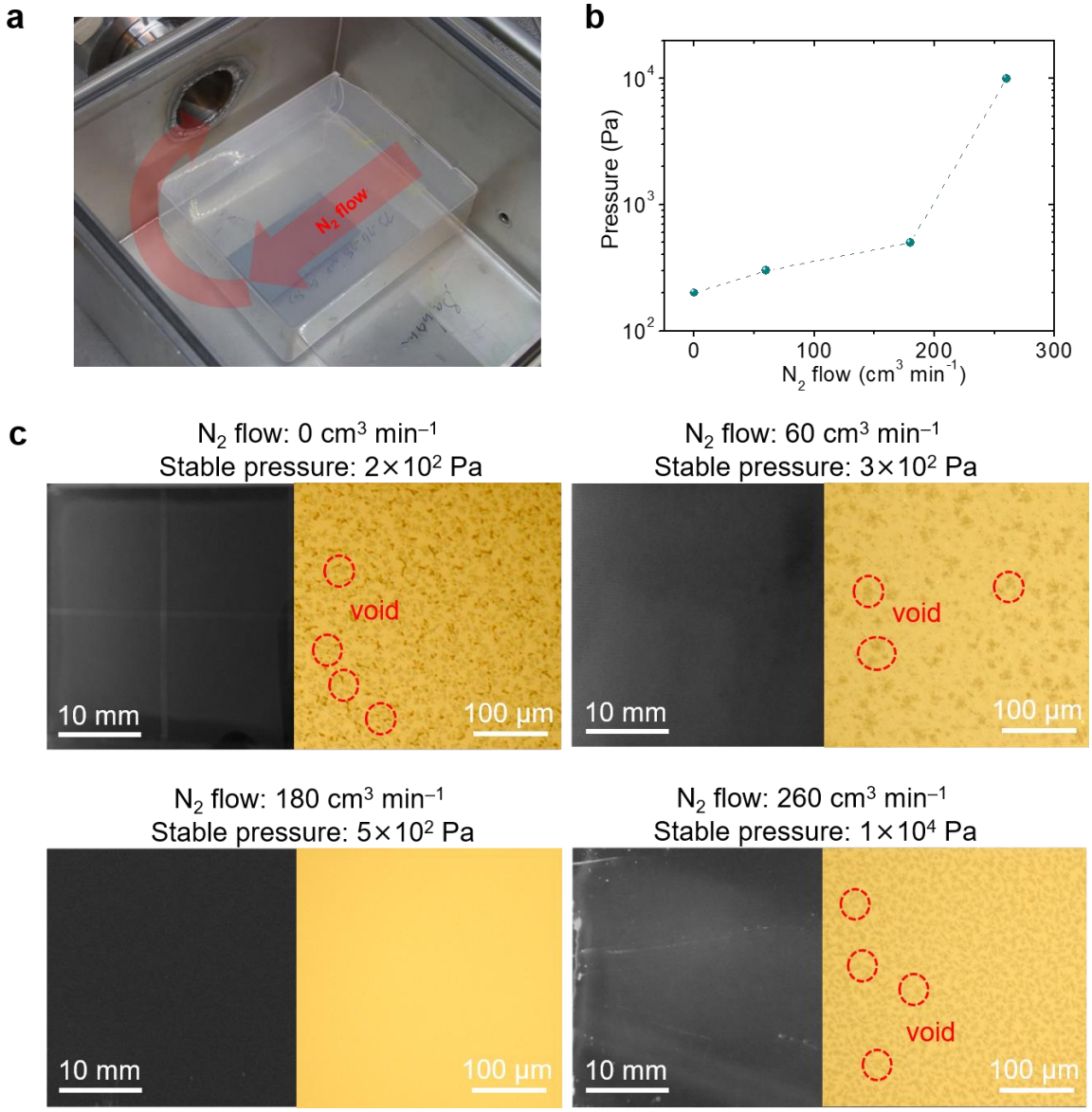

Figure 5.17. (a) Photographs the in-house designed vacuum chamber. (b) Relationship between vacuum pressure and N_2 flow. (c) Photographs and optical microscopic images of blade-coated large-area $FAPbI_3$ thin films (glass side, substrate dimension: 6.4 × 3.2 cm^2) in regulation of different N_2 flow and stable vacuum pressure. Reproduced from Supplemental information of Ref.[27] with permission of Elsevier.

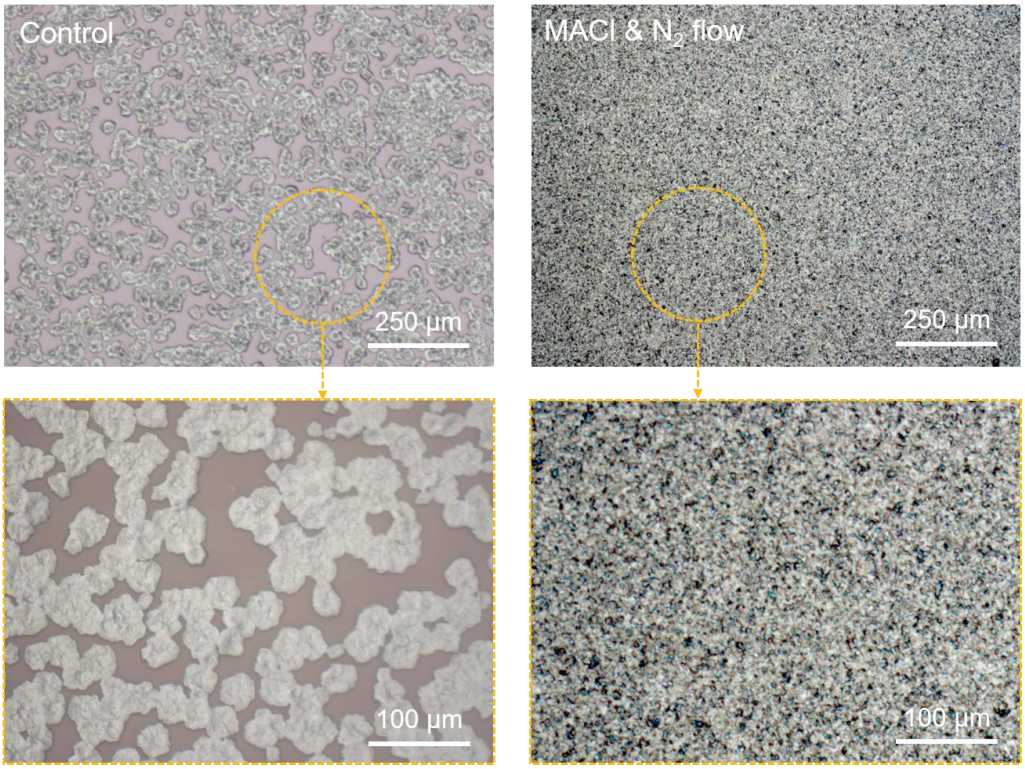

Figure 5.18. Optical microscopic images of the surface of blade-coated large-area $FAPbI_3$ thin films (substrate dimension: 6.4 × 3.2 cm^2). Adapted from Supplemental information of Ref.[27] with permission of Elsevier.

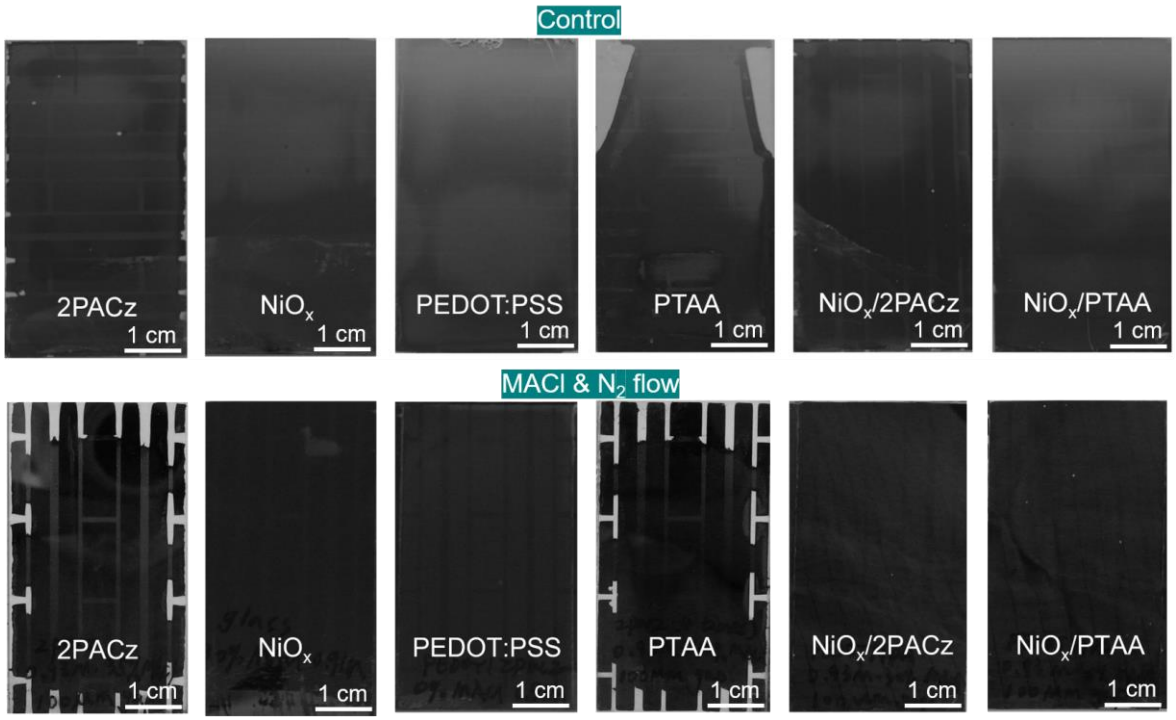

Figure 5.19. Photographs of blade-coated large-area $FAPbI_3$ thin films using control condition (no MACl and no N_2 flow) and optimized MACl & N2 route during VAG process. The perovskite thin films were blade-coated on different HTL substrates (6.4 × 3.2 cm^2): 2PACz, NiO_x, PEDOT:PSS, PTAA, NiO_x/2PACz, and NiO_x/PTAA. Adapted from Supplemental information of Ref.[27] with permission of Elsevier.

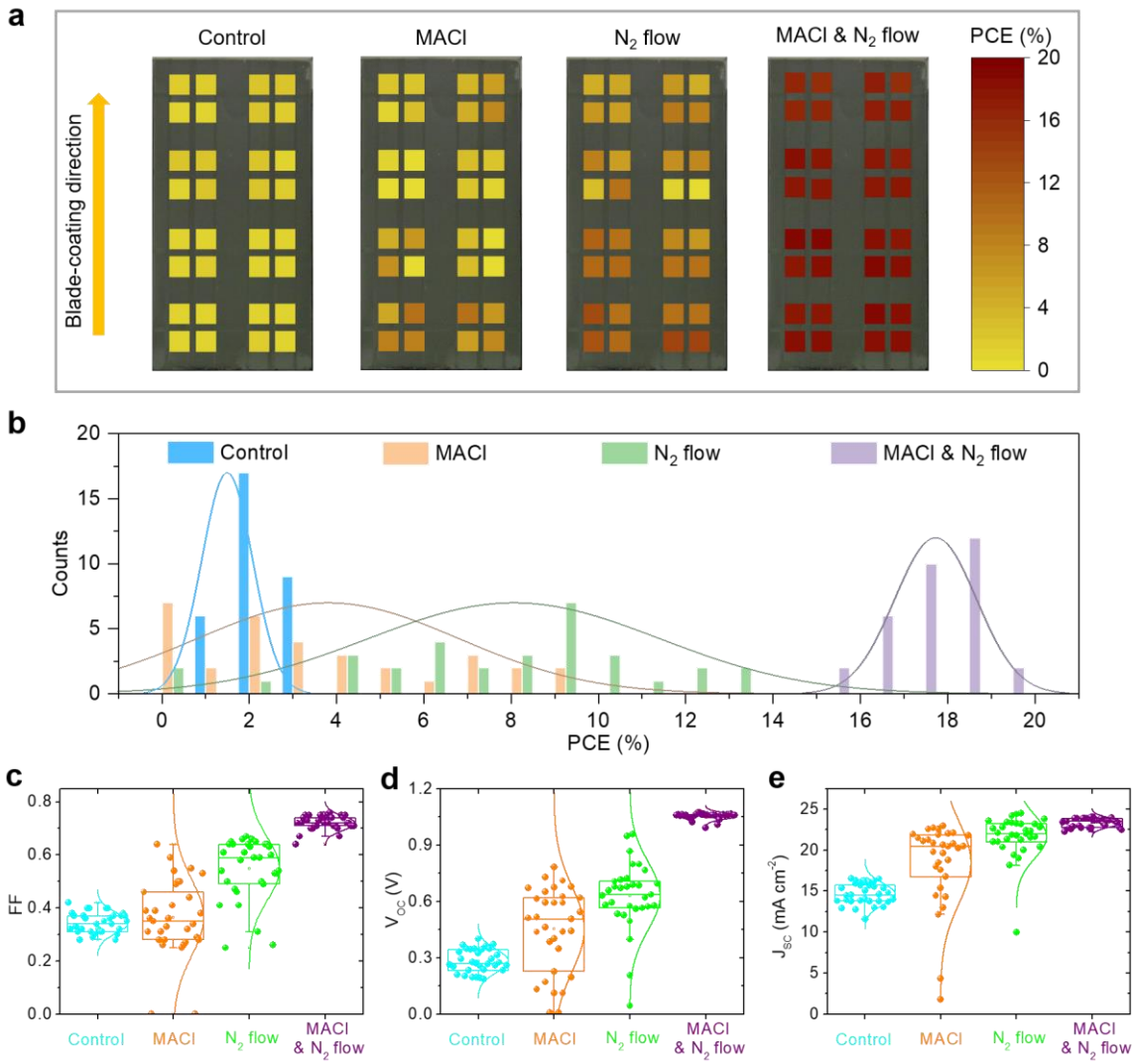

Figure 5.20. The heat map of power conversion efficiency (PCE). Statistical distribution of (b) PCE, (c) fill factor (FF), (d) open-circuit voltage (V_{OC}), (e) short-circuit current density (J_{SC}). Reproduced from Ref.[27] with permission of Elsevier.

post annealing process, facilitating the growth of high-quality $FAPbI_3$ thin films.[74,171] This explains the further promoted film quality via employing MACl for blade-coated large-area $FAPbI_3$ thin films. We observe that a lower MACl concentration less than 30 mol% similarly results in an inhomogeneity and severe interfacial voids within blade-coated $FAPbI_3$ thin films (Figure 5.15b–5.15d). For various MACl concentrations, we notice similar phenomenon in spin-coated small-area PSCs (see Figure 5.16). As shown in Figure 5.15b–5.15d, we find that using 30 mol% MACl without employing a N_2 flow still remains interfacial voids for blade-coated $FAPbI_3$ thin films. To expedite the removal of solvents during the VAG step, we meticulously well-controlled and optimized both the N_2 flow rate (~180 cm^3 min^{-1}, see Figure 5.17) and the vacuum time (30 s) for the processing of large-area substrates (see Figure 5.17–5.19). It is crucial to note that an inadequate or excessively high N_2 flow rate leads to a higher void density and an inhomogeneity (Figure 5.17c and 5.18). Achieving an optimal rate of solvent extraction through N_2 flow assists in enhancing nucleation and crystallization, forming an intermediate phase that subsequently aids the

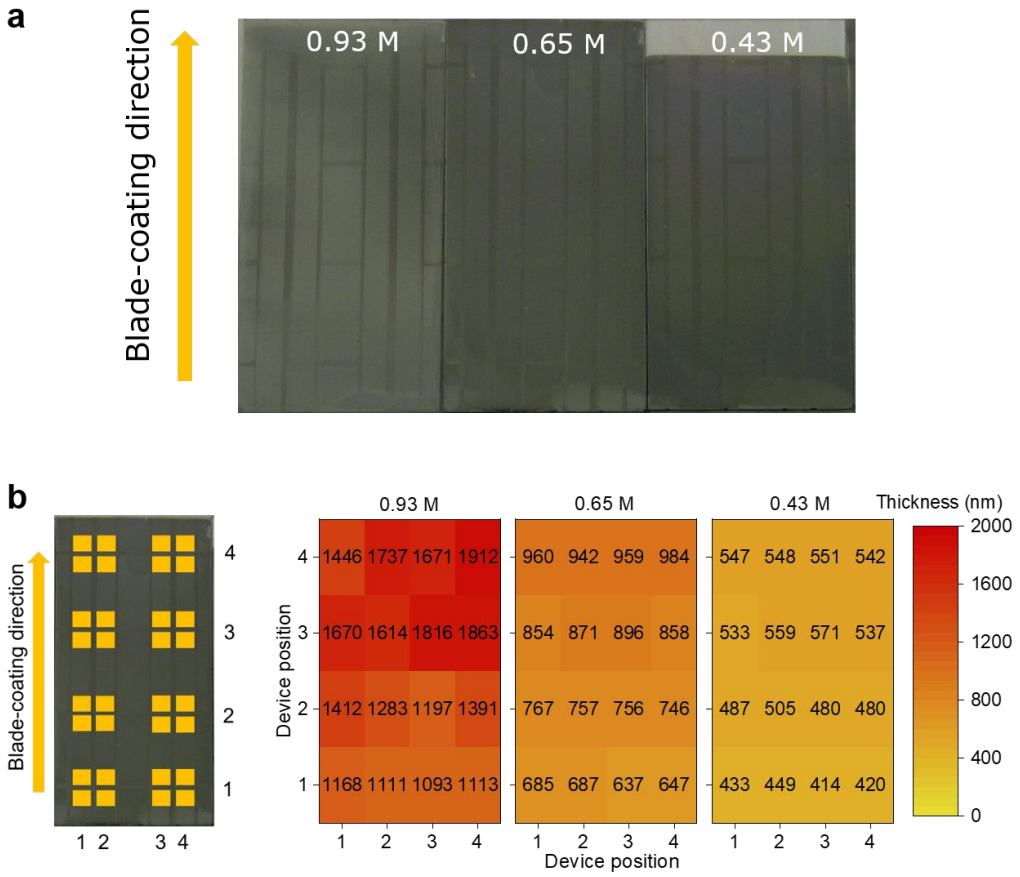

Figure 5.21. (a) Photographs and (b) heat map of thickness variation for the blade-coated $FAPbI_3$ based on ITO/NiO_x/2PACz substrate (6.4 × 3.2 cm^2) using varied precursor concentration. Adapted from Supplemental information of Ref.[27] with permission of Elsevier.

growth of the desired α-phase $FAPbI_3$ during the thermal annealing process. We conclude that the absence of MACl or N_2 flow results in the formation of numerous voids, pinholes, and inadequate coverage as evidenced in Figure 5.15c, 5.17c, and 5.18). We further illustrate that by employing the optimized MACl & N_2 flow route we can produce high-quality, void-free $FAPbI_3$ thin films on various HTLs, such as NiO_x, poly(3,4-ethylenedioxythiophene)-poly(styrenesulfonate) (PEDOT:PSS), and poly[bis(4-phenyl)(2,4,6-trimethylphenyl)amine] (PTAA), as depicted in Figure 5.19).

In summary, we have successfully achieved the fabrication of high-quality and uniform blade-coated large-area $FAPbI_3$ thin films through an optimized MACl & N_2 flow route. This approach proves to be highly effective for scaling up perovskite photovoltaics on various HTLs (as shown in Figure 5.18 and 5.19).

We then assess the PCEs of scalable PSCs. 5 nm thickness of sputtered NiO_x was used beneath of 2PACz (the patterned width was 1.5 mm, see Figure 5.19) to avoid the de-wetting issue during the blade-coating procedure. Other layers were in the same with spin-coated PSCs. A large substrate with 6.4 × 3.2 cm^2 dimension was divided into 32 small PSCs with dimension of 1.6 × 1.6 cm^2. Figure 5.20a depicts the heat map of PCEs for each divided PSC, showing the distribution at various position of a large substrate. All control PSCs (no

N_2 flow and no MACl) show very poor PCE < 3% due to many voids and low perovskite coverage on top of ITO/NiO_x/2PACz substrate. (Figure 5.15c and 5.18). The MACl-only or N_2-flow-only routes improve PCEs but still <15% in a wide range of distribution (see Figure 5.20b). The key constraints of the PV performance (see Figure 5.20c–5.20e) are the low V_{OC} and FF, which is related to the non-radiative recombination loss caused by the interfacial voids. We optimized the concentration of perovskite precursor to 0.65 M, since a higher concentration led to a large thickness variation in film and a lower concentration resulted in a thinner thin film (Figure 5.21). We highlight that the optimized MACl and N_2- flow route

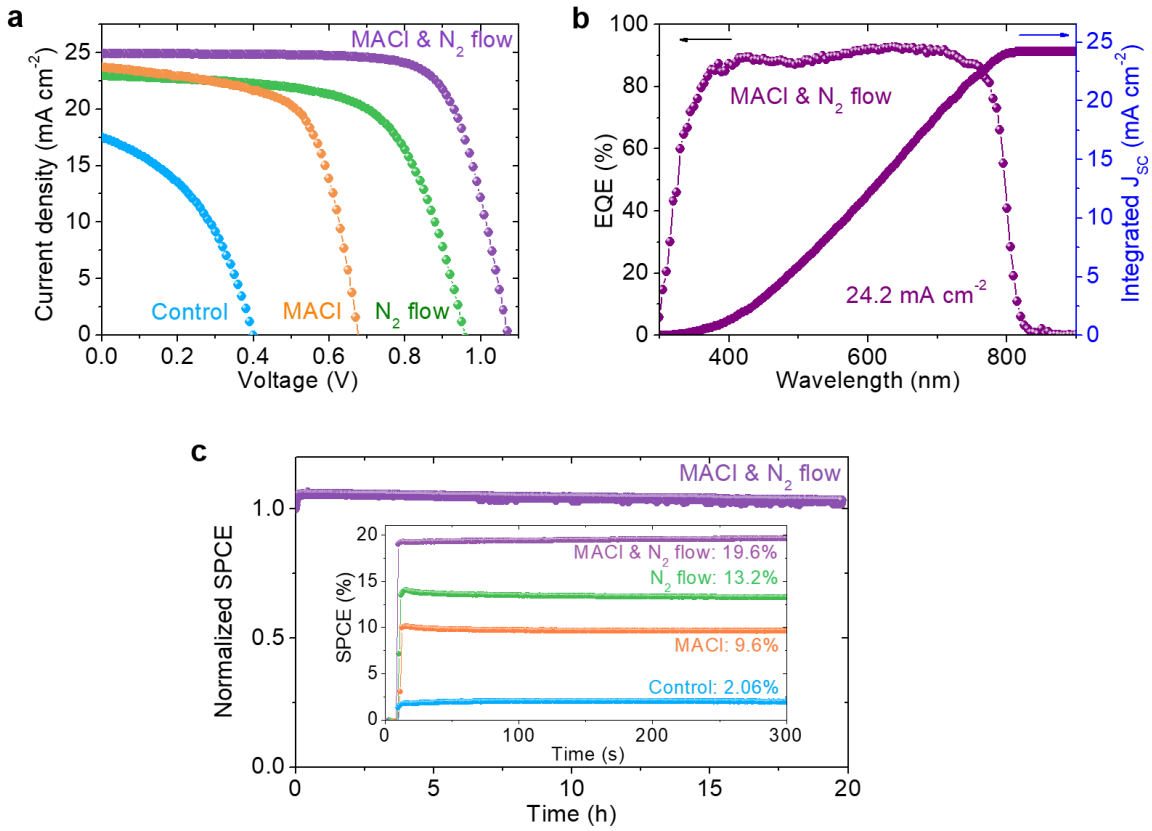

Figure 5.22. (a) Current-density-voltage (*J-V*) characteristics, (b) external quantum efficiency (EQE) spectra, and (c) stabilized power conversion efficiency (SPCE) under continuous illumination for the champion PSCs (with MgF_2 antireflection coating). Reproduced from Ref.[27] with permission of Elsevier.

Table 5.3. Summary of photovoltaic performance for scalable champion PSCs obtained from backward scan under AM 1.5G (100 mW cm^{-2}). Adapted from Supplemental information of Ref.[27] with permission of Elsevier.

	J_{SC} (mA cm^{-2})	V_{OC} (V)	FF	PCE (%)	SPCE (%)
Control	17.5	0.40	0.42	2.9	2.0
MACl	23.7	0.68	0.64	10.3	9.6
N_2 flow	23.0	0.96	0.64	14.1	13.2
MACl & N_2 flow	24.9	1.07	0.75	20.0	19.6

J_{SC}: short-circuit current density; V_{OC}: open-circuit voltage; FF: fill factor; PCE: power conversion efficiency; SPCE: stabilized power conversion efficiency.

enables high PCEs with superior yield and reproducibility (see Figure 5.20c–5.20e). The champion scalable PSC with MgF_2 antireflection layer gives a respective PCE of 20.0% (FF = 0.75, V_{OC} = 1.07 V, J_{SC} = 24.9 mA cm^{-2}, see Figure 5.22a and Table 5.3), which is significantly higher than the that of control (PCE = 2.9%), MACl (PCE = 10.3%), and N_2-flow (PCE = 14.1%). The J_{SC} obtained from EQE (Figure 5.22b) was integrated to 24.2 mA cm^2 that agrees well with the *J-V* result (Figure 5.22b). Moreover, the champion PSC fabricated through the MACl and N_2 flow approach demonstrates an excellent SPCE of up to 19.6% at MPP tracking after 20 h of continuous AM 1.5G irradiation (see Figure 5.22c).

5.7. Scalable modules

In this section, we demonstrate fully scalable $FAPbI_3$ perovskite solar mini-modules. The modules were fabricated with the same design using fully scalable deposition methods as described in section 5.6. As shown Figure 5.23a and 5.23b, the module comprises seven all-laser-scribed interconnected sub-cells, forming a monolithic architecture with a total aperture area of 12.25 cm^2 (Figure 5.23b).[66] The scribing lines P1, P2, and P3 have widths of 44, 50, and 28 µm, respectively (Figure 5.23c). We estimate a GFF of 96.3% based on 5 mm for the designed sub-cell width and the overall width of 184 µm for the dead region (see

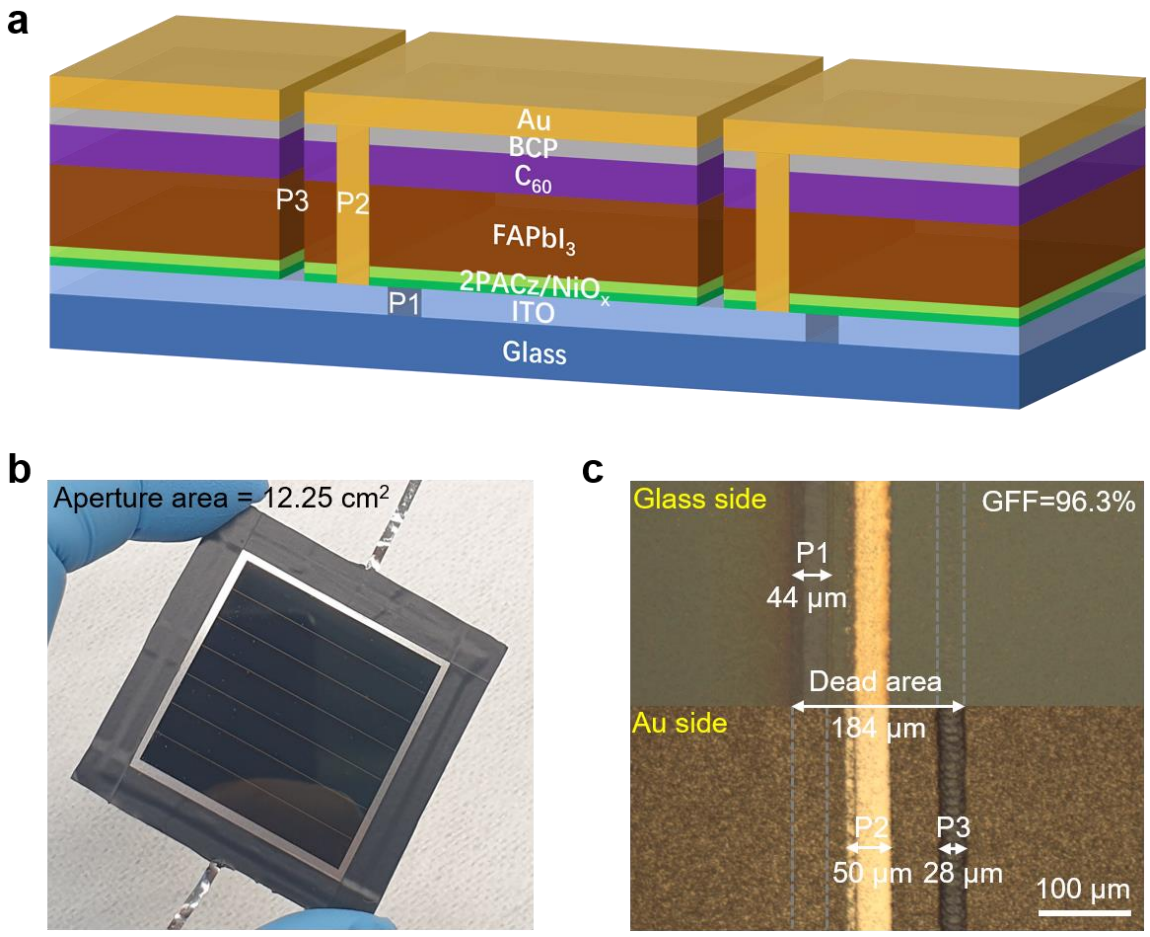

Figure 5.23. (a) Schematic illustration and (b) photograph of *p-i-n*-based $FAPbI_3$ perovskite solar module. (5.0 × 5.0 cm^2). (c) Optical microscopic images of the scribing lines. Reproduced from Ref.[27] with permission of Elsevier.

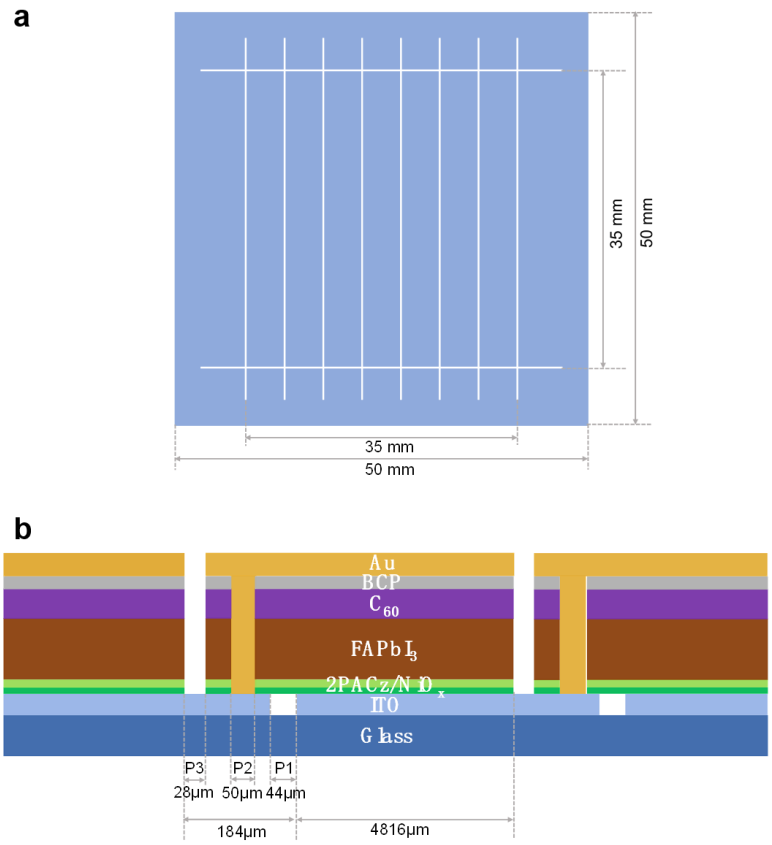

Figure 5.24. Schematic diagram of (a) the module layout design and (b) the interconnection of scribing lines. The geometrical fill factor (GFF) was calculated to be 96.3%. Adapted from Supplemental information of Ref.[27] with permission of Elsevier.

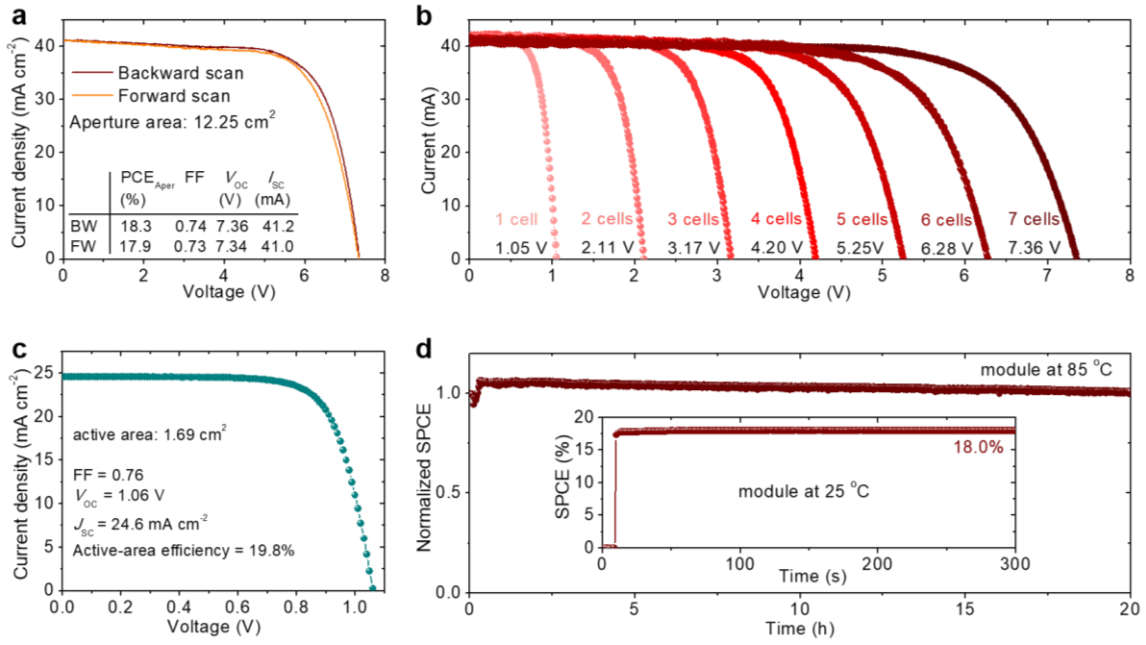

Figure 5.25. Current-density-voltage (*J-V*) characteristics of (a) the champion module, (b) sub-cells, and the champion sub-cell. All devices had MgF_2 antireflection coating. (E) SPCE under AM 1.5G continuous illumination at 85 °C and 25 °C (inset) in N_2-filled glovebox for the champion module. Reproduced from Ref.[27] with permission of Elsevier.

Table 5.4. Summary of PV performance for sub-cells in series and module obtained from backward scan under AM 1.5G (100 mW cm^{-2}). Adapted from Supplemental information of Ref.[27] with permission of Elsevier.

	I_{SC} (mA)	V_{OC} (V)	FF	Aperture-area efficiency (%)
1 cell	41.3	1.05	0.69	17.1
2 cells	41.3	2.11	0.73	18.2
3 cells	41.5	3.17	0.74	18.5
4 cells	41.5	4.20	0.76	18.9
5 cells	41.4	5.25	0.74	18.4
6 cells	41.3	6.28	0.73	18.1
7 cells (module)	41.2	7.36	0.74	18.3

I_{SC}: short-circuit current; V_{OC}: open-circuit voltage; FF: fill factor; Aperture-area efficiency: power conversion efficiency with an aperture area.

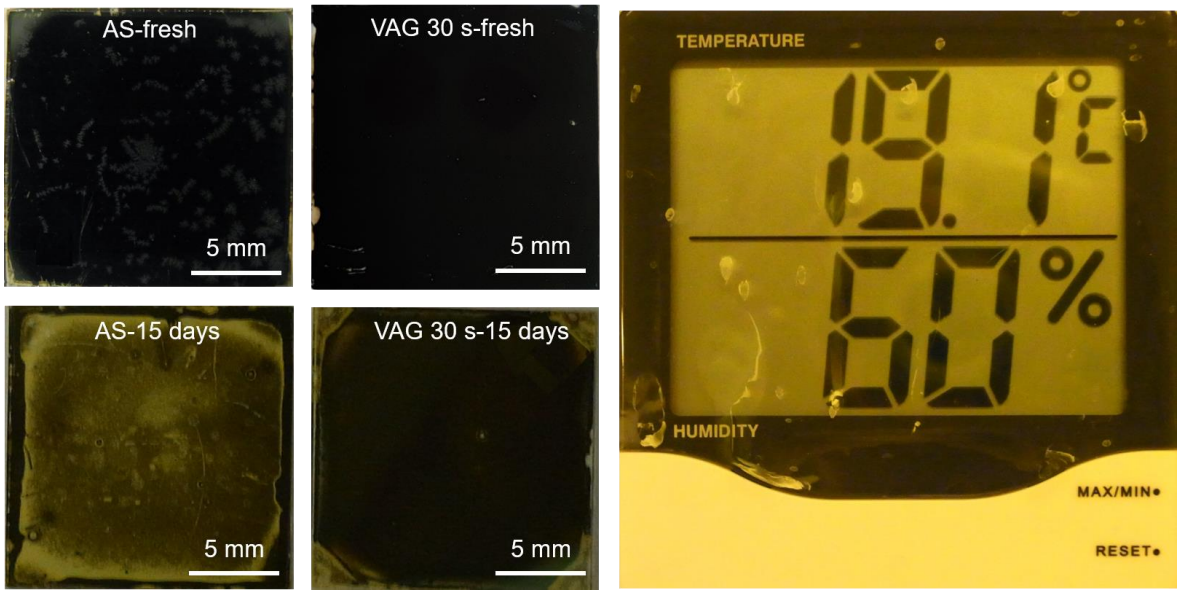

Figure 5.26. Photographs (visualized from glass side) of the fresh and aged (for 15 days) $FAPbI_3$ thin films. The perovskite thin films were spin-coated on small substrate (1.6 × 1.6 cm^2) using with MACl additive. The test condition was ~19 °C and 60% RH. Adapted from Supplemental information of Ref.[27] with permission of Elsevier.

Figure 5.24). This realized GFF was greatly improved compared to existing single-junction or 2T-all perovskite tandem solar modules[17,23,189,199,200] by optimizing the electrical characteristics of all scribing lines at minimal width and enhancing their respective alignment.[66]

The champion mini-module based on MgF_2 antireflective layer realizes a PCE of 18.3% with a V_{OC} of 7.36 V, FF of 0.74, and short-circuit current (I_{SC}) of 41.2 mA (see Figure 5.25a, 5.25b, and Table 5.4). The most efficient sub-cell within the module, featuring an active area of 1.69 cm^2, achieves an impressive active-area efficiency of 19.8% (see Figure 5.25c). This

indicates a minimal efficiency loss of only 7% during the upscaling process, highlighting the effective interconnection design and laser scribing techniques employed in scaling up these modules. It is also noteworthy that we achieve a remarkably low efficiency loss of just 1% when scaling up the blade-coated PSCs to a larger active area (PCE = 19.8% for 1.69 cm^2, see Figure 5.25c) compared to our reference smaller blade-coated PSCs (PCE = 20.0% for 0.105 cm^2, see Figure 5.22a). Each sub-cell contributes an average V_{OC} of 1.05 V (Figure 5.25b and Table 5.4), a value that is comparable to that obtained from the smaller blade-coated PSCs (1.07 V for 0.105 cm^2, see Figure 5.22a and Table 5.3), indicating minimal voltage loss during the upscaling process. Furthermore, the module maintains a high I_{SC} of 41.2 mA, demonstrating efficient current collection through the module interconnections. This value aligns well with the values of different sub-cells in series, which range from 41.3 to 41.5 mA (Table 5.4).

Furthermore, our module exhibits an excellent SPCE of up to 18.0% at MPP tracking under continuous AM 1.5G irradiation. It also maintains good stability at 85 °C in an inert atmosphere for 20 h, as depicted in Figure 5.25d. Next, we tested the stability against moisture for our $FAPbI_3$ PSCs. Notably, we observe that AS-$FAPbI_3$ thin films degraded more rapidly compared to VAG-$FAPbI_3$ thin films when stored in an ambient air environment (19°C, 60% relative humidity (RH), see Figure 5.26). After 11 days, we observe

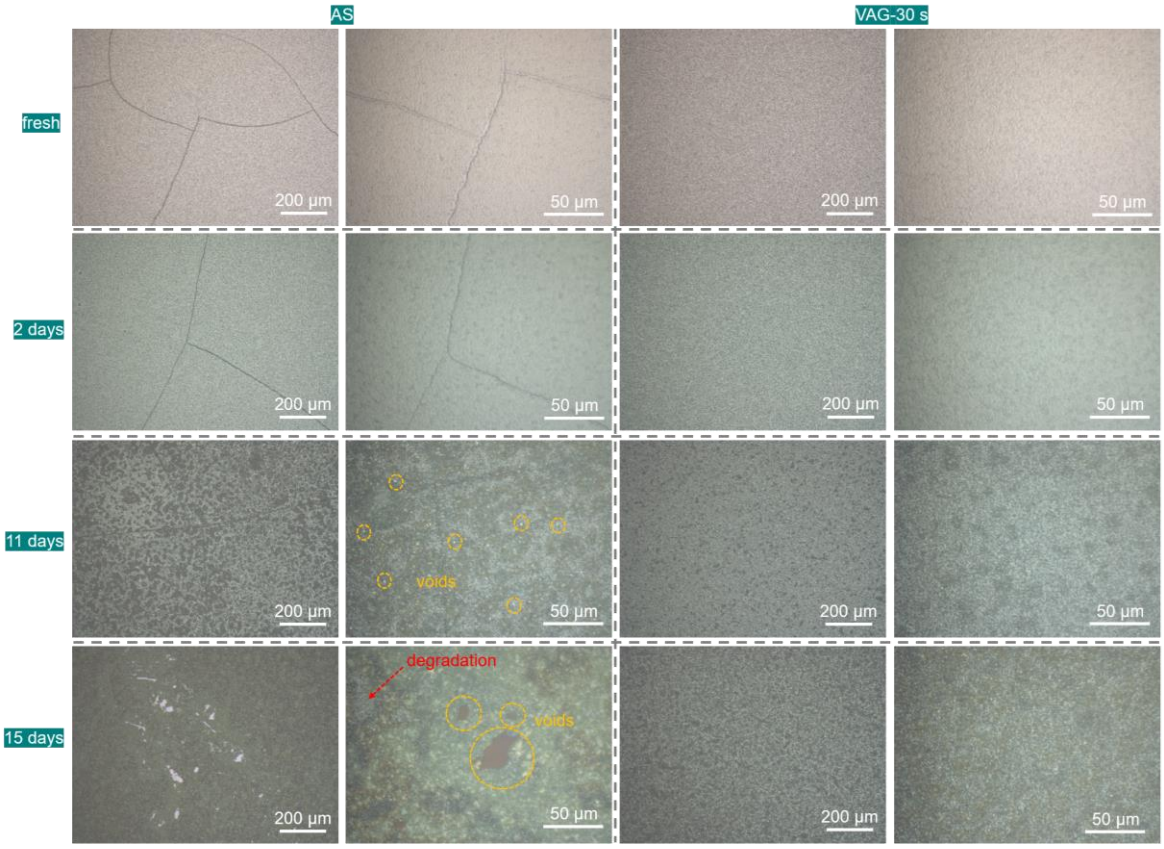

Figure 5.27. Optical microscopic images of the $FAPbI_3$ surface of the fresh and aged (for 15 days) thin films. The perovskite thin films were spin-coated on small substrate (1.6 × 1.6 cm^2) using with MACl additive. The test condition was ~19 ºC and 60% RH. Adapted from Supplemental information of Ref.[27] with permission of Elsevier.

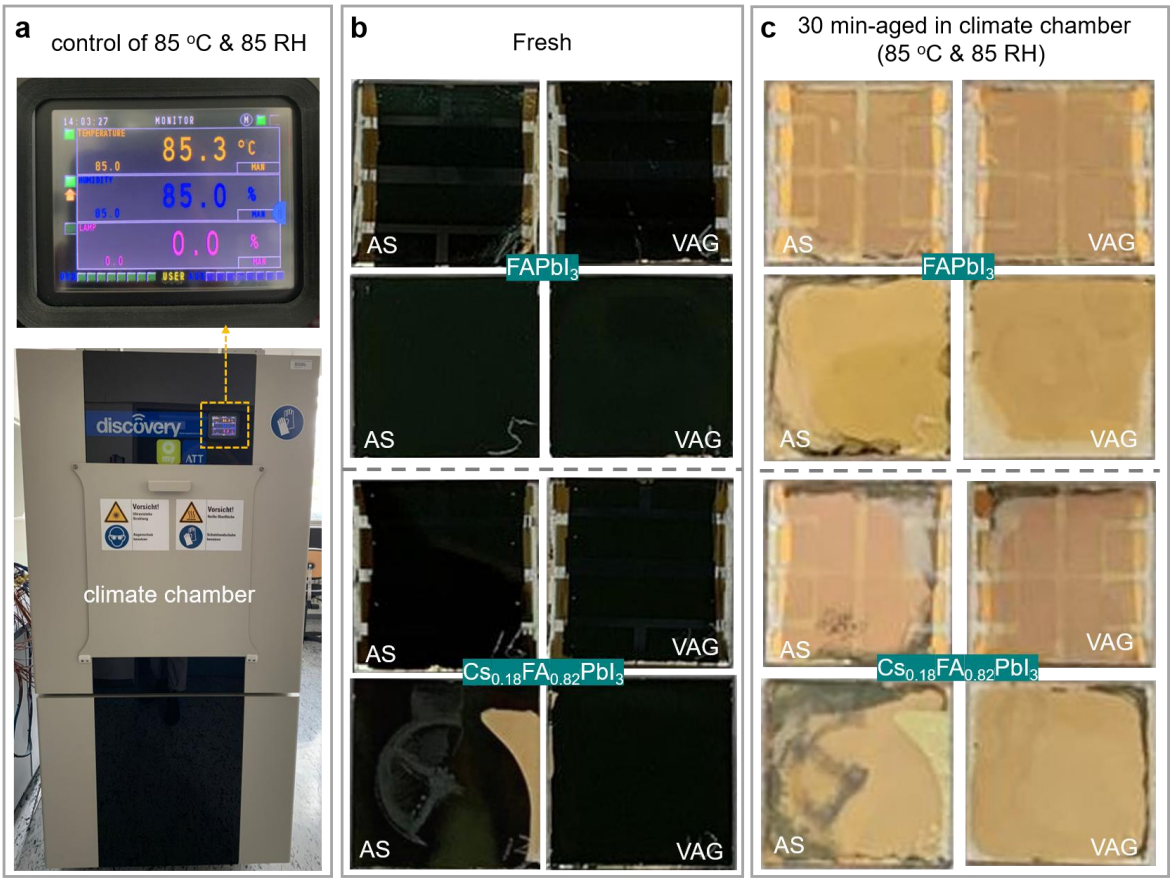

Figure 5.28. Photographs of (a) the climate chamber, (b) fresh, and (c) aged (~30 min) perovskite thin films and PSCs tested in the climate chamber at ~85 °C & 85% RH. The $FAPbI_3$ and $Cs_{0.18}FA_{0.82}PbI_3$ thin films were spin-coated on small substrate (1.6 × 1.6 cm^2) using with MACl and CsCl additives, respectively. Adapted from Supplemental information of Ref.[27] with permission of Elsevier.

apparent degradation in AS-$FAPbI_3$ thin films along with considerable voids, whereas VAG-$FAPbI_3$ thin films displays less degradation and nearly no voids (see Figure 5.27). After 15 days, severe degradation with the appearance of yellowish regions was evident in AS-$FAPbI_3$ thin films (Figure 5.26 and 5.27). The yellowish regions were also reported in the literatures that is attributed to phase transitions resulting from the emergence of the δ phase.[177–179] To further test damp-heat stability of the PSCs, we subjected them to a higher RH of 85% and an elevated temperature of 85°C in our climate chamber (see Figure 5.28a). All thin films and PSCs, based on $FAPbI_3$ and $Cs_{0.18}FA_{0.82}PbI_3$ perovskites fabricated using both the AS and VAG procedures, deteriorated in less than 30 min, as shown in Figure 5.28a and 5.28b. In conclusion, our developed VAG process demonstrates enhanced thermal stability and phase stability when compared to the reference AS quenching method. However, achieving higher levels of moisture resistance and implementing effective encapsulation techniques remain crucial for advancing the stability of $FAPbI_3$-based perovskite photovoltaics.

5.8. Summary

In this chapter, we investigate the effect of interfacial voids at the buried interface on the

non-radiative recombination and charge extraction within $FAPbI_3$-based PSCs in *p-i-n* architecture. We successfully scaled up high-efficiency PSCs to solar modules by using scalable methods with elimination of the interfacial voids. When employing conventional AS quenching method, we observe a large number of interfacial voids at the 2PACz/$FAPbI_3$ interface. In contrast, we use VAG process with optimization of vacuum time from 15 to 120 s. The optimized vacuum time of 30 s during VAG process eliminates voids and thus resulting in larger grains, which is confirmed from SEM, AFM, and optical microscopic images. Lower or higher vacuum time induces a higher void ratio. XRD results demonstrate a larger size of crystallites. We conducted TRPL and PLQY measurements on a half device stack, demonstrating the non-radiative recombination loss dominated by the buried interface of 2PACz/$FAPbI_3$. Further observations from the Mott-Schottky, dark *J-V*, light-intensity dependent V_{OC}, SCLC, and EIS analyses verify a high trap density that originated from the buried interface due to the interfacial voids. CE and delay-time-CELIV reveal the enhancement of charge extraction at the buried interface that explains a higher J_{SC}. As a result, the optimal vacuum time for VAG process achieves a champion PCE of 22.3% with a FF of 0.81, V_{OC} of 1.07 V, and J_{SC} of 25.7 mA cm^{-2}. To our best knowledge, this is the highest PCE for additive-free pure-α $FAPbI_3$ PSCs in *p-i-n* architecture. This device performance significantly exceeds the reference AS-PSCs (PCE of 19.7%, FF of 0.76, V_{OC} of 1.04 V, and J_{SC} of 24.8 mA cm^{-2}). We attribute the enhanced device performance to the decreased non-radiative recombination loss and improved charge extraction.

After achieving void-free buried interface in *p-i-n* architecture, we scaled up small PSCs (1.6 × 1.6 cm^2) to a larger substrate dimension (6.4 × 3.2 cm^2). We employed scalable methods to process perovskite and other layers, *i.e.*, blade coating for both 2PACz and $FAPbI_3$ layers, sputtering for NiO_x, vacuum deposition for C_{60}/Au/MgF_2 layer stack. We find the VAG process without any further treatment is not enough for controlling the nucleation and crystallization of large-area perovskite thin films. Therefore, we introduced MACl additive as well as a N_2 flow to accelerate the drying process, *i.e.*, fast removal of the solvent extraction. For further optimizing of additive concentration, as well as the vacuum pressure and time for regulating the N_2 flow, we realize a void-free and uniform perovskite thin film with a large area. Thus, the MACl & N_2 flow route was optimized to the optimal MACl concentration of 30 mol%, N_2 flow of ~180 cm^3 min^{-1}, and the vacuum time of ~30 s. This approach also works on different HTLs, *e.g.*, NiO_x, PEDOT:PSS, and PTAA. We realize an excellent PCE of 20.0% for the best-performing scalable PSC, with a FF of 0.75, V_{OC} of 1.07 V, and J_{SC} of 24.9 mA cm^{-2}, which is much higher than that of control (PCE = 2.9%), and MACl (PCE = 10.3%) and N_2 flow (PCE = 14.1%) routes.

Last, we present the all-laser-scribed $FAPbI_3$ perovskite solar mini-modules based on *p-i-n* architecture. We realize a champion PCE of 18.3% with V_{OC} of 7.36 V, I_{sc} of 41.2 mA, and FF = 0.74. The champion module also gives good SPCE of 18.0% and stability at 85 °C in an inert atmosphere for 20 h. The best-performing sub-cell within the module delivers (active area of 1.69 cm^2) an active-area efficiency of 19.8%. This demonstrates a low efficiency loss of just ~7% and a successful laser-scribed interconnection design in upscaling the modules. Furthermore, we realize a very low efficiency loss of only ~1% from scalable larger PSCs

(PCE = 19.8% for 1.69 cm^2) to scalable smaller PSCs (PCE = 20.0% for 0.105 cm^2). This upscaling techniques are also demonstrated negligible voltage loss and good current collection between sub-cells and the entire module.

6. Perovskite–perovskite–silicon triple-junction photovoltaics

Recent advancements in monolithic perovskite–Si and all-perovskite double-junction solar cells signify the beginning of a new era in the development of ultra-high-efficiency perovskite-based multi-junction photovoltaics. This chapter presents a remarkable triple-junction perovskite–perovskite–Si solar cell, achieving an impressive power conversion efficiency (PCE) of 24.4%. To the best of our knowledge, this is the highest record PCE for a triple-junction architecture. The key to this achievement lies in the optimization of light management for each perovskite sub-cell, with the top cell having a bandgap of approximately 1.84 eV and the middle cell around 1.52 eV. This optimization minimizes current mismatch and maximizes current generation, leading to an impressive short-circuit current density of up to 11.6 mA cm^{-2} per junction. A critical junction of this success is the development of a high-performance middle perovskite sub-cell, which incorporates a stable pure-α-phase $FAPbI_3$ perovskite thin film. These $FAPbI_3$ thin films are of exceptionally high quality, free from wrinkles, cracks, and pinholes. They are produced using a vacuum-assisted growth control method without the need for anti-solvents. This approach enables the achievement of a high open-circuit voltage, reaching up to 2.84 V in the triple-junction solar cells. Additionally, these non-encapsulated perovskite–perovskite–Si triple-junction solar cells exhibit impressive stability, retaining up to 96.6% of their initial PCE when subjected to storage in the dark at 85°C for 1081 h. This research represents a significant advancement in the field of multi-junction perovskite solar cells and provides a great promise for future high-efficiency photovoltaic technologies.

This chapter is based on our publication in *Energy & Environmental Science* by Hang Hu *et al.* with the title of "Triple-junction perovskite–perovskite–silicon solar cells with power conversion efficiency of 24.4%".[55] Most of the graphs in this chapter are adapted or reproduced with permission of The Royal Society of Chemistry.

Acknowledgments and contributions

Hang Hu, Dr. Bahram Abdollahi Nejand, and Prof. Dr. Ulrich W. Paetzold conceived the idea. Hang Hu developed research plans and designed the experiments. Hang Hu fabricated triple-junction solar cells. Sophie X. An, Seyedamir Orooji, and Fabrizio Gota contributed

to the simulation for triple-junction solar cells. Dr. Yang Li performed TRPL and PLQY. Roja Singh performed XRD. Dr. Fabian Schackmar and Felix Laufer performed EL imaging. Qihao Jin conducted AFM. Hang Hu and Thomas Feeney deposited SnO_x thin films by ALD. Dr. Bahram Abdollahi Nejand and Alexander Diercks conducted SEM. Hang Hu and Ting Pan optimized 2PACz thin films. Somayeh Moghadamzadeh optimized sputtering TCO. Hang Hu did the rest of the characterizations and data analyses. Dr. Michael Rienäcker and Dr. Robby Peibst offered the Si bottom cells and contributed to their expertise on Si solar cells. Dr. Bahram Abdollahi Nejand and Prof. Dr. Ulrich W. Paetzold supervised the project.

6.1. Introduction

Recent advancements in monolithic double-junction solar cells have started a new era in perovskite-based multi-junction PVs. They may even compete with the very high PCEs (>39%) reported for triple- and six-junction solar cells based on epitaxial grown III–V crystalline semiconductor thin films.[9,11] Unlike epitaxial grown III–V semiconductors, perovskite thin films can be manufactured using simple and cost-effective processes.[19,20] The detailed-balance limit for triple-junction photovoltaics, which is 51% (*vs.* ~45% for double-junction architecture), establishes the ultimate limit and highlights the potential for next-generation perovskite-based multi-junction PVs.[29,30] High-performance perovskite semiconductors, however, are currently only available for bandgaps as low as ~1.25 eV.[29,30] To successfully exploit the solar spectrum, monolithic perovskite multi-junctions will need to be paired with narrow bandgap Si or CI(G)S bottom solar cells, such as in perovskite–perovskite–Si designs.

Developing high-performance triple-junction perovskite-based solar cells has various obstacles including:

(1) Sequential processing of high-quality perovskite thin films: To create efficient triple-junction cells, high-quality perovskite thin films must be sequentially processed within complicated multi-layer designs. This demands precise control over the deposition and formation of each perovskite layer.
(2) Effective light management: Efficient light harvesting across all sub-cells is crucial. This requires the design of optical structures that minimize light losses and ensure that each sub-cell receives the appropriate amount of light to maximize its performance.
(3) Current matching among interconnected sub-cells: To optimize the overall performance of the triple-junction cell, currents generated by each sub-cell must be well-matched. Mismatched currents can result in significant energy losses.
(4) Low-loss tunnel and recombination junctions: The interfaces and junctions between the different sub-cells play a critical role in minimizing energy losses due to recombination and resistance. Developing low-loss tunnel and recombination junctions is essential for achieving high PCE.

Addressing these challenges requires a combination of materials science, device engineering, and advanced fabrication techniques. Optical modeling is commonly used for

identifying suitable device architectures and bandgap combinations for perovskite–perovskite–Si or all-perovskite monolithic triple-junction solar cells (MTJSC). Through the minimization of optical losses and optimization of layer stacks, it is theoretically predicted that all-perovskite and perovskite–perovskite–Si triple-junction solar cells could achieve impressive power conversion efficiencies (PCEs) of up to 36.6% and 38.8%, respectively.[19] However, the experimental realization of these theoretical predictions lags significantly behind. Only a few MTJSCs have been realized so far,[20,29,30,201–206] with maximum PCEs of 25.1%[206] and 22.2%[204] for all-perovskite and perovskite–perovskite–Si, respectively. In 2018, Werner *et al.*[20] reported on the first perovskite–perovskite–Si MTJSCs using vapor deposition combined with spin-coating method to process the perovskite sub-cells, realizing a PCE of 14.0% and an open-circuit voltage (V_{OC}) of 2.69 V. The device performance was limited by a low fill factor (FF) of < 0.7, mismatched currents in the perovskite sub-cells (low short-circuit current density (J_{SC}) < 8 mA cm^{-2}) and an imperfect recombination junction between the top and middle perovskite sub-cells. Recently, Zhang *et al.*[30] and Choi *et al.*[204] reported the improved PCEs of 20.1% and 22.2% for perovskite–perovskite–Si MTJSCs, respectively, with both V_{OC} < 2.80 V and J_{SC} < 10.2 mA cm^{-2}, limited by low current generation in the middle perovskite sub-cell. Besides these few proof-of-concepts, there are so far no reports on perovskite–perovskite–Si MTJSCs. The middle-bandgap (MBG) perovskite sub-cell is the most crucial as it is fabricated on top of the Si bottom cell and corrosion must be prevented from subsequent deposition of middle-bandgap (WBG) perovskite top cell. The MBG perovskite sub-cell must have many critical characteristics:

(1) Suitable MBG: The MBG perovskite sub-cell must have an appropriate bandgap that should be optimized to maximize J_{SC} and overall device performance.

(2) Thermal stability: The MBG perovskite sub-cell should exhibit excellent thermal stability to endure the processing steps involved in depositing the WBG perovskite top cell. Thermal stability ensures that the sub-cell maintains its performance and architectural integrity.

(3) Excellent interfaces: The MBG perovskite sub-cell should have high-quality interfaces with both recombination junctions. These interfaces play a critical role in minimizing recombination losses and maximizing device performance.

(4) Low defect density: The MBG perovskite sub-cell should have a low density of defects and pinholes. Defects can act as recombination centers, reducing the V_{OC} of the sub-cell. Pinholes induce corrosion from subsequent processing of WBG sub-cell.

According to optical modeling and simulations, MBG perovskites with bandgaps between 1.40 to 1.50 eV are favorable for maximizing J_{SC} in a triple-junction architecture.[19,20] This MBG perovskite sub-cell optimization is critical for obtaining high overall device performance in MTJSCs. It should be noted that the bandgaps below 1.50 eV have typically relied on Sn-Pb-mixed perovskite compositions, which unfortunately exhibit instability and rapid degradation in the presence of even very low amounts of oxygen and water.[16,17] This instability has limited the use of these compositions in perovskite–perovskite–Si MTJSCs. As a result, previous work has primarily employed Pb-based compositions, specifically $Cs_xFA_yMA_{1-x-y}Pb(I_zBr_{1-z})_3$.[20,30,204] $FAPbI_3$, with an optical bandgap of approximately 1.52 eV,[171,172,207] presents as a promising candidate for the middle-bandgap (MBG) perovskite

thin film. $FAPbI_3$ PSCs have showed remarkable device performance and thermal stability,[80,170–173,181,207] meeting the criteria for (1) and (2). We highlight that $FAPbI_3$ have not yet been employed in multi-junction PVs. Furthermore, it is essential that this material also meets criteria (3) and (4) to prevent deterioration during subsequent multi-stack processing of the WBG perovskite top sub-cell.[17] Conventional anti-solvent (AS) quenching methods, commonly used in perovskite thin-film fabrication, have been reported to introduce a high density of surface defects at the perovskite/ETL interface,[208,209] such as wrinkles, micro-cracks, and pinholes.[208,210–212] To address these issues, alternative AS-free quenching

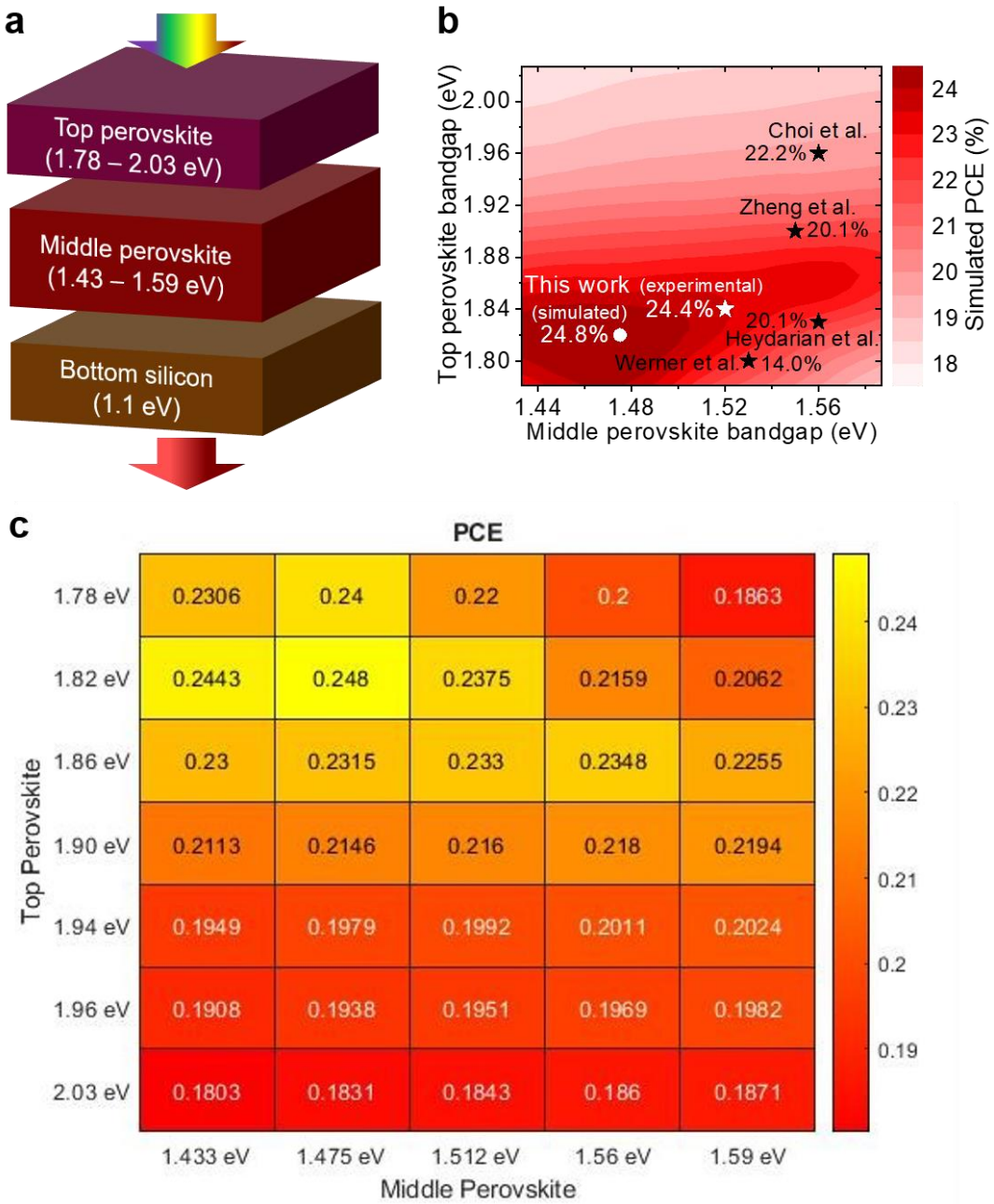

Figure 6.1. (a) Schematic illustration of triple-junction concept. (b) Contour plots[20,30,204,205] and (c) heat-map of simulated PCEs of MTJSCs with varied bandgaps of top and middle perovskites. Reproduced from Ref.[55] with permission of The Royal Society of Chemistry.

methods for processing the MBG perovskite thin film are highly encouraged. Developing such methods is crucial for realizing high-efficiency and stable multi-junction perovskite solar cells.

In this chapter, we demonstrate highly efficient perovskite–perovskite–Si MTJSCs featuring a $Cs_{0.2}FA_{0.8}Pb(I_{0.5}Br_{0.5})_3$ WBG perovskite top cell with a bandgap of ~1.84 eV, an $FAPbI_3$ perovskite middle cell with a bandgap of ~1.52 eV, and a Si bottom cell with a bandgap of ~1.1 eV. We achieve a champion PCE of 24.4%, marking it as the highest record PCE in this triple-junction architecture, particularly notable due to its active area of 0.5 cm^2. We initiated our efforts by employing optical simulations to identify the ideal combination of perovskite thin films with specific bandgaps and layer thicknesses. Through meticulous light management and current matching adjustments for the perovskite sub-cells, we were able to enhance the J_{SC} to a remarkable 11.6 mA cm^{-2}, surpassing prior achievements.[20,30,204] Of great importance, we implemented a VAG technique that resulted in the fabrication of wrinkle-free, pinhole-free, phase-stable, and high-quality $FAPbI_3$ middle perovskite sub-cells. Our MTJSCs demonstrate a superior V_{OC} of up to 2.84 V, attributed to the utilization of high-quality $FAPbI_3$ thin films with minimized non-radiative recombination at the $FAPbI_3$/ETL interfaces. In addition, non-encapsulated MTJSC exhibits excellent thermal stability, retaining 96.6% of their initial PCE after 1081 hours of storage in a nitrogen (N_2) atmosphere at 85°C.

6.2. Simulations of triple-junction solar cells

In the pursuit of maximizing the overall J_{SC} for the perovskite–perovskite–Si triple-junction architecture, we employed numerical simulations. Our aim is to minimize parasitic absorption and reflection losses while identifying the most suitable combination of bandgaps and thicknesses for the perovskite thin films in the top and middle sub-cells (with the Si bottom cell having a fixed bandgap of ~1.1 eV, as depicted in Figure 6.1a). Our simulations utilized a well-established device architecture based on previously reported prototypes and utilized material combinations known for their high-performance characteristics in all-perovskite[17,52] and monolithic perovskite–Si double-junction solar cells.[54] To perform these simulations, we employed our in-house-developed open-source modeling platform, EYcalc, which has been employed successfully in earlier studies for accurate performance and energy yield predictions of perovskite-based multi-junction solar cells.[15,52,54] Based on the optical data and electrical parameters derived from the characterization of our single-junction devices,[54] our simulations predict that the perovskite–perovskite–Si triple-junction architecture could achieve a maximum PCE of 24.8%. This ideal PCE corresponds to a bandgap combination of ~1.82 eV for the top perovskite sub-cell and ~1.48 eV for the middle perovskite sub-cell (as shown in Figure 6.1b, 6.1c, and 6.2). Previous studies on perovskite–perovskite–Si architecture used significantly different bandgap combinations. Zheng *et al.* reported a PCE of 20.1% using a bandgap combination of 1.55 and 1.90 eV,[30] whereas Choi *et al.* reported a PCE of 22.2% using a bandgap combination of 1.56 and 1.96 eV.[204] The performance of the middle sub-cell restricted both of these triple-junction devices,

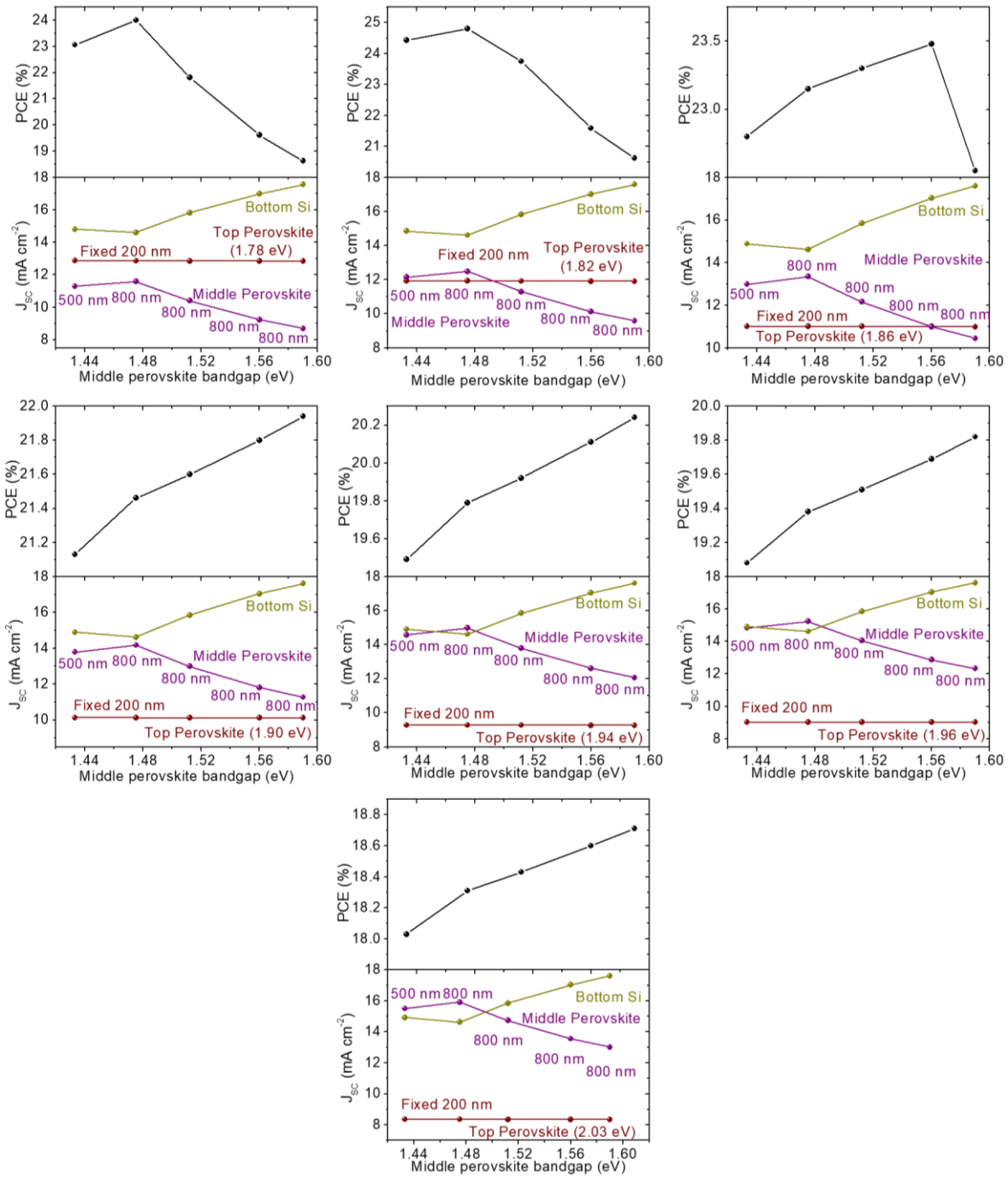

Figure 6.2. Simulated PCE and J_{SC} of MTJSCs with varied bandgaps of top and middle perovskite sub-cells. The thickness of top perovskite thin film is fixed to 200 nm. Adapted from Electronic Supplementary Information of Ref.[55] with permission of The Royal Society of Chemistry.

with J_{SC} values of 8.5 and 10.19 mA cm^{-2}, respectively.

In our triple junction, we made a slight compromise on the maximum achievable PCE to expand the range of appropriate bandgap combinations. We selected $FAPbI_3$ as a middle sub-cell with an optical bandgap of ~1.52 eV,[80,170,173,181] known for its excellent performance and thermal stability in single-junction devices.[80,170–173,181,207] We note that 1.48 eV is also described as an ideal bandgap of pure α-phase $FAPbI_3$,[171,172,207] which is quite similar to our

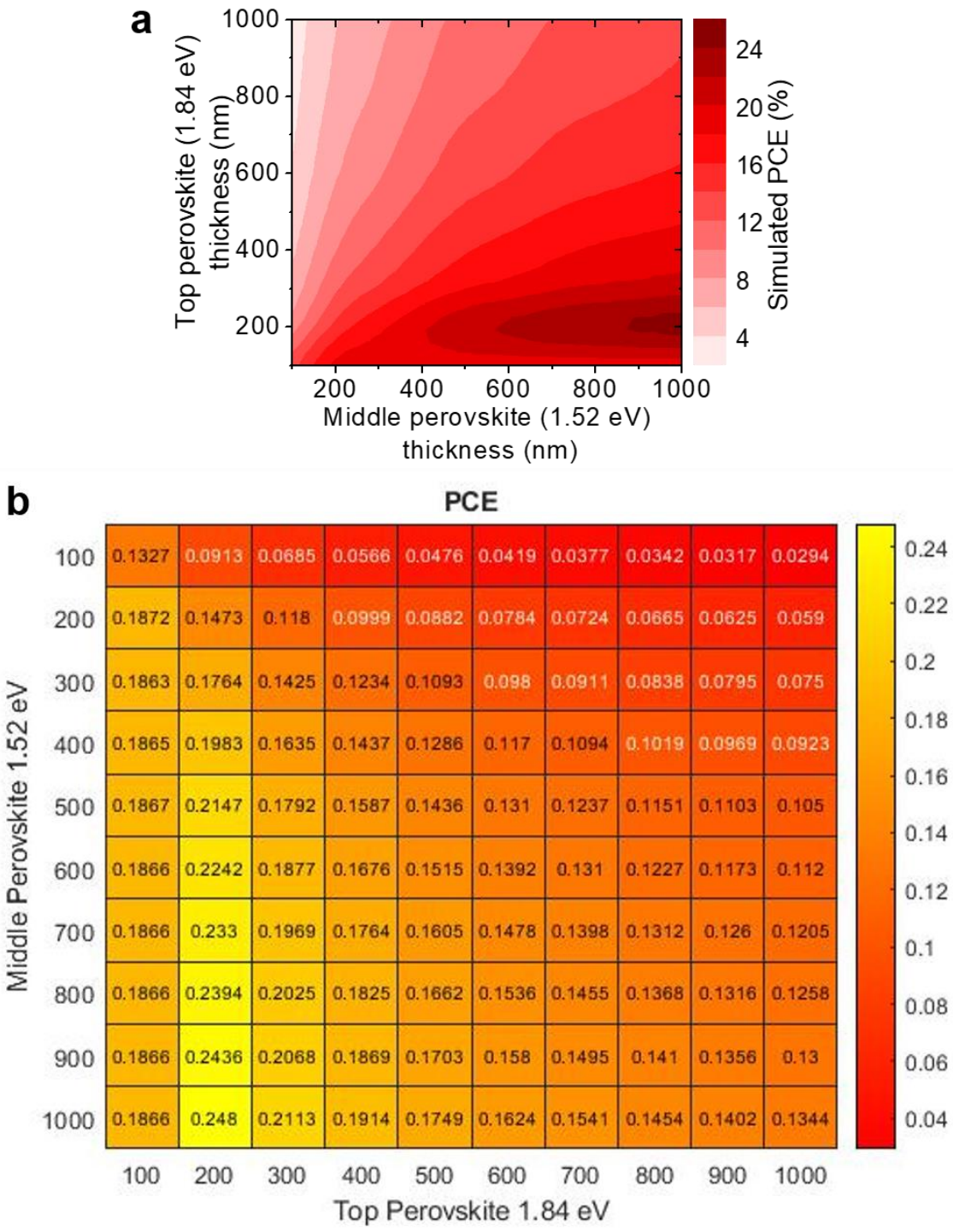

Figure 6.3. (a) Contour plots and (b) heat-map of simulated PCEs of MTJSCs with varied thickness of top (fixed to 1.84 eV) and middle (fixed to 1.52 eV) perovskite sub-cells. Reproduced from Ref.[55] with permission of The Royal Society of Chemistry.

best simulated value. Our simulations indicate that an ideal combination is ≥600 nm thick $FAPbI_3$ middle sub-cell and a WBG top cell (~1.84 eV) with a thickness of around ~200 nm (Figure 6.3 and 6.4). It is important to note that perovskite absorber layers in the top solar cell that are thinner than 200 nm or thicker than 300 nm would result in significant current mismatch between the two perovskite sub-cells, leading to an overall J_{SC} of less than 10 mA

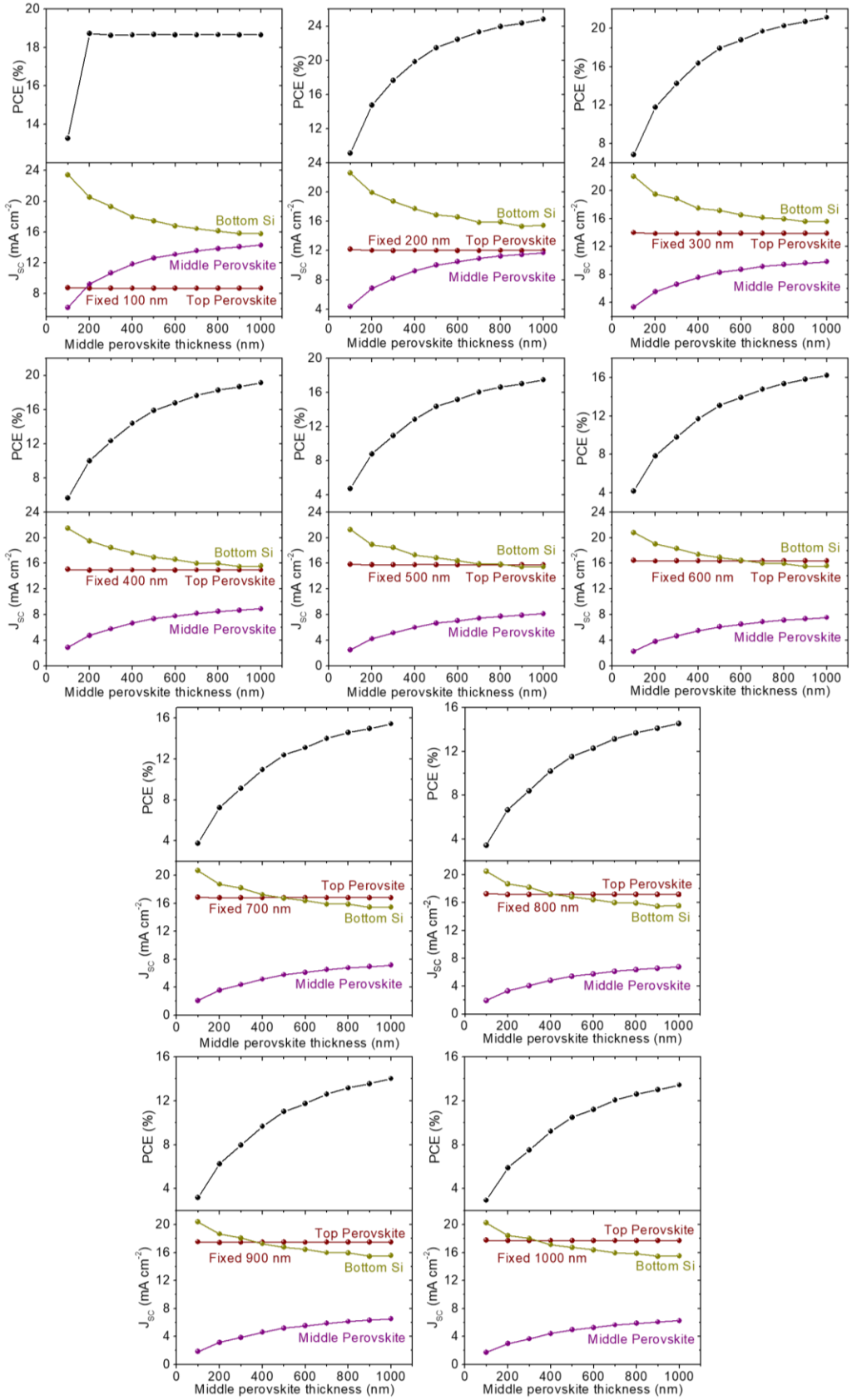

Figure 6.4. Simulated PCE and J_{SC} of MTJSCs for varied thickness of top (fixed to 1.84 eV) and middle (fixed to 1.52 eV) perovskite sub-cells. Adapted from Electronic Supplementary Information of Ref.[55] with permission of The Royal Society of Chemistry.

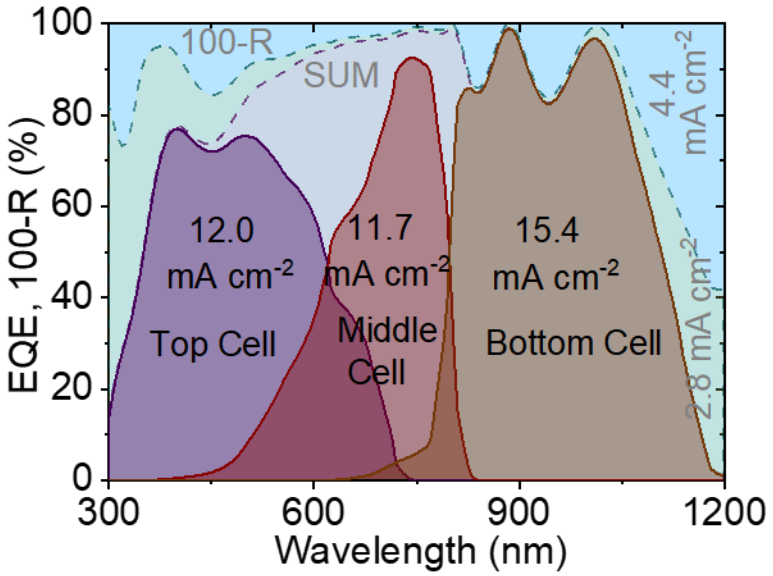

Figure 6.5. Simulated external quantum efficiency (EQE) spectra for the champion MTJSC (1.84 eV for the top cell and 1.52 eV for the middle cell). The reflection and parasitic absorption losses are calculated to be 4.4 and 2.8 mA cm^{-2}, respectively. Adapted from Ref.[55] with permission of The Royal Society of Chemistry.

cm^{-2} and substantial PCE loss (Figure 6.4). It should be noted that the excellent charge carrier extraction has been realized in our recent experimental work for *p-i-n*-based PSCs with $FAPbI_3$ thickness up to ~600 nm (also can be seen the discussion in chapter 5).[27]

In order to figure out the photocurrent generated within each sub-cell in the best simulated triple-junction architecture, we evaluate the simulated external quantum efficiency (EQE). The nearly perfect current matching between two perovskite sub-cells is shown in Figure 6.5. The photocurrent densities of the bottom, middle, and top sub-cells were integrated to 15.4, 11.7, and 12.0 mA cm^{-2}, respectively. In total, the reflection and parasitic absorption losses were minimized to 7.2 mA cm^{-2}, leaving room for further improvements in future research.

6.3. Experimental optimization for triple-junction solar cells

We fabricated perovskite–perovskite–Si MTJSCs in an optimized device architecture, as illustrated in Figure 6.6a. The top and middle perovskite sub-cells were deposited sequentially on top of Si bottom solar cell with ~200 μm thickness, which was etched with potassium hydroxide and had doped polysilicon-on-oxide (POLO) contacts with passivating electron-selective full area in the front and hole-selective partial in the rear. The full stacks of perovskite sub-cells include the following layers, starting immediately after the Si bottom solar cell: indium tin oxide (ITO)/nickel oxide (NiO_x)/[2-(9H-carbazol-9-yl)ethyl]phosphonic acid (2PACz)/ $FAPbI_3$/fullerene (C_{60})/tin oxide (SnO_x)/ITO/NiO_x/2PACz/ $Cs_{0.2}FA_{0.8}Pb(I_{0.5}Br_{0.5})_3$/lithium fluoride (LiF)/$C_{60}$/$SnO_x$/indium zinc oxide (IZO)/gold (Au)/magnesium fluoride (MgF_2). A cross-sectional scanning electron microscopy (SEM) image of our MTJSC is shown in Figure 6.6b. In the middle perovskite sub-cell, MBG $FAPbI_3$ thin film with an optical bandgap of ~1.52 eV (see Figure C1) and a

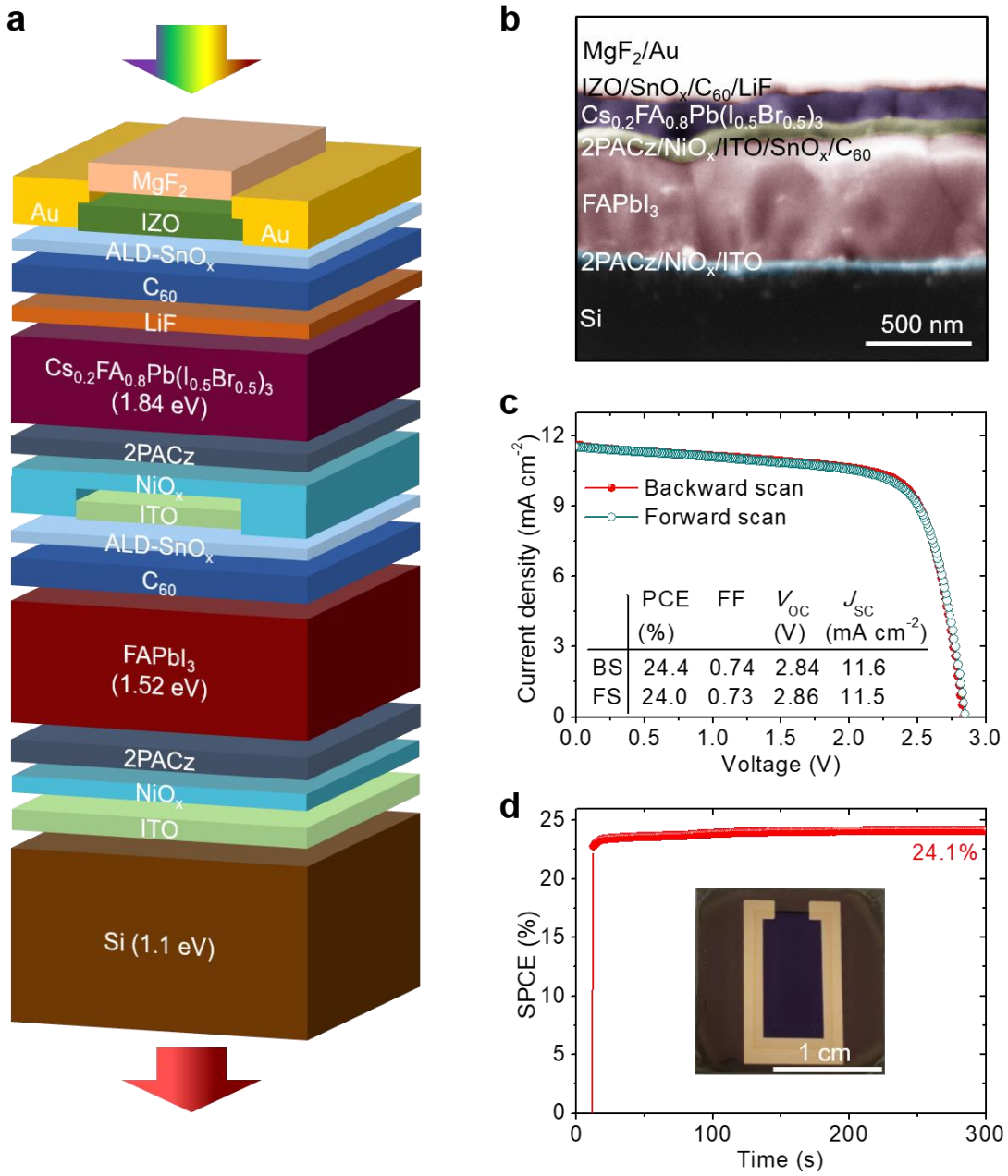

Figure 6.6. (a) Schematic illustration and (b) cross-section SEM image of perovskite–perovskite–Si MTJSC. (c) *J-V* characteristics of both forward and backward scans and (d) stabilized PCE for the champion MTJSC. The inset of (d) is the photograph of a MTJSC. Reproduced from Ref.[55] with permission of The Royal Society of Chemistry.

thickness of 650 nm was fabricated. For top perovskite sub-cell, WBG with the compositions of $Cs_{0.2}FA_{0.8}Pb(I_{0.5}Br_{0.5})_3$, an optical bandgap of ~1.84 eV (see Figure C2), and a thickness of ~ 200 nm was deposited on top of middle cell. The recombination layers were fabricated using sputtered ITO with thicknesses of 15–20 nm. It should be noted that a double HTLs of NiO_x/2PACz were used in both perovskite sub-cells.[13] This double-layer configuration has been previously demonstrated in other studies[20,30,202] to be effective to:

(1) provide superior charge carrier extraction,
(2) act as a robust barrier against the solvents of perovskite precursor,

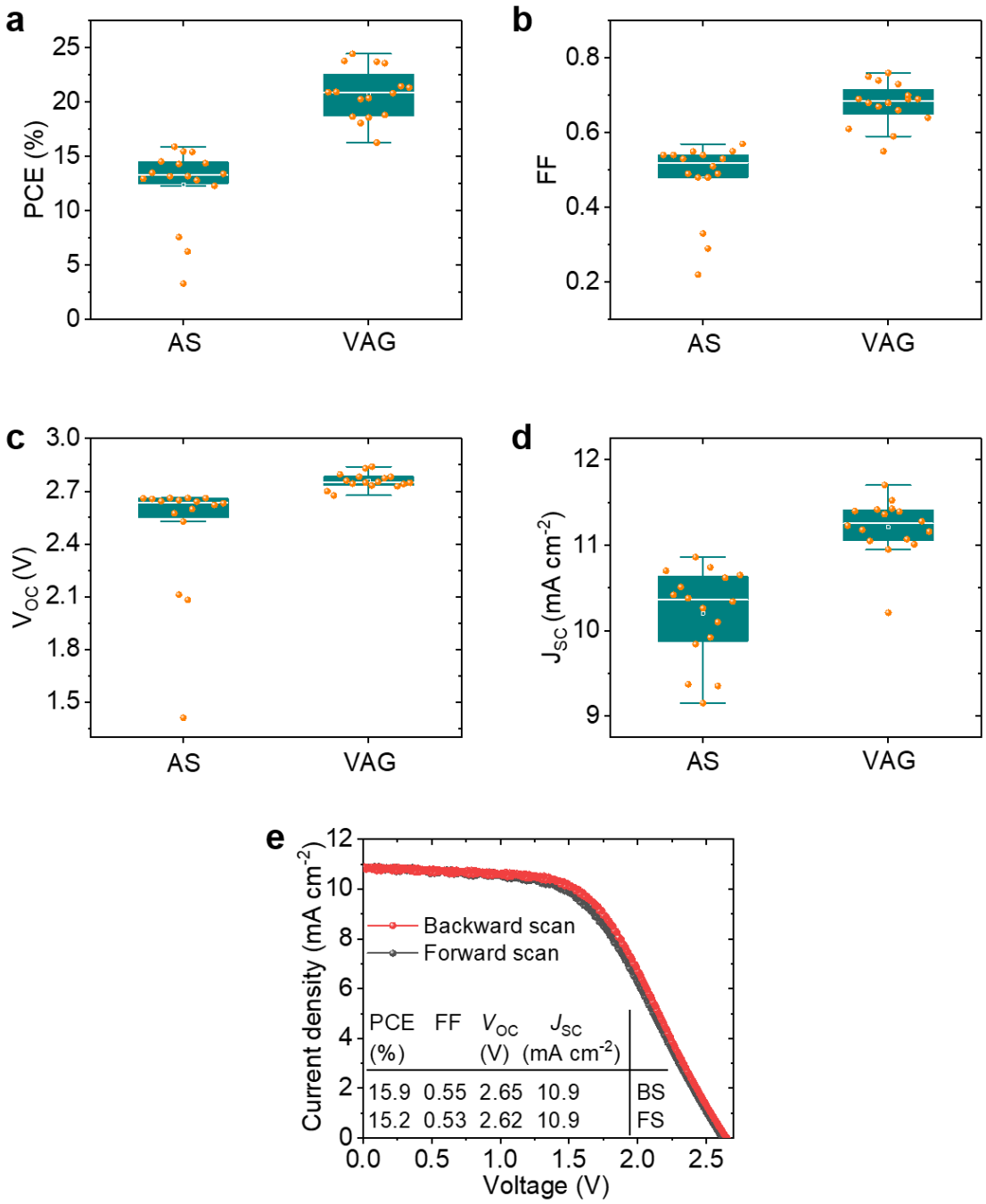

Figure 6.7. Statistical distribution of (a) PCE, (b) FF, (c) V_{OC}, and (d) J_{SC} for perovskite–perovskite–Si MTJSCs. The MBG perovskite thin films were fabricated by using VAG and AS. (e) *J-V* characteristics of both forward and backward scans for the champion perovskite–perovskite–Si MTJSC based on AS-$FAPbI_3$. Adapted from Electronic Supplementary Information of Ref.[55] with permission of The Royal Society of Chemistry.

(3) and contribute to high device yield.

The champion MTJSC achieves a PCE of 24.4% with a V_{OC} of 2.84 eV, a J_{SC} of 11.6 mA cm^{-2}, and FF of 0.74. We highlight that this is the record PCE in this kind of triple-junction architecture. The triple-junction device exhibits minimal hysteresis in its current-density-voltage (*J-V*) curves (see Figure 6.6c) and stabilized PCE up to 24.1% at continuous maximum power point (MPP) tracking under continuous AM 1.5G (100 mW cm^{-2})

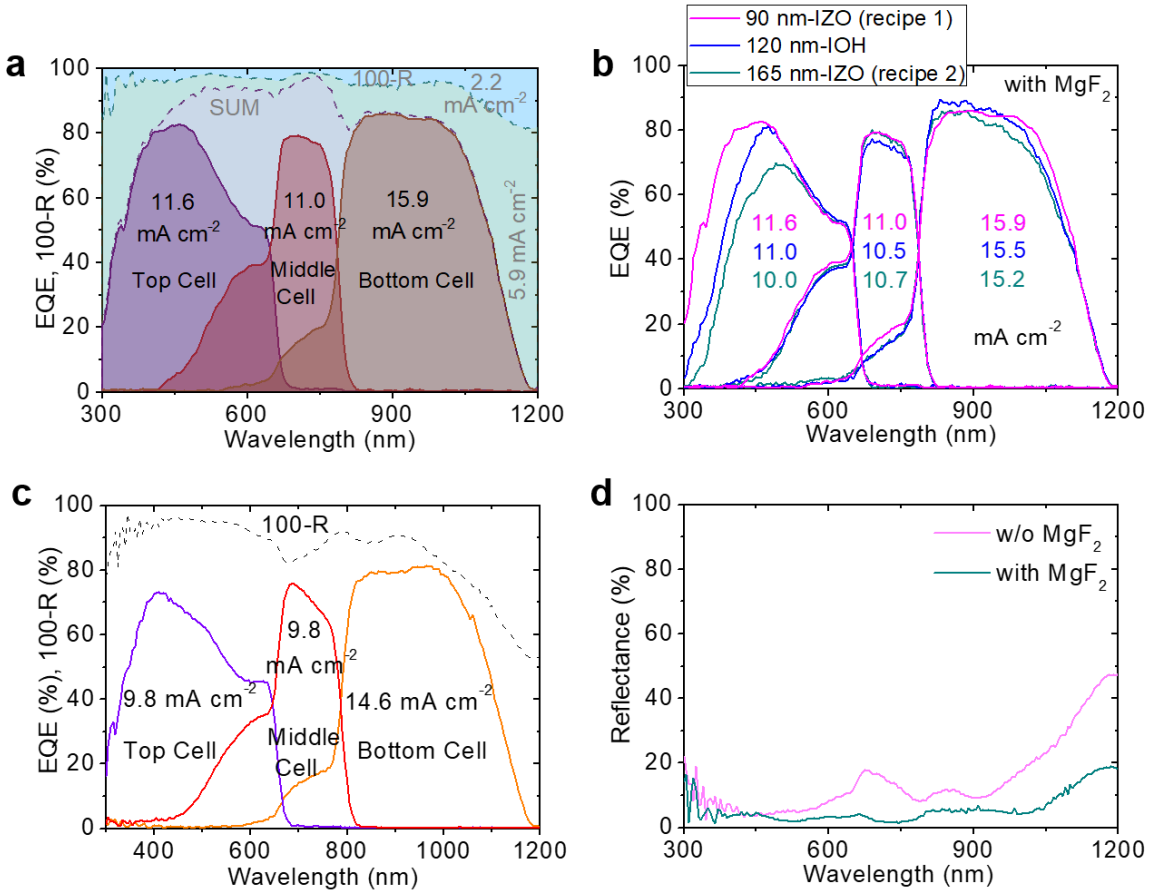

Figure 6.8. (a) EQE spectra of the champion perovskite–perovskite–Si MTJSC with MgF_2 antireflection coating. The reflection and parasitic absorption losses were integrated to 2.2 and 5.9 mA cm^{-2}, respectively. (b) EQE spectra of MTJSCs based on different TCO recipes (recipe 1: 90 nm IZO fabricated by using a low deposition pressure of 0.8 mTorr and a high power supply of 200 W; recipe 2: 165 nm IZO fabricated by using a high deposition pressure of 1.5 mTorr and a low power supply of 100 W; 120 nm IOH). (c) EQE spectra of the champion MTJSC without MgF_2 antireflection coating. (d) Reflectance spectra of the champion MTJSC with and without MgF_2 antireflection coating. Reproduced from Ref.[55] with permission of The Royal Society of Chemistry.

irradiation (see Figure 6.6d). We highlight the key development in this triple-junction architecture is utilizing VAG strategy to process high-quality MBG perovskite thin film, resulting in higher PV performance and yield compared to conventional AS method (see Figure 6.7a–6.7d). The MTJSC based on AS-$FAPbI_3$ only realizes a champion PCE of 15.9% with a V_{OC} of 2.65 eV, a J_{SC} of 10.9 mA cm^{-2}, and FF of 0.55 (see Figure 6.7e).

The external quantum efficiency (EQE) of our perovskite–perovskite–Si MTJSCs closely aligns with the simulated optimum values, as shown in Figure 6.8a and 6.5. The integrated photocurrent densities for top (~1.84 eV), middle (~1.52 eV), and bottom (~1.1 eV) cells are 11.6, 11.0, and 15.9 mA cm^{-2}, respectively. To achieve these results, a low-loss transparent and conductive oxide front electrode (TCO, see Figure 6.8b) and optimized antireflection coating layers (utilizing MgF_2, see Figure 6.8a, 6.8c, 6.8d, and C3) were employed to minimize reflection and absorption losses. Specifically, the triple-junction architecture demonstrates low absorption losses (integrated photocurrent density of ~5.9

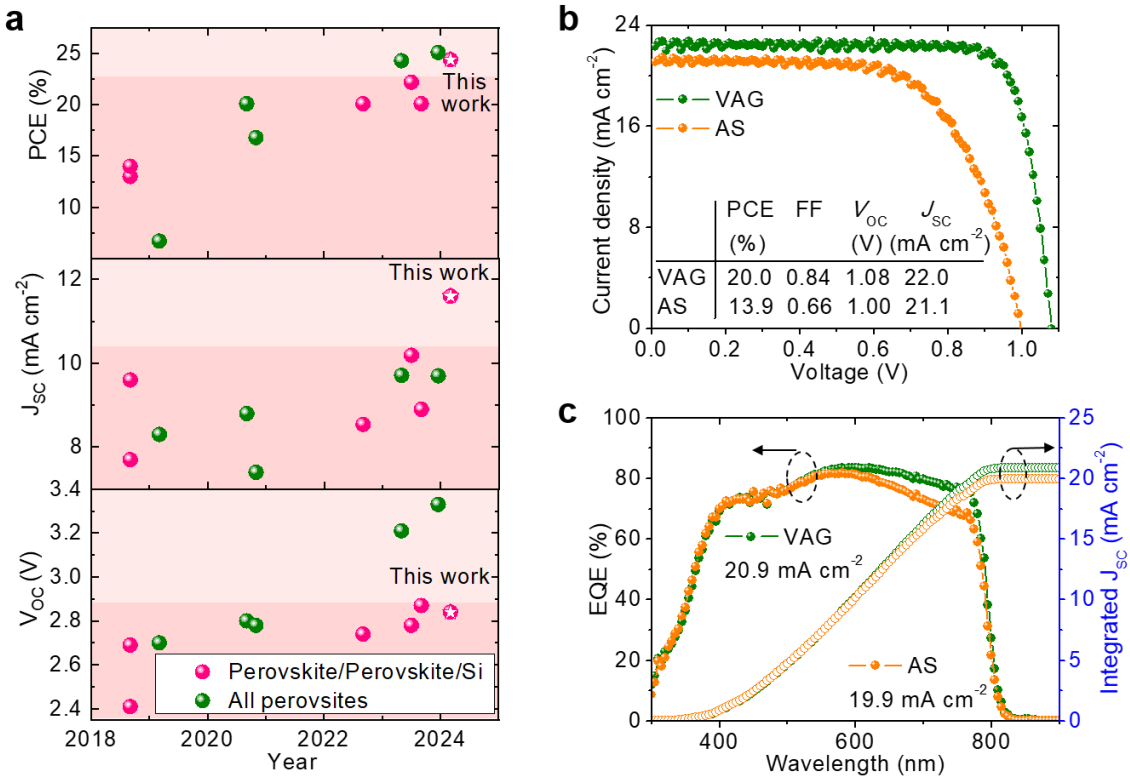

Figure 6.9. (a) Summary of the reported perovskite-based MTJSCs.[20,29,30,201–206] (b) *J-V* characteristics of backward scans and (c) EQE spectra for semitransparent single-junction PSCs fabricated using VAG and AS methods. Reproduced from Ref.[55] with permission of The Royal Society of Chemistry.

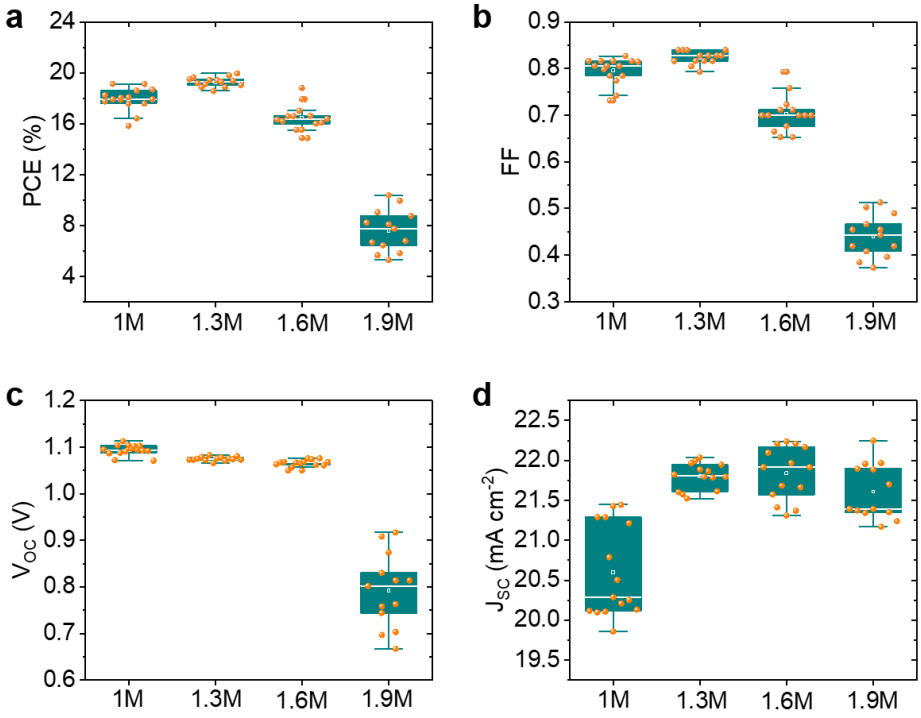

Figure 6.10. Statistical distribution of (a) PCE, (b) FF, (c) V_{OC}, and (d) J_{SC} for semitransparent single-junction middle PSCs. The MBG perovskite thin films were fabricated by using VAG method with different perovskite precursor concentration from 1.0 to 1.9 M. Adapted from Electronic Supplementary Information of Ref.[55] with permission of The Royal Society of Chemistry.

mA cm^{-2}) and reflection losses (integrated photocurrent density of ~2.2 mA cm^{-2}), as shown in Figure 6.8a. It is noteworthy that the performance of our perovskite–perovskite–Si MTJSCs represents a significant advancement in the field of multi-junction PVs, surpassing previous prototypes in terms of both J_{SC} and V_{OC}, as highlighted in Figure 6.9a.

Processing the whole stack of our perovskite–perovskite–Si MTJSCs involves numerous successive layer depositions, which presents a significant challenge. While many layers in triple-junction architecture can be deposited using physical vapor deposition for controlled conformal thin film growth, the perovskite absorber layers require spin coating. To prevent solvents (*e.g.*, DMF/DMSO) and anti-solvent (*e.g.*, EA) from penetrating the underlying layers and to achieve pinhole-free perovskite thin films, we employed VAG strategy, which has been established in our previous work for processing all-perovskite double-junction solar cells[16,17] (such as chapter 4) and high-quality $FAPbI_3$ thin films[27] (such as chapter 5). Figure 6.9b illustrates *J-V* characteristics of semitransparent $FAPbI_3$ single-junction PSCs with the same architecture as the triple-junction solar cell. VAG process realizes

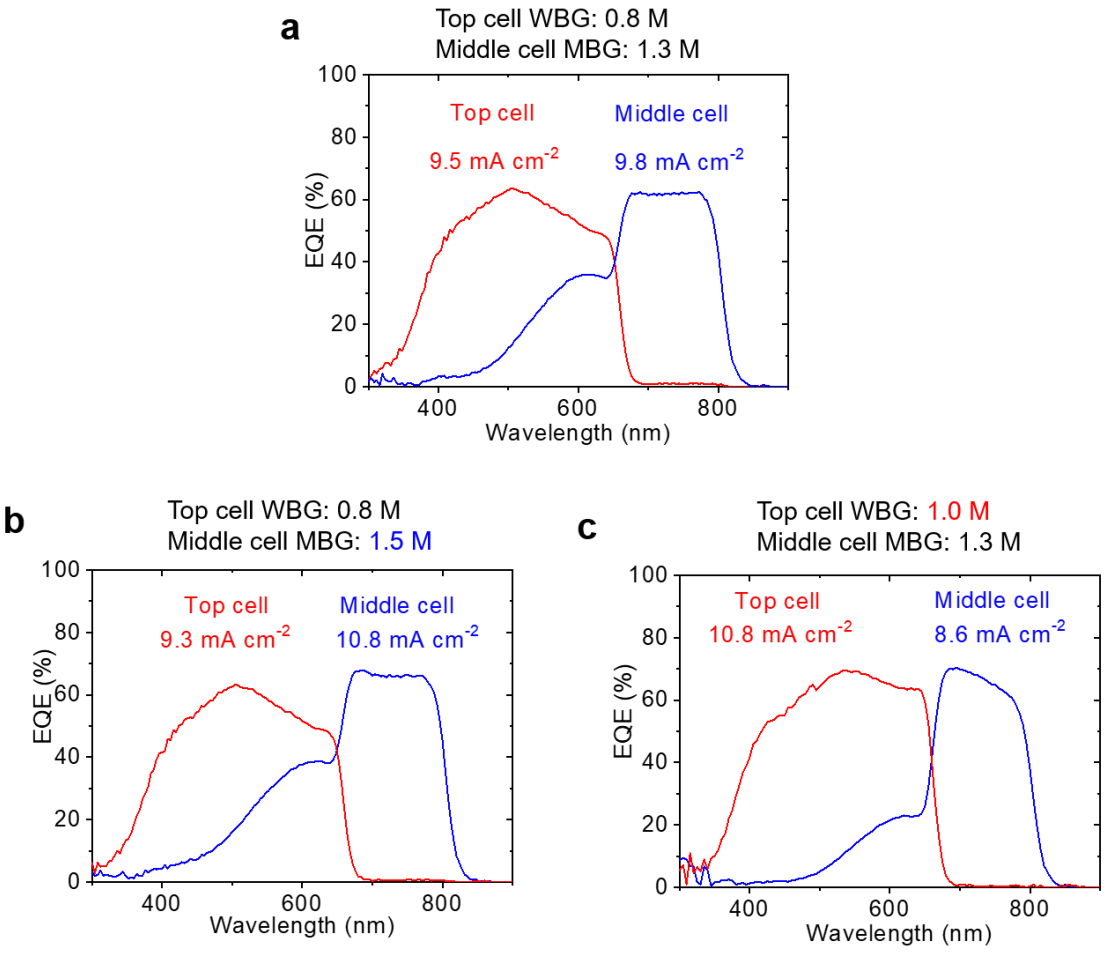

Figure 6.11. EQE spectra for the MTJSCs based on different thickness of perovskite thin films within the sub-cells. The thickness of WBG was fabricated by AS method with controlling the perovskite precursor concentration of 0.8 or 1.0 M. The thickness of MBG was fabricated by VAG method with controlling the perovskite precursor concentration of 1.3 or 1.5 M. TCO deposition was applied to recipe 2 described in Figure 6.8b. Adapted from Electronic Supplementary Information of Ref.[55] with permission of The Royal Society of Chemistry.

significantly improved performance compared to the AS method. The VAG-processed device achieves a higher PCE of 20.0%, with V_{OC} of 1.08 eV, FF of 0.84, and J_{SC} of 22.0 mA cm^{-2}, compared with the AS method with PCE of 13.9%, V_{OC} of 1.00 eV, FF of 0.66, and J_{SC} of 21.1 mA cm^{-2}. This improvement is attributed to enhancements in V_{OC} (~80 mV), FF (~0.18), and J_{SC} (~0.9 mA cm^{-2}). The increase in J_{SC} is particularly crucial for achieving good current matching between two perovskite sub-cells (see Figure 6.9c). The V_{OC} enhancement in the device processed by VAG is linked to reduced non-radiative recombination losses, which will be discussed in section 6.4.

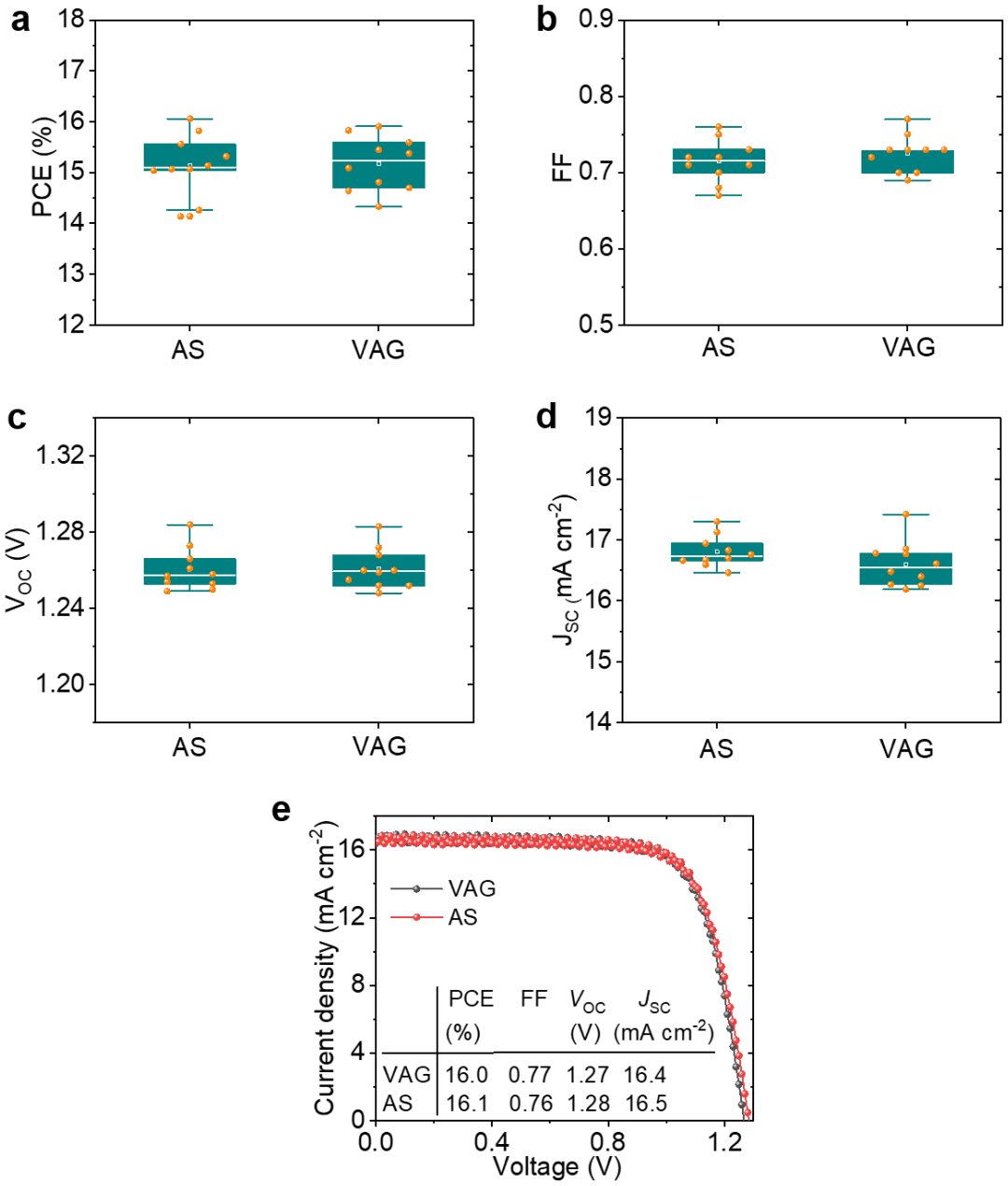

Figure 6.12. Statistical distribution of (a) PCE, (b) FF, (c) V_{OC}, and (d) J_{SC} for semitransparent single-junction top PSCs. The WBG perovskite thin films were fabricated by using VAG and AS. (e) *J-V* characteristics of backward scans for the champion semitransparent single-junction top PSCs. Adapted from Electronic Supplementary Information of Ref.[55] with permission of The Royal Society of Chemistry.

We optimize the thickness of MBG $FAPbI_3$ thin film up to ~650 nm by controlling the perovskite precursor (optimal 1.3 M, see in Figure 6.10). A thicker $FAPbI_3$ thin film within single-junction PSC result in non-recombination loss[213] (Figure 6.10c) and poor charge extraction (Figure 6.10d). A thinner $FAPbI_3$ layer does not have sufficient light absorbing (Figure 6.10d). Therefore, improper thickness of $FAPbI_3$ results in current mismatch in triple junction, as illustrated in Figure 6.11a and 6.11b. We further optimize thickness of WBG perovskite thin film to ~200 nm to match good current generation in triple junction (Figure 6.11a and 6.11c). We find similar the PV performance for semitransparent single-junction top cells fabricated by AS and VAG methods, as shown in Figure 6.12. The champion solar cells realize ~16% of PCEs in both fabrication methods (Figure 6.12e). This could be explained by (i) rapid nucleation/crystallization growth for Br-rich perovskites[214] and/or (ii) promotion of the photoactive (black) phase formation with incorporation of Br^- during the solution process.[215] These are ongoing studies in the future on the subjects of AS and VAG methods for processing high-performance WBG perovskite PVs.

6.4. Key advancement of middle perovskite thin films

In this section, we demonstrate key development of middle perovskite thin film for achieving high-performance perovskite–perovskite–Si MTJSCs. The quality of middle-junction $FAPbI_3$ thin film significantly influences the performance of triple-junction PV.[208,210] To assess this, we compare the morphology of $FAPbI_3$ thin films fabricated using both the AS and VAG methods, abbreviated as AS-$FAPbI_3$ and VAG-$FAPbI_3$, as well as the $FAPbI_3/C_{60}/SnO_x$ stack, namely AS-$FAPbI_3/C_{60}/SnO_x$ and VAG-$FAPbI_3/C_{60}/SnO_x$. Microscopic and scanning electron microscopy (SEM) images reveal the presence of

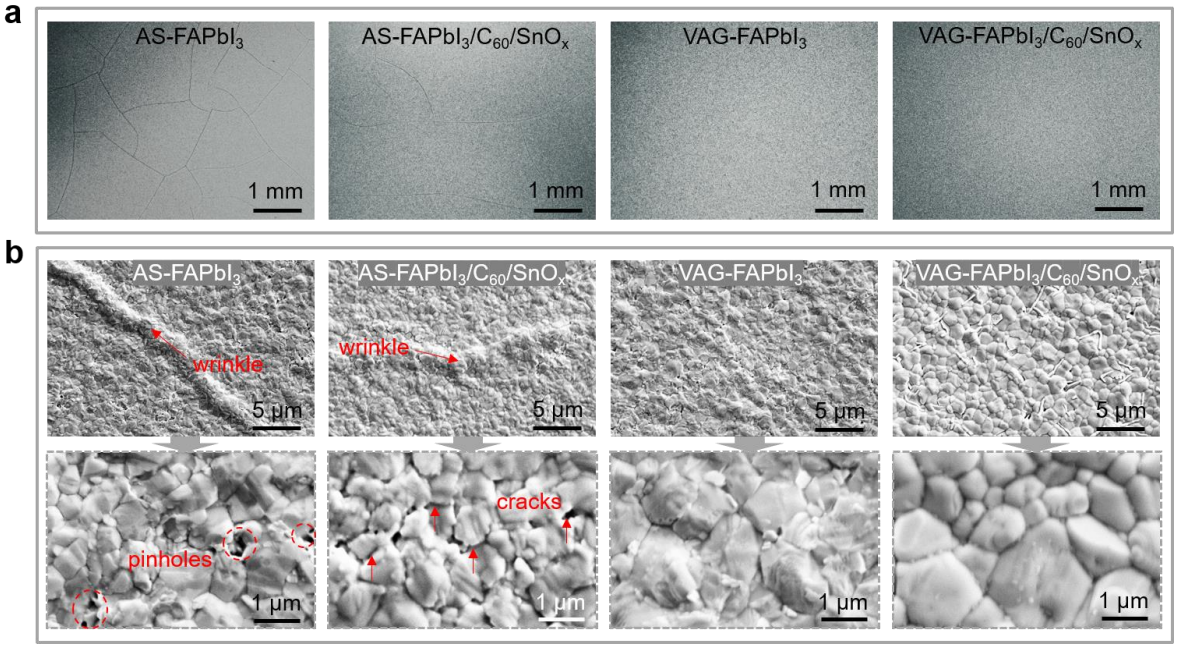

Figure 6.13. (a) Top-view optical microscopic and (b) SEM images of $FAPbI_3$ thin films and $FAPbI_3/C_{60}/SnO_x$ stacks. $FAPbI_3$ thin films were fabricated using VAG and AS methods. Reproduced from Ref.[55] with permission of The Royal Society of Chemistry.

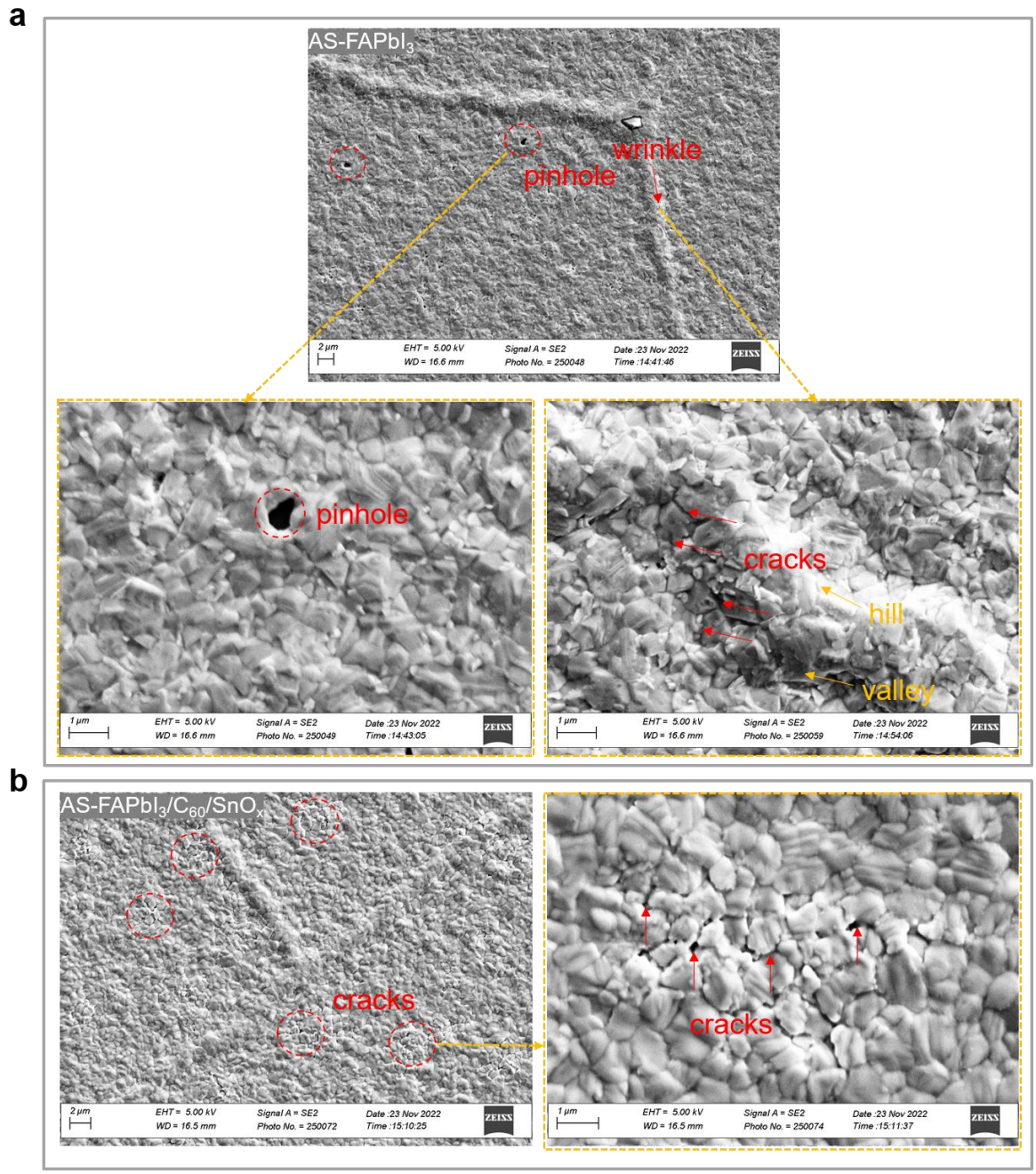

Figure 6.14. Top-view SEM images of (a) AS-$FAPbI_3$ thin film and (b) AS-$FAPbI_3$/C_{60}/SnO_x stack. Adapted from Electronic Supplementary Information of Ref.[55] with permission of The Royal Society of Chemistry.

wrinkles across the surface of AS-$FAPbI_3$ thin film and AS-$FAPbI_3$/C_{60}/SnO_x stack (Figure 6.13). These wrinkles are a common occurrence during the processing of various perovskite thin films[208,210–212] and are typically caused by the relaxation of compressive strain during the perovskite crystallization process.[209–212] This occurs because the thermal expansion coefficients of the TCO or glass substrate are significantly lower than those of the perovskite and organic thin films.[216] The compressive strain release observed in AS-$FAPbI_3$ thin film during its formation is primarily caused by the differences in thermal expansion coefficients between the various layers and the substrate. In this specific case, the substrate consists of several layers, including a Si substrate, an ITO layer, a NiO_x layer, and a layer of 2PACz.

Each of these layers has its own thermal expansion coefficient, which means how much the material expands or contracts when subjected to changes in temperature. When the perovskite precursor is deposited and begins to crystallize, it undergoes volume expansion as it transforms into its final perovskite phase. This expansion can create internal stresses within the perovskite layer, since Si/ITO/NiO_x/2PACz stack constrains the volume expansion of the perovskite during its intermediate phase formation. This constraint results in the release of energy in the form of compressive strain, leading to the formation of wrinkles and other surface features on the perovskite thin film. In the AS quenching process, the anti-solvent (*i.e.*, EA) assists to solvent extraction (*i.e.*, DMF/DMSO) but the corresponding extraction is not efficient during the formation of an intermediate phase of $FAPbI_3$ thin film, leading to the release of compressive strain.[211] In contrast, the VAG process allows for prompt extraction and controlled removal of DMF/DMSO, resulting in a faster formation of intermediate phase.[217,218] Upon post-annealing, less or no residual strain results from solvent release or perovskite volume change between the perovskite thin film and the underlying substrate.[209] AS-$FAPbI_3$ thin films display micro-wrinkles accompanied by pinholes and cracks, ranging from several hundred nanometers in depth (see Figure 6.13

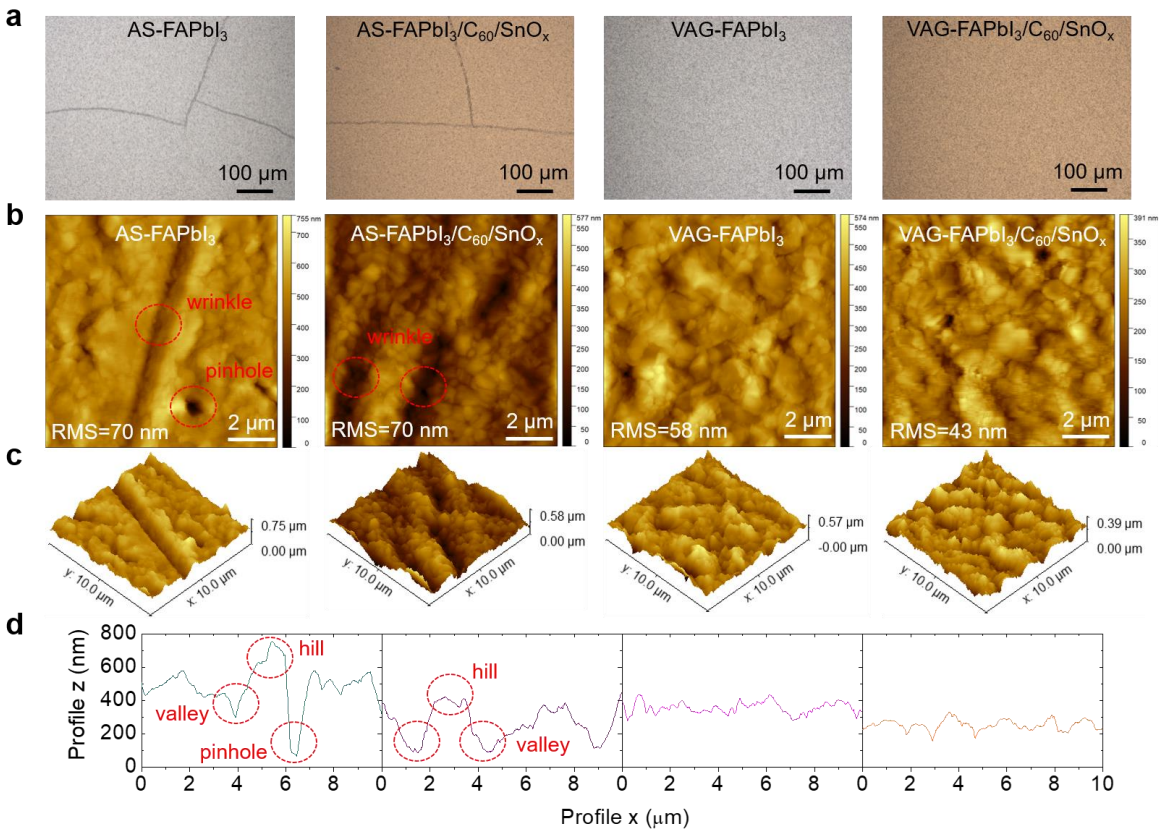

Figure 6.15. (a) Optical microscopic, (b) top-view AFM, (c) 3D AFM images, and (d) the AFM profile of $FAPbI_3$ thin films and $FAPbI_3/C_{60}/SnO_x$ stacks. $FAPbI_3$ thin films were fabricated using VAG and AS methods. The depth of observed pinholes in AS-$FAPbI_3$ thin film is over 650 nm that is comparable with the entire thickness of AS-$FAPbI_3$ thin film. This causes shunting in the middle sub-cell as well as low device yield in triple-junction architecture. A faster penetration goes through these pinholes or cracks in AS-$FAPbI_3$ thin film, *i.e.*, the corrosion from the solvents of the WBG perovskite ink to MBG perovskite. Adapted from Electronic Supplementary Information of Ref.[55] with permission of The Royal Society of Chemistry.

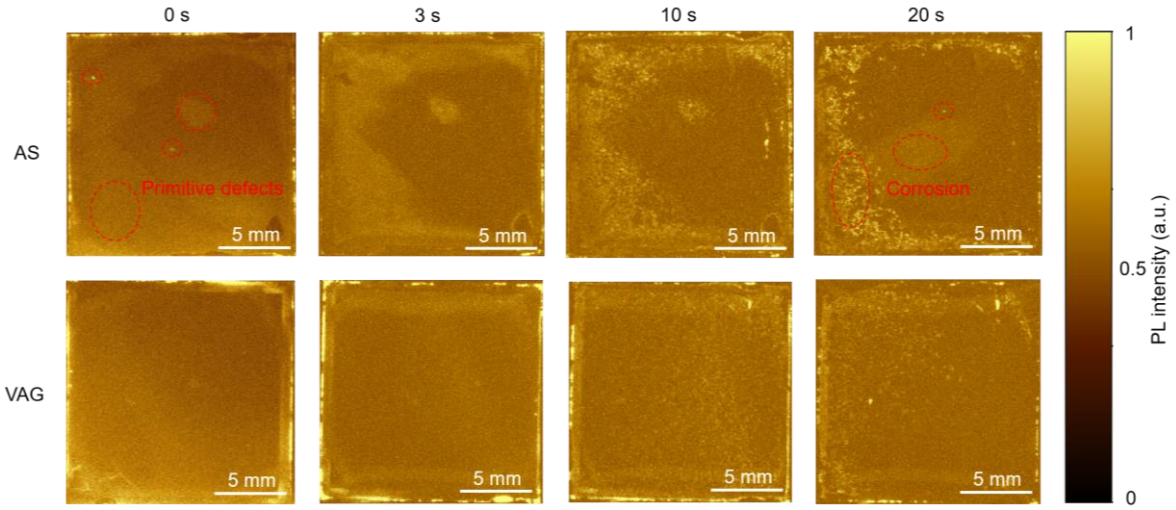

Figure 6.16. Evolution of PL imaging after dropping DMF on the stack of ITO/NiO_x/2PACz/$FAPbI_3$/C_{60}/SnO_x. $FAPbI_3$ thin films were fabricated using VAG and AS methods. When DMF was dropped at 0 s, on the stack, the PL imaging were taken at 0 to 20 s. Adapted from Electronic Supplementary Information of Ref.[55] with permission of The Royal Society of Chemistry.

and 6.14a). For the stack of AS-$FAPbI_3$/C_{60}/SnO_x, numerous cracks remained (see Figure 6.13 and 6.14b), indicating significant residual strain release during the ALD process for SnO_x thin film (*i.e.*, 90 °C deposition of ~35-nm-SnO_x over 2.5 h in our work[15,17]). The wrinkles in AS-$FAPbI_3$ and AS-$FAPbI_3$/C_{60}/SnO_x thin films generate 300–450 nm variation in the depth (*i.e.*, the depth between a hill and a valley, see Figure 6.15), resulting in higher surface roughness (Figure 6.15b and 6.15c) compared to VAG-$FAPbI_3$ thin film and VAG-$FAPbI_3$/C_{60}/SnO_x stack with a relatively flat and compact surface (Figure 6.15d) with larger grains (Figure 6.13b). Importantly, pinholes in the AS-$FAPbI_3$ thin film have a high depth of > 650 nm (Figure 6.15d) that is comparable with the overall perovskite thin film thickness, which causes shunting in the solar cell as well as triple-junction architecture due to a faster penetration of solvents (DMF/DMSO) when processing of WBG perovskite (see Figure 6.16).[17] These pinholes and cracks also acted as non-radiative recombination centers,[209] particularly at the $FAPbI_3$ and C_{60}/SnO_x interface.

The VAG process is employed to achieve stable, high-quality, and α-phase $FAPbI_3$ thin films. Key findings related to the X-ray diffraction (XRD) analysis are in the following:

(1) α-phase formation: XRD patterns confirm the presence of the α-phase in the $FAPbI_3$ thin films for both the VAG and AS fabrication methods (see Figure 6.17).
(2) Crystallite size: Compared with AS-$FAPbI_3$ thin films, VAG-$FAPbI_3$ exhibits a reduction in the full width at half maximum (FWHM), indicating larger crystallites (see Figure 6.17b). Additionally, after the deposition of C_{60}/SnO_x layers, VAG-$FAPbI_3$ shows a further increase in crystallite size, while AS-$FAPbI_3$ demonstrates smaller crystallite sizes (see Figure 6.18a).
(3) Phase stability: The yellow orthorhombic phase (δ-$FAPbI_3$) is observed in AS-$FAPbI_3$ thin films (see Figure 6.17c), and the ratio of δ-phase to (001) increases in the AS-$FAPbI_3$/C_{60}/SnO_x stack that indicates α-to-δ phase transition (see Figure

6.18b). In contrast, VAG-$FAPbI_3$ thin films remain in the pure α-phase both before and after sequential deposition of C_{60}/SnO_x layers, indicating superior phase stability (see Figure 6.18b).

(4) PbI_2 presence: An apparent PbI_2 peak is observed in all $FAPbI_3$ thin films due to the utilization of 10 mol% excess PbI_2 as a standard recipe. The peak ratio of PbI_2 to (001) remains at around 11% for both VAG-$FAPbI_3$ thin films and VAG-$FAPbI_3/C_{60}/SnO_x$ stack (see Figure 6.18c). However, the AS-$FAPbI_3/C_{60}/SnO_x$ stack exhibits an increased ratio from around 13% to over 20% (see Figure 6.18b).

(5) These XRD results demonstrate that the VAG strategy enables the fabrication of high-quality pure-α-FAPbI3 thin films with enhanced phase stability, which is crucial for subsequent high-temperature processing and deposition steps, especially in the context of the top WBG perovskite thin film and the second round of ALD for the top sub-cell.

In a short summary, VAG allows for a more controlled and uniform formation of the stable pure-α-phase $FAPbI_3$ thin films, eliminating of wrinkles, pinholes, and cracks. This high-quality $FAPbI_3$ thin film serves as an ideal substrate for sequential two rounds of temperature-dependent ALD for SnO_x (*i.e.*, ~90 °C). This substrate protection strategy safeguards the $FAPbI_3$ perovskite against high-energy sputtering of recombination layer (Figure 6.13–6.15), prevents solvent penetration during the processing of the WBG

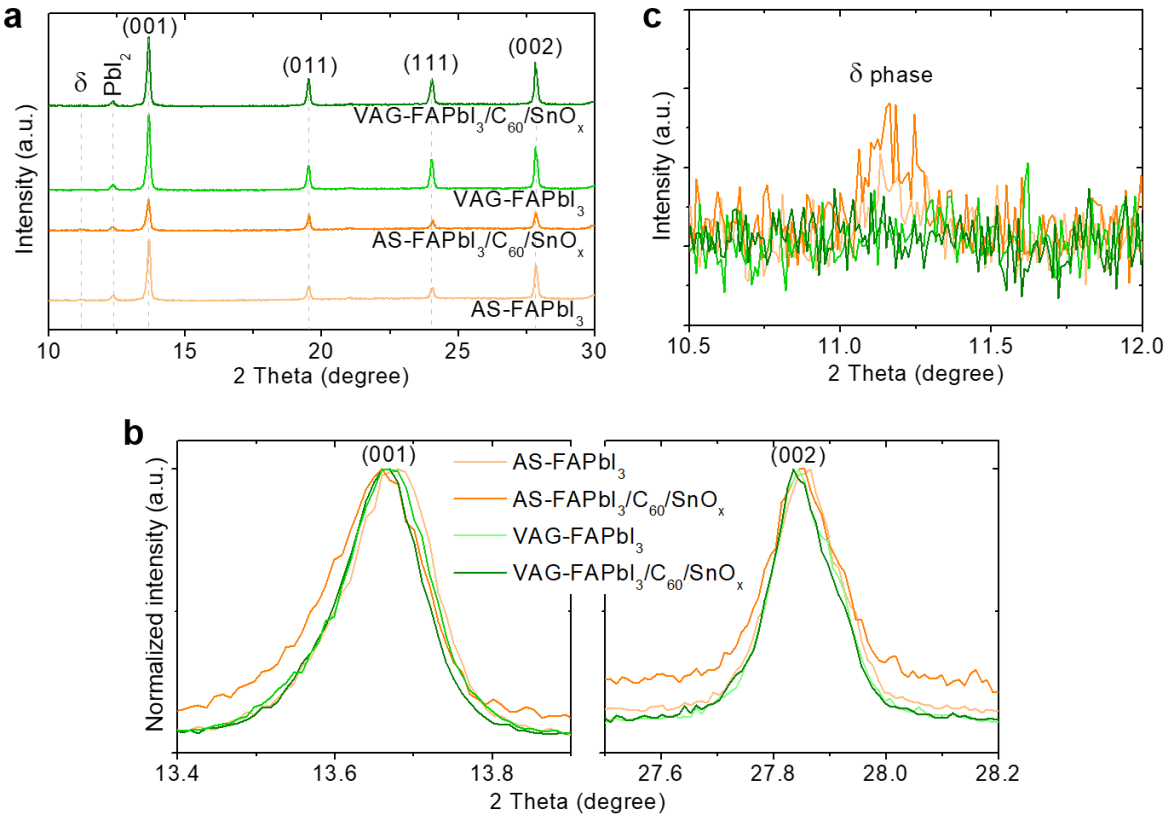

Figure 6.17. (a) Full XRD patterns and zoom-in peaks of (b) (001), (002) planes, and (c) δ phase. $FAPbI_3$ thin films were fabricated using VAG and AS methods. Reproduced from Ref.[55] with permission of The Royal Society of Chemistry.

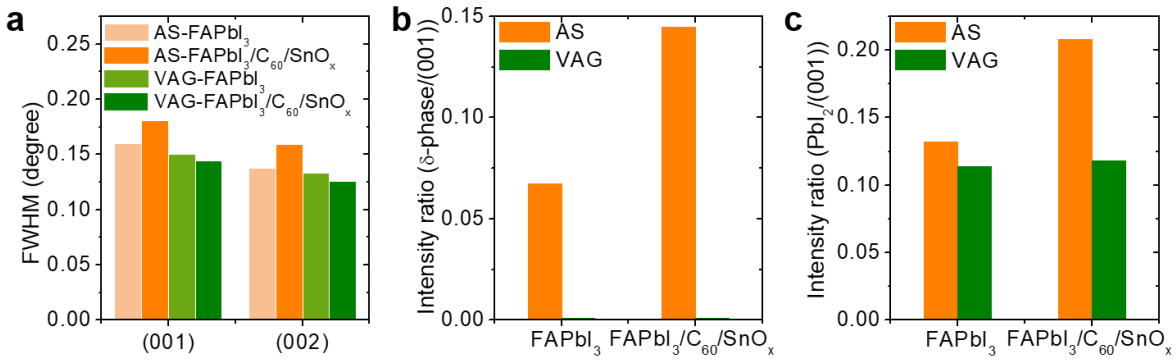

Figure 6.18. (a) Full width at half maximum (FWHM) of XRD. XRD intensity ratios of (b) δ-phase/(001) plane and (c) PbI_2/(001) plane for $FAPbI_3$ thin films and $FAPbI_3/C_{60}/SnO_x$ stack. $FAPbI_3$ thin films were fabricated using VAG and AS methods. Reproduced from Ref.[55] with permission of The Royal Society of Chemistry.

perovskite (Figure 6.16), and withstands high-temperature post-annealing steps for WBG (*i.e.*, ~150°C). These improvements significantly contribute to the high device performance achieved in the triple-junction architecture (Figure 6.6 and 6.7).

6.5. Non-radiative recombination for middle sub-cell

To understand the factors contributing to the improvement in V_{OC}, this section focuses on analyzing the middle perovskite thin films and semitransparent devices. First, time-resolved photoluminescence (TRPL) analysis is utilized to understand charge-carrier dynamics. When examining the half stack of ITO/2PACz/$FAPbI_3$ processed using both VAG and AS methods, a mono-exponential decay is observed (Figure 6.19a). The VAG approach has a somewhat longer charge-carrier lifetime (τ = 3581 ns) than the AS method (τ = 3313 ns). This improvement can be attributed to the larger grain size (*i.e.*, fewer grain boundaries, Figure 6.13b), and high-quality VAG-$FAPbI_3$ thin film (*i.e.*, free pinholes, Figure 6.13 and 6.15), as well as the presence of the pure α-phase (Figure 6.17c and 6.18b).[16,80,131] We further estimate the lifetime for the full stack up to ITO/2PACz/$FAPbI_3/C_{60}/SnO_x$ (Figure 6.19a and Table 6.1). This architecture shows a bi-exponential decay with a fast (τ_1) and a slow lifetime (τ_2). We find very short τ_1 (AS: 3 s; VAG: 4 s) in both AS and VAG methods, revealing a fast charge-carrier transfer from the $FAPbI_3$ thin film to C_{60}/SnO_x layers (Table 6.1). A longer τ_2 is observed in VAG process (τ_2 = 27 ns, Figure 6.19a), in comparison with AS (τ_2 = 16 ns), demonstrating less non-radiative recombination in the bulk of $FAPbI_3$ thin films and/or at the interfaces with carrier-selective contacts (2PACz/$FAPbI_3$ and $FAPbI_3/C_{60}/SnO_x$).[16,80,131]

To quantify the reduction of non-radiative recombination in the perovskite bulk and at the interfaces, we conduct photoluminescence quantum yield (PLQY) measurements and calculate implied open-circuit voltage ($V_{OC\text{-}imp}$).[73,187] Since the PLQY diminishes in the stack of ITO/2PACz/$FAPbI_3/C_{60}/SnO_x$ compared to stacks without C_{60}/SnO_x (*i.e.*, from 2.5×10^{-2} to 1.2×10^{-3} for VAG, from 2.0×10^{-2} to 3.9×10^{-5} for AS, see Figure 6.19b), we conclude that the primary V_{OC} loss is due to the interface between $FAPbI_3$ and C_{60}/SnO_x. The corresponding average $V_{OC\text{-}imp}$ values for the VAG and AS processes are 1.056 V and 0.969

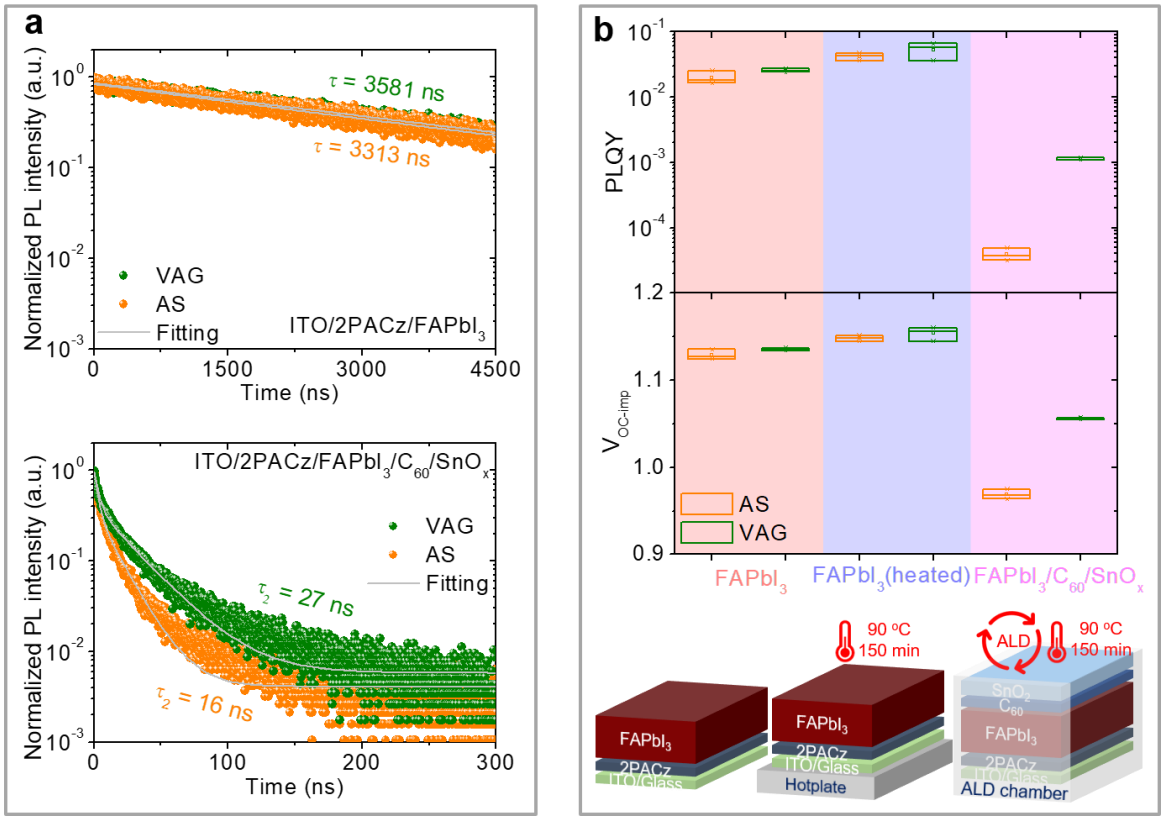

Figure 6.19. (a) TRPLs and (b) PLQYs for ITO/2PACz/$FAPbI_3$ and ITO/2PACz/$FAPbI_3$/C_{60}/SnO_x stacks. $FAPbI_3$ thin films were fabricated using VAG and AS methods. ALD process was performed at 90 °C deposition temperature for 150 min. Reproduced from Ref.[55] with permission of The Royal Society of Chemistry.

Table 6.1. Summary of TRPL measurements. Adapted from Electronic Supplementary Information of Ref.[55] with permission of The Royal Society of Chemistry.

Samples	τ_1 (ns)	Fraction 1	τ_2 (ns)	Fraction 2	t_{avg} (ns)
ITO/2PACz/VAG-$FAPbI_3$	-	-	-	-	3581
ITO/2PACz/AS-$FAPbI_3$	-	-	-	-	3313
ITO/2PACz/VAG-$FAPbI_3$/C_{60}/SnO_x	4	0.582	27	0.418	14
ITO/2PACz/AS-$FAPbI_3$/C_{60}/SnO_x	3	0.629	16	0.371	8

TRPL plots was fitted with a mono-exponential equation: $Y = A \exp(-t/\tau)$, and a bi-exponential equation: $Y = A_1 \exp(-t/\tau_1) + A_2 \exp(-t/\tau_2)$. τ_1 and τ_2 reveal a fast lifetime and a slow lifetime, respectively.

V, respectively. For the stack of ITO/2PACz/$FAPbI_3$, VAG process presents a slightly higher average PLQY of 2.5×10^{-2} (Figure 6.19b), compared to AS method with an average PLQY of 2.0×10^{-2}. This slight increase correlates to the increased grain size (Figure 6.13b) of VAG-$FAPbI_3$ thin film. The comparable average values of $V_{OC\text{-}imp}$ (VAG: 1.135 V; AS: 1.129 V; see Figure 6.19b) indicate negligible non-radiative recombination loss from the bulk and 2PACz/$FAPbI_3$ interface. These demonstrate that the perovskite/ETL interface dominates the V_{OC} loss in the *p-i-n* semitransparent device as well as triple-junction architecture in this work, which is in line with previous reports on Si based double-junction solar cells.[13,219] It should be noted that the $V_{OC\text{-}imp}$ loss is decreased to 0.079 V for VAG

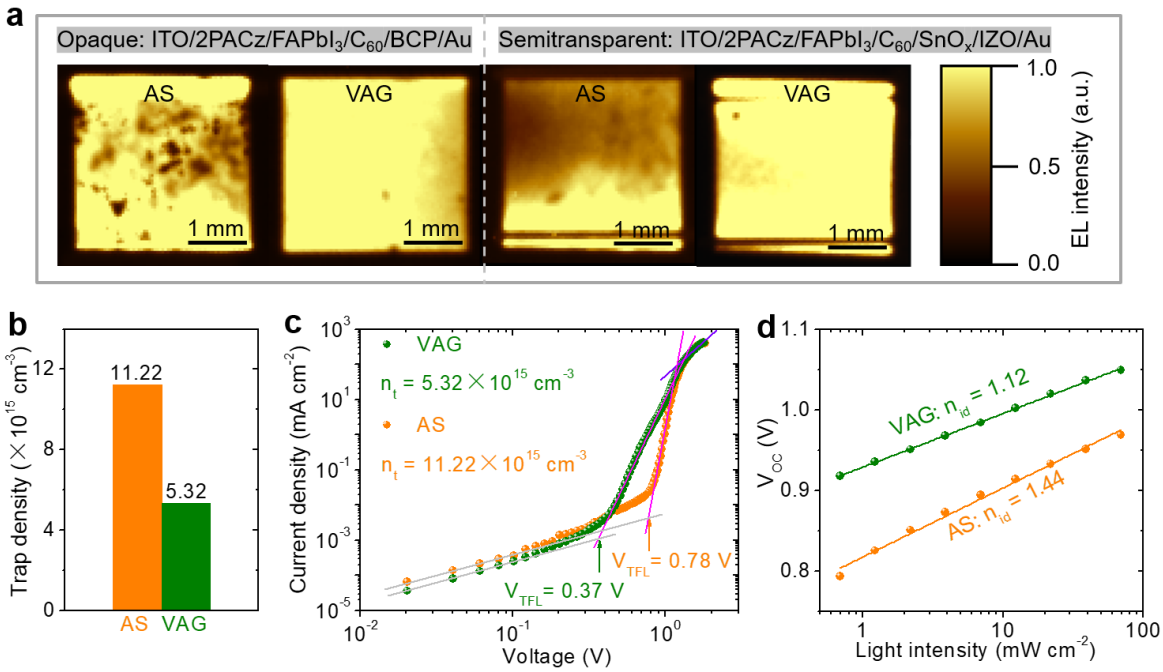

Figure 6.20. (a) EL imaging of opaque and semitransparent single-junction middle sub-cells. (b) Trap density evaluated from SCLC method, (c) SCLC analyses, and (d) light-intensity dependent V_{OC} of semitransparent single-junction middle sub-cells. Middle perovskite thin films were fabricated using VAG and AS methods. Reproduced from Ref.[55] with permission of The Royal Society of Chemistry.

process due to the interface of $FAPbI_3$ and C_{60}/SnO_x, compared to 0.160 V for AS method (Figure 6.19b). This matches well with the difference in V_{OC} (*i.e.*, 0.08 V; V_{OC} = 1.08 V for VAG, V_{OC} = 1.00 V for AS) as observed in PV performance (Figure 6.9b). Furthermore, we discover that the ALD temperature (90 ºC for 150 min) has no effect on $FAPbI_3$ thin films, as the PLYQ and $V_{OC\text{-}imp}$ slightly rise when the samples of ITO/2PACz/$FAPbI_3$ were treated at the same temperature (Figure 6.19b). The presence of a high trap density could be attributed to defects at the interface between AS-$FAPbI_3$ and C_{60}/SnO_x, likely caused by poor perovskite film quality and the unstable α phase in the AS-$FAPbI_3$. This high trap density might lead to significant trap-assisted non-radiative recombination,[13,219] as further discussed in the following characterizations.

In opaque and semitransparent $FAPbI_3$-based devices, electroluminescence (EL) imaging is employed to determine defect distribution and film uniformity. The EL intensity increases with the local-junction voltage, making dark regions indicative of local defects.[17,220,221] The VAG approach produces devices with high uniformity and minimal defects, as seen in Figure 6.20a. Devices fabricated utilizing the AS approach, however, have a high number of local defects. These defects are mainly localized at the $FAPbI_3$/ETL interface due to the presence of pinholes, cracks, wrinkles, and inactive δ-phase.[210] As discussed in section 6.1, interfacial trap states originate from these defects, leading to more severe non-radiative recombination losses at the interface of $FAPbI_3$ and C_{60}/SnO_x. Trap density (n_t) is further estimated using the space-charge-limited-current (SCLC) method.[16,79–82] Electron-only device architectures of ITO/SnO_x/$FAPbI_3$/C_{60}/SnO_x/IZO/Au were fabricated for SCLC analyses. As shown in Figure 6.20b and 6.20c, the VAG device has a lower n_t of 5.32 × 10^{15}

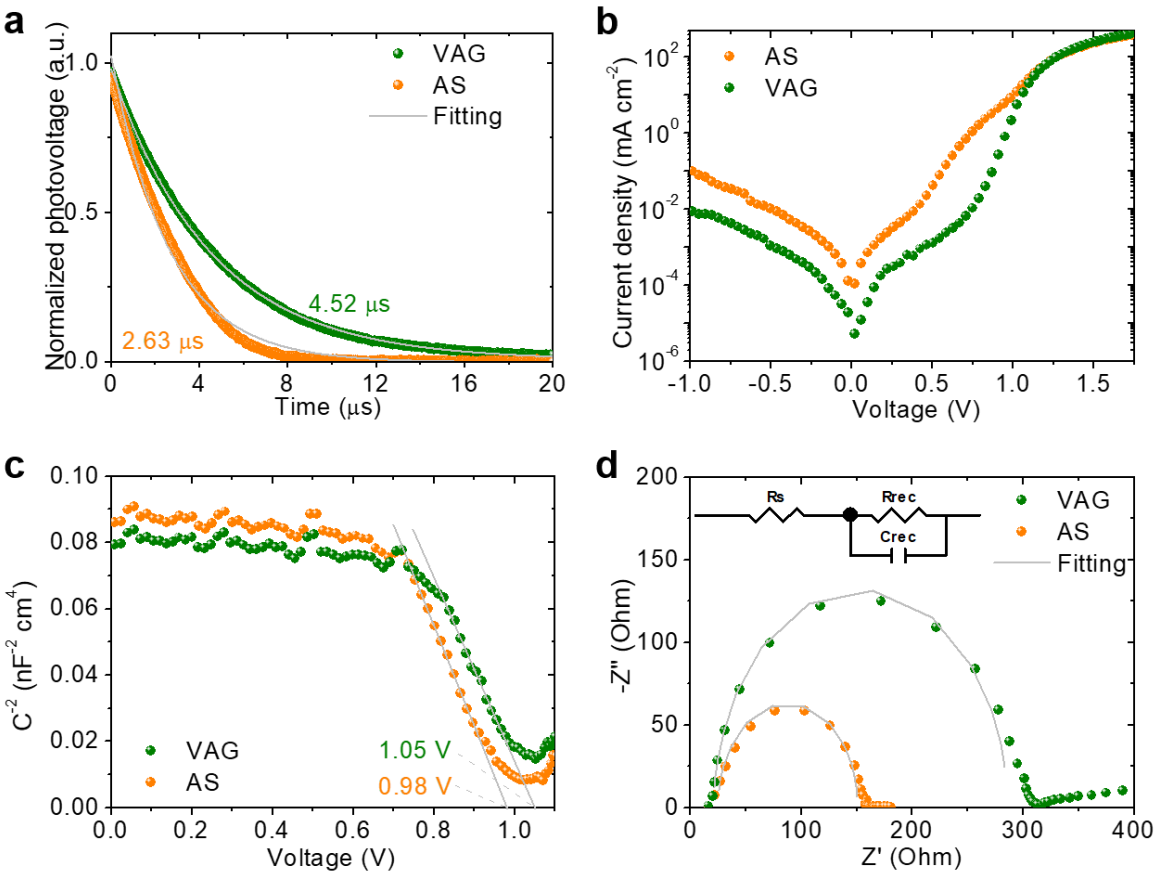

Figure 6.21. (a) Normalized transient photo-voltage decay, (b) dark *J-V* characteristics, (c) Mott–Schottky plots, and (d) Nyquist plots of semitransparent single-junction middle sub-cells. The inset in (d) illustrates an equivalent circuit. Middle perovskite thin films were fabricated using VAG and AS methods. Reproduced from Electronic Supplementary Information of Ref.[55] with permission of The Royal Society of Chemistry.

Table 6.2. Summary of EIS measurements for semitransparent single-junction middle sub-cells. Adapted from Electronic Supplementary Information of Ref.[55] with permission of The Royal Society of Chemistry.

Samples	R_s (Ω)	R_{rec} (Ω)	C_{rec} (nF)
AS	24.7	126.2	0.1
VAG	21.3	264.0	0.1

R_s: series resistance; R_{rec}: charge recombination resistance; C_{rec}: charge recombination capacitance. All data were fitted with Z-View.

cm^{-3} compared to the AS device (n_t = 11.22 × 10^{15} cm^{-3}), indicating significantly reduced trap-assisted non-radiative recombination at the interface between $FAPbI_3$ and C_{60}/SnO_x layers. This conclusion is further supported by a lower ideality factor (n_{id} = 1.12 for VAG, n_{id} = 1.44 for AS, Figure 6.20d).

Having demonstrated reduced non-radiative recombination in a half stack of devices, we further verify the charge carrier dynamics in the full stack of semitransparent devices using transient photo-voltage (TPV) measurements. It is found that the charge-recombination lifetime of VAG device (4.52 μs) is higher compared to AS device (2.63 μs, see Figure 6.21a), indicating the suppressed charge recombination pathways in VAG.[222,223] A reduced

dark saturation current density (Figure 6.21b), higher flat-band potential in Mott–Schottky plots (Figure 6.21c), and a higher charge recombination resistance in electrochemical impedance spectroscopy measurements (Figure 6.21d and Table 6.2) further indicate the slower charge recombination in VAG device, since they are consistent with TRPL, PLQY, EL, SCLC, and n_{id} analyses (Figure 6.19 and 6.20).

In brief, employing VAG strategy yields high-quality $FAPbI_3$ thin films and high-performance single-junction solar cells with minimized non-radiative recombination due to a reduced trap density at the $FAPbI_3$ and C_{60}/SnO_x interface (Figure 6.20). The latter is a result of an improved thermal stability (Figure 6.17 and 6.18) and film morphology (free of pinholes, cracks, and wrinkles, Figure 6.13–6.16) and boosts the device V_{OC} of single-junction (Figure 6.9b) and triple-junction (Figure 6.6c and 6.7) architectures.

6.6. Durability of triple-junction solar cells

The durability of our non-encapsulated perovskite–perovskite–Si MTJSCs is evaluated in this section. All stability tests were conducted in a N_2-filled glovebox. We first determined the operational stability of AS and VAG triple-junction devices at maximum power point (MPP) tracking under continuous AM 1.5G illumination at ~50 °C. The VAG device preserves 96% of its original PCE after 11 h, showing superior light stability than the AS device that retains 89% of its original PCE (see Figure 6.22a). Light-induced phase segregation in the WBG (~1.84 eV) top cell might explain the small reduction in PCE after

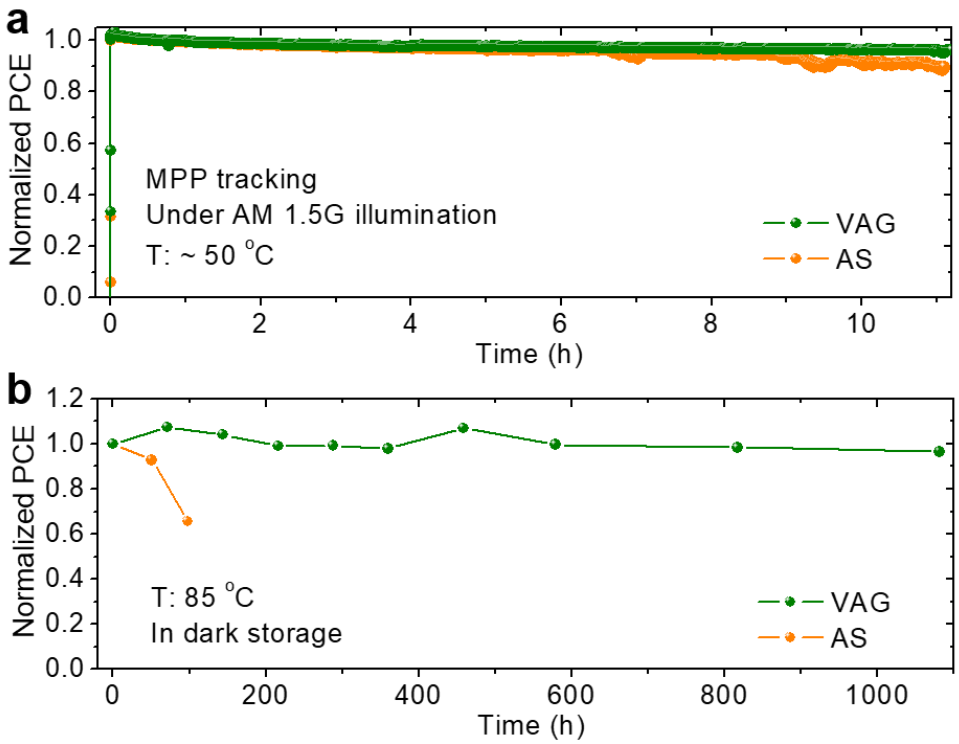

Figure 6.22. PCE evolution of non-encapsulated perovskite–perovskite–Si MTJSCs in a N_2-filled glovebox (a) under continuous AM 1.5G illumination at ~50 °C for MPP tracking and (b) in dark storage at 85 °C. Middle perovskite thin films were fabricated using VAG and AS methods. Adapted from Ref.[55] with permission of The Royal Society of Chemistry.

up to ~30 h of long-term illumination (see Figure C4) as a high Br content was applied into WBG composition (see Figure 6.23a).[30,202,224] For the triple-junction solar cell based on AS-$FAPbI_3$, the instability originates from both unstable WBG and MBG (see Figure 6.23a and 6.23b). Thermal stability was also tested in the dark at a higher temperature of 85 °C. After 1081 h, the VAG device kept 96.6% of its initial PCE (see Figure 6.22b), whereas the PCE of AS device declines to 65.6% after 98 h. We attribute the enhanced thermal stability to the stable MBG top cell fabricated by VAG method that is also demonstrated in single-junction architectures (see Figure 6.23c). We highlight that our MTJSCs realize excellent thermal stability, which are much more stable than previous reported triple-junction architectures.[20,29,30,201–205] The decrease in PCE for AS device is ascribed to the poor AS-$FAPbI_3$ perovskite film quality and α-to-δ phase transition,[27] as has been discussed in section 5.7. We conclude that the VAG technique has demonstrated its capability to produce high-quality and stable middle perovskite thin films, offering a promising approach for enhancing the long-term thermal stability in triple-junction designs. This development is a significant

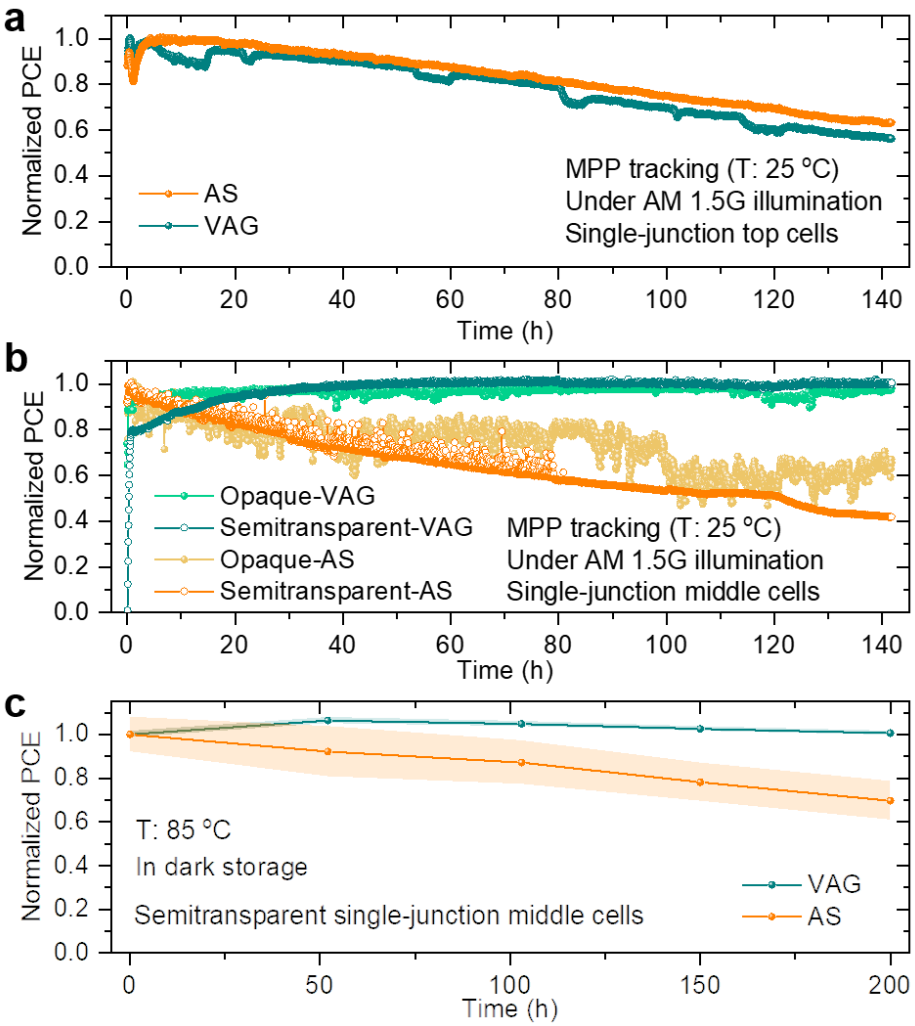

Figure 6.23. PCE Evolution for non-encapsulated devices in a N_2-filled glovebox. Single-junction (a) top and (b) middle cells (semitransparent and opaque architectures) under continuous AM 1.5G illumination at 25 °C for MPP tracking. (c) Semitransparent middle cells in dark storage at 85 °C. Reproduced from Electronic Supplementary Information of Ref.[55] with permission of The Royal Society of Chemistry.

step forward in advancing the reliability and durability of perovskite-based multi-junction technologies.

6.7. Summary

In this chapter, we demonstrate highly efficient perovskite–perovskite–Si MTJSCs. Appling results from optical simulations, we obtain optimal bandgaps and thicknesses for both perovskite thin films of the top and middle sub-cells, *i.e.*, ~1.84 eV for WBG with thickness of ~200 nm, ~1.52 eV for WBG with thickness of ≥600 nm, and ~1.1 eV for Si, as we compromise to a small extend for using $FAPbI_3$ as MBG perovskite to realize achievable PCE with maximum value of 24.8%. The simulated photocurrent densities for each sub-cell, *i.e.*, top, middle, and bottom sub-cells, are 12.0, 11.7, and 15.4 mA cm^{-2}, respectively. The reflection and parasitic absorption losses can be minimized to 4.4 and 2.8 mA cm^{-2}, respectively.

We achieve an excellent PCE of 24.4% for our champion triple-junction device based on Si cell/ITO/NiO_x/2PACz/$FAPbI_3$/C_{60}/SnO_x/ITO/NiO_x/2PACz/$Cs_{0.2}FA_{0.8}Pb(I_{0.5}Br_{0.5})_3$/LiF/$C_{60}$/$SnO_x$/IZO/Au/$MgF_2$ architecture. We highlight that this is the record PCE in this triple-junction architecture. With optimization of the both top and middle perovskite sub-cells, antireflection coating, and top TCO, we minimize the current mismatch and realize maximum current generation up to 11.6 mA cm^{-2} in triple junction. The photocurrent densities for the top, middle, and bottom cells were integrated to 11.6, 11.0, and 15.9 mA cm^{-2}, respectively. The triple-junction device demonstrates low reflection (integrated photocurrent density of ~2.2 mA cm^{-2}) and absorption (integrated photocurrent density of ~5.9 mA cm^{-2}) losses. Furthermore, we realize a record V_{OC} of 2.84 V in this triple-junction architecture as the key development is the processing of high-quality middle perovskite thin film.

Based on the SEM, AFM, and XRD characterizations, we conclude that the VAG process enable a high-quality phase-stable $FAPbI_3$ middle perovskite thin film free of wrinkles, pinholes, and cracks. EL, SCLC, light-intensity dependent V_{OC}, TPV, dark *J-V*, Mott-Schottky, and EIS analyses verify the low non-radiative recombination loss at the interface of $FAPbI_3$ and C_{60}/SnO_x layers. This explains the improved PV performance in semitransparent single-junction architecture, *i.e.*, PCE of 20.0%, V_{OC} of 1.08 eV, FF of 0.84, J_{SC} of 22.0 mA cm^{-2} for VAG process; PCE of 13.9%, V_{OC} of 1.00 eV, FF of 0.66, J_{SC} of 21.1 mA cm^{-2} for AS method.

Last, the triple-junction device based on VAG processed $FAPbI_3$ realize superior operational stability and excellent thermal stability. Under continuous AM 1.5G illumination, the VAG-processed device maintains 96% of its initial PCE after 11 h, which is more stable than AS-processed device maintaining 89% of its initial PCE. Under continuous heating up at 85 °C, VAG-processed device retains 96.6% of initial PCE after 1081 h, whereas the initial PCE drops to 65.6% after 98 h for AS-processed device.

7. Conclusions and outlook

Perovskite solar cells (PSCs) are promising next-generation technology of solar conversion. Perovskite-based multi-junction solar cells start a new era of ultra-high-efficiency photovoltaics (PVs). However, the performance, stability, and scalability are critical challenges for future commercialization. This thesis highlights the importance of interface engineering with addressing the **Challenges 1 to 8** (described in chapter 1) in small-area single-junction/multi-junction solar cells, and large-area min-modules. In brief, this thesis contributes to (i) the development of Sn-Pb based PSCs and four-terminal (4T) all-perovskite tandems and a better understanding of non-radiative recombination and charge extraction, (ii) upscaling lab-scale solar cells (< 1 cm^2) to mini-module dimensions (> 10 cm^2), and (iii) a key advancement of triple-junction perovskite–perovskite–Si solar cells.

Fullerene-derivative interlayers for Sn-Pb based perovskite in tandem photovoltaics

Chapter 4 targets with **Challenges 1 and 2** in Sn-Pb based narrow-bandgap (NBG) PSCs and all-perovskite tandem solar cells. We explore two novel solution-processed fullerene derivatives (IPB and IPH) as an interlayer at the interface of Sn-Pb based NBG and ETL. The devices incorporated with IPH interlayer achieve the best PV performance with improved open-circuit voltage (V_{OC}) and short-circuit current density (J_{SC}). The formation of a higher conduction band offset ~0.2 eV (> 0 eV) between NBG and ETL reduces the charge-carrier-back-transfer recombination. A decreased trap density at the NBG/interlayer/C_{60} interfaces minimizes the trap-assisted recombination. These contribute to the total reduction in non-radiative recombination. The enhanced charge extraction is demonstrated within PSCs and explains to the improvement in J_{SC}. By employing this strategy, 4T all-perovskite tandem solar cells achieve significant enhancement in PV performance. This work provides a promising rote in advancing the PV performance of Sn-Pb based NBG PSCs and all-perovskite tandems.

The PV performance and long-term stability of Sn-based PSCs still lag behind compared to the pure Pb-based PSCs, which is the main constrains to the 2T or 4T all-perovskite tandems. Our champion NBG device achieves only 82.5% of detailed-balance limit in V_{OC} (for the E_g of 1.26 eV),[8] suggesting a large headroom for further decreasing the V_{OC} loss in the future work. Sn-based perovskite has basically higher possibility of defects at the bulk or interfaces, since the Sn^{+2} is easily oxidized to Sn^{+4}. Therefore, the bulk passivation (*e.g.*, additive for

further preventing the Sn^{+2} oxidation) or the buried interface engineering (*e.g.*, NBG/HTL interface) are needed to reduce the non-radiative recombination and enhance the stability. In addition, the nucleation and crystallization of Sn-Pb based NBG perovskite are much more rapid than the pure Pb based perovskite during the solution-based process. Thus, it is necessary to explore well-controlled fabrication methods to obtain high-quality pinhole-free NBG perovskite thin film, like the vacuum assisted growth (VAG) strategy employed in this thesis. This method has been well-developed in our latest work of scalable all-perovskite solar modules.

The J_{SC} of our Sn-Pb based NBG is still as low as 82.7% of the theoretical limit, according to the detailed-balance calculation.[8] This thesis introduces an interlayer to modify the energy-level alignment between NBG and ETL, demonstrating the benefit of enhanced charge extraction to the J_{SC} improvement. Therefore, energy-level optimization for HTL or ETL is pivotal to further improve the PV performance. To date, PEDOT:PSS is the most widely used HTL, especially in 2T all-perovskite tandem architecture, as it is considered with ideal energy-level alignment with NBG.[225] However, its intrinsic acidity is known to scarify the device stability over time. Although > 28% PCEs have been realized in 2T or 4T all-perovskite tandems,[112–115] it is urgent to develop new HTLs or passivation its corresponding interface.

Buried interface engineering for scalable processing of *p-i-n*-based $FAPbI_3$ perovskite solar modules

Chapter 5 deals with **Challenges 1 to 4** in middle-bandgap (MBG) formamidinium lead iodide ($FAPbI_3$) PSCs and min-modules in *p-i-n* architecture. First, we study the effect of interfacial voids (located at the buried interface of perovskite/HTL) on the non-radiative recombination and charge extraction within small-area (0.105 cm^2) PSCs. The optimization of vacuum-assisted growth (VAG) process realizes void-free buried interface in small-area PSCs, whereas server interfacial voids appear in anti-solvent processed devices. The enhanced PV performance is attribute to the decreased non-radiative recombination loss and improved charge extraction. Small PSCs (1.6 × 1.6 cm^2) are scaled up to a larger dimension (6.4 × 3.2 cm^2) with elimination of interfacial voids by a novel strategy: well-controlled nitrogen (N_2) flow during VAG process and methylammonium chloride (MACl) as an additive in the perovskite precursor. High-quality, void-free, and pinhole-free large-area perovskite thin films are achieved by blade-coating process. A power conversion efficiency (PCE) of 18.3% for fully scalable $FAPbI_3$ perovskite solar mini-modules (aperture area of 12.25 cm^2, geometric fill factor (GFF) of 96.3%) is achieved with negligible voltage loss and good current collection in upscaling process. This is a remarkable improvement for improving the performance of perovskite solar module PVs.

The development of scaling-up process as well as module fabrication are crucial for the future commercialization. The most important processing is large-scale deposition for perovskite thin films. For the scalable methods, the crystallization control is critical for high-quality perovskite thin films, including additive/solvent engineering,[180] compositional engineering,[174,181], interfacial engineering.[181,182] For FA-based perovskite, the drying process

(solvent extraction speed) for the wet perovskite thin film is important to control the nucleation and crystallization that is highlighted in this thesis. This thesis employs the basic high boiling-point solvent system (DMF/DMSO) in the blade-coating process, making the drying process challenging. The further research interest could be searching low boiling-point solvents, environmental friendly/green co-solvents, or additives in the precursors to fulfill the industrial manufacturing. Moreover, the blade-coating produces a thickness variation, which is more server especially in processing of a larger substrate dimension. To address this issue, the alternative scalable methods (like developing vacuum deposition) are needed, or further improving the crystallization procedure is crucial to improve the thickness homogeneity of the large-area perovskite thin film.

Perovskite–perovskite–silicon triple-junction photovoltaics

Chapter 6 solves the **Challenges 1, 2, and 5 to 8** within two terminal (2T) triple-junction perovskite–perovskite–Si solar cell. With the advantages of optical simulation and experimental optimization in light management, the current mismatch is minimized and then maximized to 11.6 mA cm^{-2} in triple junction, which is the highest value of J_{SC} in reported triple-junction architecture. A key junction with MBG perovskite is developed using a stable pure-α-phase $FAPbI_3$ perovskite thin film with high quality (free of wrinkles, cracks, and pinholes), enabling a high V_{OC} up to 2.84 V in the triple-junction solar cells. In addition, the triple-junction solar cells are demonstrated excellent thermal stability. This is a significant advancement in perovskite-based multi-junction solar cells.

Perovskite based multi-junction PVs, such as three or more than three junctions, still lag behind with the PCEs compared to the tandem architecture. More junctions mean more complexities of layer-by-layer processing. In our presented perovskite–perovskite–Si triple-junction solar cells, the V_{OC} (2.84 V) is still less than the simulated value (2.95 V). This indicates that the non-radiative recombination loss (110 mV) can be further minimized by optimization the architecture or perovskite junctions. The most important junction, middle junction, still has a large room for enhancing the V_{OC}. We report 11.6 mA cm^{-2} of total J_{SC} in our triple junction that is limited by the MBG perovskite sub-cell (generated 11.0 mA cm^{-2}), which is also less than our simulated value (11.7 mA cm^{-2}). The further research work will focus on the optimization the middle sub-cell to improve the entire J_{SC}, such as a better light management, improved thickness of MBG perovskite, improved charge extraction at the recombination junctions, *etc*. Since our triple-junction solar cell is limited with the energy yield in lower wavelength regions, *i.e.*, the current generation is limited by top and middle sub-cells (simulated J_{SC} of 12.0, 11.7, and 15.4 mA cm^{-2} for the top, middle, and bottom sub-cells, respectively), the future work need to develop a lower E_g (1.4–1.5 eV) of middle sub-cell to maximize the J_{SC}.[19,20] However, the E_g less than 1.5 eV would be based on NBG Sn-based perovskite, *i.e.*, the stability of the triple-junction may be sacrificed. Therefore, the development of stable MBG perovskite is the key for improving the performance of triple-junction PVs. 3T architecture would be a perfect solution to gain a higher energy yield without using Sn-based perovskite sub-cell. Considering the simulated EQE data, the Si sub-cell can generate an excess current (15.4–11.7= 3.7 mA cm^{-2}) in 3T

architecture compared to the current generation from top and middle sub-cells (12.0 and 11.7 mA cm^{-2}, respectively). The extra current of 3.7 mA cm^{-2} can further contribute to the power output by Si bottom cell. For example, if the Si sub-cell produces a V_{OC} of 0.65 V and a FF of 0.72 in this junction, 3T will gain an extra PCE of ~1.73% that means a total PCE of 26.5% (26.5%=24.8%+1.37%) is possible for 3T architecture.

Appendix

A. Appendix of Chapter 4

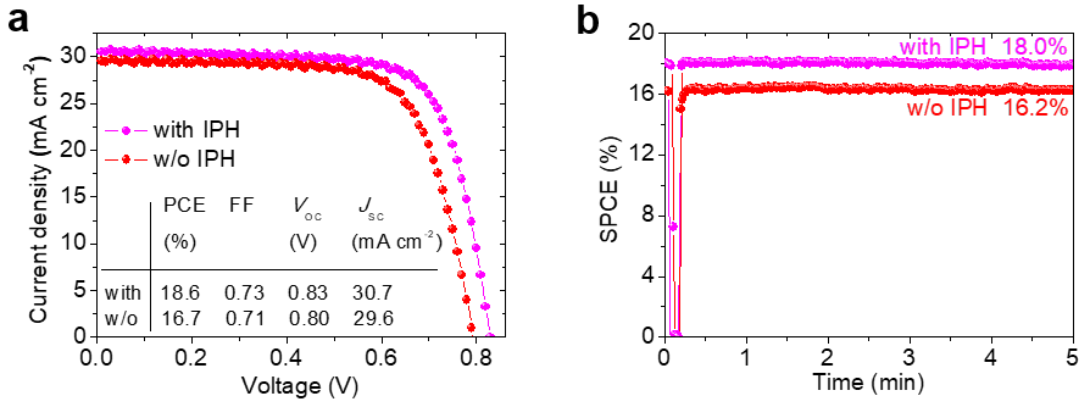

Figure A1. (a) *J-V* characteristics of the champion PSCs obtained from backward scan. (c) Stabilized power conversion efficiency (SPCE) under continuous AM 1.5G illumination of the champion PSCs. Reproduced from Ref.[16] with permission of Wiley.

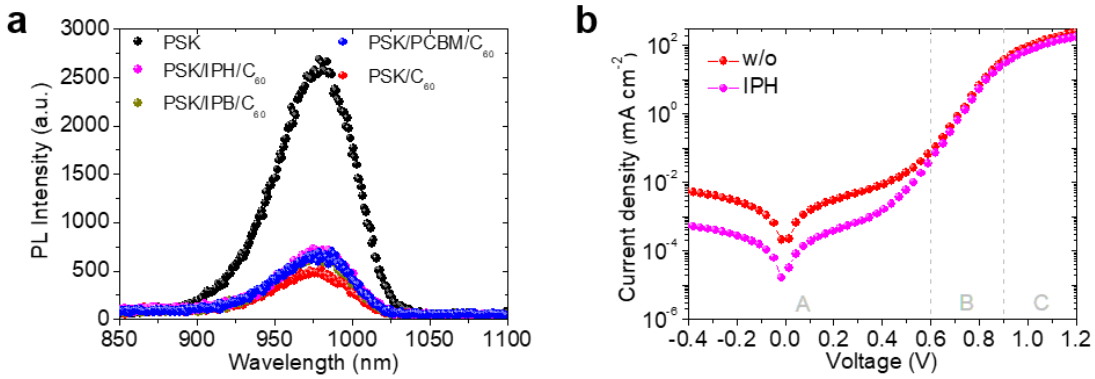

Figure A2. (a) Steady-state photoluminescence (PL) of NBG perovskite thin film and perovskite/C_{60} stack with and without fullerene derivatives. All samples were fabricated on bare glass substrates. (b) Dark current-density-voltage (*J-V*) characteristics of the champion PSCs with and without IPH interlayer. The *J-V* curves can be defined three regions: region A illustrates the leakage current region B shows exponential diode comportment, region C presents the series resistance (R_s) for the entire PSCs. Reproduced from Supporting Information of Ref.[16] with permission of Wiley.

B. Appendix of Chapter 5

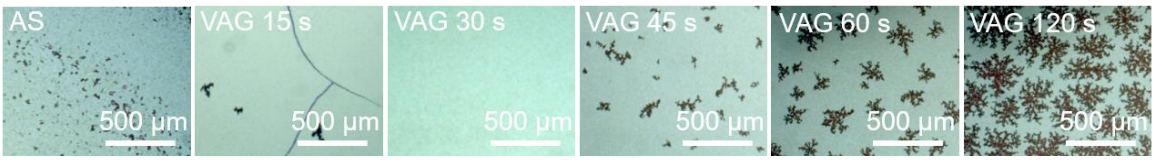

Figure B1. Optical microscopic images of $FAPbI_3$ PSCs based on *p-i-n* architecture (visualized from glass side, substrate dimension: 1.6 × 1.6 cm^2). The devices were fabricated via AS and VAG method (vacuum time varies from 15 to 120 s). The dark region indicates interfacial voids. The void ratio in area were calculated using these pictures. Reproduced from Ref.[27] with permission of Elsevier.

C. Appendix of Chapter 6

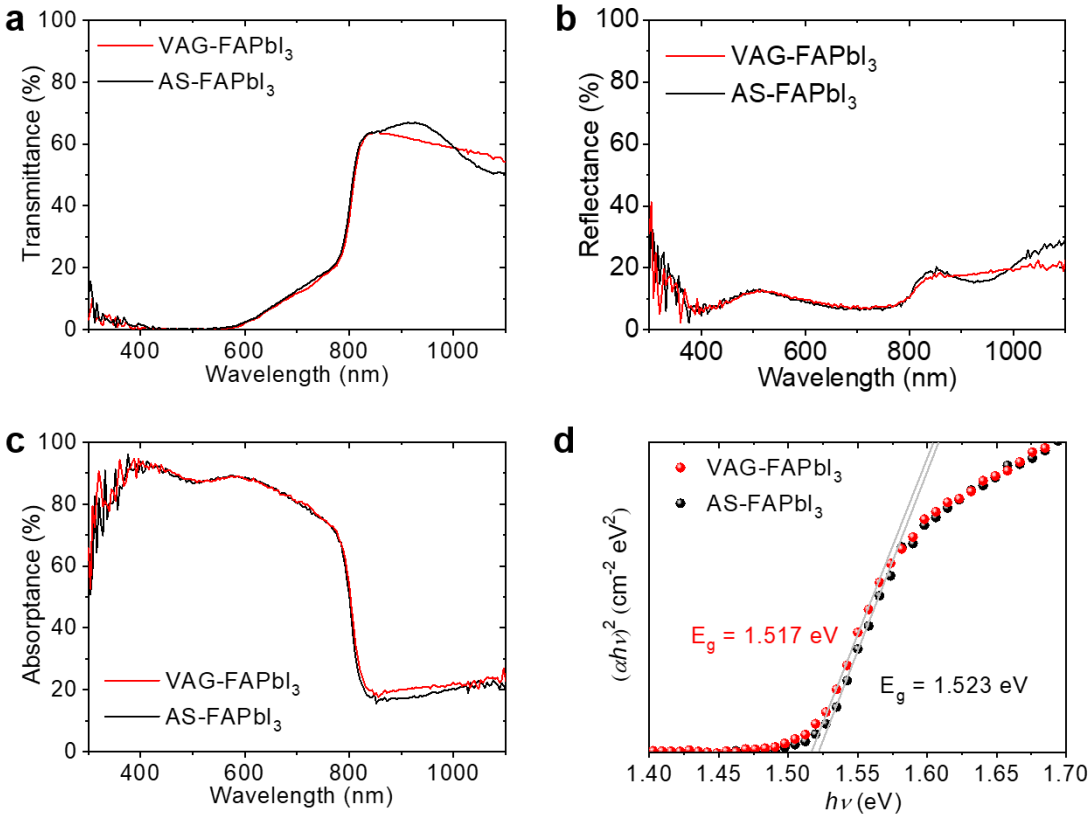

Figure C1. Optical spectra for $FAPbI_3$ perovskite thin films fabricated by AS and VAG methods. (a) Transmittance, (b) reflectance, (c) absorptance spectra, and (d) Tauc-plots. Adapted from Electronic Supplementary Information of Ref.[55] with permission of The Royal Society of Chemistry.

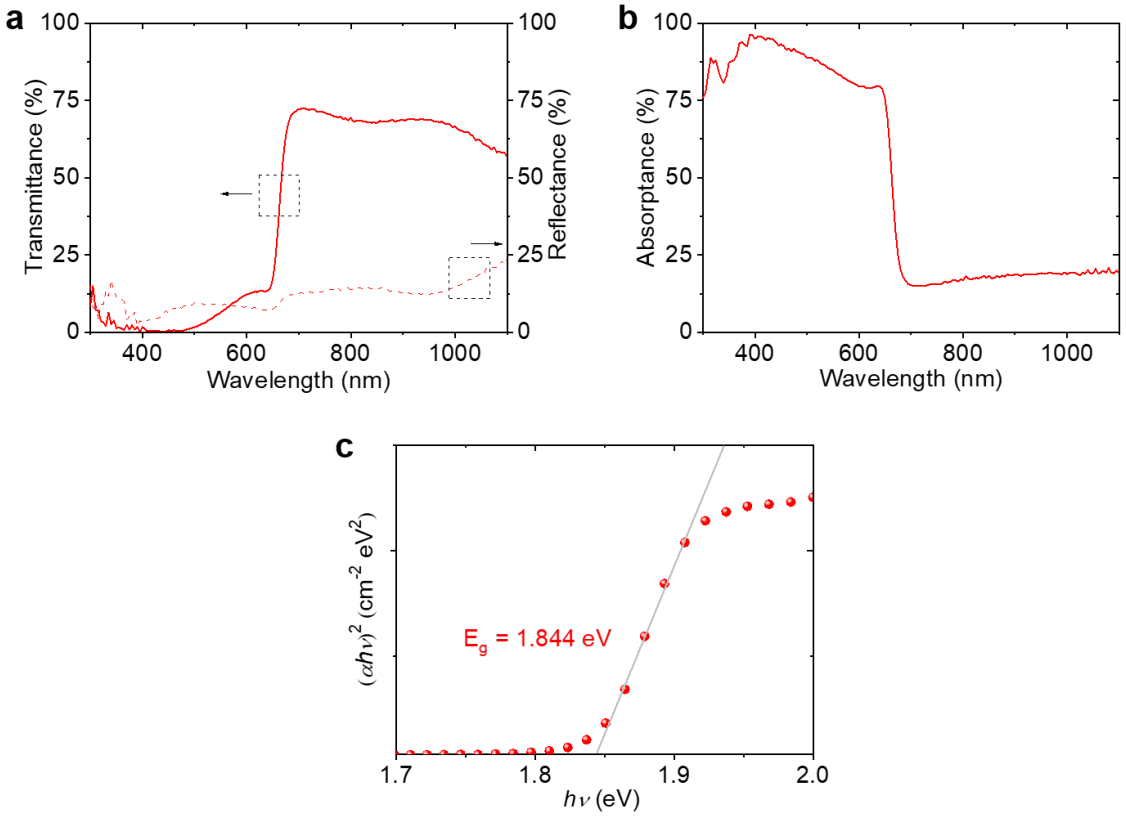

Figure C2. Optical spectra for WBG perovskite thin films fabricated by AS. (a) Transmittance and reflectance, (c) absorptance spectra, and (d) Tauc-plots. Adapted from Electronic Supplementary Information of Ref.[55] with permission of The Royal Society of Chemistry.

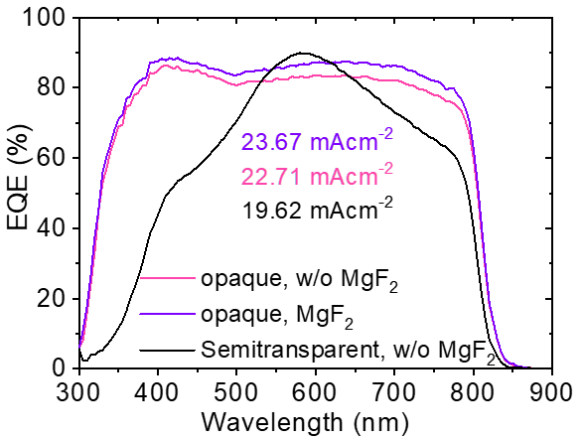

Figure C3. EQE spectra for semitransparent and opaque middle PSCs fabricated using VAG method. The semitransparent device was applied recipe 2 described in Figure 6.8b. Adapted from Electronic Supplementary Information of Ref.[55] with permission of The Royal Society of Chemistry.

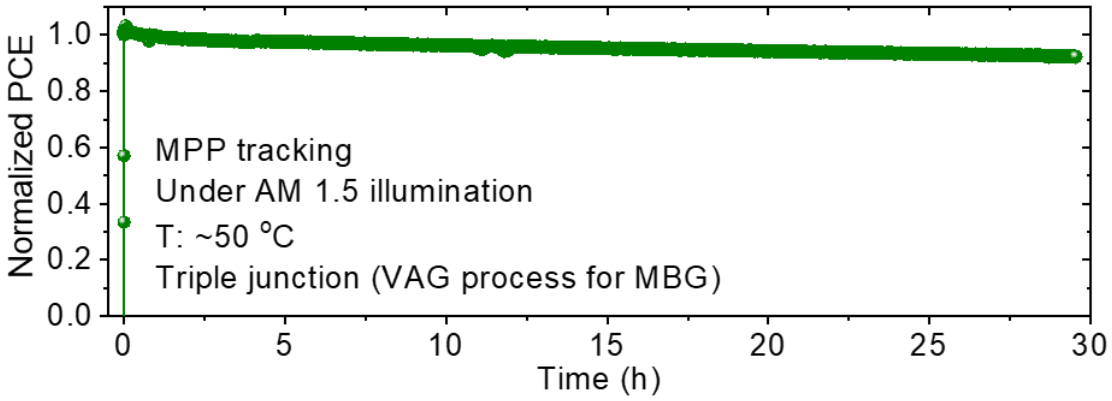

Figure C4. Evolution of SPCE of champion perovskite–perovskite–Si MTJSC under continuous AM 1.5G illumination at ~50 ºC for MPP tracking. The middle perovskite thin film was fabricated using VAG strategy. Adapted from Electronic Supplementary Information of Ref.[55] with permission of The Royal Society of Chemistry.

References

1. U.S. Energy Information Administration. Annual Energy Outlook 2023. (2023). www.eia.gov/aeo

2. Heede, R. & Oreskes, N. Potential emissions of CO2 and methane from proved reserves of fossil fuels: An alternative analysis. *Glob. Environ. Chang.* **36**, 12–20 (2016).

3. Haegel, N. M. *et al.* Photovoltaics at multi-terawatt scale: Waiting is not an option. *Science* **380**, 39–42 (2023).

4. The paris agreement. (2015). https://unfccc.int/process-and-meetings/the-paris-agreement.

5. Padture, N. P. The promise of metal-halide-perovskite solar photovoltaics: A brief review. *MRS Bull.* **48**, 983–998 (2023).

6. Li, H. & Zhang, W. Perovskite Tandem Solar Cells: From Fundamentals to Commercial Deployment. *Chem. Rev.* **120**, 9835–9950 (2020).

7. Fraunhofer Institute for Solar Energy Systems. *Levelized Cost of Electricity-Renewable Energy Technologies June 2021*. (2021).

8. Chuang, M. Calculation and visualization tools for theoretical solar cell efficiencies based on the Shockley Queisser limit. (2019). www.github.com/marcus-cmc/Shockley-Queisser-limit

9. NREL National Center for Photovoltaics. Best Research-Cell Efficiencies. (2023). https://www.nrel.gov/pv/cell-efficiency.html

10. Bremner, S. P., Yi, C., Almansouri, I., Ho-Baillie, A. & Green, M. A. Optimum band gap combinations to make best use of new photovoltaic materials. *Sol. Energy* **135**, 750–757 (2016).

11. Green, M. A. *et al.* Solar cell efficiency tables (Version 63). *Prog. Photovoltaics Res. Appl.* **32**, 3–13 (2024).

12. Hou, Y. *et al.* Efficient tandem solar cells with solution-processed perovskite on textured crystalline silicon. *Science* **367**, 1135–1140 (2020).

13. Al-Ashouri, A. *et al.* Monolithic perovskite/silicon tandem solar cell with >29% efficiency by enhanced hole extraction. *Science* **370**, 1300–1309 (2020).

14. Tockhorn, P. *et al.* Nano-optical designs for high-efficiency monolithic perovskite–silicon tandem solar cells. *Nat. Nanotechnol.* **17**, 1214–1221 (2022).

15. Ruiz-Preciado, M. A. *et al.* Monolithic Two-Terminal Perovskite/CIS Tandem Solar Cells with Efficiency Approaching 25%. *ACS Energy Lett.* **7**, 2273–2281 (2022).

16. Hu, H. *et al.* Sn-Pb Mixed Perovskites with Fullerene-Derivative Interlayers for Efficient Four-Terminal All-Perovskite Tandem Solar Cells. *Adv. Funct. Mater.* **32**, 2107650 (2022).

17. Abdollahi Nejand, B. *et al.* Scalable two-terminal all-perovskite tandem solar modules with a 19.1% efficiency. *Nat. Energy* **7**, 620–630 (2022).

18. Lin, R. *et al.* All-perovskite tandem solar cells with improved grain surface passivation. *Nature* **603**, 73–78 (2022).

19. Hörantner, M. T. *et al.* The Potential of Multijunction Perovskite Solar Cells. *ACS Energy Lett.* **2**, 2506–2513 (2017).

20. Werner, J. *et al.* Perovskite/Perovskite/Silicon Monolithic Triple-Junction Solar Cells with a Fully Textured Design. *ACS Energy Lett.* **3**, 2052–2058 (2018).

21. Kojima, A., Teshima, K., Shirai, Y. & Miyasaka, T. Organometal halide perovskites as visible-light sensitizers for photovoltaic cells. *J. Am. Chem. Soc.* **131**, 6050–6051 (2009).

22. Deng, Y. *et al.* Surfactant-controlled ink drying enables high-speed deposition of perovskite films for efficient photovoltaic modules. *Nat. Energy* **3**, 560–566 (2018).

23. Xiao, K. *et al.* Scalable processing for realizing 21.7%-efficient all-perovskite tandem solar modules. *Science* **35**, 762–767 (2022).

24. Mahesh, S. *et al.* Revealing the origin of voltage loss in mixed-halide perovskite solar cells. *Energy Environ. Sci.* **13**, 258–267 (2020).

25. Luo, D., Su, R., Zhang, W., Gong, Q. & Zhu, R. Minimizing non-radiative recombination losses in perovskite solar cells. *Nat. Rev. Mater.* **5**, 44–60 (2020).

26. Wolff, C. M., Caprioglio, P., Stolterfoht, M. & Neher, D. Nonradiative Recombination in Perovskite Solar Cells: The Role of Interfaces. *Adv. Mater.* **31**, (2019).

27. Hu, H. *et al.* Void-free buried interface for scalable processing of p-i-n-based FAPbI3 perovskite solar modules. *Joule* **7**, 1574–1592 (2023).

28. Liang, Q. *et al.* Manipulating Crystallization Kinetics in High-Performance Blade-Coated Perovskite Solar Cells via Cosolvent-Assisted Phase Transition. *Adv. Mater.* **34**, 2200276 (2022).

29. McMeekin, D. P. *et al.* Solution-Processed All-Perovskite Multi-junction Solar Cells. *Joule* **3**, 387–401 (2019).

30. Zheng, J. *et al.* Monolithic Perovskite-Perovskite-Silicon Triple-Junction Tandem Solar Cell with an Efficiency of over 20%. *ACS Energy Lett.* **7**, 3003–3005 (2022).

31. Green, M. A., Ho-baillie, A. & Snaith, H. J. The emergence of perovskite solar cells. *Nat. Publ. Gr.* **8**, 506–514 (2014).

32. Fu, Y. *et al.* Incorporating Large A Cations into Lead Iodide Perovskite Cages: Relaxed Goldschmidt Tolerance Factor and Impact on Exciton − Phonon Interaction. **5**, 1377–1386 (2019).

33. Xiao, Z. & Yan, Y. Progress in Theoretical Study of Metal Halide Perovskite Solar Cell Materials. *Adv. Energy Mater.* **7**, 1–20 (2017).

34. Miyata, A. *et al.* Direct measurement of the exciton binding energy and effective masses for charge carriers in organic-inorganic tri-halide perovskites. *Nat. Phys.* **11**, 582–587 (2015).

35. Wehrenfennig, C., Eperon, G. E., Johnston, M. B., Snaith, H. J. & Herz, L. M. High charge carrier mobilities and lifetimes in organolead trihalide perovskites. *Adv. Mater.* **26**, 1584–1589 (2014).

36. Alcocer, M. J. P., Leijtens, T., Herz, L. M., Petrozza, A. & Snaith, H. J. Electron-Hole Diffusion Lengths Exceeding Trihalide Perovskite Absorber. *Science* **342**, 341–344 (2013).

37. Tao, S. *et al.* Absolute energy level positions in tin- and lead-based halide perovskites. *Nat. Commun.* **10**, 1–10 (2019).

38. Mora-Seró, I. How Do Perovskite Solar Cells Work? *Joule* **2**, 585–587 (2018).

39. Ibrahim, A. Analysis of Electrical Characteristics of Photovoltaic Single Crystal Silicon Solar Cells at Outdoor Measurements. *Smart Grid Renew. Energy* **02**, 169–175 (2011).

40. Xia, J., Sohail, M. & Nazeeruddin, M. K. Efficient and Stable Perovskite Solar Cells by Tailoring of Interfaces. *Adv. Mater.* **35**, (2023).

41. DeQuilettes, D. W. *et al.* Impact of microstructure on local carrier lifetime in perovskite solar cells. *Science* **348**, 683–686 (2015).

42. Hu, Y. *et al.* Standardizing Perovskite Solar Modules beyond Cells. *Joule* **3**, 2076–2085 (2019).

43. Le, T. H. *et al.* Perovskite Solar Module: Promise and Challenges in Efficiency, Meta-Stability, and Operational Lifetime. *Adv. Electron. Mater.* **9**, (2023).

44. Park, N. G. & Zhu, K. Scalable fabrication and coating methods for perovskite solar cells and solar modules. *Nat. Rev. Mater.* **5**, 333–350 (2020).

45. Eggers, H. *et al.* Inkjet-Printed Micrometer-Thick Perovskite Solar Cells with Large Columnar Grains. *Adv. Energy Mater.* **10**, 1903184 (2020).

46. Lee, D. K. & Park, N. G. Materials and Methods for High-Efficiency Perovskite Solar Modules. *Sol. RRL* **6**, 1–25 (2022).

47. Le Berre, M., Chen, Y. & Baigl, D. From convective assembly to landau - Levich deposition of multilayered phospholipid films of controlled thickness. *Langmuir* **25**, 2554–2557 (2009).

48. Schackmar, F. *et al.* In Situ Process Monitoring and Multichannel Imaging for Vacuum-Assisted Growth Control of Inkjet-Printed and Blade-Coated Perovskite Thin-Films. *Adv. Mater. Technol.* **8**, 2201331 (2023).

49. Ternes, S. *et al.* Drying Dynamics of Solution-Processed Perovskite Thin-Film Photovoltaics: In Situ Characterization, Modeling, and Process Control. *Adv. Energy Mater.* **9**, 1901581 (2019).

50. Shockley, W. & Queisser, H. J. Detailed balance limit of efficiency of p-n junction solar cells. *J. Appl. Phys.* **32**, 510–519 (1961).

51. Nelson, C. A., Monahan, N. R. & Zhu, X. Y. Exceeding the Shockley-Queisser limit in solar energy conversion. *Energy Environ. Sci.* **6**, 3508–3519 (2013).

52. Gota, F., An, S. X., Hu, H., Abdollahi Nejand, B. & Paetzold, U. W. Energy Yield Modeling of Bifacial All-Perovskite Two-Terminal Tandem Photovoltaics. *Adv. Opt. Mater.* **11**, 2201691 (2023).

53. Schmager, R., Paetzold, Ulrich W. Langenhorst, M., Gota, F. & Lehr, J. EYcalc - Energy yield calculator for multi-junction solar modules with realistic irradiance data and textured interfaces. (2021). doi:10.5281/zenodo.4696257

54. Schmager, R. *et al.* Methodology of energy yield modelling of perovskite-based multi-junction photovoltaics. *Opt. Express* **27**, A507 (2019).

55. Hu, H. *et al.* Triple-junction perovskite–perovskite–silicon solar cells with power conversion efficiency of 24.4%. *Energy Environ. Sci.* **17**, 2800–2814 (2024).

56. Islam, M. R. *et al.* Recent Progress and Future Prospects for Light Management of All-Perovskite Tandem Solar Cells. *Adv. Mater. Interfaces* **9**, 1–18 (2022).

57. Moghadamzadeh, S. *et al.* In2O3:H-Based Hole-Transport-Layer-Free Tin/Lead Perovskite Solar Cells for Efficient Four-Terminal All-Perovskite Tandem Solar Cells. *ACS Appl. Mater. Interfaces* **13**, 46488–46498 (2021).

58. Yang, Z. *et al.* Stable Low-Bandgap Pb–Sn Binary Perovskites for Tandem Solar Cells. *Adv. Mater.* **28**, 8990–8997 (2016).

59. Lehr, J. *et al.* Energy Yield Advantages of Three-Terminal Perovskite-Silicon Tandem Photovoltaics. *Joule* **4**, 2387–2403 (2020).

60. Tockhorn, P. *et al.* Three-Terminal Perovskite/Silicon Tandem Solar Cells with Top and Interdigitated Rear Contacts. *ACS Appl. Energy Mater.* **3**, 1381–1392 (2020).

61. Warren, E. L. *et al.* Maximizing tandem solar cell power extraction using a three-terminal design. *Sustain. Energy Fuels* **2**, 1141–1147 (2018).

62. Dai, L. *et al.* Three-Terminal Monolithic Perovskite/Silicon Tandem Solar Cell Exceeding 29% Power Conversion Efficiency. *ACS Energy Lett.* **8**, 3839–3842 (2023).

63. Wang, Y. *et al.* Low-bandgap mixed tin-lead iodide perovskite with large grains for high performance solar cells. *J. Mater. Chem. A* **6**, 13090–13095 (2018).

64. Yang, Z. *et al.* Enhancing electron diffusion length in narrow-bandgap perovskites for efficient monolithic perovskite tandem solar cells. *Nat. Commun.* **10**, 1–9 (2019).

65. Werner, J. *et al.* Improving Low-Bandgap Tin-Lead Perovskite Solar Cells via Contact Engineering and Gas Quench Processing. *ACS Energy Lett.* **5**, 1215–1223 (2020).

66. Ritzer, D. B. *et al.* Upscaling of perovskite solar modules: The synergy of fully

evaporated layer fabrication and all-laser-scribed interconnections. *Prog. Photovoltaics Res. Appl.* **30**, 360–373 (2022).

67. Scofield, J. H. Hartree-Slater subshell photoionization cross-sections at 1254 and 1487 eV. *J. Electron Spectros. Relat. Phenomena* **8**, 129–137 (1976).

68. Tanuma, S., Powell, C. J. & Penn, D. R. Calculations of electron inelastic mean free paths. IX. Data for 41 elemental solids over the 50 eV to 30 keV range. *Surf. Interface Anal.* **43**, 689–713 (2011).

69. Yang, D. *et al.* Stable Efficiency Exceeding 20.6% for Inverted Perovskite Solar Cells through Polymer-Optimized PCBM Electron-Transport Layers. *Nano Lett.* **19**, 3313–3320 (2019).

70. Kahn, A. Fermi level, work function and vacuum level. *Mater. Horizons* **3**, 7–10 (2016).

71. Tauc, T., Kubelka, P., Munk, F., Information, S. & Tauc, T. How To Correctly Determine the Band Gap Energy of Modi fi ed Semiconductor Photocatalysts Based on UV − Vis Spectra. *J. Phys. Chem. Lett.* **9**, 6814–6817 (2018).

72. Stolterfoht, M. *et al.* How To Quantify the Efficiency Potential of Neat Perovskite Films: Perovskite Semiconductors with an Implied Efficiency Exceeding 28%. *Adv. Mater.* **32**, 2000080 (2020).

73. Gharibzadeh, S. *et al.* Two birds with one stone: Dual grain-boundary and interface passivation enables >22% efficient inverted methylammonium-free perovskite solar cells. *Energy Environ. Sci.* **14**, 5875–5893 (2021).

74. Zhang, D. *et al.* Stable α-FAPbI3 in Inverted Perovskite Solar Cells with Efficiency Exceeding 22% via a Self-Passivation Strategy. *Adv. Funct. Mater.* **2200174**, 1–9 (2022).

75. Zhu, X. *et al.* Superior stability for perovskite solar cells with 20% efficiency using vacuum co-evaporation. *Nanoscale* **9**, 12316–12323 (2017).

76. Li, F. *et al.* Effects of Alkyl Chain Length on Crystal Growth and Oxidation Process of Two-Dimensional Tin Halide Perovskites. *ACS Energy Lett.* **5**, 1422–1429 (2020).

77. Caprioglio, P. *et al.* On the Origin of the Ideality Factor in Perovskite Solar Cells. *Adv. Energy Mater.* **10**, 1–9 (2020).

78. Lin, R. *et al.* Monolithic all-perovskite tandem solar cells with 24.8% efficiency exploiting comproportionation to suppress Sn(ii) oxidation in precursor ink. *Nat. Energy* **4**, 864–873 (2019).

79. Shi, D. *et al.* Low trap-state density and long carrier diffusion in organolead trihalide perovskite single crystals. *Science* **347**, 519–522 (2015).

80. Min, H. *et al.* Efficient, stable solar cells by using inherent bandgap of a-phase formamidinium lead iodide. *Science* **366**, 749–753 (2019).

81. Akin, S., Akman, E. & Sonmezoglu, S. FAPbI3-Based Perovskite Solar Cells Employing Hexyl-Based Ionic Liquid with an Efficiency Over 20% and Excellent

Long-Term Stability. *Adv. Funct. Mater.* **30**, 2002964 (2020).

82. Han, Q. *et al.* Single Crystal Formamidinium Lead Iodide (FAPbI3): Insight into the Structural, Optical, and Electrical Properties. *Adv. Mater.* **28**, 2253–2258 (2016).

83. Dong, Q. *et al. 5、Electron-hole diffusion lengths > 175 m m in solution-grown CH 3 NH 3 PbI 3 single crystals*. *Science* **347**, (2015).

84. Li, W. *et al.* Approaching optimal hole transport layers by an organic monomolecular strategy for efficient inverted perovskite solar cells. *J. Mater. Chem. A* **8**, 16560–16569 (2020).

85. Zou, M. *et al.* Strengthened Perovskite/Fullerene Interface Enhances Efficiency and Stability of Inverted Planar Perovskite Solar Cells via a Tetrafluoroterephthalic Acid Interlayer. *ACS Appl. Mater. Interfaces* **11**, 33515–33524 (2019).

86. Wang, K. *et al.* Chlorine doping for black γ-CsPbI 3 solar cells with stabilized efficiency beyond 16%. *Nano Energy* **58**, 175–182 (2019).

87. Wang, Y. *et al.* Extrinsic Ion Distribution Induced Field Effect in CsPbIBr2 Perovskite Solar Cells. *Small* **16**, 1–10 (2020).

88. Yang, J. *et al.* Energetics and Energy Loss in 2D Ruddlesden–Popper Perovskite Solar Cells. *Adv. Energy Mater.* **10**, 1–9 (2020).

89. Fischer, M., Tvingstedt, K., Baumann, A. & Dyakonov, V. Doping Profile in Planar Hybrid Perovskite Solar Cells Identifying Mobile Ions. *ACS Appl. Energy Mater.* **1**, 5129–5134 (2018).

90. Almora, O., García-Batlle, M. & Garcia-Belmonte, G. Utilization of Temperature-Sweeping Capacitive Techniques to Evaluate Band Gap Defect Densities in Photovoltaic Perovskites. *J. Phys. Chem. Lett.* **10**, 3661–3669 (2019).

91. Chen, J. De *et al.* Single-junction polymer solar cells exceeding 10% power conversion effi ciency. *Adv. Mater.* **27**, 1035–1041 (2015).

92. Xu, G. *et al.* Integrating Ultrathin Bulk-Heterojunction Organic Semiconductor Intermediary for High-Performance Low-Bandgap Perovskite Solar Cells with Low Energy Loss. *Adv. Funct. Mater.* **28**, 1–8 (2018).

93. Kyaw, A. K. K. *et al.* Improved light harvesting and improved efficiency by insertion of an optical spacer (ZnO) in solution-processed small-molecule solar cells. *Nano Lett.* **13**, 3796–3801 (2013).

94. Xie, Y. *et al.* Post-annealing to recover the reduced open-circuit voltage caused by solvent annealing in organic solar cells. *J. Mater. Chem. A* **4**, 6158–6166 (2016).

95. Zhang, M. *et al.* Reconfiguration of interfacial energy band structure for high-performance inverted structure perovskite solar cells. *Nat. Commun.* **10**, 1–9 (2019).

96. Wu, W. Q., Rudd, P. N., Wang, Q., Yang, Z. & Huang, J. Blading Phase-Pure Formamidinium-Alloyed Perovskites for High-Efficiency Solar Cells with Low Photovoltage Deficit and Improved Stability. *Adv. Mater.* **32**, 1–8 (2020).

97. Sandberg, O. J., Tvingstedt, K., Meredith, P. & Armin, A. Theoretical Perspective on Transient Photovoltage and Charge Extraction Techniques. *J. Phys. Chem. C* **123**, 14261–14271 (2019).

98. Tran, H. N. *et al.* 17% Non-Fullerene Organic Solar Cells with Annealing-Free Aqueous MoOx. *Adv. Sci.* **7**, 2002395 (2020).

99. Kiermasch, D., Rieder, P., Tvingstedt, K., Baumann, A. & Dyakonov, V. Improved charge carrier lifetime in planar perovskite solar cells by bromine doping. *Sci. Rep.* **6**, 1–7 (2016).

100. Mozer, A. J. *et al.* Time-dependent mobility and recombination of the photoinduced charge carriers in conjugated polymer/fullerene bulk heterojunction solar cells. *Phys. Rev. B - Condens. Matter Mater. Phys.* **72**, 1–10 (2005).

101. Neukom, M., Züfle, S., Jenatsch, S. & Ruhstaller, B. Opto-electronic characterization of third-generation solar cells. *Sci. Technol. Adv. Mater.* **19**, 291–316 (2018).

102. Dahlström, S. *et al.* Extraction Current Transients for Selective Charge-Carrier Mobility Determination in Non-Fullerene and Ternary Bulk Heterojunction Organic Solar Cells. *ACS Appl. Energy Mater.* **3**, 9190–9197 (2020).

103. Chen, Y., Peng, J., Su, D., Chen, X. & Liang, Z. Efficient and balanced charge transport revealed in planar perovskite solar cells. *ACS Appl. Mater. Interfaces* **7**, 4471–4475 (2015).

104. Ginting, R. T. *et al.* Low-temperature operation of perovskite solar cells: With efficiency improvement and hysteresis-less. *Nano Energy* **27**, 569–576 (2016).

105. Aukštuolis, A. *et al.* Measurement of charge carrier mobility in perovskite nanowire films by photo-celiv method. *Proc. Rom. Acad. Ser. A - Math. Phys. Tech. Sci. Inf. Sci.* **18**, 34–41 (2017).

106. Kuik, M., Koster, L. J. A., Wetzelaer, G. A. H. & Blom, P. W. M. Trap-assisted recombination in disordered organic semiconductors. *Phys. Rev. Lett.* **107**, (2011).

107. Shao, S. *et al.* Elimination of the light soaking effect and performance enhancement in perovskite solar cells using a fullerene derivative. *Energy Environ. Sci.* **9**, 2444–2452 (2016).

108. Jahani, F., Chiechi, R. C. & Hummelen, J. C. Fullerene derivatives with increased dielectric constants. *Chem. Commun.* **50**, 10645–10647 (2014).

109. Torabi, S. *et al.* Strategy for enhancing the dielectric constant of organic semiconductors without sacrificing charge carrier mobility and solubility. *Adv. Funct. Mater.* **25**, 150–157 (2015).

110. Eperon, G. E. *et al.* Perovskite-perovskite tandem photovoltaics with optimized band gaps. *Science* **354**, 861–865 (2016).

111. Leijtens, T., Bush, K. A., Prasanna, R. & Mcgehee, M. D. Opportunities and challenges for tandem solar cells using metal halide perovskite semiconductors. *Nat. Energy* **3**, (2018).

112. Tong, J. *et al.* Tong et al. - 2019 - Carrier lifetimes larger than 1 μs in Sn-Pb perovskites enable efficient all-perovskite tandem solar cells.pdf. *Science* **364**, 475–479 (2019).

113. Guan, H. *et al.* Regulating Crystal Orientation via Ligand Anchoring Enables Efficient Wide-Bandgap Perovskite Solar Cells And Tandems. *Adv. Mater.* **2307987**, 1–10 (2023).

114. Li, C. *et al.* Low-bandgap mixed tin–lead iodide perovskites with reduced methylammonium for simultaneous enhancement of solar cell efficiency and stability. *Nat. Energy* **5**, 768–776 (2020).

115. Li, H. *et al.* All-perovskite tandem solar cells with 3D/3D bilayer perovskite heterojunction. *Nature* **620**, 994–1000 (2023).

116. Wang, J. *et al.* Enhancing Photostability of Sn-Pb Perovskite Solar Cells by an Alkylammonium Pseudo-Halogen Additive. *Adv. Energy Mater.* **13**, 1–8 (2023).

117. Gu, S. *et al.* Tin and Mixed Lead–Tin Halide Perovskite Solar Cells: Progress and their Application in Tandem Solar Cells. *Adv. Mater.* **32**, 1907392 (2020).

118. Wang, C., Song, Z., Li, C., Zhao, D. & Yan, Y. Low-Bandgap Mixed Tin-Lead Perovskites and Their Applications in All-Perovskite Tandem Solar Cells. *Adv. Funct. Mater.* **29**, 1–30 (2019).

119. Ma, L. *et al.* Carrier Diffusion Lengths of over 500 nm in Lead-Free Perovskite CH3NH3SnI3 Films. *J. Am. Chem. Soc.* **138**, 14750–14755 (2016).

120. Gupta, S., Cahen, D. & Hodes, G. How SnF2 Impacts the Material Properties of Lead-Free Tin Perovskites. *J. Phys. Chem. C* **122**, 13926–13936 (2018).

121. Tsai, C. M. *et al.* Role of Tin Chloride in Tin-Rich Mixed-Halide Perovskites Applied as Mesoscopic Solar Cells with a Carbon Counter Electrode. *ACS Energy Lett.* **1**, 1086–1093 (2016).

122. Lian, X. *et al.* Highly Efficient Sn/Pb Binary Perovskite Solar Cell via Precursor Engineering: A Two-Step Fabrication Process. *Adv. Funct. Mater.* **29**, 1–9 (2019).

123. Xu, X. *et al.* Ascorbic acid as an effective antioxidant additive to enhance the efficiency and stability of Pb/Sn-based binary perovskite solar cells. *Nano Energy* **34**, 392–398 (2017).

124. Tai, Q. *et al.* Antioxidant Grain Passivation for Air-Stable Tin-Based Perovskite Solar Cells. *Angew. Chemie - Int. Ed.* **58**, 806–810 (2019).

125. Zhu, Z., Li, N., Zhao, D., Wang, L. & Jen, A. K. Y. Improved Efficiency and Stability of Pb/Sn Binary Perovskite Solar Cells Fabricated by Galvanic Displacement Reaction. *Adv. Energy Mater.* **9**, 2–9 (2019).

126. Jiang, T. *et al.* Realizing High Efficiency over 20% of Low-Bandgap Pb–Sn-Alloyed Perovskite Solar Cells by In Situ Reduction of Sn4+. *Sol. RRL* **4**, 1–7 (2020).

127. Yokoyama, T. *et al.* Overcoming Short-Circuit in Lead-Free CH3NH3SnI3 Perovskite Solar Cells via Kinetically Controlled Gas-Solid Reaction Film

Fabrication Process. *J. Phys. Chem. Lett.* **7**, 776–782 (2016).

128. Leijtens, T. *et al.* Tin-lead halide perovskites with improved thermal and air stability for efficient all-perovskite tandem solar cells. *Sustain. Energy Fuels* **2**, 2450–2459 (2018).

129. Li, C. *et al.* Reducing Saturation-Current Density to Realize High-Efficiency Low-Bandgap Mixed Tin–Lead Halide Perovskite Solar Cells. *Adv. Energy Mater.* **9**, 1–9 (2019).

130. Zhao, B. *et al.* High Open-Circuit Voltages in Tin-Rich Low-Bandgap Perovskite-Based Planar Heterojunction Photovoltaics. *Adv. Mater.* **29**, 1604744 (2017).

131. Abdollahi Nejand, B. *et al.* Vacuum-Assisted Growth of Low-Bandgap Thin Films (FA0.8MA0.2Sn0.5Pb0.5I3) for All-Perovskite Tandem Solar Cells. *Adv. Energy Mater.* **10**, 1902583 (2020).

132. Stranks, S. D. Nonradiative Losses in Metal Halide Perovskites. *ACS Energy Lett.* **2**, 1515–1525 (2017).

133. Stolterfoht, M. *et al.* Visualization and suppression of interfacial recombination for high-efficiency large-area pin perovskite solar cells. *Nat. Energy* **3**, 847–854 (2018).

134. Li, S. *et al.* Unravelling the Mechanism of Ionic Fullerene Passivation for Efficient and Stable Methylammonium-Free Perovskite Solar Cells. *ACS Energy Lett.* **5**, 2015–2022 (2020).

135. Ball, J. M. & Petrozza, A.. Defects in perovskite-halides and their effects in solar cells. *Nat. Energy* **1**, 1–13 (2016).

136. Huang, J., Yuan, Y., Shao, Y. & Yan, Y. Understanding the physical properties of hybrid perovskites for photovoltaic applications. *Nat. Rev. Mater.* **2**, 1–19 (2017).

137. Chung, I. *et al.* CsSnI 3: Semiconductor or metal? High electrical conductivity and strong near-infrared photoluminescence from a single material. High hole mobility and phase-transitions. *J. Am. Chem. Soc.* **134**, 8579–8587 (2012).

138. Kumar, M. H. *et al.* Lead-free halide perovskite solar cells with high photocurrents realized through vacancy modulation. *Adv. Mater.* **26**, 7122–7127 (2014).

139. Aydin, E., De Bastiani, M. & De Wolf, S. Defect and Contact Passivation for Perovskite Solar Cells. *Adv. Mater.* **31**, 1–20 (2019).

140. Schulz, P., Cahen, D. & Kahn, A. Halide Perovskites: Is It All about the Interfaces? *Chem. Rev.* **119**, 3349–3417 (2019).

141. Zheng, X. *et al.* Managing grains and interfaces via ligand anchoring enables 22.3%-efficiency inverted perovskite solar cells. *Nat. Energy* **5**, 131–140 (2020).

142. Shao, S. *et al.* Enhancing the Performance of the Half Tin and Half Lead Perovskite Solar Cells by Suppression of the Bulk and Interfacial Charge Recombination. *Adv. Mater.* **30**, 1803703 (2018).

143. Wei, M. *et al.* Combining Efficiency and Stability in Mixed Tin–Lead Perovskite

Solar Cells by Capping Grains with an Ultrathin 2D Layer. *Adv. Mater.* **32**, 1–8 (2020).

144. Li, C. *et al.* Vertically Aligned 2D/3D Pb–Sn Perovskites with Enhanced Charge Extraction and Suppressed Phase Segregation for Efficient Printable Solar Cells. *ACS Energy Lett.* **5**, 1386–1395 (2020).

145. Ke, W. *et al.* Narrow-bandgap mixed lead/tin-based 2D Dion-Jacobson perovskites boost the performance of solar cells. *J. Am. Chem. Soc.* **142**, 15049–15057 (2020).

146. Tang, H., Shang, Y., Zhou, W., Peng, Z. & Ning, Z. Energy Level Tuning of PEDOT:PSS for High Performance Tin-Lead Mixed Perovskite Solar Cells. *Sol. RRL* **3**, 1–6 (2019).

147. Kapil, G. *et al.* Tin-Lead Perovskite Fabricated via Ethylenediamine Interlayer Guides to the Solar Cell Efficiency of 21.74%. *Adv. Energy Mater.* **11**, 2101069 (2021).

148. Rajagopal, A., Liang, P. W., Chueh, C. C., Yang, Z. & Jen, A. K. Y. Defect Passivation via a Graded Fullerene Heterojunction in Low-Bandgap Pb-Sn Binary Perovskite Photovoltaics. *ACS Energy Lett.* **2**, 2531–2539 (2017).

149. Kapil, G. *et al.* Highly Efficient 17.6% Tin-Lead Mixed Perovskite Solar Cells Realized through Spike Structure. *Nano Lett.* **18**, 3600–3607 (2018).

150. Moghadamzadeh, S. *et al.* Triple-cation low-bandgap perovskite thin-films for high-efficiency four-terminal all-perovskite tandem solar cells. *J. Mater. Chem. A* **8**, 24608–24619 (2020).

151. Liang, P. W., Chueh, C. C., Williams, S. T. & Jen, A. K. Y. Roles of fullerene-based interlayers in enhancing the performance of organometal perovskite thin-film solar cells. *Adv. Energy Mater.* **5**, 1–7 (2015).

152. Rajagopal, A. *et al.* Highly Efficient Perovskite–Perovskite Tandem Solar Cells Reaching 80% of the Theoretical Limit in Photovoltage. *Adv. Mater.* **29**, 1–10 (2017).

153. Ding, C. *et al.* Effect of the conduction band offset on interfacial recombination behavior of the planar perovskite solar cells. *Nano Energy* **53**, 17–26 (2018).

154. Minemoto, T. *et al.* Theoretical analysis of the effect of conduction band offset of window/CIS layers on performance of CIS solar cells using device simulation. *Sol. Energy Mater. Sol. Cells* **67**, 83–88 (2001).

155. Minemoto, T. & Murata, M. Theoretical analysis on effect of band offsets in perovskite solar cells. *Sol. Energy Mater. Sol. Cells* **133**, 8–14 (2015).

156. Raoui, Y., Ez-Zahraouy, H., Kazim, S. & Ahmad, S. Energy level engineering of charge selective contact and halide perovskite by modulating band offset: Mechanistic insights. *J. Energy Chem.* **54**, 822–829 (2021).

157. Zuo, L. *et al.* Tailoring the interfacial chemical interaction for high-efficiency perovskite solar cells. *Nano Lett.* **17**, 269–275 (2017).

158. Qin, P. L. *et al.* Stable and Efficient Organo-Metal Halide Hybrid Perovskite Solar

Cells via π-Conjugated Lewis Base Polymer Induced Trap Passivation and Charge Extraction. *Adv. Mater.* **30**, 1–12 (2018).

159. Baloch, A. A. B. *et al.* Analysis of Photocarrier Dynamics at Interfaces in Perovskite Solar Cells by Time-Resolved Photoluminescence. *J. Phys. Chem. C* **122**, 26805–26815 (2018).

160. Trimpl, M. J. *et al.* Charge-Carrier Trapping and Radiative Recombination in Metal Halide Perovskite Semiconductors. *Adv. Funct. Mater.* **30**, 1–12 (2020).

161. Bu, T. *et al.* Universal passivation strategy to slot-die printed SnO 2 for hysteresis-free efficient flexible perovskite solar module. *Nat. Commun.* **9**, 1–10 (2018).

162. Hu, H. *et al.* Atomic Layer Deposition of TiO2 for a High-Efficiency Hole-Blocking Layer in Hole-Conductor-Free Perovskite Solar Cells Processed in Ambient Air. *ACS Appl. Mater. Interfaces* **8**, 17999–18007 (2016).

163. Yang, G. *et al.* Interface engineering in planar perovskite solar cells: Energy level alignment, perovskite morphology control and high performance achievement. *J. Mater. Chem. A* **5**, 1658–1666 (2017).

164. Shi, J. *et al.* From Ultrafast to Ultraslow: Charge-Carrier Dynamics of Perovskite Solar Cells. *Joule* **2**, 879–901 (2018).

165. Moghadamzadeh, S. *et al.* In 2 O 3 :H-Based Hole-Transport-Layer-Free Tin/Lead Perovskite Solar Cells for Efficient Four-Terminal All-Perovskite Tandem Solar Cells . *ACS Appl. Mater. Interfaces* **13**, 46488–46498 (2021).

166. Gharibzadeh, S. *et al.* 2D/3D Heterostructure for Semitransparent Perovskite Solar Cells with Engineered Bandgap Enables Efficiencies Exceeding 25% in Four-Terminal Tandems with Silicon and CIGS. *Adv. Funct. Mater.* **30**, (2020).

167. Eperon, G. E. *et al.* Formamidinium lead trihalide: A broadly tunable perovskite for efficient planar heterojunction solar cells. *Energy Environ. Sci.* **7**, 982–988 (2014).

168. Lee, J. W., Seol, D. J., Cho, A. N. & Park, N. G. High-efficiency perovskite solar cells based on the black polymorph of HC(NH2)2PbI3. *Adv. Mater.* **26**, 4991–4998 (2014).

169. Conings, B. *et al.* Intrinsic Thermal Instability of Methylammonium Lead Trihalide Perovskite. *Adv. Energy Mater.* **5**, 1–8 (2015).

170. Lu, H. *et al.* Vapor-assisted deposition of highly efficient, stable black-phase FAPbI3 perovskite solar cells. *Science* **370**, (2020).

171. Kim, M. *et al.* Methylammonium Chloride Induces Intermediate Phase Stabilization for Efficient Perovskite Solar Cells. *Joule* **3**, 2179–2192 (2019).

172. Jeong, M. *et al.* Stable perovskite solar cells with efficiency exceeding 24.8% and 0.3-V voltage loss. *Science* **369**, 1615–1620 (2020).

173. Hui, W. *et al.* Stabilizing black-phase formamidinium perovskite formation at room temperature and high humidity. *Science* **371**, 1359–1364 (2021).

174. Jeong, J. *et al.* Pseudo-halide anion engineering for α-FAPbI3 perovskite solar cells.

Nature **592**, 381–385 (2021).

175. Min, H. *et al.* Perovskite solar cells with atomically coherent interlayers on SnO2 electrodes. *Nature* **598**, 444–450 (2021).

176. Du, T. *et al.* Additive-Free, Low-Temperature Crystallization of Stable α-FAPbI3 Perovskite. *Adv. Mater.* **34**, 1–10 (2022).

177. Song, Z. *et al.* Perovskite Solar Cell Stability in Humid Air: Partially Reversible Phase Transitions in the PbI2-CH3NH3I-H2O System. *Adv. Energy Mater.* **6**, (2016).

178. Chen, H. *et al.* Advances to High-Performance Black-Phase FAPbI 3 Perovskite for Efficient and Stable Photovoltaics . *Small Struct.* **2**, 2000130 (2021).

179. Fu, C. *et al.* From Structural Design to Functional Construction: Amine Molecules in High-Performance Formamidinium-Based Perovskite Solar Cells. *Angew. Chemie - Int. Ed.* **61**, e2021170 (2022).

180. Bian, H. *et al.* Unveiling the Effects of Hydrolysis-Derived DMAI/DMAPbIx Intermediate Compound on the Performance of CsPbI3 Solar Cells. *Adv. Sci.* **7**, 1–9 (2020).

181. Kim, G. *et al.* Impact of strain relaxation on performance of a-formamidinium lead iodide perovskite solar cells. *Science* **370**, 108–112 (2020).

182. Liu, Y. *et al.* Stabilization of Highly Efficient and Stable Phase-Pure FAPbI3 Perovskite Solar Cells by Molecularly Tailored 2D-Overlayers. *Angew. Chemie - Int. Ed.* **59**, 15688–15694 (2020).

183. Xie, F. *et al.* Vertical recrystallization for highly efficient and stable formamidinium-based inverted-structure perovskite solar cells. *Energy Environ. Sci.* **10**, 1942–1949 (2017).

184. Gao, Z. W., Wang, Y. & Choy, W. C. H. Buried Interface Modification in Perovskite Solar Cells: A Materials Perspective. *Adv. Energy Mater.* **12**, 1–20 (2022).

185. Yang, X. *et al.* Buried Interfaces in Halide Perovskite Photovoltaics. *Adv. Mater.* **33**, 2006435 (2021).

186. Wang, Y. *et al.* Buried interface passivation strategies for high-performance perovskite solar cells. *J. Mater. Chem. A* **11**, 8573–8598 (2023).

187. Dai, Z. *et al.* Interfacial toughening with self-Assembled monolayers enhances perovskite solar cell reliability. *Science* **372**, 618–622 (2021).

188. Dong, Q. *et al.* Interpenetrating interfaces for efficient perovskite solar cells with high operational stability and mechanical robustness. *Nat. Commun.* **12**, 1–9 (2021).

189. Chen, S. *et al.* Stabilizing perovskite-substrate interfaces for high-performance perovskite modules. *Science* **373**, 902–907 (2021).

190. Zhou, Y., Kwun, J., Garces, H. F., Pang, S. & Padture, N. P. Observation of phase-retention behavior of the HC(NH2)2PbI3 black perovskite polymorph upon mesoporous TiO2 scaffolds. *Chem. Commun.* **52**, 7273–7275 (2016).

191. He, W. *et al.* Temperature-Assisted Crystal Growth of Photovoltaic α-Phase FAPbI3 Thin Films by Sequential Blade Coating. *ACS Appl. Mater. Interfaces* **12**, 55830–55837 (2020).

192. Xu, Z. *et al.* Reducing energy barrier of δ-to-α phase transition for printed formamidinium lead iodide photovoltaic devices. *Nano Energy* **91**, 106658 (2022).

193. Lee, D., Jeong, D., Ahn, T. K. & Park, N. Precursor Engineering for a Large-Area Perovskite Solar Cell with >19% E ffi ciency. *ACS Energy Lett.* **4**, 2393–2401 (2019).

194. Deng, Y. *et al.* Tailoring solvent coordination for high-speed , room-temperature blading of perovskite photovoltaic films. *Sci. Adv.* **5**, eaax7537 (2019).

195. Fong, P. W. *et al.* Printing High-Efficiency Perovskite Solar Cells in High-Humidity Ambient Environment — An In Situ Guided Investigation. *Adv. Sci.* **8**, 2003359 (2021).

196. Yoo, J. J. *et al.* Efficient perovskite solar cells via improved carrier management. *Nature* **590**, 587–593 (2021).

197. Liu, X. *et al.* Fluoroalkyl-substituted fullerene/perovskite heterojunction for efficient and ambient stable perovskite solar cells. *Nano Energy* **30**, 417–425 (2016).

198. Jung, E. H. *et al.* Efficient, stable and scalable perovskite solar cells using poly(3-hexylthiophene). *Nature* **567**, 511–515 (2019).

199. Zhu, J. *et al.* Formamidine disulfide oxidant as a localised electron scavenger for >20% perovskite solar cell modules. *Energy Environ. Sci.* **14**, 4903–4914 (2021).

200. Zhu, J. *et al.* Defect Healing in FAPb(I1-xBrx)3 Perovskites: Multifunctional Fluorinated Sulfonate Surfactant Anchoring Enables >21% Modules with Improved Operation Stability. *Adv. Energy Mater.* **12**, 1–12 (2022).

201. Wang, J. *et al.* 16.8% Monolithic all-perovskite triple-junction solar cells via a universal two-step solution process. *Nat. Commun.* **11**, 1–10 (2020).

202. Xiao, K. *et al.* Solution-processed monolithic all-perovskite triple-junction solar cells with efficiency exceeding 20%. *ACS Energy Lett.* **5**, 2819–2826 (2020).

203. Wang, Z. *et al.* Suppressed phase segregation for triple-junction perovskite solar cells. *Nature* **618**, 74–79 (2023).

204. Choi, Y. J., Lim, S. Y., Park, J. H., Ji, S. G. & Kim, J. Y. Atomic Layer Deposition-Free Monolithic Perovskite/Perovskite/Silicon Triple-Junction Solar Cells. *ACS Energy Lett.* **8**, 3141–3146 (2023).

205. Heydarian, M. *et al.* Monolithic Two-Terminal Perovskite/Perovskite/Silicon Triple-Junction Solar Cells with Open Circuit Voltage >2.8 V. *ACS Energy Lett.* **8**, 4186–4192 (2023).

206. Wang, J. *et al.* Halide homogenization for low energy loss in 2-eV-bandgap perovskites and increased efficiency in all-perovskite triple-junction solar cells. *Nat. Energy* **9**, 70–80 (2024).

207. Turren-Cruz, S. H., Hagfeldt, A. & Saliba, M. Methylammonium-free, high-performance, and stable perovskite solar cells on a planar architecture. *Science* **362**, 449–453 (2018).

208. Hang, P. *et al.* Highly Efficient and Stable Wide-Bandgap Perovskite Solar Cells via Strain Management. *Adv. Funct. Mater.* **33**, 2214381 (2023).

209. Farag, A. *et al.* Mitigation of Open-Circuit Voltage Losses in Perovskite Solar Cells Processed over Micrometer-Sized-Textured Si Substrates. *Adv. Funct. Mater.* **33**, 2210758 (2023).

210. Kim, S. G. *et al.* How antisolvent miscibility affects perovskite film wrinkling and photovoltaic properties. *Nat. Commun.* **12**, 1–10 (2021).

211. Bush, K. A. *et al.* Controlling Thin-Film Stress and Wrinkling during Perovskite Film Formation. *ACS Energy Lett.* **3**, 1225–1232 (2018).

212. Braunger, S. *et al.* Cs x FA1- xPb(I1- yBr y)3 Perovskite Compositions: The Appearance of Wrinkled Morphology and its Impact on Solar Cell Performance. *J. Phys. Chem. C* **122**, 17123–17135 (2018).

213. Chen, J. *et al.* High-Performance Thickness Insensitive Perovskite Solar Cells with Enhanced Moisture Stability. *Adv. Energy Mater.* **8**, 1800438 (2018).

214. Zhou, Y. *et al.* Manipulating Crystallization of Organolead Mixed-Halide Thin Films in Antisolvent Baths for Wide-Bandgap Perovskite Solar Cells. *ACS Appl. Mater. Interfaces* **8**, 2232–2237 (2016).

215. Ma, J. *et al.* Unraveling the Impact of Halide Mixing on Crystallization and Phase Evolution in CsPbX3 Perovskite Solar Cells. *Matter* **4**, 313–327 (2021).

216. Liu, K., Wang, Z., Qu, S. & Ding, L. Stress and Strain in Perovskite/Silicon Tandem Solar Cells. *Nano-Micro Lett.* **15**, 1–5 (2023).

217. Li, X. *et al.* A vacuum flash-assisted solution process for high-efficiency large-area perovskite solar cells. *Science* **353**, 58–62 (2016).

218. Xiang, W. *et al.* Intermediate phase engineering of halide perovskites for photovoltaics. *Joule* **6**, 315–339 (2022).

219. Liu, J. *et al.* Efficient and stable perovskite-silicon tandem solar cells through contact displacement by MgFx. *Science* **377**, 302–306 (2022).

220. Chung, J. *et al.* Engineering Perovskite Precursor Inks for Scalable Production of High-Efficiency Perovskite Photovoltaic Modules. *Adv. Energy Mater.* **2300595**, 1–10 (2023).

221. Gerber, A. *et al.* Advanced large area characterization of thin-film solar modules by electroluminescence and thermography imaging techniques. *Sol. Energy Mater. Sol. Cells* **135**, 35–42 (2015).

222. Chen, R. *et al.* Robust hole transport material with interface anchors enhances the efficiency and stability of inverted formamidinium–cesium perovskite solar cells with a certified efficiency of 22.3%. *Energy Environ. Sci.* **15**, 2567–2580 (2022).

223. Zheng, X. *et al.* Defect passivation in hybrid perovskite solar cells using quaternary ammonium halide anions and cations. *Nat. Energy* **2**, 1–9 (2017).

224. Xu, J. *et al.* Triple-halide wide-band gap perovskites with suppressed phase segregation for efficient tandems. *Science* **367**, 1097–1104 (2020).

225. Lee, H., Kang, S. B., Lee, S., Zhu, K. & Kim, D. H. Progress and outlook of Sn–Pb mixed perovskite solar cells. *Nano Converg.* **10**, (2023).

List of publications and conference contributions

Peer-reviewed publications (first author)

Hang Hu, Sophie X. An, Yang Li, Seyedamir Orooji, Roja Singh, Fabian Schackmar, Felix Laufer, Qihao Jin, Thomas Feeney, Alexander Diercks, Fabrizio Gota, Somayeh Moghadamzadeh, Ting Pan, Michael Rienäcker, Robby Peibst, Bahram Abdollahi Nejand, and Ulrich W. Paetzold, Triple-junction perovskite–perovskite–silicon solar cells with power conversion efficiency of 24.4%. *Energy & Environmental Science*, 17, 2800–2814, 2024.

Hang Hu, David B. Ritzer, Alexander Diercks, Yang Li, Roja Singh, Paul Fassl, Qihao Jin, Fabian Schackmar, Ulrich W. Paetzold, and Bahram Abdollahi Nejand, Void-free buried interface for scalable processing of *p*-*i*-*n*-based $FAPbI_3$ perovskite solar modules. *Joule*, 7, 1574–1592, 2023.

Hang Hu, Somayeh Moghadamzadeh, Raheleh Azmi, Yang Li, Milian Kaiser, Jan C. Fischer, Qihao Jin, Julia Maibach, Ihteaz M. Hossain, Ulrich W. Paetzold, and Bahram Abdollahi Nejand, Sn-Pb mixed perovskites with fullerene-derivative interlayers for efficient four-terminal all-perovskite tandem solar cells. *Advanced Functional Materials*, 32, 2107650, 2022.

Peer-reviewed publications (co-author)

Qihao Jin, Qiaoshuang Zhang, Christian Rainer, **Hang Hu**, Junchi Chen, Tim Gehring, Jan Dycke, Roja Singh, Ulrich. W. Paetzold, Gerardo Hernández-Sosa, Rainer Kling, and Uli Lemmer, Inkjet-Printed Optical Interference Filters. *Nature Communications*, 15, 3372, 2024.

Yang Li, **Hang Hu**, Ahmed Farag, Thomas Feeney, Isabel Allegro, Uli Lemmer, Ulrich W. Paetzold, and Ian A. Howard, Enhancement of amplified spontaneous emission by electric field in $CsPbBr_3$ perovskites. *Nano Letters*, 23, 1637–1644, 2023.

Fabrizio Gota, Sophie X. An, **Hang Hu**, Bahram Abdollahi Nejand, and Ulrich W. Paetzold, Energy yield modeling of bifacial all-perovskite two-terminal tandem photovoltaics. *Advanced Optical Materials*, 11, 2201691, 2023.

Ahmed Farag, Paul Fassl, **Hang Hu**, Thomas Feeney, Aina Quintilla, Marco A. Ruiz-Preciado, Wolfram Hempel, Dominik Bagrowski, Philipp Noack, Bianca Wattenberg, Torsten Dippell, and Ulrich W. Paetzold, Mitigation of open-circuit voltage losses in perovskite solar cells processed over micrometer-sized-textured Si substrates. *Advanced Functional Materials*, 33, 2210758, 2023.

David B. Ritzer, Bahram Abdollahi Nejand, Marco A. Ruiz-Preciado, Saba Gharibzadeh, **Hang Hu**, Alexander Diercks, Thomas Feeney, Bryce S. Richards, Tobias Abzieher, and

Ulrich W. Paetzold, Translucent perovskite photovoltaics for building integration. *Energy & Environmental Science*, 16, 2212–2225, 2023.

Bahram Abdollahi Nejand, David B. Ritzer, **Hang Hu**, Fabian Schackmar, Somayeh Moghadamzadeh, Thomas Feeney, Roja Singh, Felix Laufer, Raphael Schmager, Raheleh Azmi, Milian Kaiser, Tobias Abzieher, Saba Gharibzadeh, Erik Ahlswede, Uli Lemmer, Bryce S. Richards, and Ulrich W. Paetzold, Scalable two-terminal all-perovskite tandem solar modules with a 19.1% efficiency. *Nature Energy*, 7, 620–630, 2022.

Julie Roger, Luisa K. Schorn, Minasadat Heydarian, Ahmed Farag, Thomas Feeney, Daniel Baumann, **Hang Hu**, Felix Laufer, Weiyuan Duan, Kaining Ding, Andreas Lambertz, Paul Fassl, Matthias Worgull, and Ulrich W. Paetzold, Laminated Monolithic Perovskite/Silicon Tandem Photovoltaics. *Advanced Energy Materials*, 12, 2200961, 2022.

Marco A Ruiz-Preciado, Fabrizio Gota, Paul Fassl, Ihteaz M Hossain, Roja Singh, Felix Laufer, Fabian Schackmar, Thomas Feeney, Ahmed Farag, Isabel Allegro, **Hang Hu**, Saba Gharibzadeh, Bahram Abdollahi Nejand, Veronique S Gevaerts, Marcel Simor, Pieter J Bolt, and Ulrich W. Paetzold, Monolithic two-terminal perovskite/CIS tandem solar cells with efficiency approaching 25%. *ACS Energy Letters*, 7, 2273–2281, 2022.

Somayeh Moghadamzadeh, Ihteaz M. Hossain, Moritz Loy, David B. Ritzer, **Hang Hu**, Dirk Hauschild, Adrian Mertens, Jan-Philipp Becker, Amir A. Haghighirad, Erik Ahlswede, Lothar Weinhardt, Uli Lemmer, Bahram Abdollahi Nejand, and Ulrich W. Paetzold, In_2O_3:H-based hole-transport-layer-free tin/lead perovskite solar cells for efficient four-terminal all-perovskite tandem solar cells. *ACS Applied Materials & Interfaces*, 13, 46488–46498, 2021.

Jonas A. Schwenzer, Tim Hellmann, Bahram Abdollahi Nejand, **Hang Hu**, Tobias Abzieher, Fabian Schackmar, Ihteaz M. Hossain, Paul Fassl, Thomas Mayer, Wolfram Jaegermann, Uli Lemmer, and Ulrich W. Paetzold, Thermal stability and cation composition of hybrid organic–inorganic perovskites. *ACS Applied Materials & Interfaces*, 13, 15292–15304, 2021.

Wensheng Yan, Lingyun Mao, Peiyang Zhao, Adrian Mertens, Stephan Dottermusch, **Hang Hu**, Zhong Jin, and Bryce S. Richards, Determination of complex optical constants and photovoltaic device design of all-inorganic CsPbBr3 perovskite thin films. *Optics express*, 28, 15706–15717, 2020.

Somayeh Moghadamzadeh, Ihteaz M. Hossain, Saba Gharibzadeh, Tobias Abzieher, Huyen Pham, **Hang Hu**, Paul Fassl, Uli Lemmer, Bahram Abdollahi Nejand, and Ulrich W. Paetzold. Triple-cation low-bandgap perovskite thin-films for high-efficiency four-terminal all-perovskite tandem solar cells. *Journal of Materials Chemistry A*, 8, 24608–24619, 2020.

Roja Singh, **Hang Hu**, Thomas Feeney, Alexander Diercks, Felix Laufer, Yang Li, The Duong, Fabian Schackmar, Bahram, Abdollahi Nejand, and Ulrich W. Paetzold, Stability of

perovskite solar cells: impact of stoichiometry and morphology under different stress conditions. Under review, 2024.

Contributions to conferences

Hang Hu, David B. Ritzer, Alexander Diercks, Yang Li, Roja Singh, Paul Fassl, Bahram Abdollahi Nejand, and Ulrich W. Paetzold, Scalable Efficient *p*-*i*-*n*-based $FAPbI_3$ Perovskite Solar Modules. PVSE-34, Shenzhen, China, 2023.

Roja Singh, **Hang Hu**, Thomas Feeney, Alexander Diercks, Felix Laufer, Fabian Schackmar, Bahram, Abdollahi Nejand, and Ulrich W. Paetzold, The determining factor of degradation in perovskite solar cells: material stoichiometry, quenching technique, or stress factors? ISOS14, Yokohama, Japan, 2023.

Julie Roger, Luisa K. Schorn, Minasadat Heydarian, Ahmed Farag, Thomas Feeney, Daniel Baumann, **Hang Hu**, Felix Laufer, Weiyuan Duan, Kaining Ding, Andreas Lambertz, Paul Fassl, Matthias Worgull, and Ulrich W. Paetzold, Novel lamination approach for fabrication of monolithic perovskite/silicon tandem photovoltaics. PVSEC-33, Nagoya, Japan, 2022.

Julie Roger, Luisa K. Schorn, Minasadat Heydarian, Ahmed Farag, Thomas Feeney, Daniel Baumann, **Hang Hu**, Felix Laufer, Weiyuan Duan, Kaining Ding, Andreas Lambertz, Paul Fassl, Matthias Worgull, and Ulrich W. Paetzold, Novel lamination approach for fabrication of monolithic perovskite/silicon tandem photovoltaics. Tandem PV Workshop, 2022.

Marco A. Ruiz-Preciado, Ihteaz M. Hossain, Thomas Feeney, Ahmed Farag, **Hang Hu**, Saba Gharibzadeh, Fabrizio Gota, Roja Singh, Marcel Simor, Pieter J. Bolt, and Ulrich W. Paetzold. Highly efficient perovskite-CIS monolithic tandem solar cells. Material Research Society, 2022.

Acknowledgements

Embarking on a Ph.D. journey is my fortunate as I worked with my talented and dedicated colleagues over the past few years. I express my sincere gratitude to the professors, colleagues, friends, and families who have been the pillars of support throughout my Ph.D. life. Their guidance, encouragement, support, and unwavering belief in my capabilities and talents have been shaping my personal growth and academic skills during this challenging and transformative journey.

First and foremost, I am deeply grateful to Chinese Scholarship Council (CSC) for supporting my Ph.D. study in Germany.

I would like to express my deep appreciation to my acdemic supervisor Prof. Dr. Ulrich W. Paetzold. I appreciate him for giving me the opportunity to pursue my Ph.D. in the great group. His continuous guidance, encouragement, enthusiasm, and professional support sweep many barriers away in my doctoral research work.

I would like to give my special thanks to my co-supervisor Dr. Bahram Abdollahi Nejand. I am grateful for his invaluable contribution and support to my research work. He gave me a a large freedom and support in my experimental work. His abundant experience, suggestion, motivation, and patience make my Ph.D. period less frustrated.

I would like to take this opportunity to thank all my collegues and friends in the graet taskforce group at Institute of Microstructure Technology (IMT) and the Light Technology Institute (LTI) in Karlsruhe Institute of Technology (KIT). The stunning working atmosphere and fruitful scientific discussions are supported with Dr. Yang Li, Dr. Somayeh Moghadamzadeh, Dr. Paul Fassl, Dr. Fabian Schackmar, Dr. Marco A Ruiz-Preciado Dr. Ihteaz M. Hossain, Dr. Saba Gharibzadeh, Dr. Simon Ternes, Dr. Raphael Schmager, Dr. Helge Eggers, Dr. Jonas A. Schwenzer, Dr. Isabel Allegro, Dr. Tobias Abzieher, Dr. Ahmed Farag, Roja Singh, Thomas Feeney, Alexander Diercks, David B. Ritzer, Felix Laufer, Sophie X. An, Seyedamir Orooji, Fabrizio Gota, Ting pan, Xuzheng Liu, Julie Roger, Kristina Geistert, Ronja Pappenberger, Julian Petry, Benjamin Hacene, Daniel Baumann, Raphael Pesch, Mohammad Gholipoor, Julian Petermann, Pariya Nazari, Dr. Rohit Chavan, Dr. Faranak Sadegh, Dr. Mahmoud Hassan, indeed as well as all other former and current group members. I also thank my Chinese friends at LTI for the leisure activities beyond the scientific work with Yang Li, Qihao Jin, Qiaoshuang Zhang, Junchi Chen, Ting Pan, Xuzheng Liu, Weimu Xu, Shudong Yu, Bing Guo. I had so much enjoyable time with my collegues and friends.

I sincerely acknowledge the scientific collaboration with Prof. Dr. Bryce S. Richards, Prof. Dr. Uli Lemmer, Dr. Raheleh Azmi, Dr. Julia Maibach, Dr. Milian Kaiser, Jan C. Fischer, Dr. Michael Rienäcker (ISFH), Dr. Robby Peibst (ISFH). Furthermore, I would like to thank Prof. Dr. Felix Deschler for taking his time and efforts as my second reviewer.

I want to express my deep gratitude to my families who are giving me for their unconditional love and support throughout my life. In particular, I would like to express my deepest appreciation to my beloved girlfriend Ms. Mengqin Kong who is always keeping unwavering love, trust, care, and encouragement during the long journey from master study to now on. This is the best support that we are staying together in Germany and witnessing both personal growth and enjoyable gratitude to our life.